THÈSE DE DOCTORAT
DE L'UNIVERSITÉ PARIS DIDEROT – PARIS 7
SORBONNE PARIS CITÉ

Spécialité Physique

École doctorale « Physique en Île-de-France »

réalisée

à l'UMR Matière et Systèmes Complexes CNRS 7057,
Université Paris Diderot – Paris 7 SPC

présentée par

Simon MERMINOD

pour obtenir le grade de

DOCTEUR DE L'UNIVERSITÉ PARIS DIDEROT – PARIS 7

Sujet de la thèse :

Auto-organisation de particules magnétiques vibrées : Structure, dynamique et transitions

soutenue le 6 octobre 2016

devant le jury composé de :

Prof.	Médéric ARGENTINA	Rapporteur
Dr.	Yoël FORTERRE	Rapporteur
Dr.	Thierry DAUXOIS	Président du jury
Dr.	Eric BERTIN	Examinateur
Dr.	Michel SAINT JEAN	Examinateur
Prof.	Nicolas VANDEWALLE	Examinateur
Dr.	Eric FALCON	Directeur de thèse
Dr.	Michaël BERHANU	Co-directeur de thèse

This doctoral dissertation is the outcome of my research in the laboratory *Matière et Systèmes Complexes* under the supervision of Michael Berhanu and Eric Falcon. Our work led to the publication of two papers. The first one [1] deals with the transition from a dissipative to a quasi-elastic state in a granular gas and is presented in Chapter 4, while the second one [2] focuses on the transition to a labyrinthine phase in this granular system and is reported in Chapter 5. At least three more papers containing the results of Chapter 6 and of the two ongoing collaborations mentioned in the Conclusion should be published.

Laboratoire Matière et Systèmes Complexes

UMR CNRS 7057
10, rue Alice Domon et Léonie Duquet – 75205 Paris Cedex 13 – FRANCE

Université Paris Diderot – Paris 7
Sorbonne Paris Cité

Résumé

Auto-organisation de particules magnétiques vibrées : structure, dynamique et transitions

Nous étudions l'auto-organisation dans un système modèle expérimental où l'agitation des particules et leurs interactions à distance sont en compétition. Ce système est composé de particules macroscopiques sphériques ferromagnétiques douces dans une cellule horizontale quasi-bidimensionnelle. Les particules sont agitées par vibration verticale de la cellule et acquièrent un moment magnétique induit en présence d'un champ magnétique externe vertical. En ajustant l'équilibre entre les forces dipolaires répulsives résultantes et l'agitation, nous provoquons des transitions entre des états de types fluides et solides. A faible densité de particules, nous examinons les phases et les transitions de phases rencontrées lorsque nous renforçons les interactions entre particules : d'abord un gaz granulaire dissipatif, puis un état dont les propriétés structurales et dynamiques s'approchent de celles d'un gaz idéal à l'équilibre thermodynamique, et enfin un état ordonné où les particules forment un réseau triangulaire. Nous nous intéressons aussi à l'auto-organisation du système à plus haute densité de particules, où nous observons un état labyrinthique désordonné principalement composé de chaînes de particules en contact. Ces chaînes, en zigzag entre la surface de la cellule et le couvercle, sont énergétiquement favorisées par l'anisotropie des interactions dipolaires. Nous caractérisons la transition de l'état de gaz granulaire vers cette phase labyrinthique. Enfin, nous explorons l'évolution temporelle de la phase labyrinthique au moyen d'une trempe magnétique. Nous observons une nucléation homogène aux temps courts et une augmentation de la taille typique des chaînes via une relaxation lente aux temps longs.

Mots-clés Milieux granulaires, systèmes hors équilibre, transitions de phase, états désordonnés, dynamique vitreuse.

Abstract

Self-organization of vibrated and magnetized particles: structure, dynamics and transitions

We study self-organization in an experimental model system in which particle agitation competes with remote inter-particle interactions. This system is composed of macroscopic spherical soft-ferromagnetic particles in a horizontal quasi-two-dimensional cell. The particles are agitated by vibrating the cell vertically and are magnetized as induced dipoles by an external vertical magnetic field. By tuning the balance between the resulting repulsive dipole-dipole forces and agitation, we trigger transitions between fluid- and solid-like states. At low particle density, we examine the phases and phase transitions that occur as we strengthen the inter-particle interactions: from a dissipative granular gas, to a state whose structural and dynamical properties approach those of an ideal gas at thermodynamic equilibrium, to an ordered state in which the particles form a triangular lattice. We also investigate the self-organization of the system at a higher particle density, where we observe a disordered labyrinthine state mostly composed of chains of particles at contact. These chains, buckled between the top and bottom plates, are energetically favored due to the anisotropy of the dipole-dipole interactions. We characterize the transition from the granular gas state to this labyrinthine phase. Finally, we explore the temporal evolution of the labyrinthine phase by applying a magnetic quench. We observe homogeneous nucleation at short times and coarsening via slow relaxation at long times.

Keywords Granular media, out-of-equilibrium statistical mechanics, phase transitions, disordered states, glassy dynamics.

Remerciements

Mes premiers remerciements vont aux membres de mon jury : Médéric Argentina et Yoël Forterre, pour avoir accepté de rapporter cette thèse, ainsi qu'Eric Bertin, Thierry Dauxois, Michel Saint Jean et Nicolas Vandewalle, pour avoir bien voulu faire partie de mon jury.

Michaël Berhanu et Eric Falcon m'ont patiemment guidé, constamment encouragé et énormément appris pendant ces trois années. Ils m'ont aussi laissé une précieuse liberté de travail. Je les en remercie vivement tous les deux.

Durant ces trois années, j'ai eu la chance d'échanger et de travailler avec de nombreuses personnes au laboratoire et en dehors de celui-ci. Réflechir sur le comportement de grains magnétiques, réels ou virtuels, avec Eric Opsomer et Nicolas Vandewalle, de l'Université de Liège, s'est révélé être tant intéressant et stimulant qu'agréable. Je leur en suis très reconnaissant. Notre collaboration a en partie reposé sur un financement de l'Agence Spatiale Européenne, ce pour quoi je la remercie. Merci aussi à Gustavo Castillo, de l'Universidad de Chile, pour notre collaboration portant sur la transition de cristallisation du gaz granulaire magnétique. Merci également à Claude Laroche, avec qui nous avons réfléchi aux effets d'un champ magnétique incliné sur le système, ainsi qu'à Yann Chalopin, de Centrale Paris, pour nos discussions enrichissantes et ses simulations au cours de ma premère année de thèse. Frédéric Lechenault et José Da Silva, de l'ENS, nous ont donné accès à leur outil de sandblasting ; Vincent Dupuis, de l'UPMC, a effectué les mesures de magnétisation de billes ; Maxime Costalonga a réalisé des mesures de rugosité au microscope ; je les en remercie.

Je suis particulèrement reconnaissant envers les personnes du labo avec lesquelles j'ai le plus interagi et qui nous ont apporté des idées et conseils : Bérengère Abou, Jean-Claude Bacri, Sylvain Courrech du Pont, Julien Derr, Martin Devaud, Marc Durand, Chi-Tuong Pham, Matthieu Roché, Michel Saint Jean et Julien Tailleur. Martin Devaud et Thierry Hocquet nous ont grandement aidé en nous permettant d'utiliser occasionnellement leur salle de manip et d'effectuer de longs traitements de données sur leur ordinateur. Dans l'équipe, un grand merci à Luc, Timothée, Leonardo, Florence et Annette pour le partage convivial de la salle de manip, pour nos échanges à MSC ou de l'autre côté de l'Atlantique et parfois même pour

m'avoir accueilli sous leur toit loin de Paris. Luc, Timothée et Leonardo m'ont apporté une aide précieuse pour résoudre certains problèmes numériques, en particulier au début de ma thèse.

Je tiens aussi à remercier celles et ceux qui font – ou ont fait – tourner le laboratoire : Laurent Limat et son prédécesseur Loïc Auvray, ainsi que Carole Barache, Nadine Beyer, Lucie Bouchu, Marlène Hanoomie, Maeva et Sarah Semhoun. Joëlle Taieb, de l'ED, a toujours été une interlocutrice agréable et attentive. Merci à Alexandre Lantheaume, Yann Le Goas et Laurent Réa, qui, aux ateliers, ont fabriqué mes cellules expérimentales et m'ont apporté leur aide précieuse pour des bricolages divers.

Merci bien sûr à tous les doctorants du labo avec lesquels j'ai partagé mon quotidien, que ce soit dans le thésarium 768A, autour d'un café ou d'une mousse, au séminaire thésards ou ailleurs : Agnese, Alexandre, Alexis, David, Etienne, Fanny, Florent, François, Gwennhaël, Iris, Jeanne, Kevin, Marc, Mathieu et Matthieu, Maxime, Mourtaza, Nico, Olivier, Pauline, Rémy, Ruben, Stéphane, Tanguy et Tanguy, Thomas, Tommy,... Evidemment un très grand merci à Nico et Mourtaza, pour ces moments inoubliables de grimpe et activités parallèles, du Mur à la Bourgogne en passant par le Beaufortain.

L'école d'été de Boulder 2015, *Soft Matter In and Out Of Equilibrium*, a été pour moi une expérience unique, tant exaltante scientifiquement qu'humainement. Je tiens donc à en remercier les organisateurs, Mark Bowick, William Irvine, M. Cristina Marchetti, Leo Radzihovsky et Vincenzo Vitelli, les orateurs et les étudiants. Parmi ces derniers, Sofia, Mathijs, Raphael, Benny, Lee, Tal et Paul sont ceux auxquels je pense en premier, même s'il me serait facile de citer ici une bonne moitié de l'école.

Pour finaliser ce manuscrit, j'ai eu la chance de bénéficier d'une relecture anglophone attentive et instructive ; je suis profondément reconnaissant envers la consciencieuse personne qui a consacré de son temps à cette tâche fastidieuse.

Merci également à toutes celles et ceux avec qui je passe du temps en dehors du labo. Notre agréable colocation avec Lise a été pour moi une précieuse constante au cours de cette thèse ; Benjamin, Camille, Delphine et Marc, Marion, Marjorie, Mickaël, Pierre-Louis et Pierrick m'apportent leur précieuse amitié depuis de nombreuses années et leur présence m'a été essentielle ; passer de beaux week-ends avec Marie et Yann m'a invariablement apporté une énergie nouvelle ; Pierre m'a souvent nourri de son esprit vif, ouvert et positif ; les agréables soirées avec Michou et Aurélie me resteront en mémoire, ainsi que tous ces bons moments, souvent très gastronomiques, avec Alexandre et Michael. Il va aussi sans dire que les joyeux Lémuriens, dont les rires, l'envie de partager et la soif de grimper sont extrêmement contagieux, ont été une source inépuisable d'énergie et de joie pendant ces trois années.

Je tiens enfin à remercier ma famille, pour son inestimable affection et son soutien depuis toujours. Je leur dois infiniment plus que je ne saurais l'écrire.

À mes parents,

Contents

Introduction

From sand to coffee beans to boulders, granular materials are ubiquitous in our daily life. Grains can be made of diverse materials, they have shapes of an extremely wide variety, and sizes that span several orders of magnitude, as illustrated in Fig. 1. Granular materials compose Earth's soil in large part, and for that reason take part in numbers of natural phenomena such as avalanches, landslides, erosion and dune migration —whose understanding is not only exciting from a fundamental perspective, but also crucial for obvious safety and strategical reasons. Out in space, grains aggregate to form planetary rings and celestial bodies from asteroids to natural satellites. Grains are also fundamental to many industries from pharmaceutical to construction, from agricultural to mining to chemical, and thus hold a key role in global economy. Overall, it is fascinating that some physical processes are as much relevant for the packing of cat biscuits, as for the formation of comet 67P/Churyumov–Gerasimenko in the Kuiper belt.

A granular material is an ensemble of a large number of discrete macroscopic particles. If, in the laboratory, a "large number" sometimes means a few thousand particles, it is ideally –as in most natural situations– about or more than 10^6 particles, which is typically the number of sugar grains that you can load on a teaspoon. We refer to macroscopic particles, as Andreotti *et al.* [3], for particles larger than $100\,\mu$m, so that Brownian motion is irrelevant. For instance, it is clear that thermal motion does not affect particles of typical size 1 mm and velocity $1\,\mathrm{cm.s^{-1}}$,

Figure 1 Natural granular matter: a wide variety of sizes, materials and shapes. (a) Sand pile at rest at temple Ginkaku-ji, Kyoto, Japan, of an approximate height 1.80 m. Sand grain typical size is 0.1-1 mm; (b) Coffee beans, of a typical size 1 cm (photography by Arash Toossi); (c) Boulders in Fontainebleau, France, typical size 1 m.

since their kinetic energy is about ten orders of magnitude larger than k_BT. Ensembles of particles of sizes ranging between 1 μm and 100 μm are called powders, while smaller sizes belong to colloids. For the former, van der Waals forces, capillary bridges and air drag are relevant, while for the latter, Brownian motion is often the dominant process. Note that for granular particles as for powders as for colloids, distance interactions of electrostatic or magnetic nature may also be relevant.

When no cohesive or distance forces are at play, granular materials are seemingly all but complicated: only external boundaries and gravity determine the properties of the material. Yet, despite their scientific and technological importance, no unified description of the dynamical behavior of granular media exists today. Compared to our knowledge of conventional solids, liquids and gases, our understanding of granular media is indeed very poor, despite more two centuries of research initiated by pioneering works by Coulomb (static friction, 1773), Faraday (convective instability in a vibrated powder, 1831), Reynolds (dilatancy, 1885), and other distinguished researchers. In particular, there exists no counterpart for granular media of the the Navier-Stokes equation, which provides a unified framework for describing the dynamics of viscous fluids.

The two main reasons for the complexity of granular materials are: interactions are dissipative, and thermal motion is irrelevant; and as such, they fundamentally differ from conventional materials. Indeed, grains interact through solid friction, which arises from micro-scale roughness, and through inelastic collisions, both being dissipative, highly non-linear phenomena. Moreover, in contrast with thermal systems whose agitation enables reaching equilibrium, where all possible configurations are visited according to their Boltzmann weight and where microscopic and macroscopic quantities are related, in the absence of thermal fluctuations, a system is trapped in multiple metastable, steady, out-of-equilibrium states.

The combination of these two aspects makes continuous energy injection mandatory for grains to be agitated and for different configurations to be explored. This can be realized by mechanical forcing at the boundaries (shearing or vibrating), or by bulk forces from external fields (gravitational, electric or magnetic) or from flow of interstitial fluids (water or air) [4]. Then, energy injection is balanced by energy dissipation, which enables the system to reach agitated, out-of-equilibrium stationary states. For instance, solid-, liquid- and gas-like states can be generated in granular systems depending on the quantity and means of injection of energy transferred to the grains: put a thin layer of sand on a plate; with no shaking, the ensemble of grains is at rest and looks like a solid. Now weakly shake it vertically, then grains move collectively and the system behaves like a liquid, a state in which non-trivial patterns may form [4] as illustrated in Fig. 2(a). If now you shake the grains with an acceleration well above the gravitational acceleration, they will fly around and the system may seem like a gas. These different states can even coexist under certain conditions, like in a granular avalanche, as illustrated in Fig. 2(b): grains deep in the bulk stay at rest, while they flow within a surface layer, and some may even be propelled in a ballistic motion above the surface layer [not visible in Fig. 2(b)].

A particularly interesting situation is when an ensemble of grains is strongly shaken in a box. Then, if the density is low enough, the grains interact almost only *via* binary collisions, and otherwise move independently. Even though these collisions are dissipative and energy is continuously injected into the system, it looks like a molecular gas, and for that reason, it is called a *granular gas*.

Based on this analogy, it is possible to define a *granular temperature*, T_g, from the kinetic energy of the grains [6, 7]: $T_g = \frac{2}{d}\left\langle \frac{1}{2}|\mathbf{v} - \langle \mathbf{v} \rangle|^2 \right\rangle$, where d is the dimension of the system, $\mathbf{v}$ is the velocity and $\langle \cdot \rangle$ is an ensemble average. Note that this temperature measures the agitation of

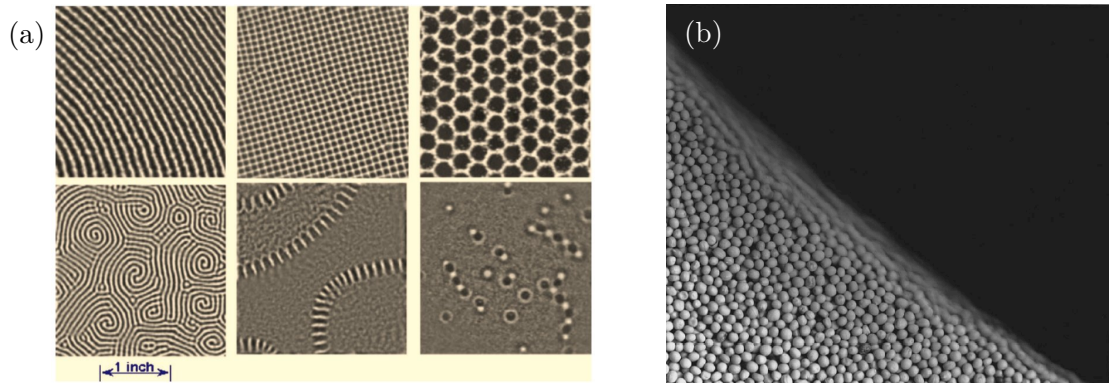

Figure 2 Granular patterns and coexisting states. (a) Representative patterns in vertically vibrated granular layers, in a liquid-like state, for various values of frequency and amplitude of the vibration: stripes, squares, hexagons, spiral, interfaces, and localized oscillons (image by Umbanhowar [4]). (b) A pile of mustard seeds tilted so as to create an avalanche. Particles flow within a surface layer, while underlying seeds stay at rest (image from [5]).

the grains (typically $mT_g \sim 10^{-10}$ J, with $m \sim 10^{-6}$ kg the particle mass), while the usual temperature is relative to the thermal agitation of their microscopic constituents ($k_BT \sim 10^{-21}$ J). Then, by analogy to the kinetic theory of molecular gases, kinetic theories of granular gases have been developed. Based on the inelastic Boltzmann equation, a first set of constitutive laws has been obtained [8], and later generalized to describe more realistic systems, for instance by using a velocity-dependent coefficient of restitution [7] and by including tangential friction [9].

However, several of the hypotheses necessary for obtaining these results —like assuming that particles and flow have well separated scales, that energy input balances energy loss, and that the density is low enough so that collisions are only binary— are strong hypotheses, which limit the range of applicability of these results to only a small number of real systems. Hence, there exists no unified description of granular systems in general [10], and even less is known about system where cohesive or distance forces are at play.

Experiments and numerical simulations of three-dimensional granular gases have lead to the discovery of a number of phenomena. These include the transition from a gas-like state to a bouncing aggregate when the density is increased, called *dynamical clustering* [11] and its equivalent with a motionless aggregate in low-gravity [12, 13], the segregation of particles by size [14] and the breakdown of equipartition in polydisperse systems [15]. Yet, a strong limitation of three-dimensional experiments is that, in general, measurements are restricted to the boundaries (*e.g.*, pressure, impact velocities, impact times, etc.) while information on the bulk of the system, and in particular on the individual particle trajectories inside the bulk, is unattainable.

In contrast, quasi-two-dimensional (Q2D) granular gases enable access to both particle positions and velocities at all times, making it possible to perform a more complete quantitative analysis of the properties of such systems. A Q2D granular gas is typically composed of a few to several thousand particles with a diameter of about 1 mm that are made of hard materials such as glass or metals. The particles are confined in an experimental cell with a fixed volume defined horizontally by walls and vertically by two parallel plates, the lateral dimensions being much larger than vertical extension (typically 10 cm *vs.* a few particle diameters). Except if specifically required, the volume boundaries are made of conducting materials (like ITO, coated glass or polycarbonate plates, metallic walls) so as to avoid electrostatic interactions.

Mechanical energy is continuously provided to the particles, most often by cell vibration [16, 17, 18, 19, 20, 21, 22, 23, 24, 25, 26], but sometimes by electrostatic shaking using an alternating

electric field [27, 28, 29], and more rarely by air flow [30, 31]. Vibrating the cell vertically at a period significantly smaller than the time-scale of the physical process of interest (*e.g.*, the typical time between two collisions), enables the transfer, on average, of the same amount of energy to each particle. In other words, the vibrating cell acts as a "thermostat" that homogeneously "heats" the particles. The motion of each grain is then approximately stochastic, but interactions between grains can make collective effects arise at the macroscopic level due to the large size of the system (thousands of particles). It is then possible, for such systems, to define "macroscopic state functions" such as granular temperature, density or pressure. Moreover, particle motion can be recorded by means of a high-speed video camera, so it is possible to know the particle positions and velocities at all times. Then, as much information as in molecular dynamics simulations is available, except for the vertical position of the particles; however an advantage of experiments it that we can *a priori* run them for much longer times than those accessible in numerical simulations. As such, Q2D granular media have been widely studied during the last two decades not only for understanding granular physics itself, but also as model systems for studying out-of-equilibrium statistical mechanics, nonlinear physics and self-organization in many-body systems.

The phenomenology of Q2D granular systems whose particles interact solely *via* inelastic collisions and friction is very rich. In a pioneering work, Olafsen and Urbach [16] explored the clustering, ordering and inelastic collapse in a vibrated Q2D granular system, shortly after Goldhirsch on Zanetti [32] demonstrated numerically that clustering arises from density fluctuations in non-vibrated "cooling" dissipative gases. These results motivated numerous works, leading to the discovery of striking characteristic properties of granular gases. For instance, in a granular gas, the particles' velocity distributions deviate from the Maxwell-Boltzmann distribution, as expected in systems at thermodynamic equilibrium with no correlations; instead, the velocity distributions are *non-Gaussian* and exhibit high-velocity stretched exponential tails, as observed experimentally [16, 17, 18, 19, 25, 33], in numerical simulations [34, 35, 36], and also predicted by models on the randomly forced inelastic Boltzmann equation [37, 38] (albeit for larger velocities than those observed in the experiments [34, 39]).

Another characteristic phenomenon in Q2D granular gases is solid-fluid *phase coexistence*. The work of Olafsen and Urbach mentioned above [16], for instance, shows the coexistence of a gaseous phase with a hexagonally packed solid cluster formed by inelastic collapse, where there is mechanical equilibrium between the two phases. Such a coexistence was observed again by Losert *et al.* [40], in a system with an amorphous solid phase. When the shaking strength is large enough so that inelastic collapse is not relevant, another type of solid phase can be observed. Indeed, when the driving amplitude or particle density exceeds a critical value [22, 41], a solid phase forms due to strong dissipative interactions between grains in the confined geometry. Castillo *et al.* [42] have shown that this transition can be of either first or second order.

Other phenomena reminiscent of microscopic and colloidal systems include, among others, caging effects [43], crystallization [44], and Kosterlitz-Thouless-Halperin-Nelson-Young (KTHNY)-type two-step melting of a hexagonally ordered solid phase [45].

It is interesting to note that Q2D granular systems with non-spherical particles also show nice analogies with thermal systems. For example, Ben-Naim *et al.* [46] found that the opening times of knots of polymer-like granular chains are well-described by a model of random walks with hard-core exclusion, and Safford *et al.* [47] have shown that the statistical properties of a similar vibrated granular chain are well described by standard models of polymers in equilibrium.

To summarize, Q2D granular gases display ordering effects and transitions that have interesting analogies to phase transitions in microscopic systems. Yet, these transitions are solely

driven by dissipative interactions at contact, namely inelastic collisions and friction, which have no microscopic counterparts. At the microscopic scale, phase transitions have a fundamentally different origin: the competition between thermal agitation and distance interactions (Coulomb, van der Waals, dipolar magnetic interactions, etc.). An exciting idea is then to attempt to generate analogous transitions in a granular model system. A Q2D granular gas with distance interactions between particles can take this role: the macroscopic counterparts of the atoms (or molecules), thermal agitation and microscopic interactions are then respectively granular particles, mechanical agitation, and distance interactions between the grains (electrostatic or magnetic). Then, "macroscopic" phase transitions can be triggered by tuning the balance between distance interactions and mechanical agitation.

Blair and Kudrolli [21] were the first to study a Q2D granular gas with distance interactions. They used permanently magnetized beads at low densities, hence creating a *dipolar fluid*, and reported transitions from gas-like to clusters to networks states. In this case, interactions are mostly attractive and chains of head-to-tail dipoles, rings and hexagonally ordered clusters can form. In similar experiments but at a higher density, Oyarte *et al.* [48] characterized the fluid-solid transition that occurs when the agitation strength is changed. Yet, in these granular dipolar fluids, frictional effects are still very much present.

It appears that granular gases with repulsive distance interactions fit best to the task of producing transitions analogous to microscopic phase transitions. Indeed, in the confined geometry of Q2D systems, self-organization can arise from repulsive distance interactions. Using a granular gas of charged particles weakly agitated, Coupier, Saint Jean and collaborators [23, 24] studied the defect-mediated melting of a crystal seen as analogous to a 2D gas of electrons, or *Wigner crystal*. More recently, Schockmel *et al.* [26] investigated the KTHNY-type two-step crystal melting in a granular gas of induced magnetic dipoles weakly agitated and successfully compared it to the analogous transition in a system of superparamagnetic colloids [49].

These first results are promising but are very few, hence the field of the study of "macroscopic" phase transitions with granular model systems is wide open. Given the great variety of phase transitions observed at the microscopic scale, one can expect a comparatively large quantity of self-organizing effects from distance-interacting granular systems, with, nevertheless, certainly some features arising from the out-of-equilibrium nature of the latter.

In this thesis, we aim at understanding the effects of magnetic dipolar repulsive interactions on the properties of a granular gas. More specifically, we address the following questions: How are the structure and dynamics of the granular gas changed by the magnetic interactions? Can we trigger novel macroscopic fluid-solid transitions analogous to microscopic phase transitions? If so, to what self-organized states? How can we control the properties of these states?

To tackle these questions, we perform experiments on a Q2D granular gas of spherical particles with induced magnetic moment. The originality of our experiments, compared to the other Q2D granular gas experiments, lies in the combination of real-time control of the strength of the particles' magnetization, with accurate control of the processing pathway thanks to complete automation of the devices. In contrast with Schockmel *et al.* [26], who generate magnetic interactions the same way as we do but with a focus on crystal melting, we develop the general understanding of the influence of distance repulsive interactions on the dynamics and structure of granular gases, and compare it to an ideal gas. Furthermore, we demonstrate that disordered labyrinthine phases arising from competing short- and long-range interactions are not restricted to thermal systems and can be obtained in a macroscopic system of particles. Finally, we evidence the non-stationary nature of the granular labyrinthine phase, and quantitatively characterize the different processes occurring at short and long time scales.

Outline of the manuscript

This thesis is composed of six chapters. In chapters 1, 2 and 3, we give technical information regarding the experimental setup and the image and data processing, and provide some theoretical tools. Chapters 4, 5 and 6 are dedicated to the results that we obtained in different regions of the parameter space of the magnetic granular gas. We finally conclude and propose some perspectives for future work.

- In Chapter 1, we introduce the devices and materials composing the experimental setup, and we describe the automated protocol that we designed to perform the experiments;
- In Chapter 2, we specify the successive steps of the image analysis and explain the principles of particle tracking. We also give some details about some key points of data processing;
- In Chapter 3, first, we study the behavior of a permanently magnetized sphere and a ferromagnetic sphere in a magnetic field, a part largely inspired from the reference book of Jackson [50]; second, we analyze the interactions of two magnetized spheres with and without gravity; and third, we provide a few theoretical tools used in Chapter 4, Chapter 5 and Chapter 6.
- In Chapter 4, we examine the magnetic granular gas at a low particle area fraction (about 20 %), when the strength of the magnetic interactions is increased. We demonstrate that, prior to the complete solidification of the granular gas into a crystalline state, the typical properties of this dissipative out-of-equilibrium granular gas are progressively lost, to approach those expected for a usual gas at thermodynamic equilibrium. These results have been published in *EPL* [1];
- In Chapter 5, we investigate the self-organization of the magnetic granular gas at a high particle area fraction (about 50 %), when the strength of the magnetic interactions is increased. We show that the system solidifies into a large scale disordered labyrinthine phase mostly composed of randomly oriented chains of particles in contact, despite the *a priori* repulsive nature of the magnetic forces. We characterize quantitatively this transition and explain the formation of the chains using a simple model. These results have been published in *Physical Review E* [2]. We discuss this simple model in an additional section;
- In Chapter 6, we explore the time evolution of the granular labyrinthine phase. We show that the formation of chains at short times is simply described by a nucleation process, while at long times, the labyrinthine phase undergoes coarsening and a dramatic slowing down of its dynamics.

During this thesis, I have also been involved in an international collaboration devoted to the study of dynamical and statistical properties of granular matter in a low-gravity environment, the Topical Team *Space Grains* of the European Space Agency [51]. The motivation for low gravity is that dissipative collisions between particles are then the only interaction mechanism. The experiments focus on clustering mechanisms, thermal fluctuations, convection, segregation and physical phenomena related to excited granular systems. I contributed to the project during workshops, and in particular to a work submitted for publication about segregation and pattern formation in low gravity.

Chapter 1

Experimental setup

Chapter 1 : Experimental setup

↑ back to contents

Chapter abstract

Our experimental setup is designed to generate a quasi-two-dimensional granular gas of soft-ferromagnetic, spherical particles that interact through tunable magnetic interactions. Particles are mechanically agitated by vertical shaking of the experimental cell, and are magnetized by an externally applied, transverse magnetic field. The horizontal motion of the particles is tracked by means of a high-speed video camera, which gives us access to particle positions and velocities at all times. The specific experimental protocol that we defined is implemented *via* a home-made automation routine. Automation enables us to efficiently probe the large experimental phase space as well as to perform repeated runs with a high level of accuracy.

1.1 Devices and materials

1.1.1 General overview

The experimental setup is mostly composed of an experimental cell of size about $10\,\mathrm{cm}\times10\,\mathrm{cm}$ containing a few thousand particles, an electromagnetic shaker for agitating them mechanically, a pair of coils generating the transverse magnetic field, a circular L.E.D. array that lightens the particles and a high-speed video camera recording the raw images from which the analysis is performed, as shown in Fig. 1.1.

The particles that we use are chromed steel beads of diameter $a = 1\,\mathrm{mm}$, which become magnetized in presence of a magnetic field. These particles are trapped inside a horizontal,

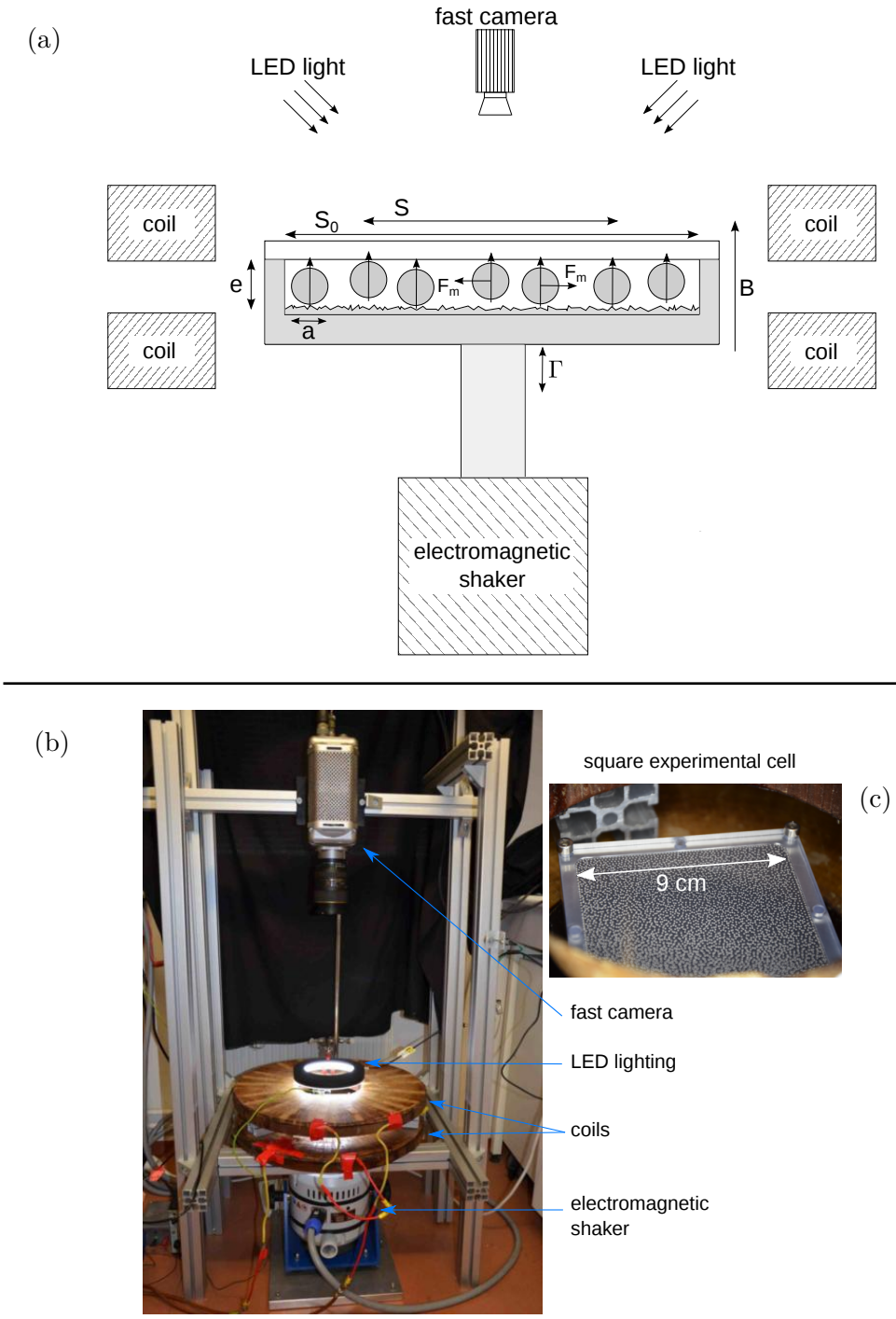

Figure 1.1 Experimental setup. (a) Schematic, side view. Soft ferromagnetic spherical particles of diameter a are placed inside a quasi-two-dimensional cell of gap size e and total area $\mathcal{S}_0$. The cell bottom plate is rough, while the top polycarbonate lid is smooth. The cell is sinusoidally shaken in the vertical direction with a maximum acceleration Γ, by means of an electromagnetic shaker. The cell is immersed in a vertical magnetic field of amplitude B generated by a pair of coils. The particles magnetize and interact *via* repulsive forces in the cell plane. A high-speed video camera records particle motion in the horizontal plane inside the square region of interest of area $\mathcal{S}$. A circular L.E.D. array provides lighting. (b) Picture of the setup. (c) Zoom on the square experimental cell with particles inside.

quasi-two-dimensional aluminum cell. The cell bottom plate is rough and opaque, while the top lid is smooth and transparent. The vertical distance between the two plates, that is, the *gap size*, e, is always larger than one particle diameter and smaller than two particle diameters: $a < e < 2\,a$. We performed experiments with two different cells: a square cell with a high roughness and a fixed gap size, and a circular cell with a lower roughness and a tunable gap size.

The injection of mechanical energy in the system is performed by means of an electromagnetic shaker, which vibrates sinusoidally and vertically the cell. The latter is screwed on top of a vertical, aluminum piston, which is itself fixed to the electromagnetic shaker. These three components are joined together. We checked that measuring the vertical acceleration from an accelerometer fixed to a moving part of the electromagnetic shaker and from another one fixed to the cell provides identical values of the acceleration. When the cell is vibrated, the roughness of the bottom plate scatters the incoming particles in all directions, therefore enhancing horizontal displacements and collisions between the particles. At low density, the horizontal motion of particles is Brownian-like, which is why such a system is called a *granular gas*.

The cell is placed at the center of a pair of coils generating a DC magnetic field in the vertical direction, which is therefore transverse to the cell plane. The magnetic field has a slight radial dependence and is maximum at the cell center. With respect to the cell center, we measured a relative change of 2% at the boundary of the region of interest $\mathcal{S}$, and of 3.5% at the border of the cell $\mathcal{S}_0$, which are both indicated in Fig. 1.1(a) We consider therefore the particles as being immersed in a transverse, homogeneous magnetic field. As such, particles can be viewed as induced magnetic dipoles generated by the transverse magnetic field and whose momentum are parallel and vertically oriented, as illustrated in Fig. 1.1(a).

The particles are lightened from the top through the transparent lid by a circular LED array. A high-speed video camera records images from the top, which constitute the raw data exploited for all analysis.

1.1.2 Particles

The particles that we use are chromed steel (alloy USA class AISI 52100, equivalent to French class 100C6) bearing balls of a diameter $a = 1\,\text{mm}$, manufactured by Marteau & Lemarié [52]. Manufacturer's grade 100 refers to accepted errors of $\pm\,2.5\,\mu\text{m}$ on the diameter and of $2.5\,\mu\text{m}$ on the sphericity, and to a roughness of $0.125\,\mu\text{m}$. The manufacturer provides a ball unitary mass of $m = 4.07 \times 10^{-3}\,\text{g}$ with a density of $\rho = 7830\,\text{kg.m}^{-3}$.

Magnetization measurements

The magnetization-magnetic excitation diagram of a two-dimensional stack of balls of the same class as our steel balls (AISI 52100) but of a diameter 1.2 mm was measured by Shah *et al.* [53]. The authors concluded that these particles do not exhibit any hysteretic behavior and that as such, they do not bear any remnant magnetic field. Note that the value of magnetic susceptibility that they obtained, $\chi = 3.6$, seems to have been used successfully in at least one magnetic granular gas study [26], where experiments were compared with a model.

However, some experimental observations led us to suspect that the balls that we use bear a remnant magnetic moment. Indeed, after immersing the balls in a magnetic field which was eventually turned off, we observed aggregation and chain formation [Fig. 1.2(a)] as reported

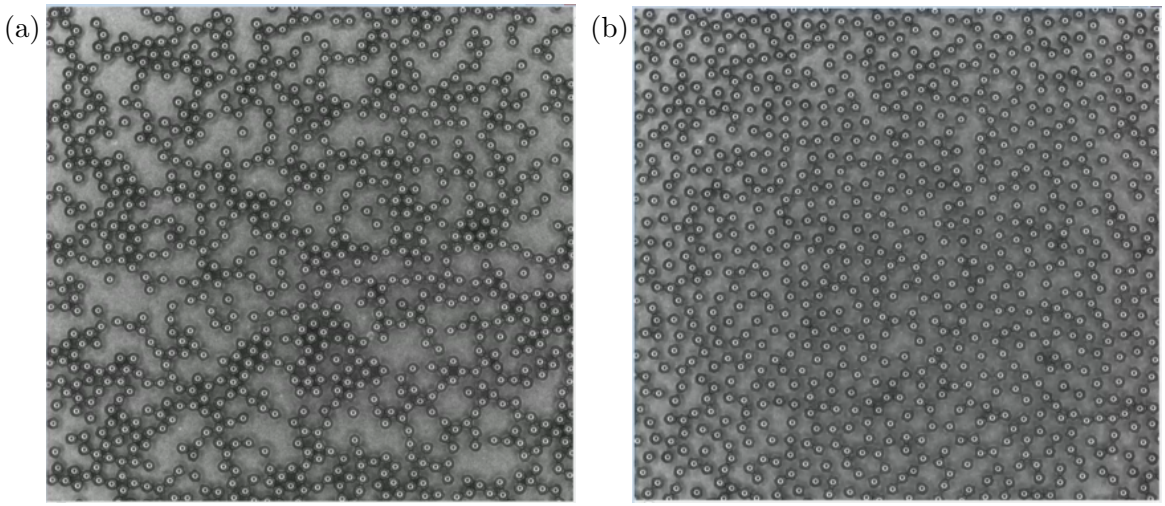

Figure 1.2 Visualizing remnant magnetization in images from experiments with the circular cell, with no shaking and no magnetic field ($\Gamma = 0$ and $B = 0\,\mathrm{G}$). (a) Patterns displayed by balls at rest after being immersed in a magnetic field of 120 G; (b) Bead arrangement after a demagnetization cycle (detailed in Section 1.2.4).

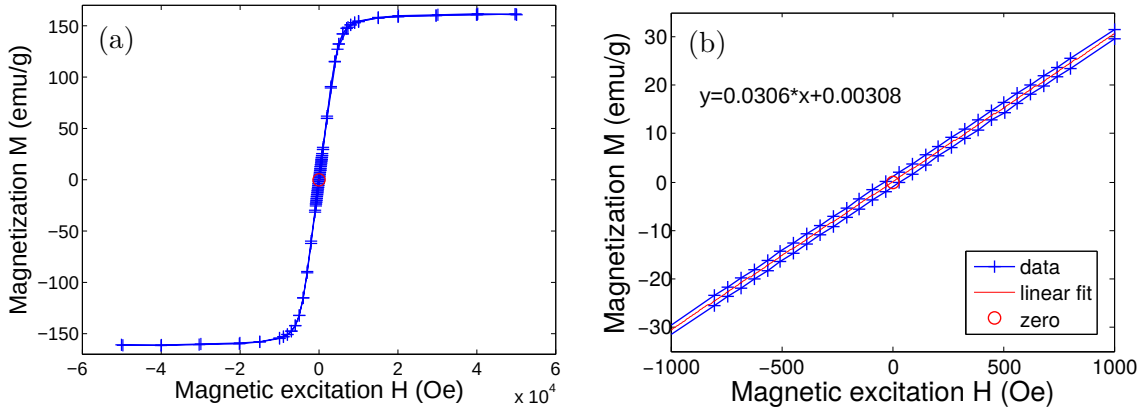

Figure 1.3 Magnetization-magnetic excitation diagram for a chromed steel ball (AISI 52100, diameter $a = 1\,\mathrm{mm}$). (a) Full diagram displaying a linear regime and saturation at $\pm 10^4$ Oe. The red circle shows the initial zero excitation data point. (b) Enlargement of $-1000\,\mathrm{Oe} < H < +1000\,\mathrm{Oe}$, where the hysteretic behavior is clearly exhibited. The red line is a linear fit from the data points showed on this plot, and leads to an estimation of the magnetic permeability of the balls of $\mu_r \sim 500$.

for vibrated permanent magnetic dipoles by Blair and Kudrolli [21]. Such a configuration significantly differs from the spatial distribution obtained with the same balls when they are not magnetized [Fig. 1.2(b)]. To clarify that point, we measured the magnetization diagram for a single ball. These measurements were performed using a Vibrating Sample Magnetometer, by Vincent Dupuis at Université Pierre et Marie Curie. The complete results are shown in Fig. 1.3(a) and the range $-1000\,\mathrm{Oe} < H < 1000\,\mathrm{Oe}$ is enlarged in Fig. 1.3(b).

From these figures we see that the response of magnetization M to magnetic excitation H can be considered linear in the range $\pm$ 1000 Oe. Note that 1 Oe of magnetic excitation corresponds to 1 G of magnetic field. Therefore, we can confidently run experiments with magnetic fields lower than 1000 G while staying in the linear regime. Second, we clearly detect a hysteretic

behavior: as depicted in Fig. 1.2(b), the magnetization curves for the increasing (top blue curve) and decreasing (lower blue curve) magnetic excitations do not match. Quantitatively, the shifts correspond to about ± 30 Oe, which leads us to the conclusion that the remnant magnetization of the balls corresponds to an effective magnetic field of about 30 G. To circumvent this problem, one could either use increasing values of magnetic excitation for successive experiments, or demagnetize the balls after every experiment using a higher magnetic excitation value than the following one (see Section 1.2.4). In practice, we used both methods.

Magnetic susceptibility and magnetic permeability

From the data within the regime of linear response, we can extract a magnetic susceptibility and a magnetic permeability for the ball. Indeed, linearly fitting the data within the ± 1000 Oe range, we obtain the linear curve [in red in Fig. 1.3(b)]:

$$y_{\text{fit}} = p\, x + y_{\text{fit},0} \tag{1.1}$$

with $p = 3.06 \times 10^{-2}$ emu/g and $y_{\text{fit},0} = 3.08 \times 10^{-3}$ emu/g/Oe.

The effective magnetic susceptibility χ_{eff} relates the magnetization M to the magnetic excitation H *via* the linear relation

$$M = \chi_{\text{eff}}\, H, \tag{1.2}$$

hence χ_{eff} corresponds to the slope of the magnetization curve, similarly to p, but is dimensionless. Given that $1\,\text{Oe} = \frac{10^3}{4\pi}$ A/m, and that we can convert the ordinate values in emu/g into A/m by multiplying by $m/V_{b,cm^3} \times 10^3$ with V_{b,cm^3} the volume of one particle in cm^3, we can relate χ_{eff} to p as:

$$\chi_{\text{eff}} = \frac{m}{V_{b,cm^3}} 10^3 \times \left(\frac{10^3}{4\pi}\right)^{-1} p, \tag{1.3}$$

which yields

$$\chi_{\text{eff}} \approx 2.98. \tag{1.4}$$

This value is very close to the limiting case $\chi_{\text{eff}}^{\infty} = 3$ corresponding to an infinite magnetic permeability, μ, as detailed in Chapter 3. Moreover, the effective susceptibility χ_{eff} and the relative magnetic permeability μ_r are related through

$$\chi_{\text{eff}} = 3\,\frac{\mu_r - 1}{\mu_r + 2} \quad \Longleftrightarrow \quad \mu_r = \frac{3 + 2\chi_{\text{eff}}}{3 - \chi_{\text{eff}}} \tag{1.5}$$

which leads to

$$\mu_r \sim 500 \gg 1 \tag{1.6}$$

therefore it is relevant to consider the magnetic permeability of these steel balls as infinite.

1.1.3 Experimental cells

We used two experimental cells made of "Dural" aluminum with a rough bottom and a smooth, transparent lid. The first one is square, while the second one is circular.

Geometries and roughness characteristics

The square cell is made of a block of Dural of size 102 mm × 102 mm × 13 mm on top of which are four confining walls of a height 1.5 mm and a width 6 mm, as illustrated in Fig. 1.4(a). The

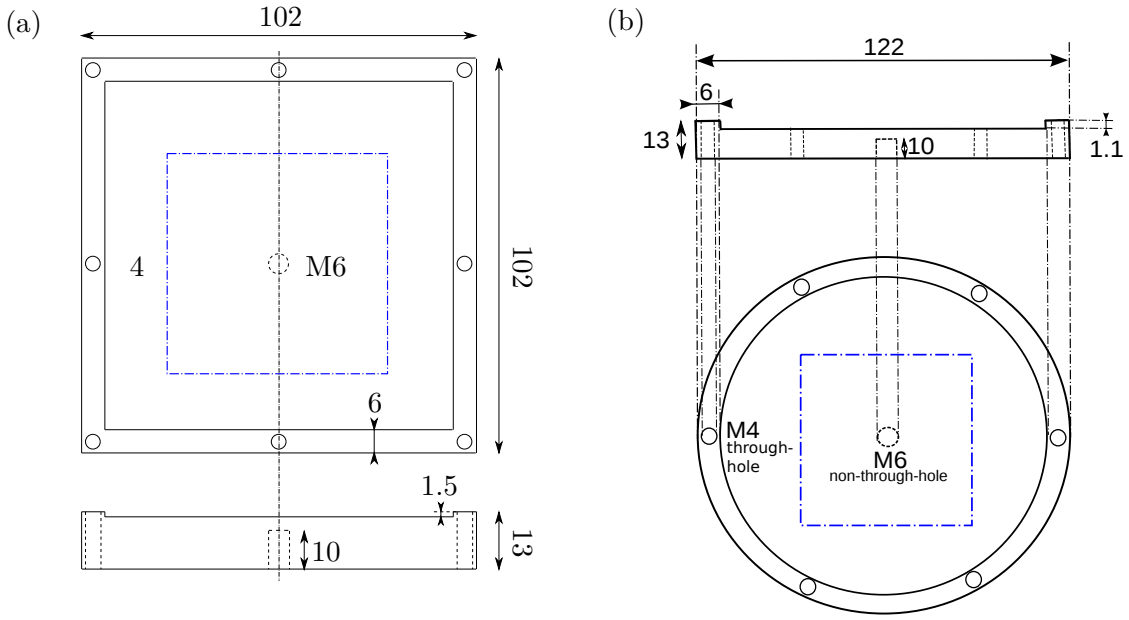

Figure 1.4 Detailed schematics of the two cells. (a) Square cell, top and side views; (b) Circular cell, side and top views. The dash-dotted blue squares show the region of interest of area $\mathcal{S} = 57\,\text{mm} \times 57\,\text{mm}$.

bottom surface is of area $\mathcal{S}_0 = 90\,\text{mm} \times 90\,\text{mm}$. We fix a sticky sandpaper square sheet on the bottom surface of the cell so that it provides roughness to the bottom surface the balls are colliding on. This roughness was characterized by Maxime Costalonga by means of an optical microscope at Université Paris Diderot, and is of RMS amplitude $20\,\mu$m, *i.e.*, about 100 times larger than the particle roughness and about 50 times smaller than a particle diameter. Note that although the confining walls are 1.5 mm high, the height that can be explored by the particles is slightly less than 1.5 mm due to the thickness of the sandpaper.

The circular cell, as shown in Fig. 1.4(b), is composed of a disk of aluminum 122 mm in diameter and of a thickness 13 mm. The confining walls are 1.1 mm high and 6 mm wide, so that the bottom surface of the cell, of area $\mathcal{S}_0$, has a diameter 110 mm. In order to tune the gap size, we use slabs of stainless steel of various thickness (0.05 mm, 0.10 mm, 0.20 mm, 0.25 mm, 0.40 mm and 0.50 mm), cut into pieces of about 1 cm$\times$ 1 cm. We place them next to the screw holes between the top of the confining walls and the polycarbonate lid.

For this cell, the roughness of the bottom surface was obtained by means of an abrasive blasting operation: we propelled a stream of glass beads under high pressure against the Dural surface. This process is called *sandblasting*. By impacting on the target surface, the propelled beads deformed it and thus generated roughness. The bead size was of $\sim$ 10-100μm, enabling us to generate a smaller roughness than the one of the sandpaper. We performed it at École Normale Supérieure, with the help of Frédéric Lechenault and of José Da Silva Quintos.

For both cells, the vertical gap available for the particles is tunable between one and two particle diameters. This way, particles can overlap partially, but never totally. Therefore it makes sense to consider our system as being *quasi-two-dimensional*.

Discussion

Choosing to design a circular cell after having used the square cell comes from two observations. The first one is that when the cell containing the particles contains some angles, particle density inhomogeneities related to this particular shape tended to appear: the density near the corners and along the cell sides is not the same. Secondly, we ware interested in having a cell with physical boundaries that are invariant by rotation, thus minimizing the influence of the self-organization of the beads into disordered patterns.

A sandpaper sheet is coated with an abrasive material whose hardness is higher than that of steel, while Dural aluminum is much softer. Consequently, the advantage of the sandpaper sheet compared to the sandblasted surface is that it is not (or very little) modified by the impact of the steel beads, while the aluminum roughened surface probably becomes smoothed out. On the other hand, the advantages of the sandblasted surface are that, first, it does not make the chromed steel bead dull, which is the case with sandpaper and can lead to particle detection difficulties; and second, its flatness is better than that of the surface with the sticky sandpaper sheet on it.

Lid

For both cells, the confined volume is vertically limited by a polycarbonate lid with an anti-static coating. Linked to the ground, this lid releases the electrostatic charges that may be temporarily carried by particles, allowing us to ignore electrostatic forces for the interactions between particles. The lids are fixed to the aluminum cells by four screws in the square cell and six screws in the circular cell, evenly spaced on the perimeter of the cell.

Area fraction of particles

Given that our system is quasi-two-dimensional, we can define a *particle area fraction*, which we denote ϕ. With N the number of particles in the region of interest of area $\mathcal{S}$ and a the particle diameter, the particle area fraction is

$$\phi = \frac{N\pi a^2}{4\mathcal{S}}. \tag{1.7}$$

In our experiments, ϕ is not a constant because the region of interest does not include the whole bottom plate surface, as illustrated in Fig. 1.4, and as such, particles can enter and exit it. Hence, in the region of interest, the number of particles is not fixed, and it depends on the experimental parameters such as the mechanical excitation and the external magnetic field. For example, for experiments with a total number $N_{\text{tot}} = 2000$ balls in the square cell, N roughly varies between 1200 and 700, implying changes on ϕ from 0.28 to 0.17. With 5000 balls, N varies between 2700 and 1900, modifying ϕ from 0.65 to 0.45.

In the following, we will be also using the *theoretical particle area fraction*, ϕ_{th}, which we define as

$$\phi_{\text{th}} = \frac{N_{\text{tot}}\pi a^2}{4\mathcal{S}_{\text{tot}}} \tag{1.8}$$

where N_{tot} is the total number of particles in the cell and $\mathcal{S}_{\text{tot}}$ is the surface of the cell. For instance, in the case of the square cell, $\phi_{\text{th}} \approx 0.194$ for $N_{\text{tot}} = 2000$ particles, and $\phi_{\text{th}} \approx 0.485$ for $N_{\text{tot}} = 5000$ particles.

1.1.4 Mechanical agitation

Technical description

A cell is vertically, sinusoidally vibrated by means of an electromagnetic shaker. We use an electromagnetic shaker LDS V400 and an amplifier LDS PA100E. The input voltage in the amplifier is controlled *via* an acquisition card (interface NI BNC-2120) itself controlled from a Matlab routine. More details about the automation routine are given in Subsection 1.2.2. We denote f the frequency of the alternating current delivered by the acquisition card to the electromagnetic shaker through the amplifier.

Definition of Γ

The alternating current feeding the electromagnetic shaker is converted into a vertical, sinusoidal displacement of the piston which connects the shaker to the experimental cell. Therefore the cell moves vertically at a frequency f and with an amplitude A according to

$$z(t) = A\sin(2\pi f t). \tag{1.9}$$

In all the experiments presented here, the frequency of mechanical excitation is $f = 300\,\mathrm{Hz}$ and the amplitude A is of the order of $10\,\mu\mathrm{m}$. This value was chosen from the qualitative observation that it optimizes particle mobility in the horizontal plane (tested in the square cell only). The value of the amplitude A was calibrated as a function of the feeding current for both cells (and therefore for both displaced weights) by means of an accelerometer fixed at the base of the piston. The maximum vertical acceleration experienced by the cell is $|\ddot{z}_m| = (2\pi f)^2 A$. From this, we define the *dimensionless acceleration*,

$$\Gamma \equiv \frac{(2\pi f)^2 A}{g} \tag{1.10}$$

where $g \equiv \|\vec{g}\| = 9.81\,\mathrm{m.s^{-2}}$ is the magnitude of the gravitational acceleration. In our experiments, Γ was typically 2 and it never exceeded 5.5.

Calibration and tests of reproducibility

We performed calibrations to relate the output tension from the acquisition card to the shaking strength Γ obtained from the electromagnetic shaker. This operation was performed with the amplifier potentiometer turned to maximum so that the results could be easily recovered later. The results of the calibration operation depend on the weight of the displaced cell. For example, Fig. 1.5 shows the calibration curve with the square cell mounted. Linear fits are satisfying, of type $\Gamma = f_{\mathrm{lin}}^{\mathrm{acc}}(U_{\mathrm{out}})$, with $f_{\mathrm{lin}}^{\mathrm{acc}}$ a linear function with coefficients adjusted for a given cell, and U_{out} the output voltage of the acquisition card.

We performed reproducibility tests for the shaker by performing several successive experiments with the same vibration strength. The goal was to observe a possible effect of the heating of the shaker on its vibrational characteristics. First, feeding with a voltage $U_{\mathrm{out}} = 0.45\,\mathrm{V}$ (generating $\Gamma \approx 2.75$, a value that is higher than most acceleration values we used) during 15 s, measuring Γ, then waiting at 0 V for 5 s, and repeating, generated the following result: the relative change in Γ from a cycle of 1 experiment to a cycle of 30 experiments is smaller than 1 %. A test in which the 0 V stage lasts 20 s instead of 5 s shows a relative change about twice as small. When we reduce U_{out} down to 0.20 V (*i.e.*, $\Gamma \approx 1.25$), no change in Γ is detected, whatever the

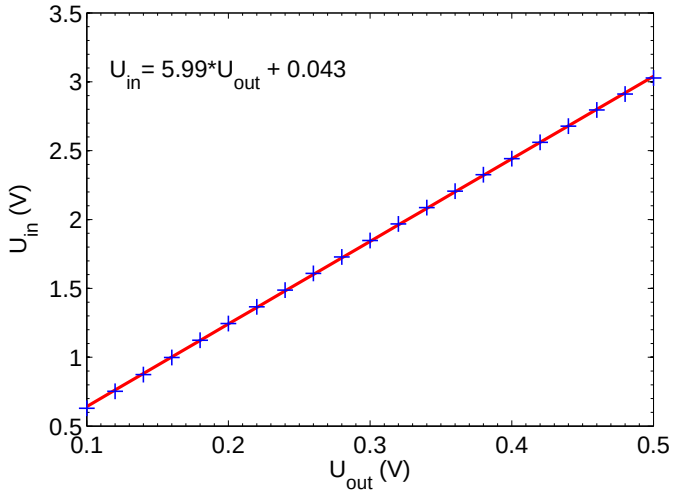

Figure 1.5 Calibration of the ensemble {amplifier LDS PA100E + shaker LDS V400 Series} with the potentiometer of the amplifier turned to maximum, for the square cell. Abscissa U_{out} is the voltage in V going out of the acquisition card (input in the Matlab protocol routine) which feeds the amplifier. Blue +'s: voltage in V recorded from an accelerometer fixed to the piston ($1\,\text{V} \leftrightarrow 1\,g$). Red line: linear fit of the input voltage providing calibration for the shaking strength Γ, whose equation is displayed on the plot.

number of experiments performed successively. We concluded that, within our common range of Γ, heating of the electromagnetic shaker has negligible effects.

It is important to note that, even though a shift from calibration may happen, we would be aware of it since we perform real-time recordings of the actual acceleration for every experiment. More importantly, we will rely on the *measured* value of this parameter, instead of the value *expected* from calibration.

1.1.5 Magnetic excitation

Technical description

In order to generate the external, vertical magnetic field in which the particles are immersed, we use two coils mounted in series and placed horizontally above and bellow the cell. These coils have an internal diameter of 75 mm, an external diameter of 225 mm, and a thickness of 30 mm. They are placed with a vertical separation of 45 mm. They are fed a continuous intensity signal by an amplifier Kepco BOP 36-12ML, which is itself controlled in voltage by the data acquisition card programmed with a Matlab routine. All values of the generated magnetic field are smaller than 500 G ($1\,\text{G} = 10^{-4}\,\text{T}$), which can be produced with a current intensity smaller than 10 A. This allows us to work without cooling the coils. We obtain a satisfyingly homogeneous magnetic field inside the region of interest (relative variation of about 2 %) and across the cell (relative variation of about 3.5 %).

Calibration and tests of reproducibility

The experimental cells are not shielded and the magnetic field generated by the internal permanent magnet of the electromagnetic shaker is about 6 G at the particle level. The calibration of the generated magnetic field as a function of the voltage going out of the acquisition card is shown in Fig. 1.6. The measurements of the vertical magnetic field are performed by means of

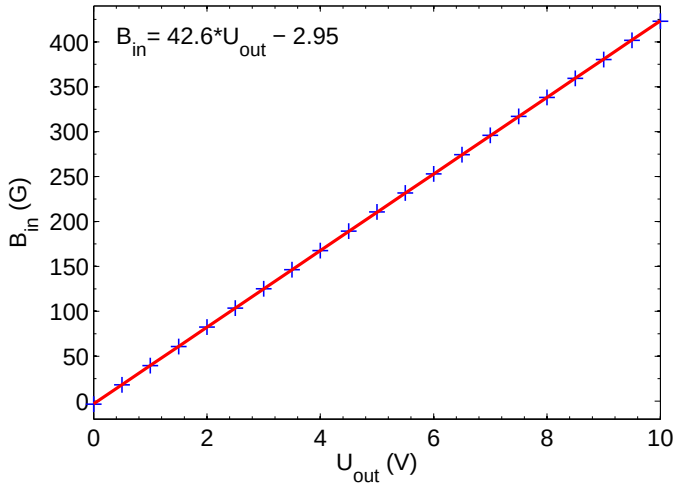

Figure 1.6 Calibration of the coils generating the magnetic field using the Kepco amplifier. Abscissa U_{out} is the voltage in V going out of the acquisition card (input in the Matlab protocol routine) and feeding the amplifier. Blue +'s: magnetic field in Gauss recorded from a Hall sensor placed above the center of the cell. Red line: linear fit of the input voltage providing calibration for the transverse magnetic field B.

a Gaussmeter placed at the center of the cell. Since we are using moderate intensities, a linear regime is obtained and thus the data are pretty well fitted by a linear function $B = f_{\text{lin}}^{\text{bob}}(U_{\text{out}})$, with $f_{\text{lin}}^{\text{bob}}$ a linear function specific to our setup.

As for the electromagnetic shaker, we test the reproducibility of the magnetic field generated by the coils during a long series of experiments. Indeed the coils may actually heat a little, and we would like to quantify this possible effect. Our protocol is as follows. First, we set U_{out} so that the expected magnetic field was of 300 G during 60 s, make a measurement of the real magnetic field B, waited 120 s and repeat. Between the 1$^{\text{st}}$ run and the 15$^{\text{th}}$ run, the magnetic field decreases linearly as the coils were being slightly heated, for a total relative decrease of about 2 %. An analogous test with an expected magnetic field of 200 G reveals a linear decrease of about 1 %. When 100 G is used, no decrease is detected. Therefore, heating does occur for the magnetic field values used in our experiments (from 0 G to more more than 400 G), but only changes of a few percents the obtained value compared to the expected one.

At any rate, as it was the case for the acceleration Γ, we perform real-time measurements of the magnetic field B and use subsequently the *measured* value as a parameter.

Response to a magnetic quench

As we will see in Chapter 6, we will be interested in increasing the magnetic field very quickly. To evaluate the maximum speed at which we can increase the magnetic field, we measure the response of the coils (the Kepco amplifier has a much shorter response time) to increases of magnetic field at different *magnetic quenching rates*,

$$\alpha_q \equiv \frac{\mathrm{d}B}{\mathrm{d}t}. \tag{1.11}$$

The results are presented on Fig. 1.7. For $\alpha_q = 3000\,\text{G.s}^{-1}$, we can consider the magnetic field increase as linear and the oscillations in the transitory regime, at the end of the ramp, as being of

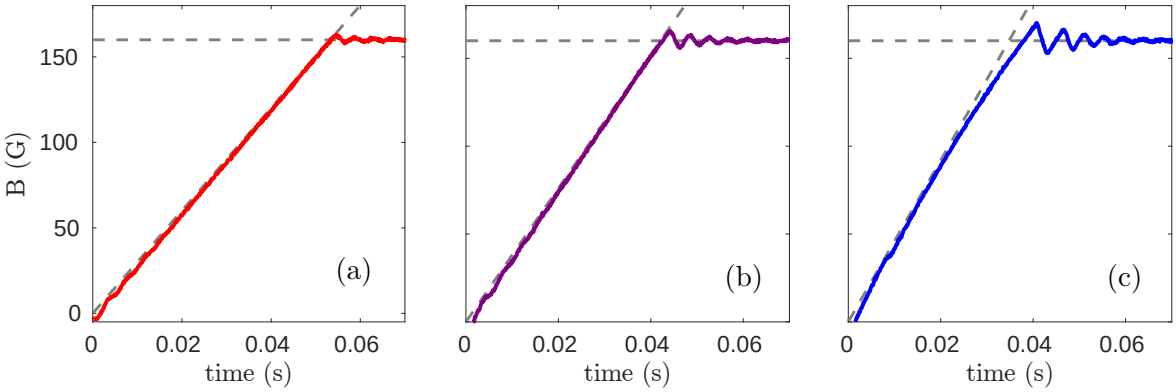

Figure 1.7 Response of the coils to a fast increase of magnetic field from 0 G up to 160 G. Grey dashed lines: expected magnetic field of the ideal response; Color curves: measured magnetic field. (a) $\alpha_q = 3000\,\mathrm{G.s^{-1}}$; (b) $\alpha_q = 3800\,\mathrm{G.s^{-1}}$; (c) $\alpha_q = 4600\,\mathrm{G.s^{-1}}$. Each plot is an average of B over 1000 successive tests.

low amplitude. This amplitude increases with α_q, as shown on the example of $\alpha_q = 3600\,\mathrm{G.s^{-1}}$. For $\alpha_q = 4600\,\mathrm{G.s^{-1}}$, the response of the coil is clearly nonlinear, preventing us from using such magnetic quenching values. From these tests, we decide to never use magnetic quenching rates α_q higher than $3000\,\mathrm{G.s^{-1}}$, and most often we stay below $1000\,\mathrm{G.s^{-1}}$.

1.1.6 Control instruments

For all experiments, we perform real time measurements of the dimensionless acceleration Γ and of the vertical magnetic field B. This way, we do not rely on the values expected from calibrations, but instead are able to use values measured in real time as parameters.

Accelerometer

We perform acceleration measurements by means of a piezoelectric accelerometer fixed to the piston linking the cells to the electromagnetic shaker. This accelerometer is from manufacturer Brüel & Kjaer, Type 4393. We analyze the signal generated by means of a charge amplifier from the same manufacturer, Type 2635, whose calibration is provided by the manufacturer. It generates an output tension that is directly proportional to the measured acceleration Γ. We record the acceleration signal *via* the acquisition card and using a Matlab routine, as detailed in Section 1.2.2.

Magnetometer

We measure the magnetic field generated by the coils by means of a magnetometer equipped with a one-directional Hall effect sensor (manufacturer FW Bell, model 5180). We use a horizontal and a vertical sensor. The output voltage verifies the relation $100\,\mathrm{G} \leftrightarrow 0.1\,\mathrm{V}$ and is recorded *via* the acquisition card using a Matlab routine.

We mainly use the horizontal sensor, since it allows us to perform both video and magnetic field measurements simultaneously. The positioning of the sensor with respect to the square cell is illustrated on Fig.1.8(a); in the case of the circular cell, we place the sensor near the edge of the cell as well. The difference of magnetic field measured at the cell center and at the edge of

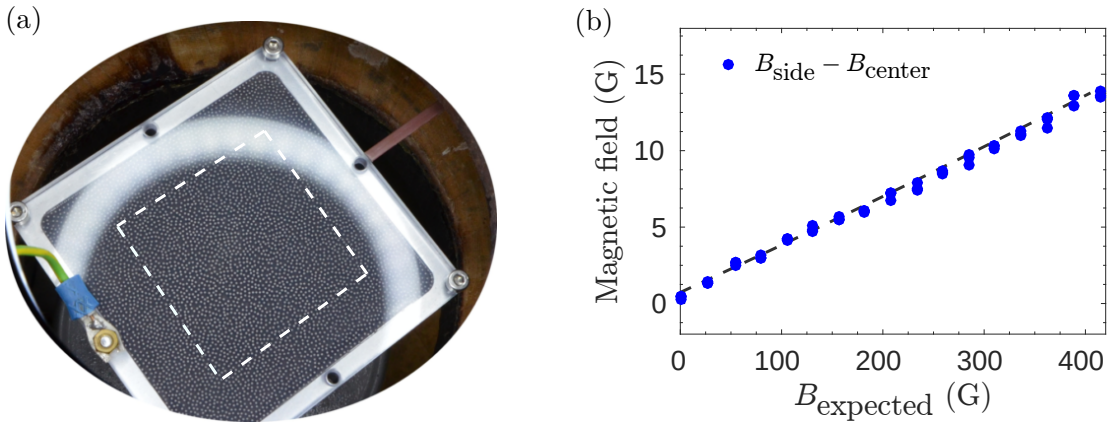

Figure 1.8 Hall effect sensor position and measurement of the inhomogeneity of the magnetic field. (a) Position of the Hall sensor (brown stick on the upper right of the image) on the side of the square cell so that we can perform magnetic field measurements while recording videos. The white dashed square indicates the region of interest. The white circular reflection is the L.E.D. array lighting system reflection. The green and yellow cable is linked to the Earth. (b) Difference of magnetic field between measurements on the side and at the center of the cell (blue dots) and linear fit (black dashed line).

the cell increases linearly with the magnetic field and corresponds to a relative difference of less than 4 %, as shown in Fig. 1.8(b).

1.1.7 Image acquisition system

All information about particle positions and velocities is extracted from high-speed video recordings.

We use a high-speed video camera Phantom V10 with a lens Tokina AT-X M100 Pro D of fixed focal length of 100 mm and an aperture a f/2.8, and a circular L.E.D. circular array of diameter 140 mm and a power 20 W from manufacturer Creative Customer Satisfaction Inc.. Both are centered along the coil axis and above the cell, the camera being positioned at a vertical distance of about one meter while the lighting system is installed about 20 mm above the coils, as visible in Fig. 1.1(b). We obtain a very good contrast between the reflection of the LED array on top of the chromed particles and the dark sandpaper of the square cell. When using the circular cell, however, the aluminum background being light, as visible in Fig. 1.2, we have to use an additional band-pass filter (extensive details are given in Chapter 2). The region of interest is square with side 57 mm and centered around the cell center, as depicted in Fig.1.8(a) on the example of the square cell. We exclude the cell borders from the region of interest in order to get rid of the boundary effects, and to increase signal resolution at the same time.

We perform almost all measurements with a camera sampling frequency of $f_{\text{acq}} = 780$ Hz, and at a few smaller ones (for instance 4 Hz and 10 Hz). The exposure time is $\tau_e = 990\ \mu$s and the resolution is of 1152 pix × 1152 pix (for a real surface of the region of interest of 5.7 mm × 5.7 mm). The particles, of a real diameter of $a = 1$ mm, have a diameter of about 20 pix in the pictures. We record images in .mat Matlab format. For experiments at very short times, as in Chapter 6, Section 6.4, we only record 2 images, while for some other experiments in the same chapter, we use 18, 000 images (*i.e.*, 23 s, which is close to the maximum of about 18, 800 images that we can record on the RAM memory of our high speed camera).

1.2 Protocol and automation

Following a well-defined protocol not only is necessary for ensuring the reproducibility of the experiments, but crucially matters when studying disordered states, which will be our case (see Chapter 5 and Chapter 6). As mentioned above, we developed a Matlab routine for controlling and recording data from the main devices described in Section 1.1: electromagnetic shaker and accelerometer, coils and magnetometer, high-speed video camera.

1.2.1 Principle of the protocol

Once a given number of particles N_{tot} is placed inside the experimental cell (*i.e.*, the theoretical particle area fraction ϕ_{th} is fixed) and the cell fixed at the center of the coils, we start running sets of experiments.

Let us denote $\Gamma_t(t)$ the time-dependant dimensionless acceleration and $B_t(t)$ the time-dependant magnetic field that are delivered, respectively, by the electromagnetic shaker and by the coils. The protocol for a given experiment is shown schematically in Fig. 1.9:

1. We linearly increase the acceleration Γ_t from 0 to the target value Γ. This generates a state of mechanically agitated grains, *i.e.*, a *granular gas*. Increasing takes a time $\tau_{\mathrm{i},1}$;

2. We wait a given time $\tau_{\mathrm{w},1}$ while shaking (Γ). The goal here is to let the granular gas homogenize;

3. We linearly increase the magnetic field B_t from 0 G to a target value B_1. Increasing takes a time $\tau_{\mathrm{i},2}$;

4. We wait a given time $\tau_{\mathrm{w},2}$ while shaking (Γ) and applying the magnetic field (B_1). This may be used to homogenize a state of granular gas with interacting particles;

5. We linearly increase the magnetic field B_t from B_1 to B_0. Note that B_0 refers to the *target value* of the magnetic field, to which we will refer very frequently in this thesis. The rate of increase of the magnetic field, or magnetic quenching rate, is $\alpha_q = \mathrm{d}B_t/\mathrm{d}t$;

6. We wait a given time τ_0 while shaking (Γ) and applying the magnetic field (B_0). This enables us to let the system undergo *aging* if it is in a non-stationary state;

7. We perform video recordings during a time τ_{rec}. The *post-quench aging time* is the duration between the end of the ramp of magnetic field and the mean time of the recordings: $\tau_{\mathrm{ag}} = \tau_0 + \tau_{\mathrm{rec}}/2$;

8. We decrease B_t quickly and Γ_t slowly, so that B_t always vanishes before Γ does: this enables us to randomize particles positions before turning off the mechanical shaking.

9. We let the devices idle during a given time τ_{p}. This may be used to let the shaker and the coils cool down.

We loop on this sequence of commands with either identical parameters (*i.e.*, in order to increase statistics for a given set of parameters, to check reproducibility, etc.) or using different sets of parameters.

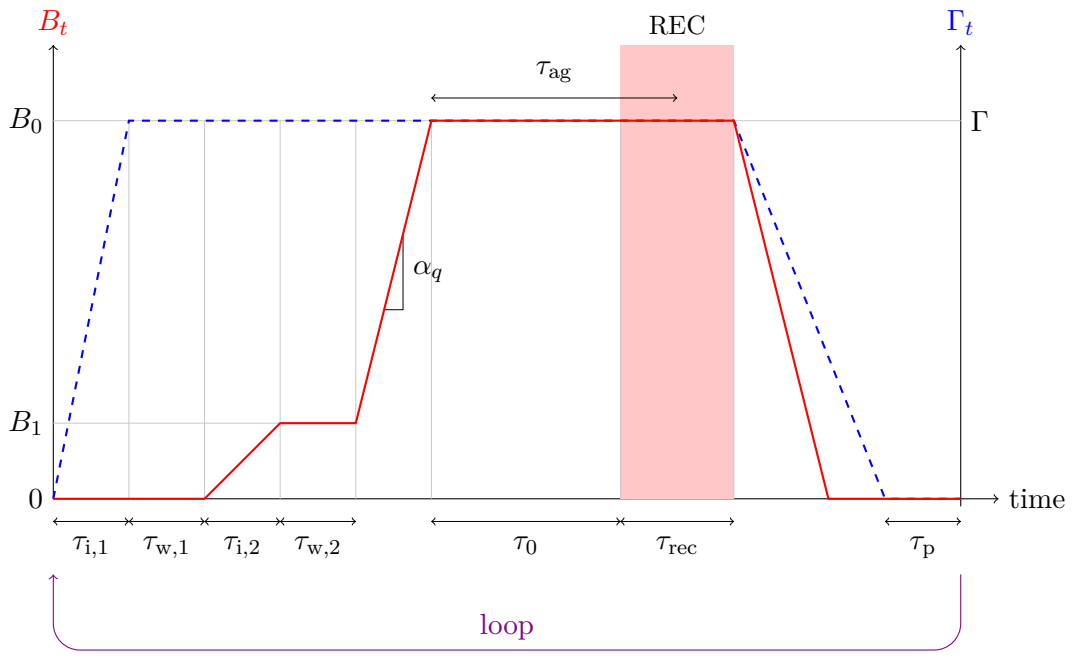

Figure 1.9 Experimental protocol. The blue dashed curve corresponds to the time-dependant acceleration, $\Gamma_t(t)$, whose plateau value is Γ. The plain red curve indicates the time-dependant vertical magnetic field, $B_t(t)$. B_1 corresponds to the intermediate plateau magnetic field, while the *taget value* of the magnetic field is B_0. The increase of B_t from B_1 to B_0 is performed at the rate $\alpha_q = \mathrm{d}B_t/\mathrm{d}t$. The time between the end of the increase of B_t to B_0 and the mean time of the recording is τ_{ag}, the *aging* time. The red shaded area corresponds to the period of image recordings.

1.2.2 Automation routine

We wrote an automation routine which combines dialogues with both acquisition card and high-speed video camera Phantom V10. We benefited from Matlab codes written by Leonardo Gordillo for the Phantom camera and from pieces of code written by Luc Deike for the acquisition card. This section concerns the technical description of this routine.

1. **Input parameters.**

   (a) Main parameters: Γ, B_1, B_0 and α_q.

   (b) Timing parameters: $\tau_{i,1}$, $\tau_{i,2}$, $\tau_{w,1}$, $\tau_{w,2}$, τ_0 and τ_p. The duration of step 5 of the protocol, namely the increase of B_t from B_1 to B_0, is not a control parameter. It is obtained from the difference $|B_0 - B_1|$ and α_q through:

   $$\tau_{B_1 \to B_0} = \frac{|B_0 - B_1|}{\alpha_q}. \tag{1.12}$$

   (c) Number of frames, n_{pic}, and frequency of the recordings, f_{acq}. These parameters, along with the waiting time of step 6, τ_0, define the *aging time*:

   $$\tau_{ag} = \tau_0 + \frac{n_{pic}}{2 f_{acq}}. \tag{1.13}$$

2. **Running one experiment.** This follows the protocol described in Section 1.2.1 and

depicted in Fig. 1.9.

(a) On the acquisition card we open 2 output channels for controlling the two amplifiers of the electromagnetic shaker and of the coils; and 2 input channels for recording the signals from the accelerometer and from the magnetometer.

(b) As a background task, we send the signals corresponding to the expected dimensionless acceleration Γ_t and to the expected magnetic field B_t. Then, we stay idle until the time at which recordings must be started (the recording period is highlighted in light red in Fig. 1.9);

(c) We start the high-speed video recordings as a foreground task, and start transferring the recorded frames from the camera to the operating computer as soon as the recording is finished, *i.e.*, while Γ_t and B_t are decreasing down to zero.

(d) We wait until the final waiting stage of duration τ_p (step 9) is completed, and save the measurements from the accelerometer and from the magnetometer performed during the video recordings.

(e) We start repeating, in a loop, as illustrated on Fig. 1.9 by the purple arrow.

1.2.3 In practice: running one set of experiments

Counting particles

In practice, first one has to pick up the number of particles N_tot required to obtain the desired theoretical particle area fraction ϕ_th given by Eq. 1.8. Since we are dealing with thousands of particles, it is not realistic to count them individually. Instead, we weigh a bunch of particles using a high-precision weighing scale (Ohaus Adventurer Pro AV 264, precision of $10^{-4}\,\mathrm{g} < m$) until we reach the required total mass m_tot given by:

$$m_\mathrm{tot} = m\,N_\mathrm{tot} = m\,\phi_\mathrm{th}\,\frac{4\mathcal{S}_\mathrm{tot}}{\pi a^2}. \tag{1.14}$$

Lid and gap size

Once particles are placed in the cell, we fix the polycarbonate lid. When using the square cell, we simply fixed it by means of four screws and performed experiments with a single gap size of about $1.4\,a$ (that is, the native gap size of 1.5 mm minus the thickness of the sandpaper sheet). With the circular cell, we use stainless steel slabs to tune the gap size (between about $1.3\,a$ and $1.8\,a$), which we slip between the aluminum walls and the acrylic lid, next to each of the six screws, as mentioned in Section 1.1.3.

Pre-checks

We screwed the cell on top of the piston fixed to the electromagnetic shaker. At this stage, we perform the following checks, systematically, prior to starting the recordings *via* the Matlab routine:

- **Diverse checks.**
  - Centering the cell with respect to the coils, by eye, so that the magnetic field B is minimum at the center of the cell.

  - Centering the camera with respect to the cell, within ±10 pix from the cell center. The latter is identified either by a cross on a removable piece of paper placed on the lid (square cell), or by a central mark from machining (circular cell).
  - Zeroing the magnetic field B by placing the Hall effect sensor at the measurement position, as illustrated on Fig. 1.8(a), and adjusting the potentiometer of the Kepco amplifier so that the measured magnetic field is zero when 0 G is requested in the Matlab routine.
  - Recording a picture with the camera lens covered, which will be used for calibrating the camera sensor (this is the *dark field* picture mentioned in Chapter 2, Section 2.1.1).

- **Horizontality of the cell.** This is the finest adjustment to be implemented when using our setup. The horizontality is extremely easily lost – even running a long series of experiments can compromise due to vibrations.
  The particles are very sensitive to small deviations from horizontality, thus we adjust it very carefully. Indeed, when the cell is slightly tilted in one direction, particles migrate accordingly and a density gradient appears. Instead, when horizontality is obtained, particle density is homogeneous across the cell (or, if a clustering effect is present, the density is invariant by rotation).
  This sensitivity to non-horizontality is probably due to the smoothness of our particles and the low roughness of the cell lower surface (either sand paper or sandblasted aluminum). However, note that the higher Γ (*i.e.*, the higher the particle mechanical agitation) and the higher B (*i.e.*, the stronger the interactions between particles), the lesser the consequences of a slight tilt of the cell.
  We adjusted the cell horizontality by means of three screws levelling the thick aluminum plate on which the electromagnetic shaker is fixed. First for a strong shaking strength, we make adjustments by eye. Then we perform a similar adjustment for a lower values of Γ, and so on, so as to refine horizontality. Once we have completed the adjustment for $\Gamma = 1.1\,g$, we assume the horizontality to be satisfying. Concretely, making this adjustment took us between 5 min and 1.5 h.

Demagnetization

If the particles appear magnetized, for instance, if they arrange as in Fig. 1.2(a), we perform demagnetization so that their remnant magnetic moment becomes negligible in the context of our experiments. More information about remnant magnetic field and demagnetization methods are given below.

Run

Finally, after all these verifications, we start a series of experiments.

1.2.4 Demagnetization method

When the particles are immersed in an external magnetic field, at the microscopic level inside the bulk of the material, magnetic domains align with the magnetic excitation. In our case, they align along the vertical axis. If the particles were paramagnetic, the magnetic domains (or Weiss domains) would reorient randomly and the mean magnetization of every particle would be vanishing, *i.e.*, there would be no remnant magnetization. If the particles were purely

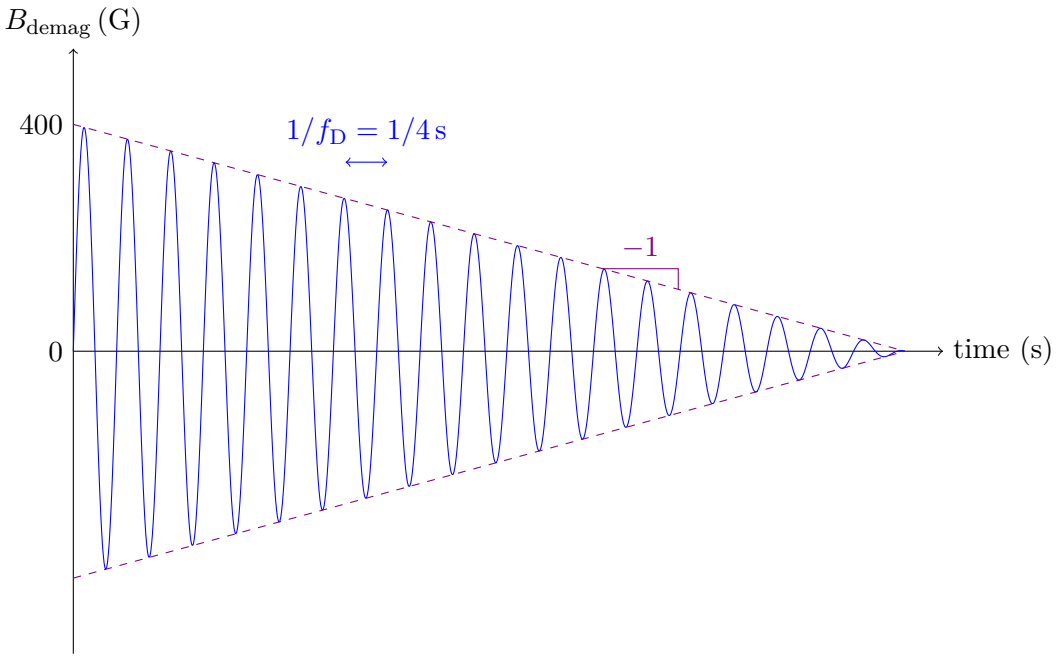

Figure 1.10 Demagnetization of remnant dipoles. Particles bearing a remnant magnetization are immersed in a vertical magnetic field oscillating at a low frequency $f_{\text{D}} = 4\,\text{Hz}$, with an initial amplitude of 400 G linearly decreasing at a rate $-1\,\text{G.s}^{-1}$.

ferromagnetic, the magnetic domains would keep their alignment, leaving the particles bear a strong remnant magnetization after the magnetic excitation is turned off.

Our particles are *soft-ferromagnetic*, *i.e.*, they bear a weak magnetization after having been immersed in an external magnetic excitation. This is not convenient for us since for our measurements at zero or low magnetic field, we need particles not bearing any other magnetization that the one that we induce, if there is any. To remove the remnant magnetization, one has two options.

On one hand, one can heat the particles up to the Curie temperature of the constituting materials so that thermal agitation randomizes the orientation of the microscopic dipoles and of the magnetic domains in the bulk of the materials. Above this temperature, the material is paramagnetic. For stainless steel SUS 405, the Curie point has been measured between 710 °C and 730 °C [54]. For our AISI 52100 particles, we expect the Curie point to be of the same order of magnitude. Heating the particles at such a temperature is not an easy task –we did not use this method.

On the other hand, it is possible to remove a material's remnant magnetization by immersing it in an oscillating magnetic field, which we denote B_{demag}, of an amplitude that linearly decreases from a high value compared to the highest magnetization experienced by the material, down to zero [55]:

$$B_{\text{demag}} = (-t + B_{\text{demag},0})\,\sin(2\pi f_{\text{D}} t), \tag{1.15}$$

where we used in practice, $B_{\text{demag},0} = 400\,\text{G}$ and $f_{\text{D}} = 4\,\text{Hz}$, as illustrated in Fig. 1.10.

Following this protocol, the magnetic domains are periodically oriented up and down, generating disorder in the orientation of the microscopic dipoles which finally results in a vanishing mean magnetization as B_{demag} tends towards zero. The two pictures of Fig. 1.2 illustrate well

the aspect of an ensemble of particles at rest before (a) and after (b) a demagnetization cycle is performed. In practice, we apply this demagnetization protocol only when we run an experiment with a magnetic field B_0 lower than the previous experiment.

1.3 Personal contribution

The totality of the experiments presented in this thesis were performed using the experimental setup described above. We built it in the early stage of my PhD, and implemented minor modifications and refinements along the way. When I began my work, the square machined aluminum cell was vertically mounted on an electromagnetic shaker *via* a piston, and the coils were placed at a convenient height on a low Norcan aluminum structure. At this stage, preliminary experiments could be run since all essential devices (experimental cell, electromagnetic shaker and coils) were in place.

I reinforced the aluminum structure and extended it vertically so as to create a reliable attachment point for the heavy high-speed video camera about one meter above the cell along the axis of the coils. I also added pieces of rubber under the electromagnetic shaker and under the aluminum structure in order to better reduce vibration transmission between them and the lab bench on which I moved the setup. I fixed an accelerometer on the vibrating piston and a rack and pinon system at the height of the cell to support and move the Hall effect sensor horizontally. I connected both coils and shaker amplifiers, plus the accelerometer and magnetometer amplifying devices, to an acquisition card for automation purposes, and, most importantly, I developed the protocol and automation routine describe in Section 1.2.

I performed all the experiments and data analysis presented in this thesis unless otherwise specified.

Chapter 2

Image and data processing

Chapter 2 : Image and data processing ↑ back to contents

Chapter abstract

The basic ingredients for all our analysis are the particles' positions and displacements, *i.e.*, their trajectories. The positions are obtained from images recorded by the high-speed video camera, in which centers are identified with pixel accuracy using a cross-correlation technique, itself eventually brought to a sub-pixel accuracy by means of a simple centroid method. Finally, a tracking algorithm builds up individual particle trajectories from the particles' positions on successive frames. This particle tracking technique is highly accurate, relatively fast to implement, and highly reliable. Finally, we give some details on our methods of computation of some key quantities such as collision rate, cluster detection, real-time measurement and numerical assignment of particle vertical positions, and magnetic energy computation.

2.1 Image processing

Raw images are recorded using a high-speed video camera, as explained in Section 1.1.7. These images are not directly usable for the centers' detection, and eventually the tracking algorithm. We need to start by calibrating these images according to the sensor's offset and sensitivity, and to additionally optimize them by an adjustment method optionally complemented by a high-pass filter for removing large inter-particle bright patches. Only then can we look for the particle centers, which we need to locate with the highest accuracy possible and within a reasonable computational time. For this, as a first step, we determine the centers at a pixel accuracy by cross-correlating the images with an ideal particle signal designed to closely fit the real one. However, such a low resolution is not satisfying, hence we improve it by computing the centroid of the intensities in the area surrounding each center. Finally, from these refined position data, obtained for successive frames, we estimate the most likely frame-to-frame displacements of each particle and rebuild individual trajectories.

2.1.1 From raw to processed images

Calibration relative to the camera sensor

As recorded by the camera sensor without considering any calibration, a raw image does not accurately reflect reality. Indeed, the sensor's response to light is linear according to a *gain* matrix, M_s, and a non-vanishing *offset* matrix, I_0, both of which we have to measure. While M_s is related to physical properties of the pixels and does not depend on the environmental conditions, I_0 varies, for instance, with the camera temperature. Therefore, M_s is measured once and for all, but I_0 is ideally measured prior to every experiment.

Let us denote I_{raw} a *raw* image and I_{real} the corresponding *real* image (both being of size $1152\,\text{pix} \times 1152\,\text{pix}$ for all our experiments). The real image is obtained from the raw image through the operation:

$$I_{\text{real}} = (I_{\text{raw}} - I_0)./M_s \tag{2.1}$$

where ./ is the term-by-term matrix division operator. This operation can be implemented *via* two methods: either by using the software provided with the high-speed camera, or manually.

Using the Phantom Camera Controller (PCC) software to do this is the most straightforward method if your recordings are performed *via* this software. Once PCC is started and prior to recording, cover the camera lens and click once on the Current Session Reference (CSR) button. This records a dark picture in the RAM memory of the camera, which is used as offset matrix I_0 until PCC is turned off or another CSR measurement is done. The images that are then saved are *real* ones, obtained from Eq. 2.1 with the gain matrix provided by the manufacturer and stored in the internal camera memory, as default for M_s.

When controlling the camera without making use of the camera software, as it is the case for us with our automation routine, one must proceed differently. Here we describe the protocol that has to be followed so that one can explicitly implement Eq. 2.1 in a numerical routine with M_s and I_0 obtained manually. We acknowledge Leonardo Gordillo for his kind assistance and for his routines performing the dialogue between Matlab and the camera Phantom V10.

The *gain* matrix, M_s, is computed once and for all following these steps:

1. Remove the lens of the camera and orient the sensor towards a uniformly illuminated field;
2. Tune the exposure time, τ_e, so that the signal gets close to saturation: the highest intensity over all pixels must be lower than, but as close as possible to, $2n_b - 1$, with n_b the number of bits of the frame quality (for us $n_b = 8$);
3. Record this raw picture, which we denote $I_{\text{raw flat}}$, for *flat field*;
4. With the same exposure time, generate a dark picture with the lens covered. This is the offset picture $I_{0,\text{flat}}$;
5. Now, according to Eq. 2.1, M_s can be computed as

$$M_s = (I_{\text{raw flat}} - I_{0,\text{flat}})./I_{\text{real flat}} \tag{2.2}$$

where $I_{\text{real flat}}$ is the real image of the flat white field, that is, the identity matrix of the image size. Finally, we obtain the *gain* matrix as:

$$M_s = I_{\text{raw flat}} - I_{0,\text{flat}}. \tag{2.3}$$

An example of such a matrix is shown in Fig. 2.1(a).

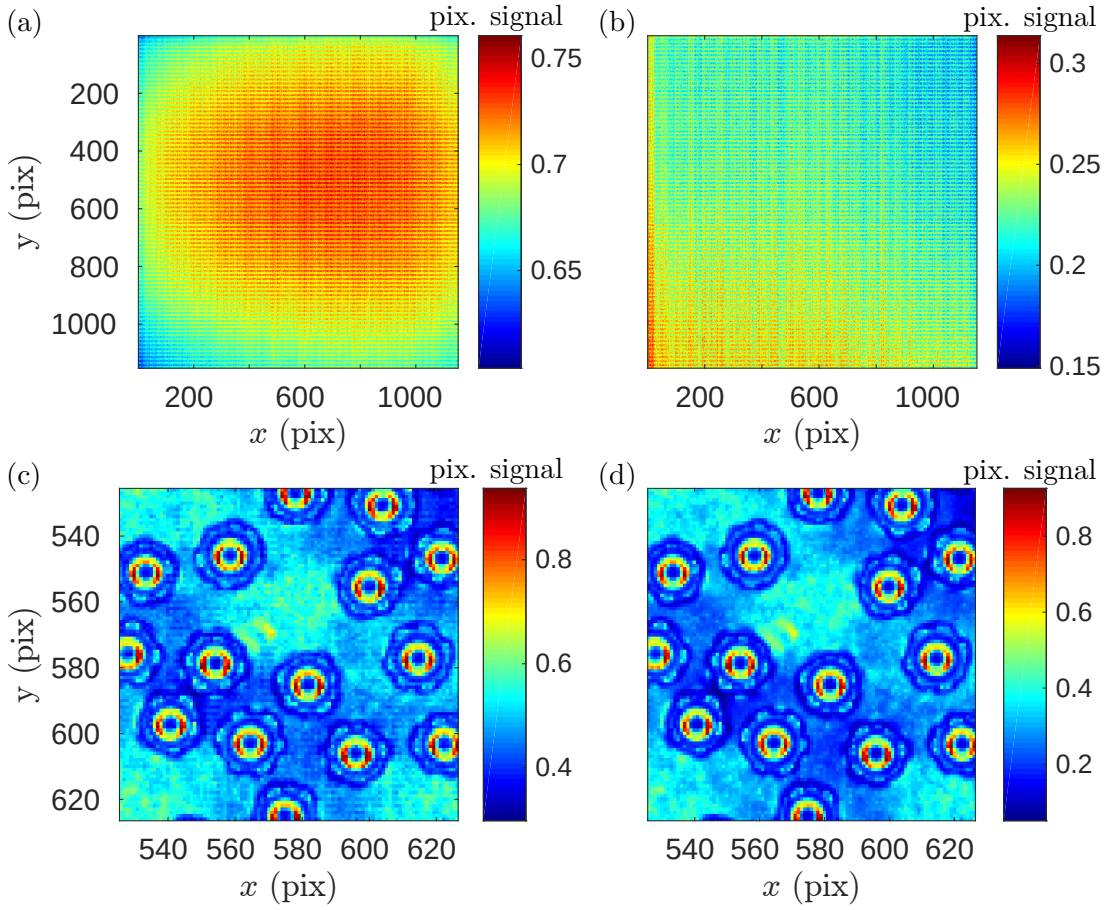

Figure 2.1 High-speed camera sensor calibration (a,b) and example of zoomed images from experiments with the circular cell (c,d). Colorbars indicate signal intensity: 0 (resp. 1) corresponds to an absence of signal from the pixel (a saturation of the pixel). (a) Gain matrix M_s; (b) Example of an offset matrix I_0; (c) Example of a raw frame I_{raw} (zoom), and (d) associated real frame I_{real} (zoom). Note the various ranges of the colorbars, revealing in particular the improvement in contrast between (c) and (d).

For the offset matrix, set the exposure time τ_e to the value that will be used in the coming recordings, cover the lens and record a picture: this is I_0. An example of an offset matrix is shown in Fig. 2.1(b).

Within the routine analyzing the images, insert a calibration section which computes for every raw frame I_{raw} the real image I_{real} according to Eq. 2.1, prior to any further frame analysis. As an illustration of this image processing step, we show a portion of a raw image in Fig. 2.1(c), and the associated real image in Fig. 2.1(d). Note that the patterning visible on the raw image has disappeared on the real image, and that the different ranges of the two colorbars reveal a better contrast on the real image. This latter image, I_{real}, is used as a starting point for the next image processing steps.

In practice, we implemented the manual method for all our experiments. We updated the offset matrix I_0 prior to every set of experiments, rather than prior to each and every experiment, which, nevertheless, provided images of very good quality.

Stretching with thresholds

Such images do not necessarily make the best use of the 256 grey-scale levels that are available for our 8-bits frames. Indeed, particles may lose reflectivity and consequently reflect a signal with a lower intensity than expected and significantly below the maximum value. In the mean time, the background intensity level remains unchanged: darker than the particles for the square cell coated with the sandpaper sheet, and lighter for the circular cell with sandblasted aluminum surface. For the former, applying a lower threshold is possible, since the background is darker than the particles but of non-zero intensity, while for the latter, this cannot be done without losing particle signal.

Based on these observations, we stretch our images in order to optimize contrast. We map the values in the real image I_{real} to new values in a new, *optimized* image I_{opti} such that grey-scale values between a_{low} and a_{high} map to values between b_{low} and b_{high}:

$$I_{\text{opti}} = \mathcal{M}(I_{\text{real}}; a_{\text{low}}, a_{\text{high}}, b_{\text{low}}, b_{\text{high}}) \tag{2.4}$$

where the *mapping* operator, $\mathcal{M}$, is defined for a matrix X and adjustment parameters a_{low}, a_{high}, b_{low} and b_{high} as,

$$\mathcal{M}(X; a_{\text{low}}, a_{\text{high}}, b_{\text{low}}, b_{\text{high}}) = \frac{X - a_{\text{low}}}{a_{\text{high}} - a_{\text{low}}} \left(b_{\text{high}} - b_{\text{low}}\right) + b_{\text{low}}. \tag{2.5}$$

In practice, we always chose for a_{high} a value close to the maximum value of the signal of interest (*i.e.*, the L.E.D. circular array reflection), $b_{\text{low}} = 0$ and $b_{\text{high}} = 1$ so that the generated picture is optimized and normalized. For the square cell, the value taken for a_{low} is slightly above the grey level of the dark background, so it acts as a lower brightness threshold. In the case of the circular cell, as we mentioned above, applying a lower threshold a_{low} at the background level would make the particle signal partially disappear. Therefore, we chose this threshold to be zero. However, since we do need to remove this light background in order to be able to clearly identify the particles, we implemented an additional filtering operation.

High-pass filter

This operation consists of applying a high-pass filter to optimized frames I_{opti} for experiments with the circular cell only. The idea is to remove the bright patches between the particles while leaving particle signals undeformed. In this section, we explain the general principle of band-pass filters for images, whose high-pass filters are a sub-class, before concluding on the use we make of them in our image processing.

The role of a band-pass filter is to remove both short wavelengths (*e.g.*, pixel noise) and long wavelengths (*e.g.*, inter-particles light areas), while letting pass free the characteristic wavelength of the signal of interest (*e.g.*, the L.E.D. circular array reflection). To this end, we used the freely available algorithm from Daniel Blair and Eric Dufresne [56] (itself a translation into Matlab of IDL routines written by John Crocker and David Grier).

A band-pass algorithm performs two separate two-dimensional convolutions and finally subtracts the one to the other, as we will see below. Two-dimensional convolutions are frequently used in image processing because they can be used to implement filter effects such as sharpening, smoothing, and detection of the edges. Here, we may be interested in smoothing short-wavelength and enhance long-wavelength patterns.

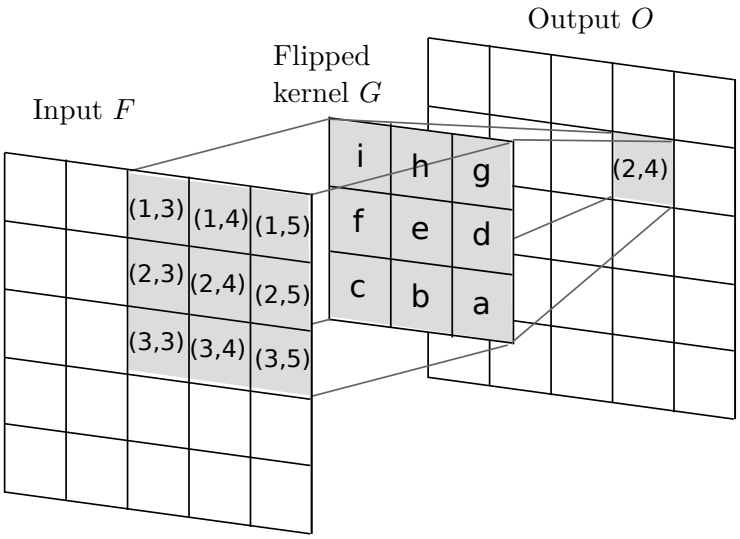

Figure 2.2 Graphical representation of a 2D discrete convolution described by Eq. 2.8. In image processing, the input matrix F is the frame that is to be filtered, the flipped kernel G is the filter to be applied to F, and the output matrix O is the filtered image (inspired by [57]).

The convolution of two continuous functions f and g defined in $\mathbb{R}^2$ is defined as:

$$f * g = [f * g](\vec{x}_0) = \int_{\mathbb{R}^2} f(\vec{x}) g(\vec{x}_0 - \vec{x}) \, \mathrm{d}\vec{x} \tag{2.6}$$

with

$$\int_{\mathbb{R}^2} g(\vec{x}) \, \mathrm{d}\vec{x} = 1. \tag{2.7}$$

The function g is called *kernel*, or *filter*, and its nature defines the type of filtering that is applied. Note that on Eq. 2.6, g is flipped. The operation where g is not flipped is the cross-correlation of f and g.

Digital image processing requires to consider a discretized version of Eq. 2.6. Let us consider an image array F and a kernel array G, both of dimensionality 2 but of different sizes, respectively $M \times N$ and $m \times n$. Note that the size of the kernel is usually similar to the size of the signal to enhance (this is equivalent to considering it to be zero elsewhere), and is thus much smaller than the size of the image. The array produced, O, is of dimension 2 as well and is of size $M \times N$.

Performing the discrete convolution consists of sliding the flipped kernel G over the image F so that it explores all the positions where it entirely fits within the boundaries of the image. To each kernel position (i, j) corresponds a single output value:

$$O(i, j) = \sum_{k=1}^{M} \sum_{l=1}^{N} F(k, l) G(i - k, j - l) \tag{2.8}$$

where $G(x, y) = 0$ if $x \notin [1, m]$ or if $y \notin [1, n]$, and,

$$\sum_{i=1}^{m} \sum_{j=1}^{n} G(i, j) = 1. \tag{2.9}$$

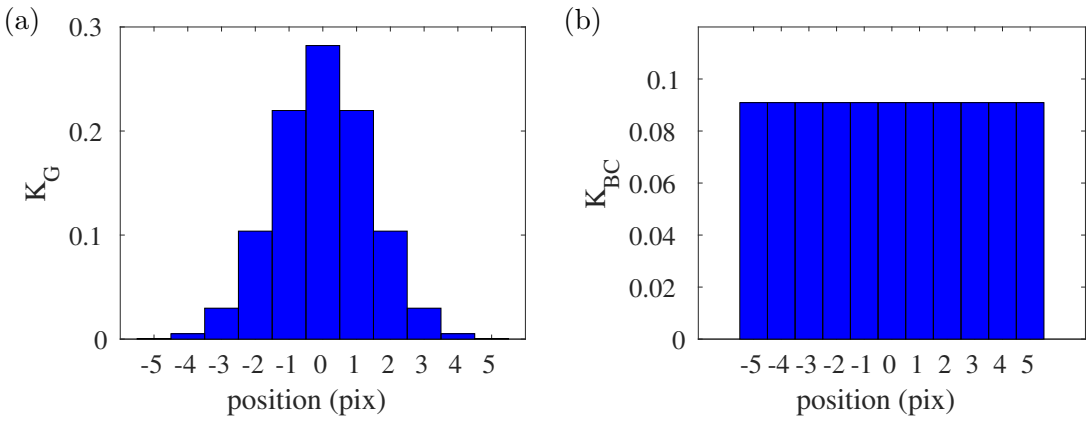

Figure 2.3 Examples of kernels in one dimension (1D). (a) Gaussian 1D kernel for smoothing a noise of 1 pixel; (b) Boxcar 1D kernel enhancing objects of a size of 5 pixels.

A graphical representation of this operation is presented on Fig. 2.2. Note that there exist different methods to tackle the problem of what happens at the edges of the image, but we will not describe them here (more details can be found in reference books such as [58]).

The choice of the kernel G depends on the pattern that is being looked for and thus defines the type of filtering that is performed. For instance, a *Gaussian kernel* of a size of a few pixels, for which a one-dimensional example is shown in Fig. 2.3(a), is efficient at smoothing pixel noise, while *boxcar kernels* of a given size, like in Fig. 2.3(b), are used for identifying patterns of a similar typical size.

A band-pass operation consists of performing a convolution of the image with a short-wavelength *Gaussian kernel*, K_G, in order to smooth pixel noise, from which is subtracted the convolution of the image with a long-wavelength *boxcar kernel*, K_{BC}, so as to remove long-wavelength patterns. The resulting image I_{bp} is obtained from the formula:

$$I_{\mathrm{bp}}(\vec{x}_0) = \int I_{\mathrm{opti}}(\vec{x}) * [K_G(\vec{x}_0 - \vec{x}) - K_{BC}(\vec{x}_0 - \vec{x})]\,\mathrm{d}\vec{x} \tag{2.10}$$

where the domain of integration is over the full region of interest.

In our images, background noise is actually low enough that we do not have to use a Gaussian kernel, which has the advantage of leaving our images unsmoothed (concretely, we replace it in the routine by the single-pixel identity kernel $I_{1\times1} = 1$). However, we are very much interested in removing the bright areas between particles, clearly visible in Fig. 2.1(d), hence we set the half-width of the boxcar kernel to 5 pixels, as in the example of Fig. 2.3(b). Note that the target size of 5 pixels is significantly larger than the width of the peaks of the double-peak particle signal, which is of 2–3 pixels, the diameter of the double-peak signal being of about 10 pixels. Hence, particle signal quality is not degraded by the use of the high-pass filter.

In a nutshell, we apply to our images a high-pass filter with a threshold at about 10 pixels, which removes the bright patches between the particles while leaving particle signals undeformed. The filtered images are systematically stretched through an operation similar to the one given by Eq. 2.5, and using an operator $\mathcal{M}$ with as parameters $a_{\mathrm{low}} = 0$ and $a_{\mathrm{high}} = 0.9$ in order to stretch lower intensities towards 1, and $b_{\mathrm{high}} = 0$ and $b_{\mathrm{low}} = 1$ so that the resulting image is normalized. An illustration of the effects of the high-pass filter is shown in Fig. 2.4, starting from a mapped image, $I_{\mathrm{opti}} = \mathcal{M}(I_{\mathrm{real}})$ [Fig. 2.4(a)], to obtain a filtered image, $\mathcal{M}(I_{\mathrm{bp}})$ [Fig. 2.4(b)].

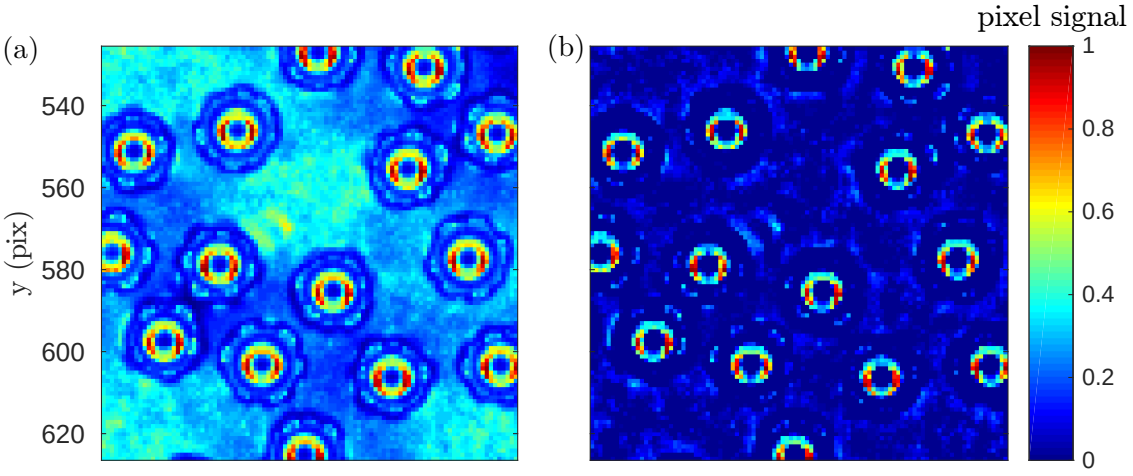

Figure 2.4 High-pass filter implementation. (a) Mapped real image $I_{\text{opti}} = \mathcal{M}(I_{\text{real}})$ from Eq. 2.4; (b) Mapped band-passed real image $\mathcal{M}(I_{\text{bp}})$ (see Eq. 2.10). The filter removes the large bright patches while leaving particle signals untouched.

2.1.2 Particle center position at pixel accuracy

Images are now optimized for particle tracking. The first step towards getting particle trajectories consists of obtaining, for every successive frame, the center of every particle. We start by computing the coordinates of the centers with pixel accuracy, and in the next section we will refine this measurement to reach a sub-pixel accuracy. We base our image analysis on a convolution-based least-squares fitting particle detection routine written by Mark Shattuck [59] and used for instance by Reis *et al.* [25], which we adapted to our signal characteristics.

Real and idealized particle signals

The L.E.D. circular array reflection on top of a chromed particle generates a circular signal, as seen in previous pictures, and shown more specifically in Fig. 2.5(a). From the data points at $y = 556$ on this plot (indicated by the horizontal white dashed line), we obtain a one-dimensional version of the signal, as shown by the red curve in Fig. 2.5(b). We model this signal by means of portions of hyperbolic tangents generating a double-peak curve, which is represented by the blue curve in Fig. 2.5(b). The fitting parameters for this curve, $\mathcal{I}_{1\text{D}}$, are the peak-to-peak distance, d_{fit}, and the sharpness of the peaks, s_{fit},

$$\mathcal{I}_{1\text{D}}\left(x, d_{\text{fit}}, s_{\text{fit}}\right) = 2 - \left[\tanh\left(\frac{\left|x + \frac{d_{\text{fit}}}{2}\right|}{s_{\text{fit}}}\right) + \tanh\left(\frac{\left|x - \frac{d_{\text{fit}}}{2}\right|}{s_{\text{fit}}}\right)\right]. \tag{2.11}$$

By assuming that the particle signal is unchanged by a rotation, which is actually not verified, as visible in Fig. 2.5(a), we extrapolate the one-dimensional idealized signal of Eq. 2.11,

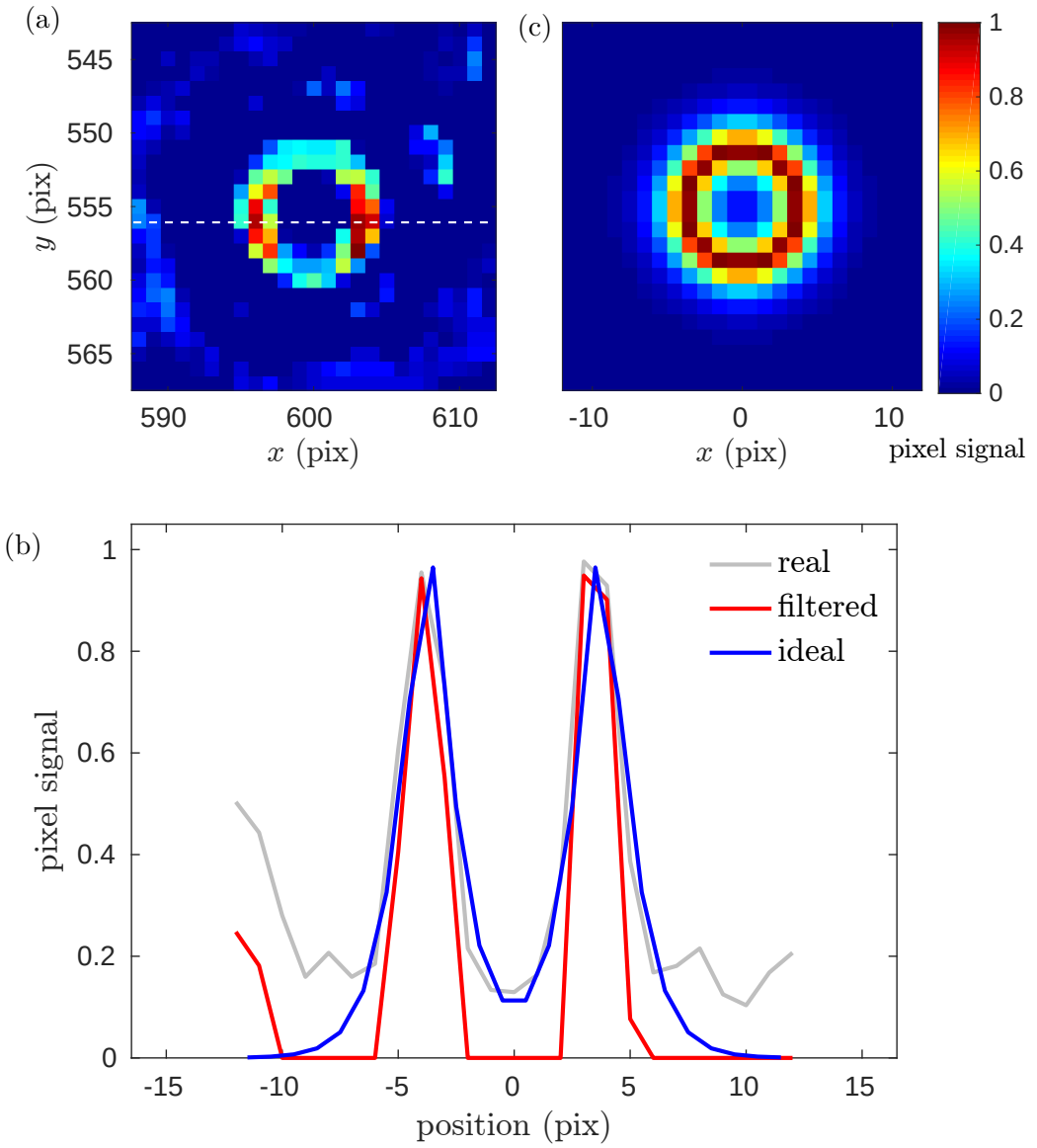

Figure 2.5 Real and idealized particle signals. (a) Zoom on a real particle of the image in Fig. 2.4(b). The superimposed white dashed line indicates the line of pixels used for plotting the "filtered" curve in (b); (b) Comparison of the one-dimensional real, filtered and ad hoc idealized particle signals. The "filtered" curve is obtained from the data points of (a) along the line $y = 556$; (c) Particle signal from Eq. 2.12 with $d_{\text{fit}} = 7.5\,\text{pix}$ and $s_{\text{fit}} = 2\,\text{pix}$.

$\mathcal{I}_{1D}(x, d_{\text{fit}}, s_{\text{fit}})$, into the two-dimensional idealized signal,

$$\mathcal{I}_{2D}\left(\vec{r}, d_{\text{fit}}, s_{\text{fit}}\right) = 2 - \left[\tanh\left(\frac{\left\|\vec{r} + \frac{\vec{d_{2D}}(d_{\text{fit}})}{2}\right\|}{s_{\text{fit}}}\right) + \tanh\left(\frac{\left\|\vec{r} - \frac{\vec{d_{2D}}(d_{\text{fit}})}{2}\right\|}{s_{\text{fit}}}\right)\right] \tag{2.12}$$

where

$$\vec{r} = (x,\ y)\,, \quad \text{and} \quad \vec{d_{2D}}(d_{\text{fit}}) = d_{\text{fit}}\left(\frac{\vec{r}}{\|\vec{r}\|}\cdot\vec{e_x},\ \frac{\vec{r}}{\|\vec{r}\|}\cdot\vec{e_y}\right) \tag{2.13}$$

in the normal basis $(\vec{e_x}, \vec{e_y})$. The resulting signal with $d_{\text{fit}} = 7.5\,\text{pix}$ and $s_{\text{fit}} = 2\,\text{pix}$ is shown on Fig. 2.5(c). The comparison with the real particle signal shows good agreement, which will be verified below when computing cross-correlations. In practice, in order to determine the values of our fitting parameters, we compare one-dimensional versions of both these signals and manually adjust the fitting parameters until we are satisfied.

Least-square fitting [59]

From $\mathcal{I}_{\text{2D}}$, we can compute the most likely position of a particle center using a least-square-fitting method. To this end, let us first denote $\mathcal{I}$ the real processed image obtained once the operations described in Section 2.1.1 are completed, and second, let us define a *square distance* between this real picture and the two-dimensional idealized signal,

$$\chi^2(\vec{r_0}, d_{\text{fit}}, s_{\text{fit}}) = \int \left[\mathcal{I}(\vec{r}) - \mathcal{I}_{\text{2D}}\left(\vec{r} - \vec{r_0}, d_{\text{fit}}, s_{\text{fit}}\right)\right]^2 \mathrm{d}\vec{r} \tag{2.14}$$

where the domain of integration is the full region of interest. Note that because our particle signals are well separated and our signal-to-noise ratio is very satisfying, we do not use any weighing function, which can, however, be useful when one of these two condition is not present [59]. Instead, we obtain a direct cross-correlation by developing χ^2:

$$\begin{aligned}\chi^2(\vec{r_0}, d_{\text{fit}}, s_{\text{fit}}) &= \int \left[\mathcal{I}(\vec{r})^2 - 2\mathcal{I}(\vec{r})\mathcal{I}_{\text{2D}}\left(\vec{r} - \vec{r_0}, d_{\text{fit}}, s_{\text{fit}}\right) + \mathcal{I}_{\text{2D}}\left(\vec{r} - \vec{r_0}, d_{\text{fit}}, s_{\text{fit}}\right)^2\right] \mathrm{d}\vec{r} \quad (2.15)\\ &= \int \mathcal{I}(\vec{r})^2 \mathrm{d}\vec{r} - 2\mathcal{I} \otimes \mathcal{I}_{2D} + \left\langle {\mathcal{I}_{\text{2D}}}^2 \right\rangle \quad (2.16)\end{aligned}$$

where we used the cross-correlation operator, $\otimes$, defined for two functions f and g as

$$f \otimes g = [f \otimes g](\vec{x_0}) = \int f(\vec{x}) g(\vec{x} - \vec{x_0})\, \mathrm{d}\vec{x} \tag{2.17}$$

and

$$\langle f \rangle = 1 \otimes f. \tag{2.18}$$

Note that the cross-correlation defined by Eq. 2.17 is related to the convolution defined by Eq. 2.6 through

$$f(\vec{x}) \otimes g(-\vec{x}) = \int f(\vec{x}) g(\vec{x_0} - \vec{x}) \mathrm{d}\vec{x} = [f * g](\vec{x_0}) = f * g. \tag{2.19}$$

In Eq. 2.16, the first term does not depend on $\vec{r_0}$, and the third term depends on it only near the edges of the image. Therefore, the only term that depends on $\vec{r_0}$ in the region of interest with a physical meaning is the second term, $-2\mathcal{I} \otimes \mathcal{I}_{2D}$. Given that $\mathcal{I} \otimes \mathcal{I}_{2D}$ corresponds to the cross-correlation between the real image and the idealized signal, it is maximum around the particles centers, where, in return, χ^2 is minimum.

Consequently, in order to find the particle centers, the first step is to find all the minima of χ^2. Among these minima, we remove those that correspond to noise and do not indicate particle centers, by using a threshold on the value of χ^2. Because of the high quality of our signal, we never lose more than a few particles in every frame, *i.e.*, typically 0.1 %, if any. Most of the time, especially when using the circular cell, which provides very high-quality images, it seems that we do not lose a single particle in this operation. The accuracy at which the minima of χ^2 are obtained is one pixel.

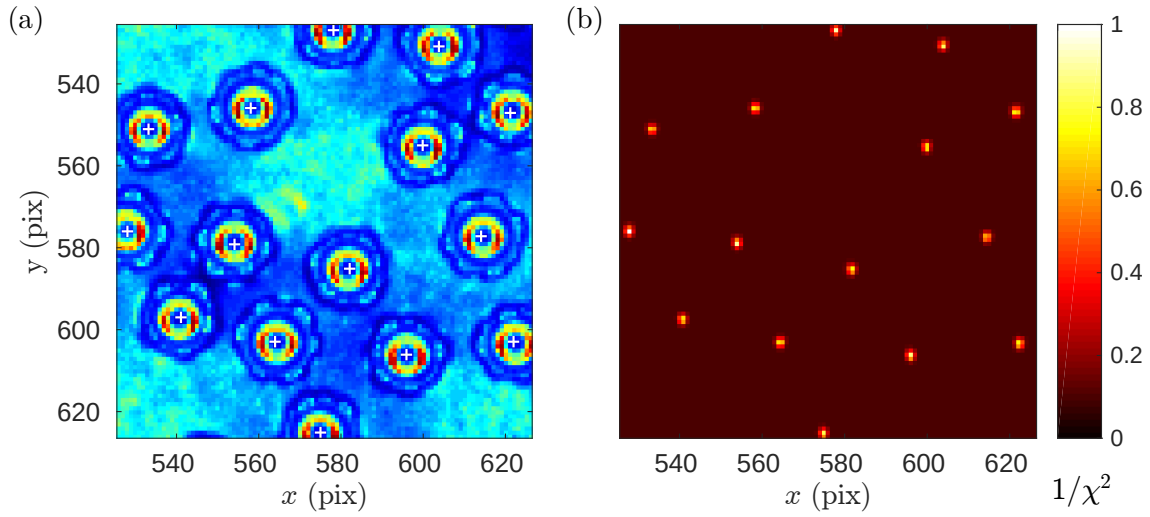

Figure 2.6 Computing the center positions with pixel accuracy. (a) Real image I_{opti} with centers superimposed (pixel accuracy, from χ^2 minimization); (b) Normalized $1/\chi^2$, where the spikes indicate particle centers.

We present in Fig. 2.6(a) a real picture on which we superimposed + symbols indicating the positions of the particle centers as computed from the least-square fitting method. The minima of χ^2, or equivalently, the maxima of $1/\chi^2$ can be easily spotted in Fig. 2.6(b) where each spike's summit corresponds to a + in the picture on the left.

2.1.3 Particle center positions with sub-pixel accuracy

For the magnification that we use, one pixel corresponds to $1/20^{\text{th}}$ of a particle's diameter, that is, about 0.05 mm. Given the high acquisition frequency, $f_{\text{acq}} = 780$ Hz, the displacement of the particles between two frames is very small. Indeed, as we will see, the typical fastest particle velocities are of about $10\,\text{cm.s}^{-1}$, implying maximum frame-to-frame displacements of about 0.13 mm; while most of the particles' speed will be of the order of magnitude of $1\,\text{cm.s}^{-1}$, thus corresponding to 0.01 mm frame-to-frame displacements. It is therefore obvious that we cannot satisfy ourselves with an accuracy of 0.05 mm on the center detection: we need to obtain a result with sub-pixel accuracy, which should be significantly lower than 0.01 mm.

One possibility: Minimization of χ^2

Refining the least-square-fitting estimate can provide such an improvement. As proposed in [59], one can minimize χ^2 with respect to d_{fit}, s_{fit} and the $\vec{x}_n$'s:

1. Find $d^\star_{\text{fit}}$ and $s^\star_{\text{fit}}$ such as
$$\begin{cases} \dfrac{\partial \chi^2(\vec{x}_0; d^\star_{\text{fit}}, s^\star_{\text{fit}})}{\partial d^\star_{\text{fit}}} = 0 \\ \dfrac{\partial \chi^2(\vec{x}_0; d^\star_{\text{fit}}, s^\star_{\text{fit}})}{\partial s^\star_{\text{fit}}} = 0 \end{cases} \tag{2.20}$$
2. Find $\vec{x}^\star_n$'s such as
$$\frac{\partial \chi^2(\vec{x}^\star_n; d^\star_{\text{fit}}, s^\star_{\text{fit}})}{\partial \vec{x}^\star_n} = 0 \tag{2.21}$$

The author [59] performs these minimizations using Newton's method and explains that he can reach the impressive accuracy of $1/1000^{\text{th}}$ of a pixel. However, this operation has a significantly high computational cost. Give that a lower accuracy can meet our needs, we chose to use another method.

Our method: Centroids of the intensities

Implemented by a home-made routine, this method consists of determining the position of a particle center with sub-pixel accuracy by exploiting the circularity of a particle signal. Around the particle center determined by least-square-fitting, we compute the position of the centroids $(\bar{x}, \bar{y})$ of the intensities of the real processed image $\mathcal{I}$:

$$\begin{cases} \bar{x} = \dfrac{\iint x\,\mathcal{I}(x,y)\,\mathrm{d}x\,\mathrm{d}y}{\iint \mathcal{I}(x,y)\,\mathrm{d}x\,\mathrm{d}y} \\ \bar{y} = \dfrac{\iint y\,\mathcal{I}(x,y)\,\mathrm{d}x\,\mathrm{d}y}{\iint \mathcal{I}(x,y)\,\mathrm{d}x\,\mathrm{d}y} \end{cases} \tag{2.22}$$

where the domains of integration are bounded to the circular region centered on the pixel-accuracy position and with an adjustable diameter d_{bary}, as depicted in Fig. 2.7(a) for $d_{\text{bary}} = 14\,\text{pix}$. We chose this parameter d_{bary} large enough so that the circular region includes all the pixels having a significant grey level (*i.e.*, we capture as much information as possible), but we restrict it to be smaller than one particle diameter in order to do not include in the computation the reflection of neighboring particles on the side of the particle of interest, which are clearly visible when particles are close to each other (as is the case for the particle in Fig. 2.7). The resulting center position determined at a sub-pixel accuracy is indicated by the red cross on Fig. 2.7(b). Concretely, for most experiments, we chose $d_{\text{bary}} = 14\,\text{pix}$, but this value depends on the magnification that is used. This method was found to be significantly faster to implement than the one performing χ^2 minimizations which we briefly described above.

Accuracy

However, our method provided a lower accuracy. Estimating the accuracy of centroid algorithms has been much debated. Recently, Puglisi *et al.* [33] estimated that the accuracy of such an algorithm, for Gaussian blobs of diameter d_{blob} of a few pixels, is given by

$$\delta_g \approx \frac{1}{\sqrt{d_{\text{blob}}}}. \tag{2.23}$$

Extrapolating this result to our double-peak, quasi-rotational-invariant particle signal leads to estimating the accuracy on our positions as being

$$\delta \approx 0.27\,\text{pix} \approx 0.013\,\text{mm} \tag{2.24}$$

where we have taken $d_{\text{blob}} = 14\,\text{pix}$. This result is to be compared to the displacement of a particle moving at a speed of $1\,\text{cm.s}^{-1}$ during $f_{\text{acq}}^{-1}\,\text{s}$, which is of 0.013 mm too. Therefore, according to this estimate, it is in principle impossible for us to measure velocities smaller than $1\,\text{cm.s}^{-1}$. However, as we will see below, it seems that we can in reality access much smaller velocities.

An extensive study tackling the question of detection accuracy for 1D, 2D and 3D Gaussian signals is from Patwardhan [60]. The dependence of the error of the centroid algorithm for

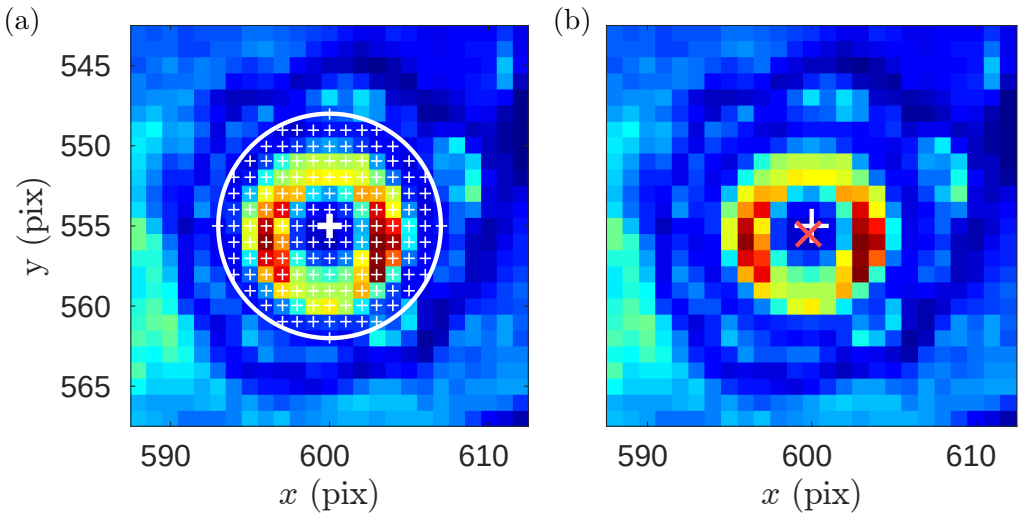

Figure 2.7 Zoom on a particle with sub-pixel centroid algorithm depiction. (a) Thick + is the pixel accuracy center, the circle shows the limit of the domain of integration for computing the centroid (see Eq. 2.22) which is centered on the thick + and is of diameter $d_{\text{bary}} = 14\,\text{pix}$, and small +'s show the pixels that are actually used in the calculation; (b) White + is the pixel accuracy center, and the red cross is the computed centroid, *i.e.*, the center at sub-pixel accuracy. Note that the neighboring particles' reflections (clear spots on the particle's side) are excluded from the circular domain of integration.

Gaussian signals is studied in particular as a function of the threshold level (*i.e.*, the background intensity level) and the signal diameter. In particular, the author demonstrates that for a 2D Gaussian signal of diameter 14 pixels and of a threshold intensity of 10% of the maximum amplitude, as it is approximately the case for us, the expected error is about 0.01 pixel. Again extrapolating this result to our double-peak signal leads us to estimating our error as

$$\delta \approx 0.01\,\text{pix} \approx 0.0005\,\text{mm} \tag{2.25}$$

which implies that we can detect the displacements of particles moving at velocities as low as $v_{\text{min}} = \delta\, f_{\text{acq}} = 0.039\,\text{cm.s}^{-1}$, *i.e.*, of the order of magnitude of $0.1\,\text{cm.s}^{-1}$, which seems reasonable.

When the parameters controlling the sub-pixel accuracy detection (and specifically, d_{bary}) are not properly tuned and we do not reach the expected accuracy, one can clearly see that particle displacements are not smooth but are discontinuous instead.

2.1.4 Particle tracking

We now have the positions at sub-pixel accuracy. From these, we aim at computing the individual particle trajectories. Particle Image Velocimetry relies on the cross-correlation of the ensemble of some seeding particle positions between successive frames. This Eulerian method provides velocity fields but not individual particle trajectories. In contrast, Particle Tracking Velocimetry (PTV) is a Lagrangian approach which gives access to individual particle trajectories.

Principle

This technique relies on the estimation of the most likely displacement of each particle between two frames and can be implemented in different ways. Whatever the specific method of implementation, the PTV analysis algorithm has to be given the ensemble of the center positions on every successive frame. In this thesis, we used the open-source *tracking* algorithm written in Matlab by Daniel Blair and Eric Dufresne [56], translated from the IDL tracking code by John Crocker and David Grier [61].

The basic idea of this tracking algorithm is, in the case of a system with a fixed number of particles, N, to look for the most probable set of N identifications between the N locations in the two consecutive images. Note that this algorithm was originally written for tracking colloidal particles. Therefore, it starts from the assumption that particle trajectories are Brownian, but it still works well for other types of trajectories, as noticed by the authors themselves [61].

Implementation

The probability for a Brownian particle to diffuse a distance δ_B in the horizontal plane within a time τ is

$$P(\delta_B|\tau) = \frac{1}{4\pi D\tau} \exp\left(-\frac{\delta_B^2}{4D\tau}\right) \tag{2.26}$$

where D is the particle self-diffusion coefficient. For an ensemble of N non-interacting identical particles, the corresponding probability distribution is the product of single particle results:

$$P(\{\delta_{B,i}\}\,|\tau) = \left(\frac{1}{4\pi D\tau}\right)^N \exp\left(-\sum_{i=1}^{N} \frac{{\delta_{B,i}}^2}{4D\tau}\right). \tag{2.27}$$

The most likely assignment of particle labels from one image to the next, is the one which maximizes $P(\{\delta_{B,i}\}\,|\tau)$, or equivalently, minimizes $\sum_{i=1}^{N} \delta_{B,i}^2$. The authors discuss the applicability of such a criterion to interacting particles, and conclude that if displacements between two frames are small enough compared to the interparticle spacing, the algorithm still works well.

Criteria on f_{acq}

Consequently, a criterion which is sufficient, even though not necessary, is that typical particle displacements $\langle\delta\rangle$ must be significantly smaller than a particle diameter:

$$\langle\delta\rangle = \frac{v_{\max}}{f_{\mathrm{acq}}} < a \tag{2.28}$$

where $v_{\max}$ is the maximum velocity of the particles. When this condition is verified, there is no risk of misattribution of position assignments, hence trajectories are properly built. In practice, we have $v_{\max} \sim 10\,\mathrm{cm.s^{-1}}$ and $a = 1\,\mathrm{mm}$, which leads to the condition $f_{\mathrm{acq}} > 100\,\mathrm{Hz}$. With $f_{\mathrm{acq}} = 780\,\mathrm{Hz}$, not only are we making sure that the tracking algorithm will work well, but we are also making it possible to observe collisions events, which are fast events. Two examples of trajectories are presented in Fig. 2.8(a) and (b) for a filling fraction $\phi \sim 0.5$, a dimensionless acceleration $\Gamma \approx 2$, and a magnetic field $B_0 = 120\,\mathrm{G}$.

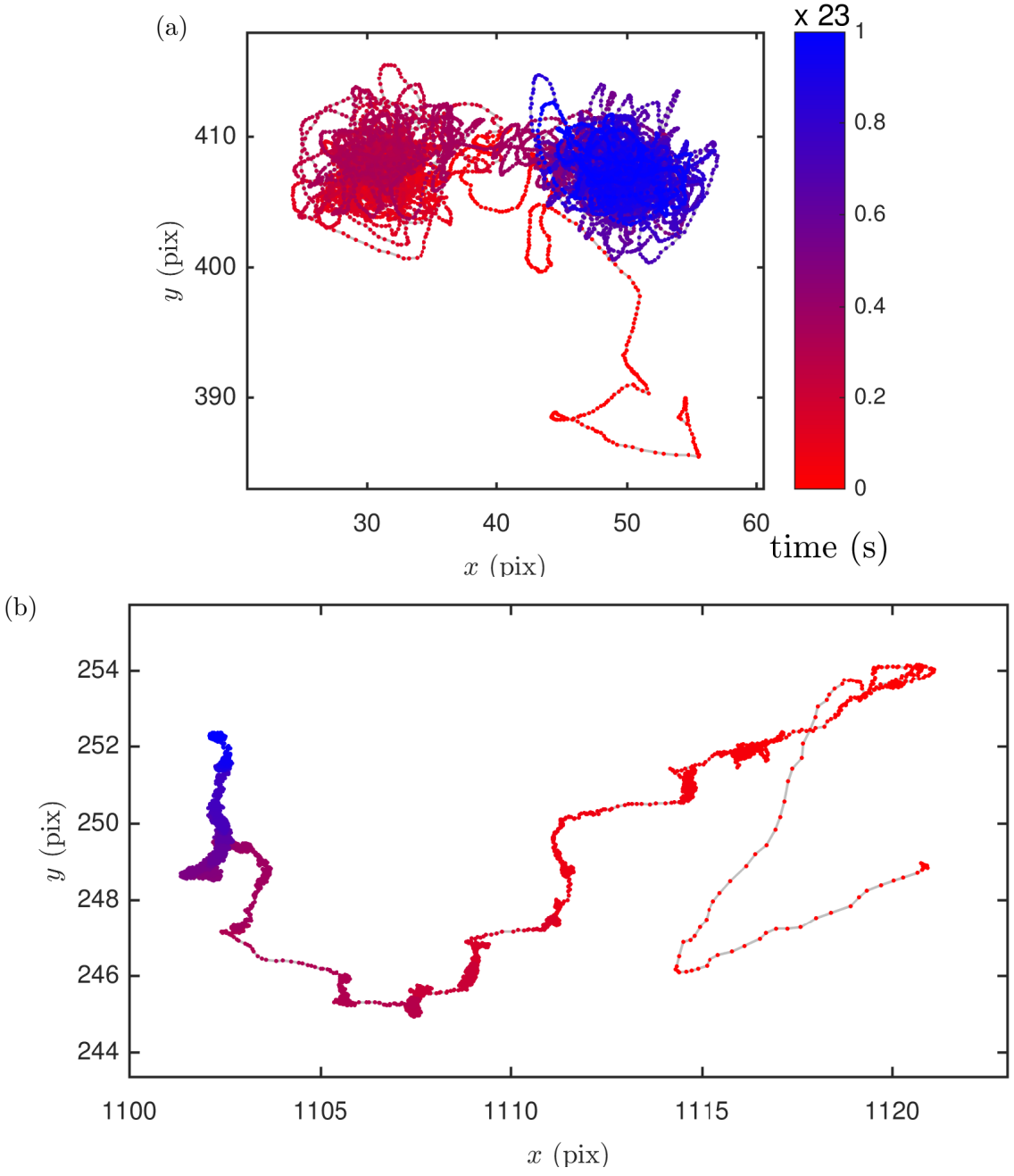

Figure 2.8 Two examples of particle trajectories in the horizontal plane, from an experiment with $\phi = 0.5$, $\Gamma = 2$ and $B = 120\,\mathrm{G}$, for $18,000$ successive positions at $f_{\mathrm{acq}} = 780\,\mathrm{Hz}$. (a) A particle gets trapped in a potential well (red), escapes and gets trapped again in a neighboring well (blue); (b) A particle with a more linear displacement. Note that a particle's diameter is about 20 pixels. Changes of directions are due to collisions with the bottom and top surfaces, as well as interactions with neighboring particles.

Refinements

Refinements are implemented in the routine that we use. For instance, instead of scanning the full region of interest, one can restrict the search to a limited region around the last known particle position, say of size L. Analytically, this means using a single-particle probability distribution $P(\delta_B|\tau)$ truncated at $\delta_B = L$. One can also allow a particle to disappear from the region of interest for a given number of time steps, and connect its trajectory when it reappears. If the particle disappears for too long, or if the new trajectory cannot be assumed to belong to the same particle, then a new particle label is used and a new trajectory is built.

The latter feature is of particular interest to us. Indeed, our region of interest does not encompass the full cell area, allowing particles to enter and exit it, and hence letting their number vary as time goes. Another reason for which a trajectory can be artificially broken by the tracking algorithm is blinking of the signal, which is encountered in anomalous particles displaying an inhomogeneous reflectivity. We faced this problem when using the square cell, because the sandpaper sheet tended to rapidly make particles dull. In contrast, the aluminum cell allowed us to work with high-quality particle signals.

2.2 Data analysis

We give here some details about a few technical aspects of data analysis, regarding detecting collisions and contact in clusters, measuring the vertical positions of the particles, and performing a measure of the mean magnetic energy of the ensemble of particles.

2.2.1 Collision and cluster detection

Thanks to the high speed video camera, we are able to accurately resolve the approach of two particles prior to a collision, and their subsequent separation too. Yet, the duration of a collision remains very short, even when we do recordings at 780 Hz, and the particles separate quickly. In order to detect binary collisions, we wrote an algorithm applying a distance criterion: when particles approach each other at a distance r smaller than a given distance d_{coll}, chosen by us, then we consider that a collision has happened. Typically, we use $d_{\text{coll}} = 1.03\,a$. Some measures of collision rates are used in Chapter 4.

We perform the detection of *clusters* of particles, or ensemble of particles permanently at contact, in an analogous way. The base of our code is a routine written by Peter J. Lu [62]. As we will see in Chapter 5 and Chapter 6, in our system, particles which stay in contact are in a *buckled* configuration, where particles are in contact with each other and alternatively with the top or bottom plate. Then, the distance between two centers measured in the horizontal plane, x_g, is smaller than one particle diameter, a. The criteria that we apply to detect aggregated particles, analogously to when detecting collisions, is that the distance between two particles, r, is smaller than a given distance, d_{clus}. Note that for the algorithm detecting clusters, $d_{\text{clus}} < a$ due to the *buckled* configuration. In practice, we adapt d_{clus} to the gap size of the cell: it is comprised between the theoretical smallest value of x_g (which is fixed by the gap size) and a. For instance we use $d_{\text{clus}} = 0.88\,a$ for a gap size $e = 1.48\,a$. A cluster is defined as a continuum of particles respectively separated by less than d_{clus}. In order to do not consider as clustered two particles that are simply colliding, we verify if the two particles are still at contact about 0.1 s after the first detection. If yes, then we consider that they form a cluster from the time of the first detection.

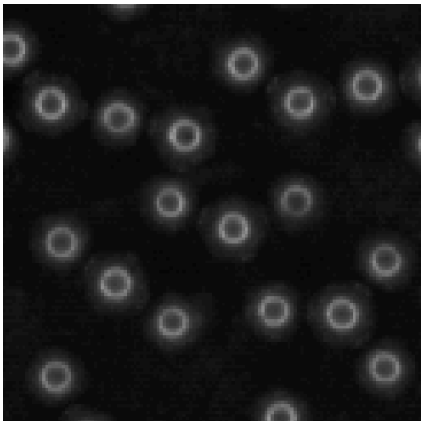

Figure 2.9 Example of particles at contact. The circular signal on the top of the particles touching the bottom plate is partially reflected on the side of the particles touching the top plate.

2.2.2 Vertical position of the particles

From real signal

Unlike in numerical simulations, in experiments on quasi-two-dimensional granular gases, the vertical positions of the particles is generally not known. Indeed, there is no simple means to measure them. Here, we explain how we can measure them under some specific conditions, namely when they are part of a cluster.

As illustrated in Fig. 2.9, when particles are in contact in a cluster, the signal of the particles touching the bottom plate, which we call *down* particles, is partially reflected on the side of the particles touching the top plate, or *up* particles. By eye, the two types of particles are therefore distinguishable. Now, how to automatize their assignment to either *up* or *down* type? We exploit the signal reflection on the side of the *up* particles. For every particle, we perform a radial average of the grey level of the image around the center. As illustrated in Fig. 2.10(a) for an *up* particle and in Fig. 2.10(b) for a *down* particle, the obtained signals look similar. Yet, integrating the area under the blue curve between the vertical dashed red line, indicating a distance set by us, r_{pop}, and the minimum of the grey level curve, indicated by the vertical blue dashed line, makes possible to distinguish the two types of particles. Indeed, when we plot the distribution of the integrated areas (to which a constant is subtracted), as shown in Fig. 2.10(c), two well separated populations appear. Those with a small integrated area correspond to particles with a low intensity signal, *i.e.*, these are the *down* particles, while the other population is the one of the *up* particles. The level of success of this operation relies, in particular, on the choice of r_{pop}, which we make by hand. An example of result of an operation of assignment of *up* and *down* positions to all the particles is shown in Fig. 2.11.

Note, however, that the main limitations of this routine are, first, when the signals do not have the required quality, and second, when particles overlap so much that the reflection on the side of the *up* particles disappear partially. The latter problem is related to the value of the gap size.

Virtually

In order to avoid the problem mentioned above on the impossibility of detecting a usable reflected signal, and for the sake of speed of implementation, we designed another method. This technique

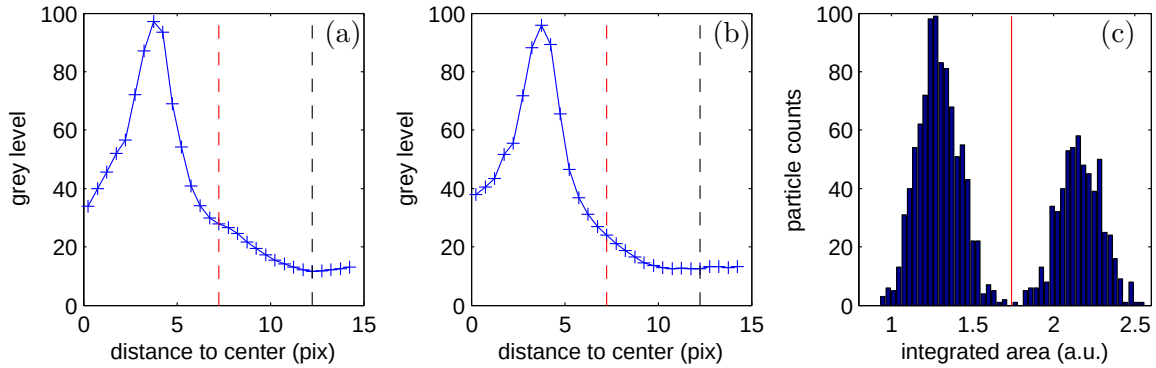

Figure 2.10 Distinguishing *up* from *down* particles. (a) Example of radially averaged grey level of an *up* particle; (b) Example of radially averaged grey level of a *down* particle; (c) Histogram of the area integrated under the curves of radially averaged grey level, between the arbitrary distance (chosen by the operator) marked by the vertical red line in (a) and (b), and the minimum of grey level automatically computed and marked by the black dashed vertical line in (a) and (b). The reflection on the side of the *up* particles induces a larger integrated area than for the *down* particles, which generates two well separated populations: left, *down* particles, and right, *up* particles. The vertical red line indicates the limit set by the operator to define the two populations.

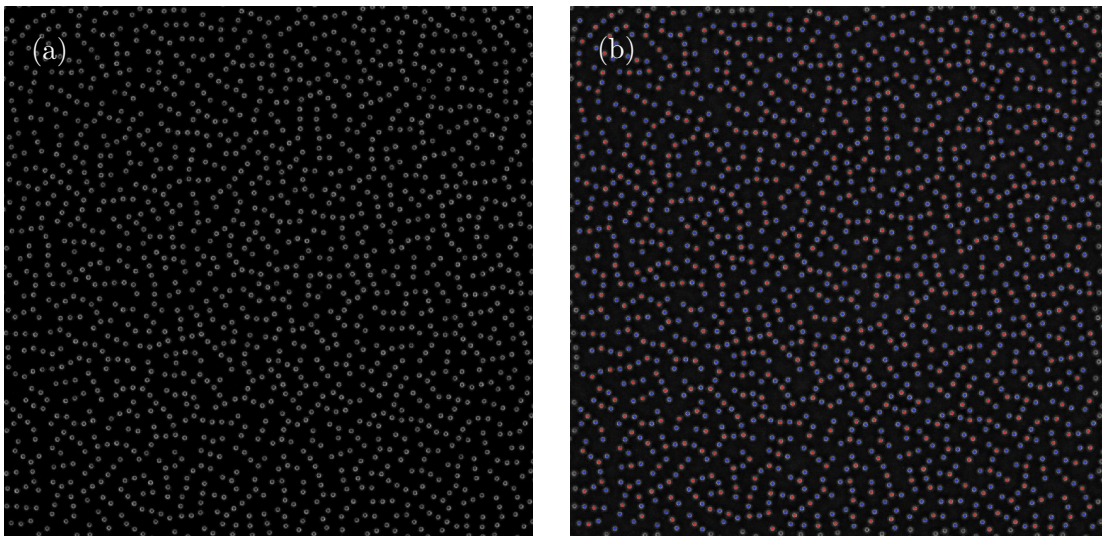

Figure 2.11 Illustrating at the full cell scale the *up* and *down* positions of the particles in a structure where all particles are in contact. (a) Real image; (b) Superimposed red (resp., blue) dots indicate the *up* (*down*) position of the particles.

does not rely at all on the real images. Instead, it is based on data obtained from the algorithm detecting the clusters, namely, the positions of the particles assigned to given clusters, and on the observation that the greater part of the ends of the chains are *down* in measures from real signal. This algorithm proceeds as follows. For a given cluster, first, it detects which particles are chain ends, if there are any. Then, it randomly chooses one of these ends, and assigns to it the *down* position, after which it assigns alternatively *up* and *down* positions from closest neighbor to closest neighbor inside the cluster. We show the result of such an operation in Fig. 2.12, which is taken from an experiment which also includes particles not attached to chains (black dots in

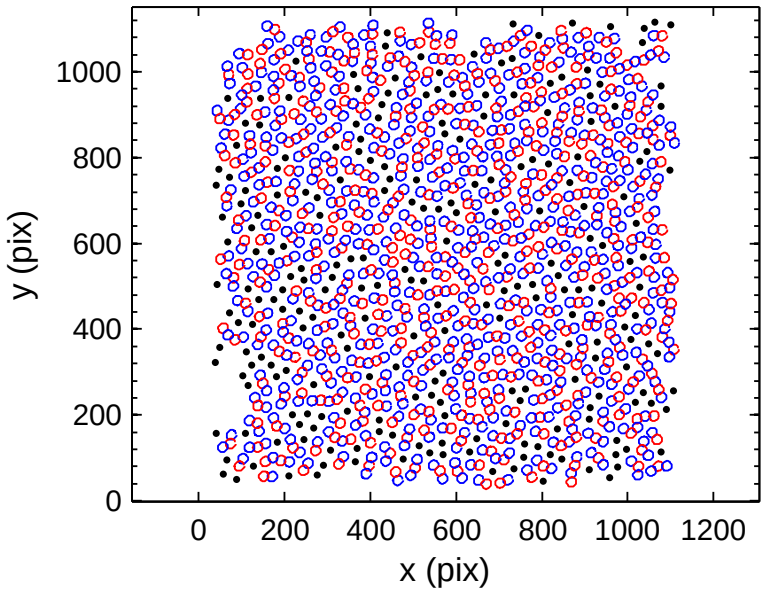

Figure 2.12 Virtually allocating *up* or *down* position to particles. Red (resp. blue) circles represent *up* (*down*) particles. Black dots are particles not attached to a chain. The algorithm picks up one end of a chain, assigns to is the *down* position, and then assigns iteratively *up* and *down* positions to the rest of the particles of the chain.

the figure). Note that such a method is approximative, but we consider that it is sufficient for estimating, in particular, the mean kinetic energy of interaction of particles inside a phase with particles in clusters.

2.2.3 Magnetic energy

The mean magnetic energy of interaction per particle, E_m, is defined in Chapter 3: it is calculated from the sum of all the pairwise energies of interactions of the particles. In practice, computing such a sum is numerically very costly, and it is preferable to reduce the distance up to which neighboring particles are considered to significantly interact with the reference particle. However, one must be careful when choosing such a threshold, since it must be large enough so that significantly interacting particles are not rejected from the algorithm. In our case, the measure of E_m increases up to approximately saturating for a distance of integration near 10 particles diameters. Based on this result, we choose to compute the mean magnetic energy per particle by using particles as far as $10\,a$.

2.3 Personal contribution

During this experimental PhD, aside from automating the experiments, as detailed in the end of Chapter 1, I largely dedicated myself to image processing and data analysis. Even though I benefited from a few crucial open source codes for particle detection and tracking, putting them all together, complementing and adapting them to our various experimental conditions revealed to be a substantial task. Moreover, I developed nearly all data analysis routines, some of which are mentioned above.

Chapter 3

Theoretical tools

Chapter 3 : Theoretical tools

↑ back to contents

Chapter abstract

First, we describe the behavior of a particle immersed in a magnetic field, for a permanently magnetized particle and for a particle with an induced magnetic moment. Second, we study the interactions of two magnetized particles, in general and in the quasi-two-dimensional geometry of our experiments. Finally, we provide some theoretical tools that we will use in Chapter 4, Chapter 5, and Chapter 6. A brief description of the kinetics of granular systems is given in Appendix A. For a more comprehensive description of the kinetics and of the complex microscopic properties of granular matter —including elastic, viscous, adhesion and friction forces, the dissipation of energy at the grain level and the meaning of the coefficient of restitution— we suggest to the reader the reference books of Brilliantov and Pöschel [7] and of Andreotti *et al.* [3].

3.1 Magnetization of one particle

This thesis' work originality consists in using granular particles that can be magnetized and interact at a distance in a tunable way, in contrast to classical dissipative granular particles. Let us now first briefly demonstrate the relation between the magnetic scalar potential and the magnetization, and then apply this result to the case of a permanent magnetic dipole and of an

induced magnetic dipole. Most of the results of this section are inspired from Jackson's *Classical Electrodynamics* [50] and Griffiths's *Introduction to Electrodynamics* [63].

3.1.1 Maxwell's equations and the magnetic scalar potential

James Maxwell published in the 1860's the *Maxwell's equations* describing how electric and magnetic fields are generated and altered by each other and by charges and currents. In their modern differential form, the *Maxwell's equations* write:

$$\boldsymbol{\nabla} \cdot \mathbf{E} = \frac{\rho}{\epsilon_0} \tag{3.1}$$

$$\boldsymbol{\nabla} \cdot \mathbf{B} = 0 \tag{3.2}$$

$$\boldsymbol{\nabla} \times \mathbf{E} = -\frac{\partial \mathbf{B}}{\partial t} \tag{3.3}$$

$$\boldsymbol{\nabla} \times \mathbf{B} = \mu_0 \left(\mathbf{J} + \varepsilon_0 \frac{\partial \mathbf{E}}{\partial t} \right) \tag{3.4}$$

where $\boldsymbol{\nabla} = \frac{\partial}{\partial \mathbf{r}}$ is the partial derivative with respect to space, $\mathbf{E}(\mathbf{r}, t)$ is the electric field strength, $\mathbf{B}(\mathbf{r}, t)$ is the magnetic field strength, $\rho(\mathbf{r}, t)$ is the electric charge density, $\mathbf{J}(\mathbf{r}, t)$ is the electric current density, $\varepsilon_0 \approx 8.85\,10^{-12}\,\mathrm{F.m^{-1}}$ is the vacuum electric permittivity and $\mu_0 = 4\pi 10^{-7}\,\mathrm{V.s.A^{-1}.m^{-1}}$ is the vacuum magnetic permeability. In the following, we will only make use of Eq. 3.2 and Eq. 3.4.

In addition to these fields, let us define the *magnetization field*, or simply *magnetization*, $\mathbf{M}$, which is the vector field corresponding to the density of magnetic dipoles in a magnetic material:

$$\mathbf{M} = \frac{\mathrm{d}\mathbf{m}}{\mathrm{d}V}, \tag{3.5}$$

where $\mathrm{d}\mathbf{m}$ is the elementary magnetic moment in the volume element $\mathrm{d}V$.

Magnetic dipoles can be either permanent or induced. A permanent magnet is composed of a material, or an ensemble of materials, which naturally remains magnetized and creates its own persistent magnetic field, or *remnant* magnetic field, after it has been immersed in an external magnetic field. A permanent magnet is made of a ferromagnetic material, such as iron, nickel or alloys of rare earth metals. In contrast, the magnetic moment of an induced magnet only exists when an external magnetic field is applied, and it vanishes when this magnetic field is turned off. *Hard* ferromagnetic materials tend to keep their acquired magnetic moment unchanged, *i.e.*, it decreases very slowly, while for *soft* ferromagnetic materials, it tends to decrease significantly fast. The chromed steel balls that we use in our experiments are made of a steel alloy, AISI 52100, as detailed in Section 1.1.2, which is a soft ferromagnetic material. As we have seen in Section 1.1.2, these particles lose rapidly most of their magnetization, but a small amplitude remnant magnetic moment still remains when the external magnetic field is turned off.

From Eq. 3.4, it is possible to make a new field appear, which is called the *magnetic excitation field*, $\mathbf{H}$, and is related to the magnetic field $\mathbf{B}$ and the magnetization $\mathbf{M}$ through

$$\mathbf{B} = \mu_0(\mathbf{H} + \mathbf{M}). \tag{3.6}$$

For isotropic materials that do not bear a remnant magnetic moment, that is, whose magnetization cycle $[B = f(H)]$ does not display any hysteretic behavior, there exists a linear

relationship between $\mathbf{M}$ and $\mathbf{H}$ inside the material:

$$\mathbf{M} = \chi_m \mathbf{H}, \tag{3.7}$$

where the dimensionless quantity χ_m is called the *magnetic susceptibility*. This implies that inside the material, $\mathbf{B}$ and $\mathbf{H}$ are linearly related through:

$$\mathbf{B} = \mu_0 \mu_r \mathbf{H} = \mu \mathbf{H}, \tag{3.8}$$

where $\mu_r \equiv 1 + \chi_m$ is the *relative magnetic permeability*, and $\mu \equiv \mu_0 \mu_r$ is the *magnetic permeability* of the materials.

Let us now consider a point of space either inside or outside the magnetized materials. Let us assume that there are no current in the problem and that we are studying a steady state. Under these circumstances, it can be shown from Eq. 3.4 that at any point of space, the magnetic excitation is irrotational:

$$\boldsymbol{\nabla} \times \mathbf{H} = 0. \tag{3.9}$$

This leads us to the conclusion that there exists a *magnetic scalar potential* ϕ_m such as $\mathbf{H} = -\boldsymbol{\nabla}\phi_m$. This result, along with Eq. 3.2 and Eq. 3.6, implies that the magnetic scalar potential at any point of space is given by the Poisson's equation:

$$\nabla^2 \phi_m = \boldsymbol{\nabla} \cdot \mathbf{M}, \tag{3.10}$$

where ∇^2 is the Laplace operator.

3.1.2 Magnetic field generated by a uniformly magnetized sphere

Let us consider a sphere of radius σ, bearing a uniform permanent magnetization $\mathbf{M} = M\mathbf{e}_z$ and surrounded by vacuum. Under these circumstances, Eq. 3.10 simplifies into

$$\nabla^2 \phi_m = 0, \tag{3.11}$$

which is Laplace's equation. Here we use spherical coordinates, as defined in Fig. 3.1, for the objects that we are studying are spheres. Moreover, $\mathbf{M} = M\mathbf{e}_z$, hence our problem has azimuthal symmetry. Consequently, Eq. 3.11 can be written as

$$\frac{\partial}{\partial r}\left(r^2 \frac{\partial \phi_m}{\partial r}\right) + \frac{1}{\sin\theta}\frac{\partial}{\partial \theta}\left(\sin\theta \frac{\partial \phi_m}{\partial \theta}\right) = 0. \tag{3.12}$$

This equation can be solved by separating the variables r and θ [63]. The general solution that is then obtained is the linear combination of separable solutions:

$$\phi_m(r,\theta) = \sum_{l=0}^{\infty} \left(A_l r^l + \frac{B_l}{r^{l+1}}\right) P_l(\cos\theta), \tag{3.13}$$

where A_l and B_l are constants and $P_l(\cos\theta)$ are Legendre polynomials in the variable $\cos\theta$, $P_l(x)$ being defined as:

$$P_l(x) = \frac{1}{2^l l!}\left(\frac{\mathrm{d}}{\mathrm{d}x}\right)^l (x^2 - 1)^l, \tag{3.14}$$

which gives $P_0(x) = 1$, $P_1(x) = x$, $P_2(x) = (3x^2 - 1)/2$, etc.

We can find the coefficients A_l and B_l by imposing boundary conditions on the potential ϕ_m:

- ϕ_m is finite inside the sphere, in particular when $r \to 0$. Hence, $B_l = 0$ inside the sphere:

$$\phi_m(r < \sigma, \theta) = \sum_{l=0}^{\infty} A_l r^l P_l(\cos\theta). \tag{3.15}$$

- ϕ_m is finite outside the sphere, in particular when $r \to \infty$. Hence, $A_l = 0$ outside the sphere:

$$\phi_m(r > \sigma, \theta) = \sum_{l=0}^{\infty} \frac{B_l}{r^{l+1}} P_l(\cos\theta). \tag{3.16}$$

- ϕ_m is continuous at the sphere boundary, that is, $\phi_m(r = \sigma_-, \theta) = \phi_m(r = \sigma_+, \theta)$. Hence:

$$B_l = A_l \sigma^{2l+1}. \tag{3.17}$$

Let us now apply Eq. 3.2 in the integral form $\oint \mathbf{B} \cdot \mathrm{d}\mathbf{a} = 0$ to a Gaussian pillbox enclosing a small piece of sphere surface and extending a little above and below this surface. We obtain for the perpendicular component of the magnetic field, $B_\perp(r = \sigma_-) = B_\perp(r = \sigma_+)$, which writes in terms of $\mathbf{H}$ and $\mathbf{M}$, using Eq. 3.6:

$$H_\perp(r = \sigma_+) - H_\perp(r = \sigma_-) = -[M_\perp(r = \sigma_+) - M_\perp(r = \sigma_-)]. \tag{3.18}$$

From this equation, using the relation $\mathbf{H} = -\boldsymbol{\nabla}\phi_m$, Eq. 3.15 and Eq. 3.16, we get:

$$\sum_{l=0}^{\infty} A_l l \sigma^{l-1} P_l(\cos\theta) - \sum_{l=0}^{\infty} B_l \left(-\frac{l+1}{\sigma^{l+2}}\right) P_l(\cos\theta) = -M\cos\theta. \tag{3.19}$$

For $l = 1$, we find $A_1 = \dfrac{M}{3}$ and $B_1 = \dfrac{M}{3}\sigma^3$; and for all $l \neq 1$, $(2l+1)A_l = 0$, that is, $A_l = 0 = B_l$. Consequently, the magnetic scalar potential ϕ_m writes:

$$\phi_m(r, \theta) = \frac{1}{3} M r \cos\theta \qquad \text{if} \quad r < \sigma \tag{3.20}$$

$$\phi_m(r, \theta) = \frac{1}{3} M \frac{\sigma^3}{r^2} \cos\theta \qquad \text{if} \quad r > \sigma \tag{3.21}$$

Now, using the relation $\mathbf{H} = -\boldsymbol{\nabla}\phi_m$ and using the definition of the magnetic moment $\mathbf{m} = \frac{4}{3}\pi\sigma^3\mathbf{M}$, we obtain the magnetic excitation field for the uniformly vertically magnetized sphere,

$$\mathbf{H}_{\text{ums}} = -\frac{1}{3}\mathbf{M} \qquad \text{if} \quad r < \sigma \tag{3.22}$$

$$\mathbf{H}_{\text{ums}} = \frac{1}{4\pi}\left[-\frac{\mathbf{m}}{r^3} + \frac{3(\mathbf{m}\cdot\mathbf{r})\mathbf{r}}{r^5}\right] \qquad \text{if} \quad r > \sigma \tag{3.23}$$

According to Eq. 3.6, these equations yield the magnetic field generated by a uniformly

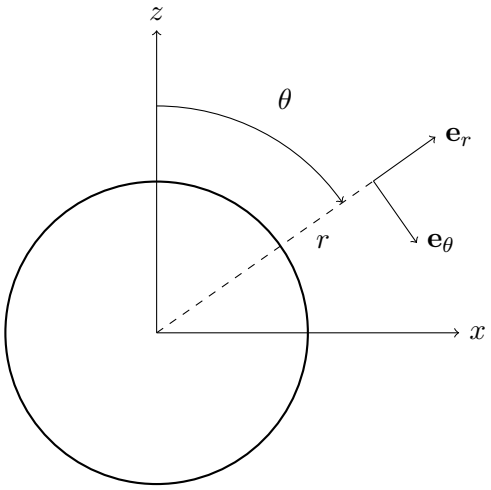

Figure 3.1 Definition of the spherical coordinates (r, θ) in the vertical plane (x, z). Note that the azimuthal coordinate is not represented here because the problem has azimuthal symmetry. The reference ball is centered at the origin of the frame.

vertically magnetized sphere:

$$\mathbf{B}_{\text{ums}} = \frac{2}{3}\mu_0 \mathbf{M} \qquad \text{if} \quad r < \sigma \tag{3.24}$$

$$\mathbf{B}_{\text{ums}} = \frac{\mu_0}{4\pi}\left[-\frac{\mathbf{m}}{r^3} + \frac{3(\mathbf{m}\cdot\mathbf{r})\mathbf{r}}{r^5}\right] \qquad \text{if} \quad r > \sigma \tag{3.25}$$

which reads in spherical coordinates,

$$\mathbf{B}_{\text{ums}} = \frac{2}{3}\mu_0 M(\cos\theta \mathbf{e}_r - \sin\theta \mathbf{e}_\theta) \qquad \text{if} \quad r < \sigma \tag{3.26}$$

$$\mathbf{B}_{\text{ums}} = \frac{1}{3}\mu_0 M \frac{\sigma^3}{r^3}(2\cos\theta \mathbf{e}_r + \sin\theta \mathbf{e}_\theta) \qquad \text{if} \quad r > \sigma \tag{3.27}$$

Such a magnetic field is illustrated in Fig. 3.2(a), where both amplitude and field lines are depicted.

3.1.3 Soft-ferromagnetic sphere in an external magnetic field

Let us now consider a ferromagnetic sphere of radius σ and magnetic permeability μ, which initially does not bear any magnetic moment. We immerse this sphere in an external uniform magnetic field $\mathbf{B}_0 = B_0\mathbf{e}_z$. We aim at calculating the magnetization of the sphere and the resulting total magnetic field, inside and outside the sphere.

At every point of space, the total magnetic field, $\mathbf{B}_{\text{tot}}$, is the sum of the magnetic field generated by the magnetized sphere and of the external magnetic field:

$$\mathbf{B}_{\text{tot}} = \mathbf{B}_{\text{ums}} + \mathbf{B}_0, \tag{3.28}$$

where $\mathbf{B}_{\text{ums}}$ is given by Eq. 3.24 and Eq. 3.25. Similary, the resulting magnetic excitation writes,

$$\mathbf{H}_{\text{tot}} = \mathbf{H}_{\text{ums}} + \frac{1}{\mu_0}\mathbf{B}_0. \tag{3.29}$$

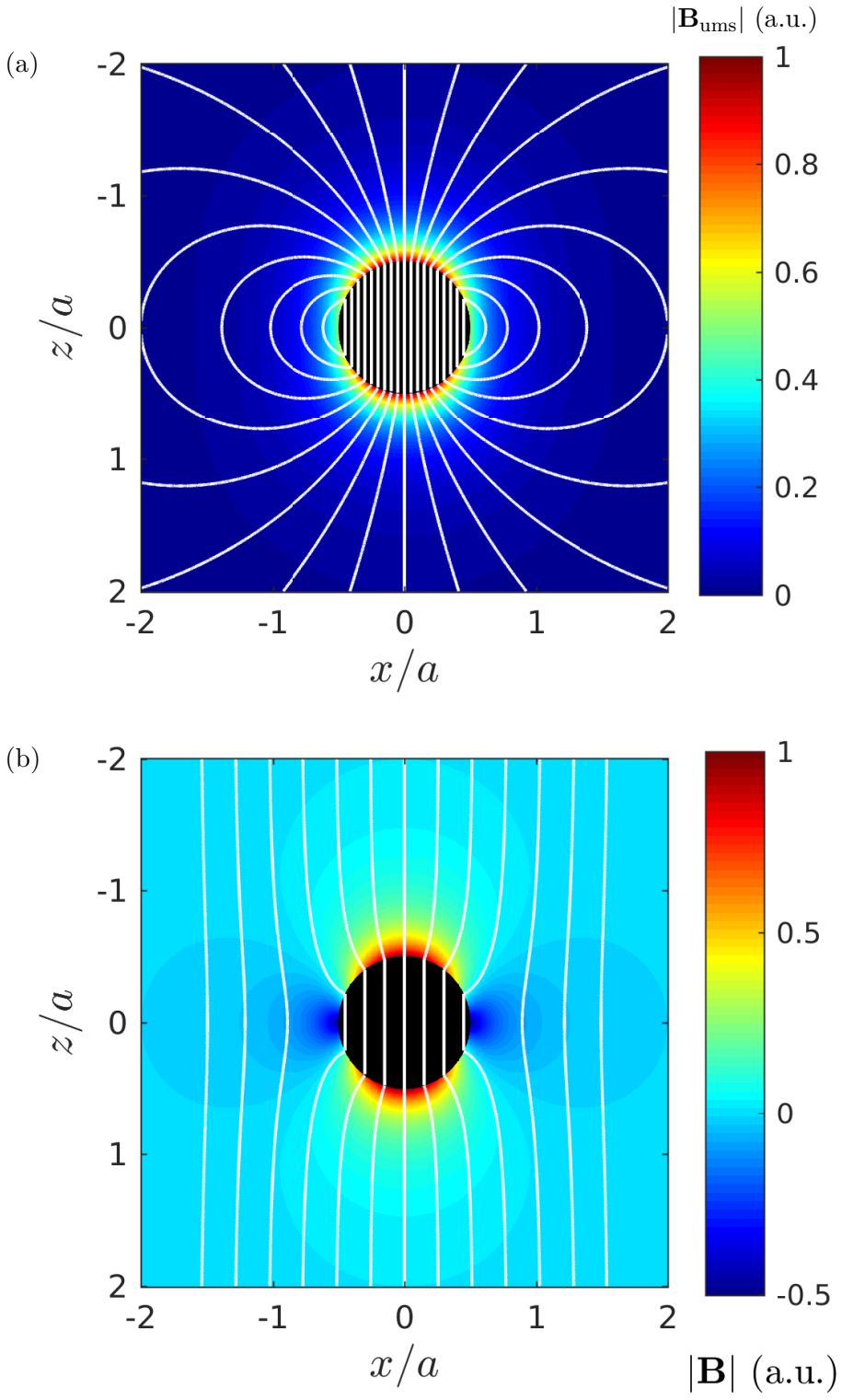

Figure 3.2 Magnetic fields and magnetic field lines. The black disk represent the particle of diameter $a = 2\sigma$. The white lines are field lines. (a) Magnetic field generated by a uniformly magnetized sphere with $\mathbf{M} = M\mathbf{e}_z$, namely $\mathbf{B}_{\text{ums}}$, as defined by Eq. 3.24 and Eq. 3.25. (b) Magnetic field generated by a ferromagnetic sphere of infinite magnetic permeability in an external field $\mathbf{B}_0 = B_0\mathbf{e}_z$, namely $\mathbf{B}_{\text{tot}}$, as defined by Eq. 3.32 and Eq. 3.33.

The *induced* magnetization of the sphere, $\mathbf{M}$, depends on the external magnetic field, $\mathbf{B}_0$, and of the way the sphere material responds to it, which is quantified by the magnetic permeability, μ. In order to determine $\mathbf{M}$, let us write the total magnetic field inside the sphere, $\mathbf{B}_{\text{tot}}(r < \sigma)$, as a function of the total magnetic excitation inside the sphere, $\mathbf{H}_{\text{tot}}(r < \sigma)$, using Eq. 3.8,

$$\mathbf{B}_{\text{tot}}(r < \sigma) = \mu \mathbf{H}_{\text{tot}}(r < \sigma) \tag{3.30}$$

which yields, using Eq. 3.24, Eq. 3.28 and Eq. 3.29,

$$\mathbf{M} = \frac{3}{\mu_0} \left(\frac{\mu - \mu_0}{\mu + 2\mu_0} \right) \mathbf{B}_0. \tag{3.31}$$

From this result, used in Eq. 3.24 and Eq. 3.25, and finally injected in Eq. 3.28, we obtain the magnetic field inside and outside of the uniformly magnetized ferromagnetic sphere,

$$\mathbf{B}_{\text{tot}} = \left[1 + 2 \left(\frac{\mu - \mu_0}{\mu + 2\mu_0} \right) \right] \mathbf{B}_0 \qquad \text{if} \quad r < \sigma \tag{3.32}$$

$$\mathbf{B}_{\text{tot}} = \left[1 - \frac{\sigma^3}{r^3} \left(\frac{\mu - \mu_0}{\mu + 2\mu_0} \right) \right] \mathbf{B}_0 + \frac{3\sigma^3}{r^5} \left(\frac{\mu - \mu_0}{\mu + 2\mu_0} \right) (\mathbf{B}_0 \cdot \mathbf{r})\mathbf{r} \qquad \text{if} \quad r > \sigma \tag{3.33}$$

Materials whose magnetic permeability μ verifies, $\mu \gg \mu_0$ (or equivalently, $\mu_r \gg 1$), are considered to be of *infinite magnetic permeability*. This is the case for our steel balls, for which we measured $\mu_r \gtrsim 500$ (see Section 1.1.2). For instance, the magnetic permeability of cobalt 99 % pure ranges between 70–250, of nickel 99 % pure between 110–600, and of iron 99.95 % pure between 10, 000–200, 000 [64], all being ferromagnetic materials. For paramagnetic materials such as platinum or aluminum, it is usually much lower and closer to 1.

In the limit of infinite permeability, which in particular applies to our steel balls, the magnetization of the sphere writes from Eq. 3.31,

$$\lim_{\mu \to \infty} \mathbf{M} = \frac{3}{\mu_0} \mathbf{B}_0, \tag{3.34}$$

and the total magnetic field becomes,

$$\lim_{\mu \to \infty} \mathbf{B}_{\text{tot}} = 3\, \mathbf{B}_0 \qquad \text{if} \quad r < \sigma \tag{3.35}$$

$$\lim_{\mu \to \infty} \mathbf{B}_{\text{tot}} = \left[1 - \frac{\sigma^3}{r^3} \right] \mathbf{B}_0 + \frac{3\sigma^3}{r^5} (\mathbf{B}_0 \cdot \mathbf{r})\mathbf{r} \qquad \text{if} \quad r > \sigma \tag{3.36}$$

which writes in spherical coordinates,

$$\lim_{\mu \to \infty} \mathbf{B}_{\text{tot}} = 3\, B_0 \left(\cos\theta \mathbf{e}_r - \sin\theta \mathbf{e}_\theta \right) \qquad \text{if} \quad r < \sigma \tag{3.37}$$

$$\lim_{\mu \to \infty} \mathbf{B}_{\text{tot}} = B_0 \cos\theta \left[\frac{2\sigma^3}{r^3} + 1 \right] \mathbf{e}_r + B_0 \sin\theta \left[\frac{\sigma^3}{r^3} - 1 \right] \mathbf{e}_\theta \qquad \text{if} \quad r > \sigma \tag{3.38}$$

We show in Fig. 3.2(b) the magnetic field and magnetic field lines around a sphere of infinite magnetic permeability. This represents well the magnetic field around one of the steel balls of our system when it can be considered far enough from the other ones.

3.2 Interactions between two magnetic dipoles

We focused so far on the magnetic field generated by a single particle, when it bears a permanent or an induced magnetic moment. Our system is composed of an ensemble of particles bearing induced dipoles and hence interacting with each others through dipolar interactions. Computing the magnetization and potential interaction forces for an ensemble of induced magnetic dipoles is a task that cannot be exactly done analytically and which we discuss at the end of this section. Here we consider the case of two spheres with an induced magnetization resulting from the applied magnetic field, B_0, as defined in Eq. 3.31, and which do not influence each other, *i.e.*, we assume that the amplitude of the magnetic field generated by each sphere, $\mathbf{B}_{\text{ums}}$, is small compared to B_0. We describe, first, the interaction of these two spheres in a general context, and then, we study the consequences in the specific geometry of our experiments (some of our results are similar to those found in [65]). In particular, we investigate the effect of gravity on the stability of a pair of partially overlapping magnetized particles, which is a relevant situation for our experiments, as we will see in Chapter 5 and Chapter 6.

3.2.1 Potential energy of one magnetized sphere in the magnetic field of another sphere

Let us consider two spheres bearing magnetic moments $\mathbf{m}_1$ and $\mathbf{m}_2$ in the spherical frame centered on particle 1, as defined in Fig. 3.3. Particle 1 is called the *reference particle*, and particle 2, the *test particle*. The potential energy of magnetic interaction for the test particle, which is immersed in the magnetic field $\mathbf{B}_1$ generated by the particle of magnetic moment $\mathbf{m}_1$, writes

$$E_p^{\text{mag}}(r,\theta) = -\mathbf{m}_2 \cdot \mathbf{B}_1(r,\theta). \tag{3.39}$$

Using the formula of the magnetic field generated by a uniformly magnetized sphere, $\mathbf{B}_{\text{ums}}$, given in Eq. 3.25, we write $\mathbf{B}_1$ in terms of $\mathbf{m}_1$ and obtain:

$$E_p^{\text{mag}}(r,\theta) = -\frac{\mu_0}{4\pi r^3}\left[3\left(\mathbf{m}_1 \cdot \mathbf{e}_{12}\right)\left(\mathbf{m}_2 \cdot \mathbf{e}_{12}\right) - \mathbf{m}_1 \cdot \mathbf{m}_2\right], \tag{3.40}$$

where $\mathbf{e}_{12} = \mathbf{e}_r$ is the unit vector from the center of the reference particle (particle 1) to the center of the test particle (particle 2).

As detailed in Section 1.1.2, in our experiments, particles are all made of the same ferromagnetic material (chromed steel AISI 52100) and are of the same diameter, $a = 2\,\sigma$. It follows that all of them have the same magnetic susceptibility χ_m, and same induced magnetic moments, $\mathbf{m}_1 = \mathbf{m}_2 = \mathbf{m}$ along $\mathbf{e}_z$, when they are immersed in an external, uniform and vertical magnetic field, and sufficiently far from each other. Assuming that these magnetic dipoles do not influence each other even at short distances, we can write the potential energy of magnetic interaction for any $r > \sigma$ using Eq. 3.31,

$$E_p^{\text{mag}}(r,\theta) = -\frac{4\pi}{\mu_0}\frac{\sigma^6}{r^3}\left(\frac{\mu-\mu_0}{\mu+2\mu_0}\right)^2\left[3\left(\mathbf{B}_0 \cdot \mathbf{e}_{12}\right)^2 - \|\mathbf{B}_0\|^2\right], \tag{3.41}$$

which becomes, with $\mathbf{B}_0 = B_0\,\mathbf{e}_z$,

$$E_p^{\text{mag}}(r,\theta) = -\frac{4\pi}{\mu_0}B_0^2\frac{\sigma^6}{r^3}\left(\frac{\mu-\mu_0}{\mu+2\mu_0}\right)^2\left[3\cos^2\theta - 1\right]. \tag{3.42}$$

The force to which is submitted the test particle when gravity is not considered, $\mathbf{F}^{\text{mag}} =$

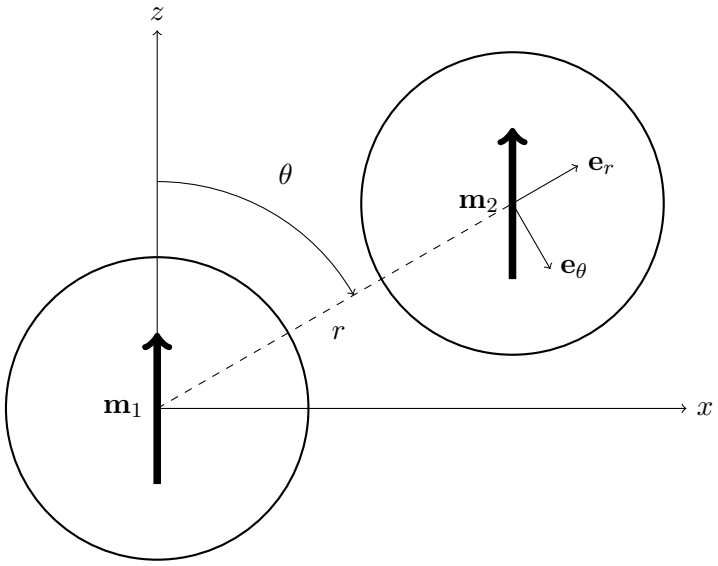

Figure 3.3 Two magnetic moments $\mathbf{m}_1$ and $\mathbf{m}_2$ represented at the center of two spherical particles in a spherical frame (r, θ).

$-\boldsymbol{\nabla} E_p^{\text{mag}}$, is therefore,

$$\mathbf{F}^{\text{mag}} = -\frac{12\pi}{\mu_0} B_0^2 \frac{\sigma^6}{r^4} \left(\frac{\mu - \mu_0}{\mu + 2\mu_0} \right)^2 \left[\left(3\cos^2\theta - 1 \right) \mathbf{e}_r + \sin(2\theta)\, \mathbf{e}_\theta \right]. \tag{3.43}$$

Now, taking into account the contribution of the gravitational potential energy of one ball of a mass m, whose origin we take at $z = 0$, yields the total potential energy:

$$E_p^{\text{tot}}(r, \theta) = -\frac{4\pi}{\mu_0} \frac{\sigma^6}{r^3} \left(\frac{\mu - \mu_0}{\mu + 2\mu_0} \right)^2 B_0^2 \left[3\cos^2\theta - 1 \right] + mgr\cos\theta. \tag{3.44}$$

The total force to which is submitted the test particle is given by $\mathbf{F}^{\text{tot}} = -\boldsymbol{\nabla} E_p^{\text{tot}}$, that is,

$$\begin{aligned} \mathbf{F}^{\text{tot}} = & \left[-\frac{12\pi}{\mu_0} B_0^2 \frac{\sigma^6}{r^4} \left(\frac{\mu - \mu_0}{\mu + 2\mu_0} \right)^2 \left(3\cos^2\theta - 1 \right) - mg\cos\theta \right] \mathbf{e}_r \\ & + \left[-\frac{12\pi}{\mu_0} B_0^2 \frac{\sigma^6}{r^4} \left(\frac{\mu - \mu_0}{\mu + 2\mu_0} \right)^2 \sin(2\theta) + mg\sin\theta \right] \mathbf{e}_\theta. \end{aligned} \tag{3.45}$$

In Fig. 3.4, we compare the potential energy landscapes without and with gravity, E_p^{mag} and E_p^{tot}, and the related force fields, $\mathbf{F}^{\text{mag}}$ and $\mathbf{F}^{\text{tot}}$.

As shown in Fig. 3.4(a), without gravity, the energy landscape and the force field are symmetrical not only with respect to the plane perpendicularly intersecting the figure at $x = 0$, but also with respect to the equatorial plane of the reference particle (perpendicularly intersecting with the figure at $z = 0$). The two magnetic dipoles are purely repulsive in this plane, purely attractive when vertically aligned and always tend to vertically align. From Eq. 3.43, it is straightforward to show that, for $\theta \in [0, \pi]$, the radial force, $F_r^{\text{mag}} = \mathbf{F}^{\text{mag}} \cdot \mathbf{e}_r$, is attractive for $\theta < \theta_{\text{att}}^{\text{mag}} \equiv \arccos\left(1/\sqrt{3}\right) \approx 0.955\,\text{rad} \approx 54.7°$ and for $\theta > \pi - \theta_{\text{att}}^{\text{mag}}$. The polar force, $F_\theta^{\text{mag}} = \mathbf{F}^{\text{mag}} \cdot \mathbf{e}_\theta$, vanishes along $\theta = \theta_{\text{top}}^{\text{mag}} \equiv \pi/2$ and is attractive towards the closest pole.

In contrast, with gravity, the energy landscape loses its up-down symmetry because the

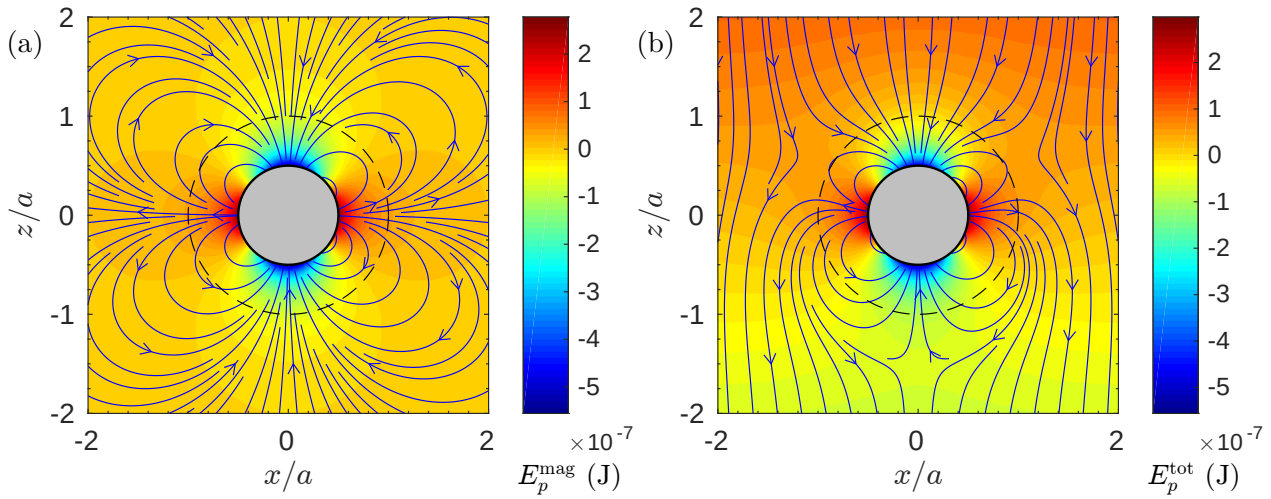

Figure 3.4 Potential energy landscapes and force fields around a reference ball as seen by a second test magnetized ball, for $B_0 = 150\,\mathrm{G}$ and $\mu_r = 500$. Only the reference ball is drawn. (a) Potential energy of magnetic interaction, E_p^{mag}, given in Eq. 3.42 and field of the magnetic force $\mathbf{F}^{\mathrm{mag}}$, given in Eq. 3.43; (b) Total potential energy, E_p^{tot}, including gravity, given in Eq. 3.44 and field of the total force $\mathbf{F}^{\mathrm{tot}}$, given in Eq. 3.45. Note that the center of the second ball cannot access the region around the reference ball such as $r < 2\sigma$ which is limited by the dashed black circle.

gravitational potential energy increases upwards, as shown in Fig. 3.4(b). The symmetry with respect to the plane perpendicularly intersecting the figure at $x = 0$ is conserved. An attractive basin is formed around the top of the reference particle. Two unstable equilibrium positions appear at the two saddle points of the potential energy landscape, *i.e.*, where the radial and polar forces, respectively $F_r^{\mathrm{tot}} = \mathbf{F}^{\mathrm{tot}} \cdot \mathbf{e}_r$ and $F_\theta^{\mathrm{tot}} = \mathbf{F}^{\mathrm{tot}} \cdot \mathbf{e}_\theta$, simultaneously vanish. For $\theta \in [0, \pi/2]$, we can show from Eq. 3.45 that F_r^{tot} vanishes along the curve $\theta_{\mathrm{att}}^{\mathrm{tot}}$ given by

$$\theta_{\mathrm{att}}^{\mathrm{tot}}(r, B_0) = \arccos\left[G(r, B_0)\left(\left(1 + \frac{1}{3G(r, B_0)^2}\right)^{1/2} - 1\right)\right], \tag{3.46}$$

with

$$G(r, B_0) = \frac{mgr^4}{18}\left[\frac{4\pi}{\mu_0}\sigma^6 B_0^2\left(\frac{\mu - \mu_0}{\mu + 2\mu_0}\right)^2\right]^{-1}, \tag{3.47}$$

while the radial force F_θ^{tot} vanishes along the curve $\theta_{\mathrm{top}}^{\mathrm{tot}}$ such as

$$\theta_{\mathrm{top}}^{\mathrm{tot}}(r, B_0) = \arccos\left[3G(r, B_0)\right], \tag{3.48}$$

for r such as $G(r, B_0) < 1/3$. By computing $\theta_{\mathrm{att}}^{\mathrm{tot}} = \theta_{\mathrm{top}}^{\mathrm{tot}}$, or equivalently, $\mathbf{F}^{\mathrm{tot}} = \mathbf{0}$ from Eq. 3.45, we find that the saddle point of the energy landscape in the region $\theta \in [0, \pi/2]$ is located along the line $\theta = \theta_{\mathrm{sp}} \equiv \arccos(1/\sqrt{5}) \approx 1.11\,\mathrm{rad} \approx 63.4°$, a polar angle which does not depend on B_0, and at a distance $r_{\mathrm{sp}} \propto \sqrt{B_0}$.

In the following, we consider that the test particle, which is not drawn in Fig. 3.4, not only moves in the force fields that we discussed, but is additionally vertically confined. Note that we will make use of the formula of $\theta_{\mathrm{top}}^{\mathrm{tot}}$, but not of that of $\theta_{\mathrm{att}}^{\mathrm{tot}}$.

3.2.2 Consequences in the quasi-two-dimensional geometry of our experiments

Let us consider one ball placed on a horizontal surface and bearing a magnetic moment $\mathbf{m}$, as represented in Fig. 3.5. Let us now consider a second ball, of identical magnetic moment $\mathbf{m}$, and positioned at *at contact* with the first one, that is, at a distance $r = a$. The vertical position of the second ball is limited by a second horizontal surface separated from the lower one by a distance e. These two parallel plates represent the top and bottom physical boundaries of our cells, which are respectively the polycarbonate lid and the lower rough surface (sand-blasted aluminum for the circular cell, and sandpaper for the square cell, as detailed in Section 1.1). As we explained then, we perform all our experiments with gap sizes, e, that are smaller that two particle diameters, so as to do not allow more than a partial overlap between particles. A gap size defines a vertical confinement of the particles, and therefore it constraints the range of accessible polar angles. As illustrated in Fig. 3.5, to each value of e corresponds a *minimum polar angle*, $\theta_{\min}$, which is the polar angle between the two particles' centers when the second particle is positioned *at contact* and when it is touching the lid. This angle is geometrically calculated as

$$\theta_{\min}(e) \equiv \arccos\left(\frac{e}{a} - 1\right). \tag{3.49}$$

The polar angle $\theta = 0$ can only be accessed if $e = 2a$ and corresponds to a complete overlap, while $\theta = \theta_{\max} = \pi/2$ is accessible for any $e \geq 1$ and corresponds to the largest accessible polar angle. Therefore, the range of accessible polar angles for a given gap size is:

$$\theta_{\min}(e) < \theta < \theta_{\max} = \frac{\pi}{2}. \tag{3.50}$$

Let us now consider the second ball stuck at contact ($r = a$, that is, with its center on the black dashed portions of circles in Fig. 3.6) and touching the lid, that is, at the minimum accessible polar angle, $\theta = \theta_{\min}(e)$ (as depicted in Fig. 3.5). Let us call this configuration *buckled*. Will this ball stay in place, buckled, or will it fall instead? To answer this question, one must carefully consider the geometry of the problem. With respect to the top boundary, that is, the lid, the ball is stable in the buckled configuration if the horizontal force is oriented along $-\mathbf{e}_x$, *i.e.*, if $F_x = \mathbf{F}^{\text{tot}} \cdot \mathbf{e}_x = \mathbf{F}^{\text{mag}} \cdot \mathbf{e}_x < 0$, at contact. In the mean time, the other condition is that the radial force, F_θ^{tot}, be negative at contact, otherwise the ball would slide down along the first ball.

From Eq. 3.45, we obtain the horizontal force,

$$F_x(r,\theta) = -\frac{12\pi}{\mu_0} B_0^2 \frac{\sigma^6}{r^4} \left(\frac{\mu - \mu_0}{\mu + 2\mu_0}\right)^2 \sin\theta \left(5\cos^2\theta - 1\right), \tag{3.51}$$

which changes sign for the trivial angles $\theta = 0(\pi)$ and for the critical angle,

$$\theta_x \equiv \arccos\left(\frac{1}{\sqrt{5}}\right) \approx 1.11\,\text{rad} \approx 63.4^\circ. \tag{3.52}$$

which is also the value of the polar angle along which the saddle point of the energy landscape is found, namely θ_{sp}, as we saw in Section 3.2.1. More precisely, if $\theta < \theta_x$, $F_x < 0$, which stabilizes the balls in the buckled configuration, while if $\theta > \theta_x$, $F_x > 0$. In Fig. 3.6, we show the potential energy landscapes and the force fields without and with gravity, as in Fig. 3.4, but here in a region corresponding to the geometry of our experiments, that is, with a gap size not exceeding $2\,a$, and with the reference ball placed on the "bottom". We indicate the critical polar angle θ_x

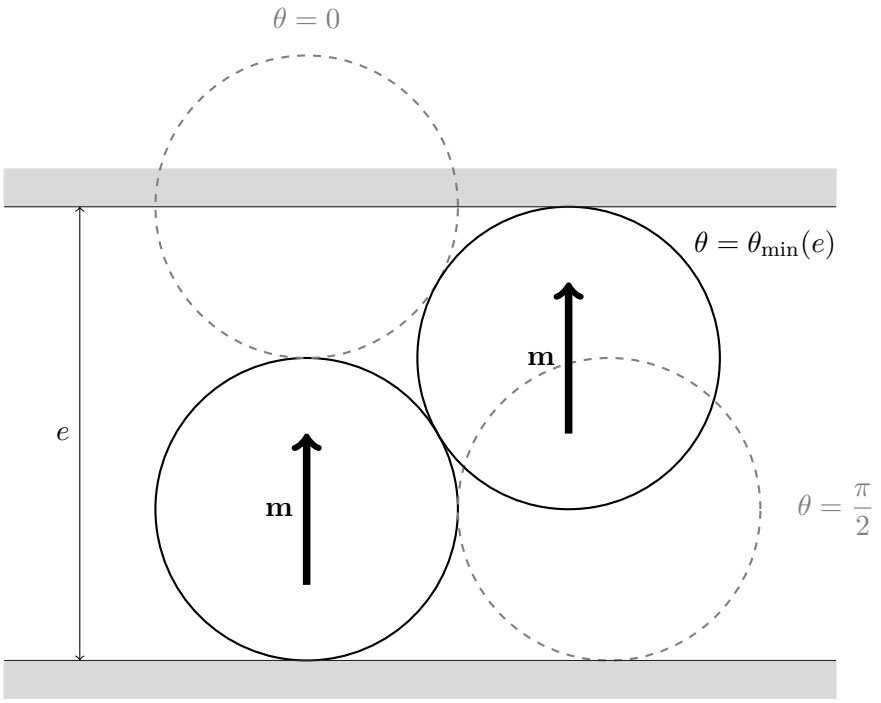

Figure 3.5 Different possible configuration at contact (*i.e.*, $r = a$) for two balls with magnetic moments. The polar angle $\theta_{\min}(e)$ is the minimum polar angle attainable when two plates are separated by a gap e. The grey dashed circles represent two other possible configuration, $\theta = 0$ being accessible only if $e = 2a$, while $\theta = \pi/2$ can always be reached for $e \geq 1$.

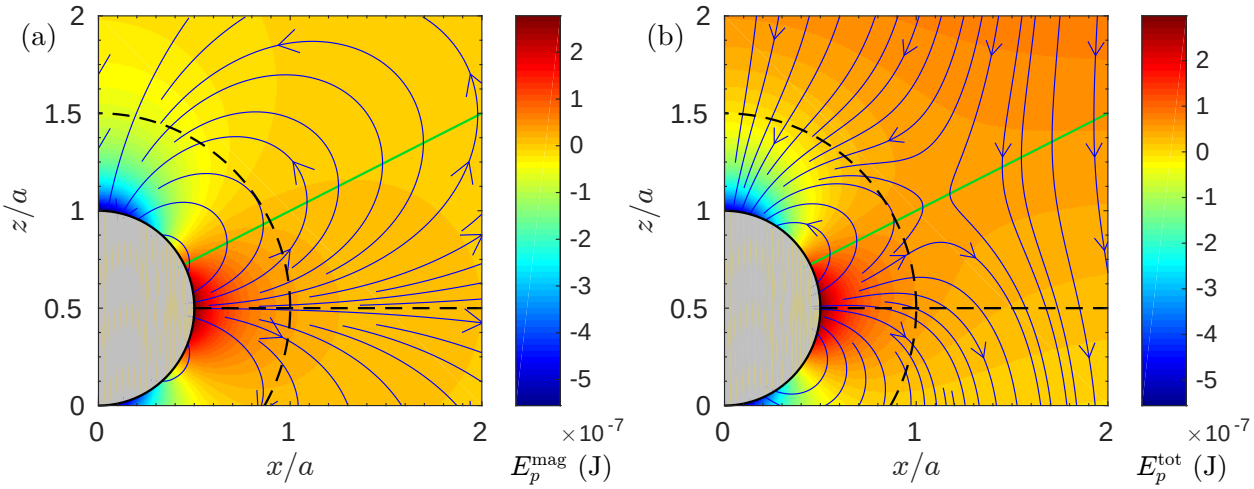

Figure 3.6 Potential energy landscapes and force fields (a) without gravity, and (b) with gravity, for $B_0 = 150\,\text{G}$ and $\mu_r = 500$. The dashed black portions of circles are plotted at a distance $r = 2\sigma$ from the reference ball center and correspond to the possible positions of the second ball center, when it is at contact with the reference ball. The horizontal dashed black lines show the lowest possible positions of the second ball center, when it is touching the bottom plate. The green dashed lines represent the vanishing horizontal force, F_x, given in Eq. 3.51, and correspond to the polar angle $\theta_x = \arccos(1/\sqrt{5})$ given in Eq. 3.52. F_x is negative on the top-left of this line.

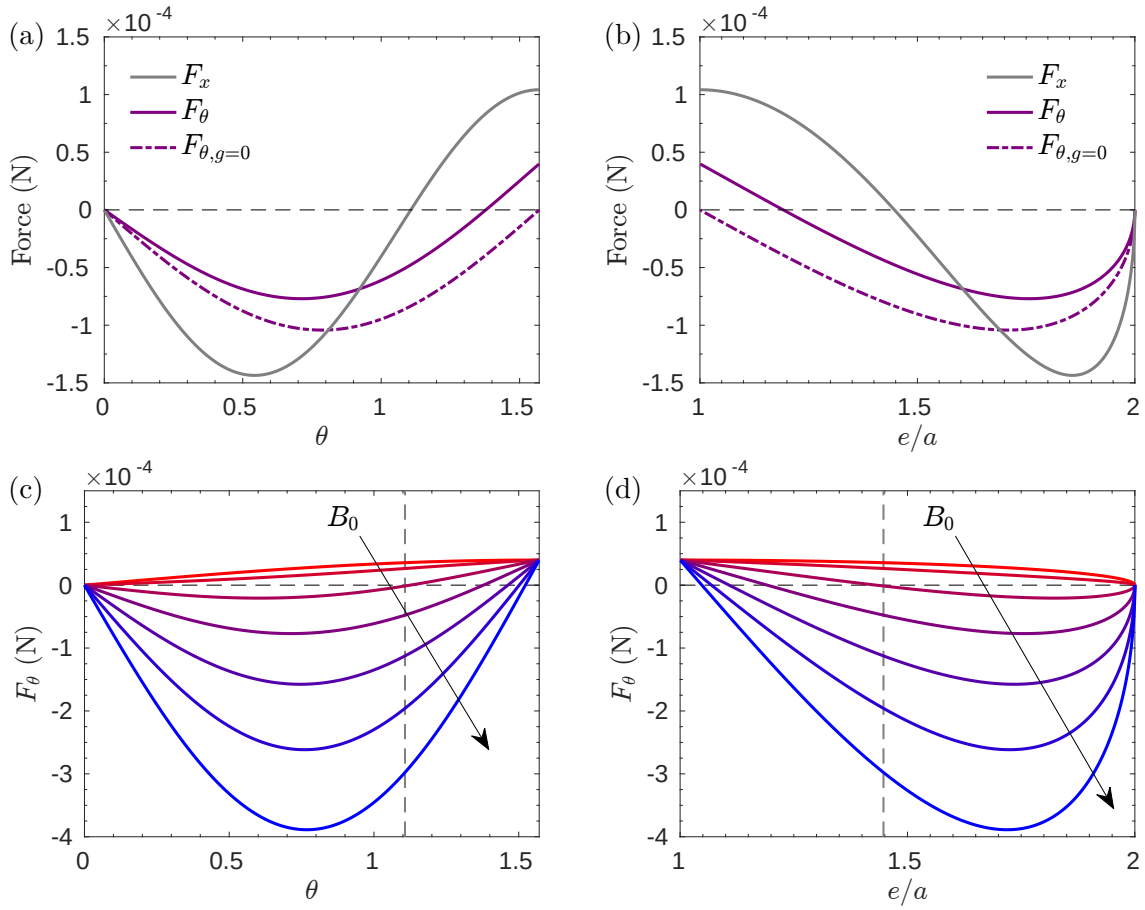

Figure 3.7 Forces F_x and $F_\theta^{\rm tot}$ acting on a ball at contact ($r = a$), with $\mu_r = 500$. The values of gap size e/a in (b, d) are related to the angles θ in (a, c) by Eq. 3.49. (a, b) F_x is negative for $\theta < \theta_x \equiv \arccos(1/\sqrt{5})$ (resp. $e/a > e_x/a \approx 1.45$) for all values of B_0. $F_\theta^{\rm tot}$ vanishes for values of θ which depend on B_0 when gravity is considered (here plotted for $B_0 = 150\,\mathrm{G}$). Without gravity, $F_\theta^{\rm tot}$ is always negative. (c, d) $F_\theta^{\rm tot}$ for B_0 from 0 G to 400 G with 50 G increments. The vertical grey dashed line indicates the value at which F_x vanishes, namely θ_x.

by the green line.

This angle is related to a critical gap size *via* Eq. 3.49, namely

$$e_x \equiv e(\theta_{\rm min} = \theta_x) = a\,(\cos\theta_x + 1) \approx 1.45\,a. \tag{3.53}$$

If the gap e is larger than e_x, then $F_x(r = 2\sigma, \theta = \arccos(e/a - 1)) < 0$ and the buckled configuration is stable with respect to F_x; else it is unstable.

On the other hand, the tangential force at contact,

$$F_\theta^{\rm tot}(r = 2\sigma, \theta) = -\frac{3\pi}{4}\frac{B_0^2\sigma^6}{\mu_0}\left(\frac{\mu - \mu_0}{\mu + 2\mu_0}\right)^2 \sin(2\theta) + mg\sin\theta, \tag{3.54}$$

vanishes for $\theta = \theta_{\rm top}^{\rm tot}(r = 2\sigma, B_0) = \arccos\left[3G(r = 2\sigma, B_0)\right]$, where $\theta_{\rm top}^{\rm tot}$ is given in Eq. 3.48 and $G(r, B_0)$ is defined in Eq. 3.47, as we saw in Section 3.2.1. The value of $\theta_{\rm top}^{\rm tot}$ at contact hence depends on B_0.

In order to visualize the shapes and vanishing points of the horizontal and tangential forces

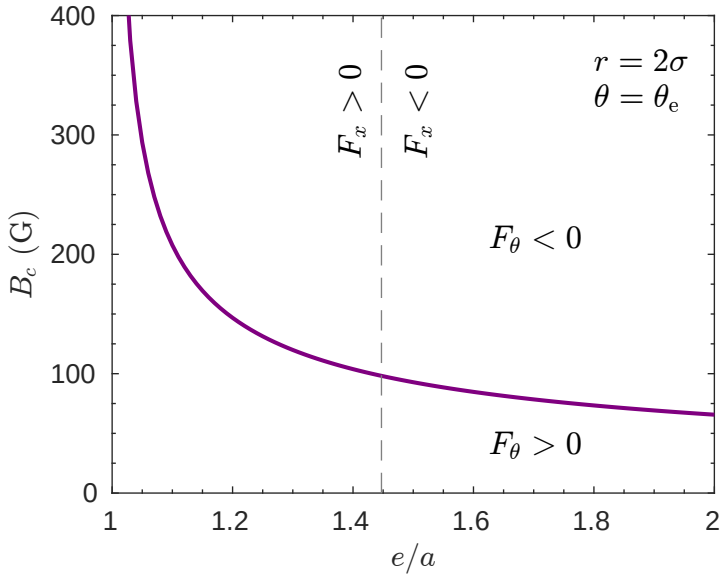

Figure 3.8 Stability diagram of the buckled configuration for two magnetized balls with gravity, but with no friction and no other neighbors. The configuration is stable when both horizontal force, F_x, and tangential force, F_θ^{tot}, are negative, *i.e.*, inside the top-right region of the graph. The equation of the purple curve indicating $F_\theta^{\text{tot}} = 0$ is Eq. 3.55. The vertical dashed line for $F_x = 0$ corresponds to $e = e_x$, given in Eq. 3.53.

at contact, $F_x(r = 2\sigma, \theta)$ and $F_\theta^{\text{tot}}(r = 2\sigma, \theta)$, we plot them as functions of the polar angle θ and of the gap size $e(\theta = \theta_{\min})$ for various values of B_0, as shown in Fig. 3.7. Fig. 3.7(a, b) show the forces for $B_0 = 150\,\text{G}$. The domain of stability of the *buckled* configuration corresponds to $F_x < 0$ and $F_\theta^{\text{tot}} < 0$ simultaneously verified, and it exists for this value of magnetic field, namely for angles smaller that $\theta_x \approx 1.11\,\text{rad}$, or equivalently for gap sizes larger than $e_x \approx 1.45\,a$. However, even though the horizontal force vanishes whatever the magnetic field B_0 for the same angle θ_x defined in Eq. 3.52 (*i.e.*, for the same gap size e_x given in Eq. 3.53), this is not the case of the tangential force. Indeed, the value of the angle at which vanishes this force, $\theta_{\text{top}}^{\text{tot}}(r = 2\sigma, B_0)$, does strongly depend on the magnetic field, as illustrated in Fig. 3.7(c, d). If the magnetic field is too low, there exists no angle such as $F_\theta^{\text{tot}} < 0$ and the *buckled* configuration is unstable with respect to the tangential force F_θ^{tot}. If B_0 is high enough, there exists such an angle and it increases with B_0.

More quantitatively, we calculate the values of magnetic field, B_0, for which F_θ^{tot} vanishes at $r = 2\sigma$ and $\theta = \theta_{\min}$, as a function of the gap size, e, using Eq. 3.48 and Eq. 3.49,

$$B_c(e) = \left[\frac{a^5}{e-a} \frac{mg}{6} \left(\frac{4\pi}{\mu_0} \sigma^6 \left(\frac{\mu - \mu_0}{\mu + 2\mu_0} \right)^2 \right)^{-1} \right]^{1/2} . \tag{3.55}$$

The buckled configuration is stable with respect to F_θ^{tot} if $B_0 > B_c(e)$; it is unstable otherwise.

Our results on the stability of two particles in the buckled configuration are illustrated and summarized in the stability diagram in Fig. 3.8. The only stable region is the one where both horizontal and tangential forces at contact vanish, namely on the top-right of the graph.

3.2.3 Discussion: what is missing?

So far, our reasoning is based on the analysis of the magnetic forces for two magnetic moments of constant value, generated from an external magnetic field, and perfectly vertically aligned. There are here several points that should be should be discussed, among which the fact that the magnetic moments actually influence each other through their demagnetizing field, that friction may stabilize the particles in the buckled configuration, and that we neglected the presence of other neighboring particles.

Induced magnetic moments are coupled

Two induced magnetic moments actually influence each other's value and orientation, because they influence their respective immersing magnetic fields. Let us give an example of this effect using Eq. 3.36. This equation shows us that the presence of a ferromagnetic particle of infinite magnetic permeability increases its surrounding magnetic field with respect to $\mathbf{B}_0$ at a distance of one particle diameter, above and below it, as

$$\lim_{\mu\to\infty} \mathbf{B}_{\text{tot}}(r = 2\sigma, \theta = 0) = \frac{5}{4}\mathbf{B}_0, \tag{3.56}$$

and decreases its surrounding magnetic field in the horizontal plane as

$$\lim_{\mu\to\infty} \mathbf{B}_{\text{tot}}(r = 2\sigma, \theta = \frac{\pi}{2}) = \frac{7}{8}\mathbf{B}_0. \tag{3.57}$$

Therefore, at a point situated in the equatorial plane of a vertically magnetized particle, at a distance of one particle diameter from its center, the magnetic field is $1/8^{\text{th}}$ lower than if no magnetic dipole was present. Hence, another ferromagnetic particle brought at this location would have an induced magnetization lower than the one that would be obtained if it were alone in the external magnetic field. Furthermore, its own presence would imply changes in the magnetization of the first particle, and so on. In the end, both magnetic moment are identical, but they have lower values than the ones expected if they were not influenced by another magnetic moment. Hence the field of one particle at the location of the other particle is called *demagnetizing* magnetic field. Note that when particles can vertically align, the opposite effect occurs: the dipoles increase each other's amplitude.

N neighboring magnetic moments

Now, when an induced magnetic moment is part of an ensemble of N induced magnetic moments, magnetic interactions between them are coupled and nonlinear.

Let us start with the magnetization of a ferromagnetic particle i, which can be expressed as a modified form of Eq. 3.7,

$$\mathbf{M}_i = \chi_m \, \mathbf{H}^{\text{loc}}(\mathbf{r}_i), \tag{3.58}$$

where $\mathbf{H}^{\text{loc}}(\mathbf{r}_i)$ is the *local* magnetic excitation at the position of particle i. Considering that this particle is surrounded by $N-1$ other particles influencing the local field $\mathbf{H}^{\text{loc}}$, the latter can be written as

$$\mathbf{H}^{\text{loc}}(\mathbf{r}_i) = \mathbf{H}_0 + \sum_{j\neq i} \mathbf{H}_j^{\text{ums}}(\mathbf{r}_i) + \mathbf{H}_{j\neq i}^{\text{cpl}}(\mathbf{r}_i), \tag{3.59}$$

where $\mathbf{H}_j^{\text{ums}}$ is the field from the uniformly magnetized particle $j \neq i$, and $\mathbf{H}_{j\neq i}^{\text{cpl}}$ is an non-linear coupling field between the $N-1$ other magnetic dipoles and i. This non-linear coupling term

and the second term of the RHS of Eq. 3.59 make determining $\mathbf{H}^{\text{loc}}$ analytically impossible. However, it is possible to use self-consistent numerical methods for determining $\mathbf{H}^{\text{loc}}$ from the ensemble of the $\mathbf{H}_j^{\text{ums}}$'s, and reciprocally, when the coupling term is dropped off [66, 67] or when it is not [68].

The magnetic interactions between an ensemble of induced dipoles are therefore extremely complex. Yet, let us remark from Eq. 3.36, that in the horizontal plane ($\theta = \frac{\pi}{2}$), the total magnetic field on the outside of a sphere of infinite magnetic permeability decreases as r^{-3}. This corresponds to a fast decay in space: the relative change of total magnetic field with respect to B_0, by one particle, is already as low as about $1\,\%$ at a distance of two diameters from a particle's center. Therefore, it is tempting to consider that the demagnetizing effect acts only for particles at contact.

For what concerns two magnetized particles in the *buckled* configuration, as studied in Section 3.2.2, this coupling effect should be non-negligible, because particle centers are only separated by one particle diameter. However, note that depending on the polar angle θ at which the particles are relative to each other, it would go from *demagnetizing* in the plane $\theta = \pi/2$, to *magnetizing* when they are vertically aligned, *i.e.*, when $\theta = 0$. In the former case, the particle magnetic moments are lower and the buckled configuration less stable, which would be marked by an upwards shift of the purple curve indicating $F_\theta^{\text{tot}} = 0$ in Fig. 3.8; in the latter case, this configuration would be more stable, and the curve of $F_\theta^{\text{tot}} = 0$ would be shifted downwards.

Friction

Particle-particle friction, as well as particle-plate friction, may also play an important role in the stability of the *buckled* configuration, because, by definition, in this configuration both particle have contacts with one plate, in addition to touching each other. In fact, we will see in Chapter 5, Section 5.5, that this assumption is relevant, based on the observation of particles in this *buckled* configuration for gap values, e, lower than the critical value, e_x, which corresponds to the unstable region on the left part of the stability diagram in Fig. 3.8.

3.3 Diverse tools

3.3.1 Quantifying the competition between agitation and distance interactions: ε

In our system, self-organization arises from the competition between kinetic agitation and magnetic interactions. A parameter that measures the strength of the interactions relative to agitation, is, as similarly defined in [26, 69],

$$\varepsilon \equiv \frac{E_m}{E_c}, \tag{3.60}$$

where E_m and E_c are defined as follows. E_m is the *mean magnetic energy per particle*,

$$E_m = \left\langle \frac{1}{N_p} \sum_{i=1}^{N_p} \sum_{j=i+1}^{N_p} E_p^{\text{mag}}(r_{ij}, \theta_{ij}) \right\rangle_t \tag{3.61}$$

where $\langle \cdot \rangle_t$ denotes a temporal average, N_p is the number of particles used in the computation, r_{ij} (resp., θ_{ij}) the distance (the polar angle) between particles i and j (as defined in Fig. 3.3),

and E_p^{mag} is the potential magnetic energy of interaction of a pair of particles, given in Eq. 3.42,

$$E_p^{\text{mag}}(r,\theta) = -\frac{4\pi}{\mu_0} B_0^2 \frac{\sigma^6}{r^3} \left(\frac{\mu-\mu_0}{\mu+2\mu_0}\right)^2 \left(3\cos^2\theta - 1\right), \tag{3.62}$$

with μ_0 (resp. μ) the vacuum permeability (the permeability of the beads), B_0 the perpendicular applied magnetic field, and $\sigma = a/2$ the particle radius.

The other quantity in Eq. 3.60 is E_c, which is the *mean kinetic energy per particle* in the horizontal plane, also defined as the two-dimensional *granular temperature* in Appendix A,

$$E_c = \frac{1}{2} m \left\langle \frac{1}{N_p} \sum_{i=1}^{N_p} \left(v_{x,i}^2 + v_{y,i}^2\right) \right\rangle_t \tag{3.63}$$

with m the mass of a particle, and $v_{x,i} = \mathbf{v_i} \cdot \mathbf{e}_x$ (resp. $v_{y,i} = \mathbf{v_i} \cdot \mathbf{e}_y$) the x-component (y-component) of the velocity vector of particle i.

As long as the polar angle between the particles remains smaller than $\theta_{\text{att}}^{\text{mag}} = \arccos(1/\sqrt{3}) \approx 54.7°$, which corresponds to a gap size $e(\theta_{\min} = \theta_{\text{att}}^{\text{mag}}) = a\left(\sqrt{3}+1\right)^{-1} \approx 1.58\,a$, E_p^{mag} is positive. This is the case of the very large part of our experiments presented below. Then, increasing the external magnetic field, B_0, leads to an increase of E_m that scales as B_0^2. Therefore, unless E_c increases faster than B_0^2 (which we did not observe), parameter ε increases when B_0 increases, indicating a strengthening of magnetic interactions relative to mechanical agitation.

3.3.2 Characterizing the structure

A quantity that we are going to use in all three next chapters is the *pair correlation function*, $g(r)$, which is a measure of the probability of finding a particle center at a distance r from a reference center.

Let us consider the ensemble of particles of diameter a depicted in Fig. 3.9. The reference particle is pictured in dark grey. Computing $g(r)$ consists in counting the number of particles whose center is found in the shell at the distance r from the reference particle and of width dr (in red in Fig. 3.9), to ensemble average and to proceed to a normalization operation, such as

$$g(r) = \left\langle \frac{\mathcal{S}_p}{2\pi r N_p^2} \sum_{i=1}^{N_p} \sum_{j\neq i}^{N_p} \delta\left(r - r_{ij}\right) \right\rangle_t \tag{3.64}$$

where $\mathcal{S}_p$ is the full surface of integration, δ is the Dirac symbol, i is the reference particle index, and r_{ij} is the distance between the reference particle and particle j.

For an ensemble of particles with no correlation, the pair correlation function vanishes below the particle diameter, that is, $g(r<a) = 0$, and it equals 1 beyond it, that is, $g(r>a) = 1$. This means that there is equiprobability at all r of finding a particle center. Now, if correlations exist between the particles, $g(r)$ is not flat anymore, and can take various shapes depending on the nature of the correlations. The latter can be long-ranged, for instance if they are of electrostatic nature, but can also be simply due tot the finite size of the particles.

We will also use the two-dimensional Fourier transform of the center positions, namely the

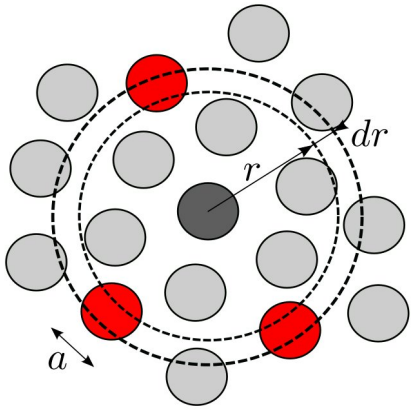

Figure 3.9 Computing the pair correlation function, $g(r)$, for an ensemble of particles of diameter a, with increments dr.

static structure factor, $S(\mathbf{k})$, which is defined as

$$S(\mathbf{k}) = \left\langle \frac{1}{N_p} \sum_{j=1}^{N_p} \sum_{k=1}^{N_p} \mathrm{e}^{-i\mathbf{k}(\mathbf{r}_j - \mathbf{r}_k)} \right\rangle_t \tag{3.65}$$

where $\mathbf{k} = k_x\,\mathbf{e}_x + k_y\,\mathbf{e}_y$ is the wave vector in the horizontal plane, $\mathbf{r}_i$ (resp., $\mathbf{r}_j$) is the position of particle i.

The comments that we made about the pair correlation function apply also to the static structure factor. However, $S(\mathbf{k})$ has the advantage that it is defined in the whole plane, and as such it can be used for characterizing the orientational properties of the ensemble of particles, as we will see, for instance, in Chapter 6.

3.3.3 Magnetic pressure

In the next chapters, we will sometimes use the term *magnetic pressure*, for referring to the energy density carried by the magnetic field of the magnetized particles.

We calculate it in analogy with the pressure in molecular dynamics simulations [70]. From the Virial theorem and in the limit of negligible collisions, we can calculate a pressure, P, in an ensemble of particles of area fraction ϕ, of a thickness e (analogous to the gap size in our experiments), characterized by a pair correlation function $g(r)$, and interacting *via* a potential $U(r)$,

$$P = -\frac{\phi^2}{\pi e \sigma^4} \int_0^\infty r^2 \frac{\mathrm{d}U}{\mathrm{d}r} g(r) \mathrm{d}r. \tag{3.66}$$

If now we replace the potential $U(r)$ by the potential energy of interaction of two magnetized particles, $E_p^{\mathrm{mag}}(r,\theta)$, given in Eq. 3.42, with $\theta = \pi/2$ and $\mu \to +\infty$, that is,

$$U(r) = \frac{4\pi}{\mu_0} B_0^2 \frac{\sigma^6}{r^3}, \tag{3.67}$$

and if additionally we suppose that the system has no long-range correlations, that is, $g(r <$

$a) = 0$ and $g(r > a) = 1$, we obtain the pressure

$$P = 12\phi^2 \frac{\sigma}{e} \frac{B_0^2}{\mu_0}. \tag{3.68}$$

Hence, P is proportional to the magnetic pressure used in the plasma physics, $\frac{B_0^2}{2\mu_0}$, up to a dimensionless factor. For $\phi = 0.5$, for instance, we have $P = 314\,\mathrm{Pa}$ with $B_0 = 100\,\mathrm{G}$, and $P = 5094\,\mathrm{Pa}$ with $B_0 = 400\,\mathrm{G}$. The corresponding forces are much larger than the weight of the particles. Consequently, at such a particle density, magnetic pressure significantly helps stabilizing a pair of particles in the *buckled* configuration discussed in Section 3.2.2. Also, in the confined geometry of our experiments, this magnetic pressure induces self-ordering effects even in the absence of attractive force, as we will see in the next three chapters.

3.3.4 Characterizing the velocity distributions

The velocity density function (VDF) for a particle undergoing a Brownian motion is a Maxwell-Boltzmann distribution, which yields Gaussian distributions for the velocity components on each direction α ($\alpha = x, y$ or z), namely v_α,

$$f_G(v_\alpha) = \frac{1}{\sqrt{2\pi}\sigma_\alpha} \exp\left[-\frac{(v_\alpha - \langle v_\alpha \rangle)^2}{2\sigma_\alpha^2}\right], \tag{3.69}$$

where $\langle \cdot \rangle$ denote an ensemble average and $\sigma_\alpha = \sqrt{\langle v_\alpha^2 \rangle}$ is the standard deviation of the α-axis VDF.

For particles that are correlated, the VDF deviate from the Gaussian distribution. In particular, as briefly discussed in Appendix A, and in more details in the reference books [7, 3], for granular gases, the VDF exhibit over-populated high-velocity tails.

A relevant quantity for characterizing such tails on a distribution is the kurtosis, or fourth standardized moment, which is also called *flatness* and which we denote F,

$$F = \frac{(v_\alpha - \langle v_\alpha \rangle)^4}{\sigma_\alpha^4}, \tag{3.70}$$

where $\alpha = x$ or y for a quasi-two-dimensional granular gas.

The flatness of a distribution enables a good measure of the extreme events, that is, in our case, the high-velocity events. For a Gaussian distribution, $F = 3$, while for a distribution that displays high velocity tails, such as stretched exponential tails or exponential tails, as illustrated in Fig. A.1, F is larger than 3. This is the case for granular gases [7, 3]. A distribution with less extreme events than the Gaussian distribution has a flatness $F < 3$.

Chapter 4

Transition from a dissipative to a quasi-elastic state

Chapter 4 : Transition from a dissipative to a quasi-elastic state

↑ back to contents

Chapter abstract

A two-dimensional system of particles with tunable repulsive interactions is experimentally investigated. Soft ferromagnetic particles are placed on a vibrating rough plate and vertically confined, so that they perform a horizontal Brownian motion in a cell. When immersed in an external vertical magnetic field, the particles become magnetized and thus interact according to a dipolar repulsive law. As the amplitude of the magnetic field is increased, magnetic repulsion raises and the rate of inelastic collisions decreases. Studying notably the pair correlation function and the particle velocity distributions, we show that the typical properties of such a dissipative out-of-equilibrium granular gas are progressively lost, to approach those expected for a usual gas at thermodynamic equilibrium. For stronger interaction strengths, the system gradually solidifies towards a hexagonal crystal. This new setup could consequently be used as a model experimental system for out-of-equilibrium statistical physics, in which the distance to the quasi-elastic limit can be accurately controlled.

4.1 Introduction

Statistical mechanics provides, with the assumption of thermodynamic equilibrium, a precise description of molecular gases composed of thermally agitated microscopic particles. In contrast, in granular gases, macroscopic particles are mechanically driven. Since the collisions between these particles are dissipative, energy must be continuously provided into the system from outside to reach a stationary out-of-equilibrium state. In consequence, granular gases have been extensively studied as a model system for out-of-equilibrium statistical physics [39] theoretically [38, 32], numerically [71] and experimentally [16, 72, 17]. Two-dimensional granular gases, *i.e.*, particles lying on a horizontal plate vertically vibrated, were especially studied because particle trajectories can be reconstructed using fast imaging and tracking algorithms [16, 72, 17, 25, 33].

Nevertheless, as we stressed in the Introduction of this thesis, few studies investigated the case in which non-contact interactions between particles compete with kinetic agitation and thus introduce spatial correlations differing from those observed for an inelastic hard-sphere gas. In a

granular gas composed of particles owing a permanent magnetic dipole, the anisotropic dipole-dipole interactions lead to dipole alignment, then attraction and clustering [21, 73, 48]. In contrast, physics differs strongly using ferromagnetic particles with a low remnant magnetic field. As we saw in Chapter 3, when immersed in an external static magnetic field, such particles acquire an induced magnetization so that inter-particle dipolar interactions become tunable by the operator. Applying this protocol to a granular packing, a first-order fluid-solid transition [74] and a surface instability due to competition between gravity and magnetic forces [75], are observed. Now, if such particles are confined in a plane and immersed in an external perpendicular magnetic field, the magnetic interactions between particles are purely repulsive, since their dipoles are all aligned in the vertical field direction. At low packing fraction, low agitation and high magnetic field, Schockmel and collaborators demonstrated that such a system forms a hexagonal lattice [26]. As mechanical agitation is increased, crystal melting is observed, that is, translational and orientational orders disappear, as in some other two-dimensional systems of interacting particles [76, 77, 78, 79, 23, 24].

4.2 Motivation

To our knowledge, the influence of dipolar interactions on the particle velocity distributions has only been studied in a case dominated by attractive interactions by Kohlstedt *et al.* [29]. Note that the free-cooling, *i.e.*, the evolution without external energy input, of three-dimensional granular gases with electrostatic repulsions has been investigated theoretically and numerically [80, 81].

In this chapter, we study the effects of repulsive dipolar magnetic interactions on the structural and dynamical properties of a quasi-two-dimensional granular gas. We proceed as follows. We start from the well-studied case of a two-dimensional granular gas [25, 33] where mechanical agitation is provided to the particles by the vibration of a horizontal rough bottom plate. Then, we immerse the system in a vertical magnetic field, which generates repulsive dipolar interactions between particles. The rate of inelastic collisions between particles can be easily tuned: increasing the amplitude of the magnetic field enhances magnetic repulsion and thus decreases the number of inelastic collisions. As the dissipation rate due to inelastic collisions is proportional to the number of collisions, the total dissipation in the system is reduced. We thus show that the system undergoes a transition from a dissipative to a quasi-elastic state to a crystalline state when the magnetic field is increased. Across the transition, we analyse quantitatively the structural and dynamical changes by means of particle tracking.

In the context of this thesis, understanding how our system, as a low density granular gas, responds to changes in the strength of magnetic interactions is a cornerstone from which we can perform further investigations, in particular when density and gap size are varied, and novel self-organized states are explored.

4.3 Main results

The experimental setup is described in details in Chapter 1, and illustrated in Fig. 1.1(a). We perform all the experiments presented in this chapter with the square experimental cell, of side 9 cm and covered with sandpaper in order to provide roughness. In this cell we put $N_0 = 2000$

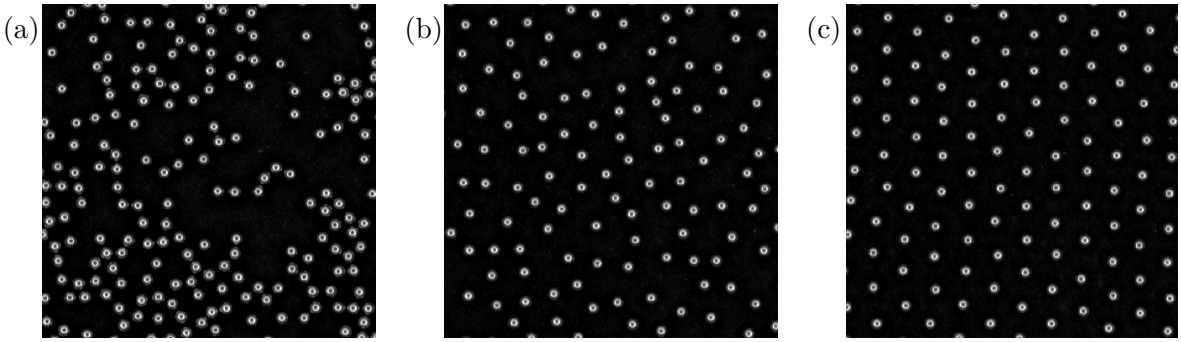

Figure 4.1 Snapshots of the magnetic granular gas in (a) the inelastic regime for $B_0 = 0\,\mathrm{G}$ ($\varepsilon = 0$); (b) the quasi-elastic regime for $B_0 = 127\,\mathrm{G}$ ($\varepsilon = 16.2$); and (c) the hexagonal crystal-like regime for $B_0 = 436\,\mathrm{G}$ ($\varepsilon = 283$). The acceleration is $\Gamma = 3.32$ and the snapshot size is $3.5\,\mathrm{cm} \times 3.5\,\mathrm{cm}$.

soft ferromagnetic particles, of a diameter $a = 1\,\mathrm{mm}$, so that the particle area fraction for a homogeneous spatial distribution, defined in Eq. 1.8, is $\phi_{\mathrm{th}} \sim 0.2$. The gap size of this cell is about $1.5\,a$. In order to reach an out-of-equilibrium steady state, this cell is driven sinusoidally in the vertical direction by means of an electromagnetic shaker. The dimensionless acceleration, defined in Eq. 1.10, is $\Gamma = (2\pi f)^2 A/g$, with $f = 300\,\mathrm{Hz}$ the frequency and A the amplitude of the sinusoidal forcing, g being the gravitational acceleration. Two coils generate a vertical magnetic field $\mathbf{B_0}$ perpendicular to the cell plane and spatially homogeneous across the cell volume with a 2% accuracy. We record images of the system from the top by means of a high-speed video camera in a square region of interest of side 5.7 cm, around the cell center and at an acquisition frequency of 779 Hz, as detailed in Section 1.1.7. We perform video recordings once we estimate that the stationary state is reached, namely after a waiting time $\tau_0 = 60\,\mathrm{s}$, as defined in Section 1.2.1. We detect particles individually and record their trajectories by means of a tracking algorithm, as detailed in Chapter 2.

We performed two set of experiments with an increasing external magnetic field, of magnitude $B_0 = |\mathbf{B_0}|$, and respectively, an acceleration of $\Gamma = 2.45$ and $\Gamma = 3.32$. Immersed in the magnetic field B_0, particles become induced magnetic dipoles, as detailed in Section 3.1, which are parallel and vertically oriented. In the range of parameters used for the experiments of this chapter, interactions between these dipoles are purely repulsive. Then, since the potential energy of interaction of two dipoles, E_p^{mag}, increases proportionally to B_0^2 (Eq. 3.42), so do the repulsive forces. We tune the strength of repulsion *via* the magnetic field B_0.

To each value of B_0 corresponds a specific state of the magnetic granular gas, with its own structural and dynamical properties. When no magnetic field is applied, the system is a classical dissipative granular gas, as illustrated in Fig. 4.1(a) for $B_0 = 0\,\mathrm{G}$. As the magnetic field is increased, magnetic repulsive interactions become stronger, the particle collision rate decreases, and the system looks more similar to a liquid, as shown in Fig. 4.1(b) for $B_0 = 127\,\mathrm{G}$. At high enough values of magnetic field, strong repulsion makes the system to organize into a crystalline state in which particles are located at the nodes of a triangular lattice, as illustrated in Fig. 4.1(c) for $B_0 = 436\,\mathrm{G}$.

The pair correlation function, $g(r)$, defined in Section 3.3, is related to the probability to find two particle centres separated by a distance r and as such it is convenient to quantify the structural changes in the system. We show $g(r)$ in Fig. 4.2(a) for characteristic values of $\varepsilon = E_m/E_c$ and for $\Gamma = 3.32$. At $\varepsilon = 0$, $g(r)$ displays a sharp peak at the contact value $r = a$, as

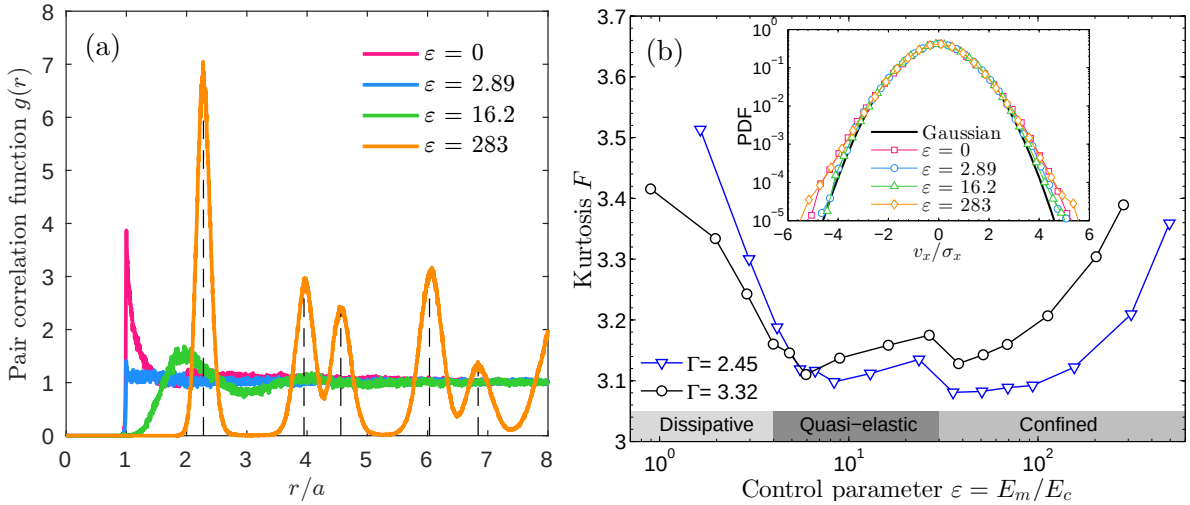

Figure 4.2 Structural and dynamical characteristics of the magnetic granular gas for a varying repulsive strength $\varepsilon = E_m/E_c$. (a) Pair correlation function for relevant values of ε, for $\Gamma = 3.32$. For $\varepsilon = 283$, the peak positions for a hexagonal crystal are indicated by the vertical black dashed lines as multiples of the lattice distance, namely $r/a = 2.28$, for factors 1, $\sqrt{3}$, 2, $\sqrt{7}$, and 3. (b) Flatness of the velocity probability density functions (PDF) as a function of ε. Inset: velocity PDF for different ε, for $\Gamma = 3.32$. The black curve is the Gaussian distribution.

in usual granular gases [16, 72]. This confirms that most collisions occur in horizontal planes and validates the two-dimensional description. Collisions happening out of horizontal planes, when viewed from the top, produce indeed a partial overlapping, leading to non-vanishing values of $g(r)$ for $r < a$. When ε is slightly increased, the amplitude of the first peak decreases to almost 1, giving a nearly flat $g(r)$ (see the blue curve for $\varepsilon = 2.89$). This shows that radial correlations are then quasi-absent as for a non-dissipative perfect gas whose $g(r)$ is zero for $r < a$ and 1 elsewhere in the vanishing density limit. When ε is further increased, this feature is gradually lost. Due to magnetic repulsions, $g(r = a)$ decreases towards zero and a first peak appears at $r > a$, indicating the appearance of a preferential distance between particles. A similar transition of $g(r)$ has been observed numerically for a three-dimensional repulsive granular gas with a Coulomb interaction potential [80]. For high enough values of ε, the system structure approaches the one of a hexagonal crystal [26]. In this case, once the lattice cell size is set to the first-peak position, theoretical secondary-peak positions can be predicted from geometrical calculations and are indeed found to be close to the measured values, indicated by the vertical dashed lines in Fig. 4.2(a).

Structural modifications imply important changes on dynamics, especially on the particle trajectories and velocity distributions. We show in the inset of Fig. 4.2(b), the probability density functions (PDF) of velocities (x-component) normalised by their standard deviation, v_x/σ_x, with $\sigma_x \equiv \sqrt{\langle v_x^2 \rangle}$, $\langle \cdot \rangle$ denoting an ensemble average, for a fixed Γ and for different values of ε. They are compared to the Gaussian distribution expected for a perfect gas at thermal equilibrium. Identical results are found for v_y due to system isotropy in the central region. As predicted for an infinite system [82] and reported in other experiments [72, 17, 25, 33], at $\varepsilon = 0$ the velocity distribution presents a deviation from the Gaussian. In fact, this behaviour is expected for out-of-equilibrium systems, as Gaussian distribution is predicted for equilibrium gases. The reported overpopulation of the high-velocity tails is characteristic of granular gases, although there is no simple argument to justify it [39]. As ε is increased, the PDF become

progressively closer to the Gaussian until $\varepsilon \approx 10$ but then depart for higher values.

This behavior is better depicted by plotting the flatness of the velocity distributions, which we defined in Section 3.3 as $F = (v_x - \langle v_x \rangle)^4 / \sigma_x^4$, and which is shown in Fig. 4.2(b). For a purely Gaussian distribution F equals 3 and is larger for more spread distributions. A range of significantly low values of F can be defined for $4 < \varepsilon < 30$, where the granular gas can be considered as quasi-elastic. Indeed, energy exchanges between particles should occur mainly through magnetic repulsive interactions, which are dissipationless. Note that the lower bound in ε is fairly consistent with the value $\varepsilon = 2.89$ separating the usual granular gas regime and the one with negligible collisions, as can be seen in Fig. 4.2(b). For $\varepsilon > 30$, displacements become progressively constrained by magnetic repelling and the system can be seen as an assembly of confined particles [26]. F then increases with ε, highlighting a heterogeneity of velocities, as particles are individually more or less confined.

4.4 Conclusion

We have studied the effects of tunable repulsive dipolar interactions on a quasi–two-dimensional granular gas. For fixed dimensionless accelerations Γ and in a low density regime ($\phi \sim 0.2$), we increased the magnetic field B_0. The rise of the ratio ε between magnetic interaction and kinetic agitation leads to a continuous phase transition from a dissipative granular gas state at $\varepsilon = 0$, to a collisionless hexagonal nearly crystalline state at high ε. More interesting, in the intermediate range of ε, structural and dynamical properties of the magnetic granular gas display similar features to those expected for a molecular gas at thermal equilibrium (quasi-Gaussian velocity distributions and nearly flat pair correlation functions). This transition from a dissipative to a quasi-elastic granular gas, when B_0 is increased, comes from the decrease of the dissipative collision rate, which leads to the reduction of the total dissipation. Hence, the two-dimensional granular gas is then closer to the quasi-elastic limit. We were thus able to produce a macroscopic system whose distance to the quasi-elastic limit could be precisely controlled through the applied magnetic field. We may also wonder how the results found here with repulsive dipolar interactions can be generalised for other interaction potentials, like the Coulombian one [80, 81].

Future studies with this new system could be useful to validate theoretical works about out-of-equilibrium dissipative gases, by investigating velocity correlations and coupling with the forcing viewed as a thermal bath [33, 83]. Another perspective is to apply a magnetic quench to the system, in order to try to solidify it into a low-density disordered state, which could be analogous to a colloidal glass [84]. Moreover, for denser regimes and for high ε, we observe other complex disordered states, on which we focus in Chapter 5 and Chapter 6. Our experimental system could indeed be used to mimic, at the macroscopic scale, geometric frustration [85, 86] or topological defects [87] arising in various physical systems.

Let us mention two more perspectives. In granular gases, there is a break down of fluctuation-dissipation relations [88] because the usual hydrodynamic shear viscosity must be replaced, then, by a viscosity parameter present in the granular hydrodynamics equations [89]. Being able to tune the interactions between particles in our system *via* the external magnetic field, B_0, we should be able to tune this viscosity parameter, and hence change the fluctuation-dissipation relations depending on B_0. How close to the result for Brownian particles can we approach by tuning the magnetic field? An idea of experiment could be to locally perturb the otherwise uniform magnetic field, wait for a steady state to be reached and then remove this perturbation

and study the response and fluctuations of the system.

Finally, one could imagine using this experimental setup with a mixture of particle with two different magnetic permeabilities, but otherwise identical. Immersed in the external magnetic field, the induced magnetic moments of these two types of particles would be different, hence the particles would have two different *effective sizes* (a term discussed in our *EPL* article [1] presented in this chapter). Aside from an expected segregation by size [90], the crystallization transition should lead in this case to a "macroscopic alloy", instead of the homogeneous crystalline phase described in this chapter. The self-organization properties of this media are certainly not trivial, and certainly involve interesting questions regarding for instance lattice defects and geometric frustration [85, 86].

A Letters Journal Exploring the Frontiers of Physics

May 2014

EPL, **106** (2014) 44005
doi: 10.1209/0295-5075/106/44005

www.epljournal.org

Transition from a dissipative to a quasi-elastic system of particles with tunable repulsive interactions

S. Merminod, M. Berhanu and E. Falcon

Université Paris Diderot, Sorbonne Paris Cité, MSC, CNRS (UMR 7057) - 75013 Paris, France

received 24 March 2014; accepted in final form 5 May 2014
published online 27 May 2014

PACS 45.70.-n – Granular systems
PACS 64.70.-p – Specific phase transitions

Abstract – A two-dimensional system of particles with tunable repulsive interactions is experimentally investigated. Soft ferromagnetic particles are placed on a vibrating rough plate and vertically confined, so that they perform a horizontal Brownian motion in a cell. When immersed in an external vertical magnetic field, the particles become magnetised and thus interact according to a dipolar repulsive law. As the amplitude of the magnetic field is increased, magnetic repulsion raises and the rate of inelastic collisions decreases. Studying notably the pair correlation function and the particle velocity distributions, we show that the typical properties of such a dissipative out-of-equilibrium granular gas are progressively lost, to approach those expected for a usual gas at thermodynamic equilibrium. For stronger interaction strengths, the system gradually solidifies towards a hexagonal crystal. This new setup could consequently be used as a model experimental system for out-of-equilibrium statistical physics, in which the distance to the quasi-elastic limit can be accurately controlled.

Introduction. – Statistical mechanics provides, with the assumption of thermodynamic equilibrium, a precise description of molecular gases composed of thermally agitated microscopic particles. In contrast, in granular gases macroscopic particles are mechanically driven. Since the collisions between these particles are dissipative, energy must be continuously provided into the system from outside to reach a stationary out-of-equilibrium state. In consequence, granular gases have been extensively studied as a model system for out-of-equilibrium statistical physics [1] theoretically [2,3], numerically [4] and experimentally [5–7]. Two-dimensional granular gases, *i.e.*, particles lying on a horizontal plate vertically vibrated, were especially studied because particle trajectories can be reconstructed using fast imaging and tracking algorithms [5–9]. Nevertheless, few studies investigated the case in which non-contact interactions between particles compete with kinetic agitation and thus introduce spatial correlations differing from those observed for an inelastic hard-sphere gas. In a granular gas composed of particles owing a permanent magnetic dipole, the anisotropic dipole-dipole interactions lead to dipole alignment, then attraction and clustering [10–12]. In contrast, physics differs strongly using ferromagnetic particles with a low remnant magnetic field. When immersed in an external static magnetic field, such particles acquire an induced magnetisation so that inter-particle dipolar interactions become tunable by the operator. Applying this protocol to a granular packing, a first-order fluid-solid transition [13] and a surface instability due to competition between gravity and magnetic forces [14], are observed. If such particles are confined in a two-dimensional plane and immersed in an external perpendicular magnetic field, the magnetic interactions between particles are purely repulsive, since their dipoles are all aligned in the vertical field direction. At low packing fraction, low agitation and high magnetic field, the system forms a hexagonal lattice [15]. As mechanical agitation is increased crystal melting is observed, that is, translational and orientational orders disappear, as in some other 2D systems of interacting particles [16–20].

In this letter, we study a 2D granular gas with such tunable repulsive magnetic interactions. To our knowledge, the influence of dipolar interactions on the particle velocity distributions has only been studied in a case dominated by attractive interactions [21]. Free-cooling of 3D granular gases with electrostatic repulsions has also been investigated theoretically and numerically [22,23]. In our experiment, we start from the well-studied case of a two-dimensional granular gas [8,9] where mechanical agitation is provided to the particles by the vibration of a horizontal

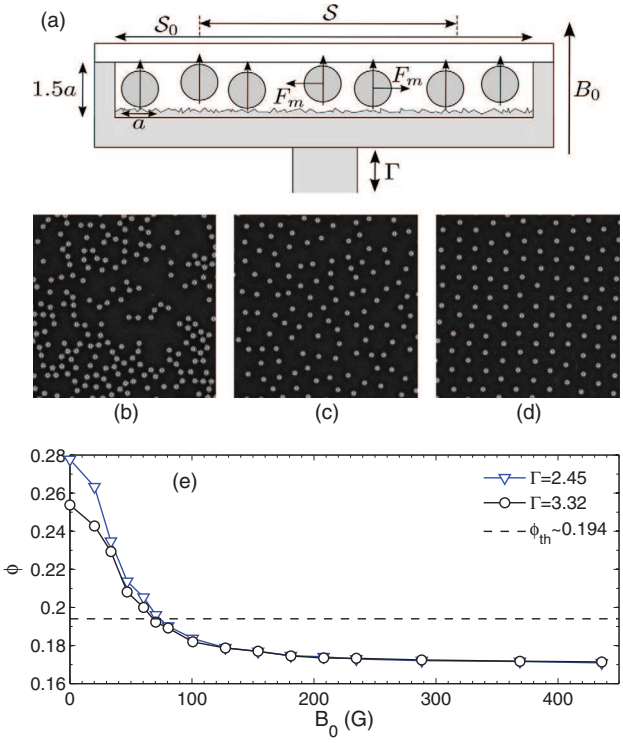

Fig. 1: (Color online) (a) Experimental setup (see text). (b) Snapshots in the inelastic regime for $B_0 = 0\,\mathrm{G}$ ($\varepsilon = 0$), (c) the quasi-elastic regime for $B_0 = 127\,\mathrm{G}$ ($\varepsilon = 16.2$), and (d) the hexagonal crystal-like regime for $B_0 = 436\,\mathrm{G}$ ($\varepsilon = 283$). Snapshots size is $3.5\,\mathrm{cm} \times 3.5\,\mathrm{cm}$, and $\Gamma = 3.32$. For the full time evolution, see the supplementary video `movie1.m4v`. For the stationary state of each of the three regimes, see supplementary slow-down videos `movie2.m4v`, `movie3.m4v` and `movie4.m4v`. (e) Area fraction of balls ϕ in the area $\mathcal{S}$ *vs.* B_0 for $\Gamma = 2.45$ and 3.32. The dashed line corresponds to the area fraction for a homogeneous particle distribution $\phi_{\mathrm{th}} = N_0\pi\sigma^2/\mathcal{S}_0 \approx 0.194$.

rough bottom plate. Additionally, a vertical magnetic field is then applied, leading to repulsive dipolar interactions between particles. Using particle tracking techniques, we analyse quantitatively the structural changes within the granular gas and its dynamical properties. The rate of inelastic collisions between particles can be easily tuned. Indeed, increasing the amplitude of the magnetic field enhances magnetic repulsion and thus decreases the number of inelastic collisions. As the dissipation rate due to inelastic collisions is proportional to the number of collisions, the total dissipation in the system is reduced. We thus show that the system undergoes a transition from a dissipative to a quasi-elastic system when the magnetic field is increased.

Experimental setup. – The experimental cell is depicted in fig. 1(a). It consists of a horizontal, square duraluminium bottom plate of area $\mathcal{S}_0 = 9\,\mathrm{cm} \times 9\,\mathrm{cm}$ and covered by a sandpaper sheet in order to provide roughness (RMS amplitude of $20\,\mu\mathrm{m}$). The cell is filled with $N_0 = 2000$ chrome steel (AISI 52100) spherical particles with a diameter $a = 2\,\sigma = 1\,\mathrm{mm} \pm 2.5\,\mu\mathrm{m}$ and a mass $m = 4.07 \times 10^{-6}\,\mathrm{kg}$. These balls are confined by rigid aluminium walls and by a rigid, smooth, antistatic coated polycarbonate lid placed $1.5a$ above the bottom plate. In order to reach a non-equilibrium steady state, this cell is driven sinusoidally in the vertical direction by means of an electromagnetic shaker. The dimensionless acceleration is $\Gamma \equiv (2\pi f)^2 A/g$ with $f = 300\,\mathrm{Hz}$ the frequency and A the amplitude of the sinusoidal forcing, g being the gravitational acceleration. Γ is measured using an accelerometer screwed on the cell. Two coils generate a vertical magnetic field $\boldsymbol{B}_0$ which is perpendicular to the cell plane and is spatially homogeneous within the cell volume with a 2% accuracy. A high-speed camera (Phantom V10) is located above the centre of the cell. A diffusive LED ring encircling the cell illuminates from the top the particles that appear as bright rings on a dark background. The camera acquisition rate is fixed to 779 frames per second in order to detect the collisions between particles. Video recordings are performed once the stationary state is reached (waiting time of 60 s) and last at least 3.85 s. To avoid measurement issues at the boundaries, we choose a region of interest $\mathcal{S}$ of $5.7\,\mathrm{cm} \times 5.7\,\mathrm{cm}$ around the cell centre. The particle diameter then corresponds to 20 pixels. We performed individual detection of particles from the video recordings using first a convolution-based least-squares fitting particle detection routine [8,24] completed by an intensity-weighted centre detection algorithm. This provides particle centre positions with a resolution of less than 0.3 pixel $\sim 0.015a$ [9]. Finally, individual trajectories were reconstructed using a tracking algorithm [25,26]. Hence, from highly resolved particle position data, we compute their velocity distributions, pair correlation functions, mean square displacements as well as collision rate estimations.

Experimental parameters. – Let us now describe the influence of the external magnetic field $\boldsymbol{B}_0$ on the chrome steel particles. These balls are soft ferromagnetic, *i.e.*, with a low remnant magnetic field and a high magnetic permeability. When placed in a vertical magnetic field of amplitude B_0, each particle is uniformly magnetised. It behaves as an induced magnetic dipole of magnetic moment $\frac{4}{3}\pi\sigma^3\frac{\chi_m}{\mu_0}B_0\,\boldsymbol{e}_z$, with χ_m the volume magnetic susceptibility, μ_0 the vacuum permeability, and $\boldsymbol{e}_z$ the upward unit vector along the vertical axis. For a purely 2D system of two identical spheres i and j with $\boldsymbol{B}_0$ perpendicular to $\boldsymbol{r}_{ij}$ (the horizontal vector between the particle centres), the potential energy of magnetic interaction reads [27]:

$$E_{m,\langle i,j\rangle} = \frac{4\pi}{\mu_0}{B_0}^2\frac{\sigma^6}{|\boldsymbol{r}_{ij}|^3} \qquad (1)$$

in the limit of high intrinsic magnetic permeability. We point out that without taking into account the geometry of the magnetisation and the demagnetising magnetic field,

an effective susceptibility χ can be defined [15,18], yielding an expression of the magnetic energy proportional to eq. (1). The repulsive force between these two particles, $\boldsymbol{F}_{m,\langle i,j\rangle} = -\boldsymbol{\nabla} E_{m,\langle i,j\rangle}$, decreases with $|\boldsymbol{r}_{ij}|^{-4}$ and is directed along $\boldsymbol{r}_{ij}$. Therefore the repulsion between particles can be tuned by the amplitude of the magnetic field B_0. If particles are not exactly in the same horizontal plane between the two confining plates, the horizontal repulsive force is reduced due to 3D effects. Nevertheless, further results in this letter show that a 2D analysis is relevant to describe the system behaviour, by considering $E_{m,\langle i,j\rangle}$ from eq. (1) as a scale of the actual magnetic energy of two interacting particles.

In addition to parameters Γ and B_0, the last important parameter is the dimensionless area fraction $\phi \equiv N\,\pi\sigma^2/\mathcal{S}$, with N the number of particles detected in the region of interest $\mathcal{S}$. As can be expected for a system of particles with increased repulsive interactions, we observe (fig. 1(e)) an expansion of the system when B_0 is increased. ϕ is found to be a decreasing function of B_0, which differs from the expected value $\phi_{\rm th} = N_0\,\pi\sigma^2/\mathcal{S}_0 \approx 0.194$ computed for the full cell area. Indeed, $\phi \approx 0.27$ for $B_0 \approx 0\,\mathrm{G}$ due to clustering [3,5,28–30] in the cell central region. As B_0 is increased, the horizontal magnetic repulsive forces cause the granular gas to expand and to reach a state of smaller and homogeneous area fraction in the region of interest $\mathcal{S}$. It is well known that a higher particle density near the boundaries is induced by non-repulsive boundary conditions [22] and a weak magnetic field radial gradient. Nevertheless, we point out that ϕ is found to be homogeneous in the region of interest $\mathcal{S}$ whatever $B_0 > 0\,\mathrm{G}$, the inhomogeneity of ϕ being confined within the area outside $\mathcal{S}$.

Competition between kinetic and magnetic energies. – From the parameters B_0, Γ and ϕ, we define now the relevant physical quantities, that we use to describe the behaviour of our system. Considering a 2D assembly of N particles mechanically agitated and immersed in B_0 inside the region of interest $\mathcal{S}$, we compute its kinetic energy per particle from velocity measurements, namely $E_c = \frac{1}{2}m\,\overline{\langle {v_x}^2 + {v_y}^2\rangle}$, where v_x (respectively v_y) denotes the horizontal velocities in the x-direction (y-direction), $\langle\cdot\rangle$ an ensemble average and $\overline{\cdot}$ the temporal average. Note that E_c is directly proportional to the granular temperature usually defined as $T_g = \frac{E_c}{m}$ [8,9]. We also compute the magnetic energy per particle $E_m = \frac{1}{N}\sum_{i=1}^{N}\sum_{j=i+1}^{N} E_{m,\langle i,j\rangle}$, with $\langle i,j\rangle$ a pair of particles within $\mathcal{S}$ and $E_{m,\langle i,j\rangle}$ its potential energy from eq. (1). The magnetic potential energy depends on the local configuration of the particles, and therefore it fluctuates in time. Finally, a dimensionless interaction parameter is defined by the ratio $\varepsilon \equiv E_m/E_c$ between the magnetic and kinetic energies [15,18]. When ε is increased, the system undergoes a continuous transition from an inelastic granular gas (fig. 1(b)) to a quasi-elastic granular gas (fig. 1(c)) since inelastic collisions between particles are progressively replaced by elastic magnetic interactions. At higher ε, the system self-organises in a condensed-like phase showing a 2D-hexagonal crystal lattice (fig. 1(d)) as particle displacements become constrained due to magnetic repulsions. This evolution of the system is also shown in the supplementary video `movie1.m4v` for a continuous increase of B_0 at fixed Γ.

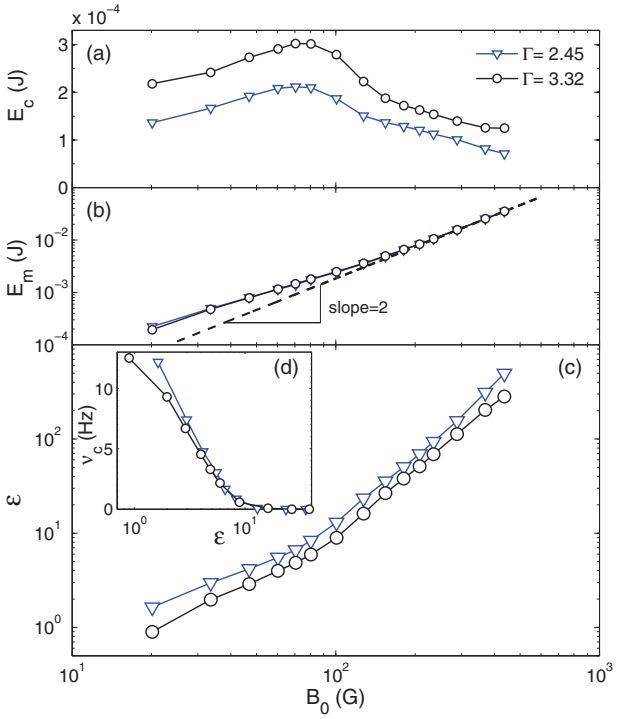

Fig. 2: (Color online) (a) Particle kinetic energy E_c as a function of the magnetic field B_0 for accelerations $\Gamma = 2.45$ and 3.32. (b) Particle magnetic potential energy E_m *vs.* B_0. (c) Ratio of the energies $\varepsilon = E_m/E_c$ *vs.* B_0. (d) Collision rate ν_c (number of collision per particle and time unit) *vs.* ε.

We present now experimental results obtained for increasing B_0 and for fixed Γ (2.45 or 3.32). These values correspond to the bounds of the range of Γ where E_c increases linearly [8]. The evolutions of E_c, E_m and ε with B_0 are depicted in fig. 2(a)–(c). Note that ε is larger than 1 for $B_0 > 20\,\mathrm{G}$, meaning that regimes dominated by magnetic repulsions are reached for moderate values of B_0. We also notice a non-monotonous evolution of E_c, which reaches a maximum for $B_0 \approx 70\,\mathrm{G}$ ($\varepsilon \approx 5$). The rate of inelastic collisions between particles ν_c is indeed strongly reduced for increasing values of ε as depicted in fig. 2(d). Due to the magnetic energy barrier, only particles with sufficient kinetic energy can collide [22]. The average number of collisions per particle and per time unit, ν_c, is evaluated using an algorithm detecting individual collisions through a distance criterion selective process. ν_c decreases with ε, vanishes below 0.1 Hz for $\varepsilon > 10$ and is strictly zero for $\varepsilon > 30$. For greater ε, particle displacements become bounded [15]. Indeed, in fig. 2(b) E_m is found to be proportional to ${B_0}^2$ for $B_0 > 150\,\mathrm{G}$ ($\varepsilon > 30$), because particle geometrical arrangement becomes a fixed

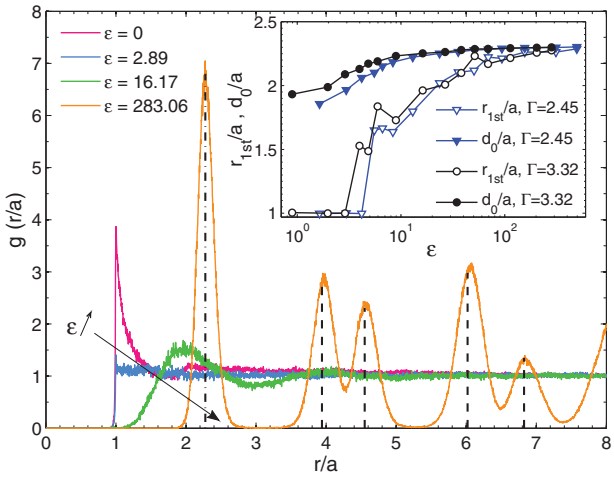

Fig. 3: (Color online) Pair correlation function $g(r)$ for $\Gamma = 3.32$ and $\varepsilon = 0$, 2.89, 16.2 and 283. For the last value, peak positions for a hexagonal crystal are shown in dashed lines as multiples of the lattice distance $r_{1\mathrm{st}}/a = 2.28$, for factors $1, \sqrt{3}, 2, \sqrt{7}$, and 3. Inset: position of the first peak $r_{1\mathrm{st}}/a$ *vs.* ε and compared with d_0/a expected for a hexagonal crystal (see text).

parameter in the calculation of E_m, once they are magnetically confined.

Radial pair correlation function. – This energetic description is also associated with important structural changes, which can be enlightened by computing the radial pair correlation function $g(r) \equiv \left[\sum_{i=1}^{N}\sum_{j\neq i}\delta(r-r_{ij})\right]\mathcal{S}/(2\pi r N^2)$, with r_{ij} the distance between the particles i and j. This function gives the probability to find two particle centres separated by a distance r. $g(r)$ is shown in fig. 3 for characteristic values of ε and at fixed Γ. At $\varepsilon = 0$, $g(r)$ displays a sharp peak at the contact value $r = a$, as in usual granular gases [5,6]. This confirms that most collisions occur in horizontal planes and validates the 2D description. Collisions happening out of horizontal planes, when viewed from the top, produce indeed a partial overlapping, leading to non-vanishing values of $g(r)$ for $r < a$. When ε is slightly increased, the amplitude of the first peak decreases to almost 1, giving a nearly flat $g(r)$ (see the curve for $\varepsilon = 2.89$). This shows that radial correlations are then quasi-absent as for a non-dissipative perfect gas whose $g(r)$ is zero for $r < a$ and 1 elsewhere in the vanishing density limit. When ε is further increased, this feature is gradually lost. Due to magnetic repulsions, $g(r = a)$ decreases towards zero and a first peak appears at $r > a$, indicating the appearance of a preferential distance between particles. A similar transition of $g(r)$ has been observed numerically for a 3D repulsive granular gas with a Coulomb interaction potential [22]. For high enough values of ε, the system structure approaches the one of a hexagonal crystal [15]. In this case, once the lattice cell size is set to the first-peak position, theoretical secondary-peak positions can be predicted from geometrical calculations and are indeed found to be close to the measured values (see the vertical dashed lines in fig. 3). The dimensionless position of the first peak of the pair correlation function $r_{1\mathrm{st}}/a$ *vs.* ε (fig. 3(inset)) can be used to discriminate the different regimes. Indeed, for $\varepsilon < 2.89$ ($\Gamma = 3.32$), $r_{1\mathrm{st}}/a = 1$, which corresponds to a gas-like state becoming more and more elastic as ε increases. Then, for higher values of ε, $r_{1\mathrm{st}}/a > 1$ means that a fluid-like phase with a negligible collision rate is reached. A system solidification progressively occurs: $r_{1\mathrm{st}}/a$ grows slowly with ε and gradually approaches the value expected for the hexagonal lattice $d_0/a = \sqrt{\pi/(2\sqrt{3}\phi)}$, which depends on ϕ since measured in $\mathcal{S}$. A distance to the hexagonal crystal is thus provided by the calculation of $d_0/a - r_{1\mathrm{st}}/a$.

Recently, such a crystal formation has also been observed in a 2D granular system of repulsive particles [15], and this crystal was found to melt through a hexatic phase in good agreement with the Kosterlitz-Thouless-Halperin-Nelson-Young (KTHNY) scenario [31]. In our experiments, the computations of the pair correlation function and of the orientational correlation function (not shown here) lead to qualitatively similar results as in [15]. Finally, the behaviour of the collisionless nearly crystalline state at strong enough ε can be understood as follows. We can consider our non-contact repulsive particles as effective larger particles in a close packing of disks. Their effective diameter would be given by $r_{1\mathrm{st}}$, the first-peak position of $g(r)$, leading to an effective area fraction $\phi_{\mathrm{eff}} = (r_{1\mathrm{st}}/a)^2\,\phi$, varying roughly between 0.44 and 0.90. Therefore, when the system is collisionless, increasing ε can be understood as rising the effective density ϕ_{eff}. This explains why a transition similar to the one occurring in 2D close-packed particle systems [32] might be found in our study where non-contact interactions between particles are involved.

Mean square displacements. – Another way to characterise structural and dynamical changes consists in measuring the mean square displacements (MSD) of the particles $\langle|\boldsymbol{R}(t+t_0) - \boldsymbol{R}(t_0)|^2\rangle$, where $\boldsymbol{R}(t)$ is the particle position at time t, t_0 being an arbitrary time origin. For particles experiencing a Brownian motion in two dimensions, the MSD equals $4D_b t$, where D_b is the diffusion coefficient. MSD normalised by the particle diameter are plotted in fig. 4. For $\varepsilon < 30$, at short times a ballistic regime occurs (MSD $\propto t^2$), followed by a normal diffusive regime at longer times (MSD $\propto t$). Therefore, in this regime, particles perform a horizontal quasi-Brownian motion in the experimental cell. For $\varepsilon > 30$, the diffusion becomes anomalous: a fit of the MSD by a power law t^α would provide $\alpha < 1$, showing that particles undergo a sub-diffusive motion. We point out that simultaneously, the collision rate becomes zero, marking a change of behaviour of the particles as magnetic interactions become stronger. Moreover, the derivative of the MSD vanishes at finite times as the MSD locally saturates, shedding light

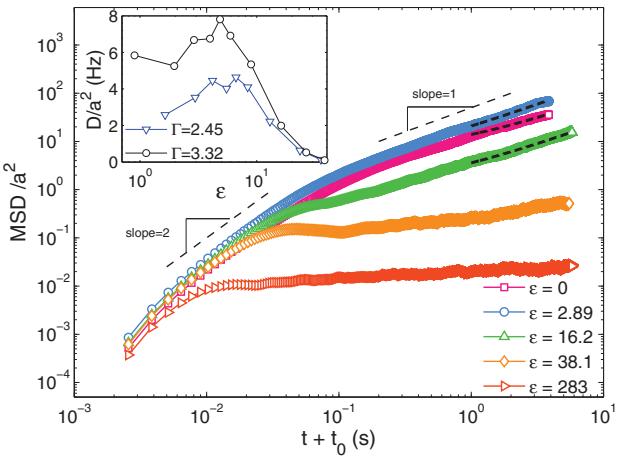

Fig. 4: (Color online) Mean square displacements (MSD) for $\Gamma = 3.32$ and $\varepsilon = 0$, 2.89, 16.2, 38.1 and 283. The thin dashed lines indicating slopes of values 1 and 2 are guides to the eye. The thick dashed lines superimposed on MSD data from $t = 1\,\mathrm{s}$ to the end of the recordings are linear fits performed in the normal diffusive regime. Inset: slopes of the linear fits divided by 4, D, which can be identified with a diffusion coefficient.

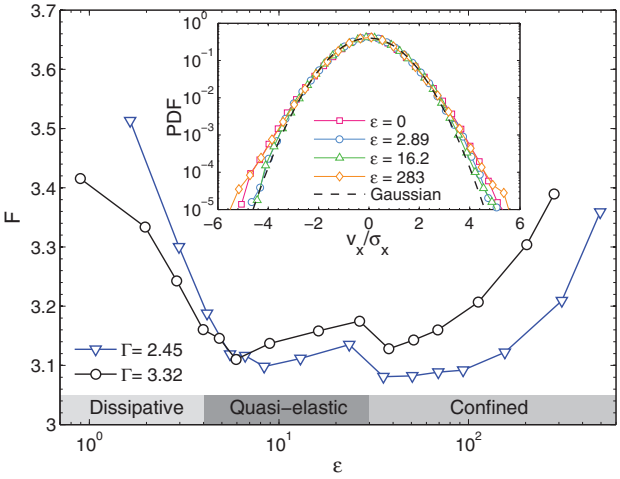

Fig. 5: (Color online) Flatness of the velocity probability density functions as a function of ε. For $B_0 = 0\,\mathrm{G}$ (*i.e.*, $\varepsilon \to -\infty$), $F = 3.52$ for $\Gamma = 3.32$ (respectively, $F = 3.63$ for $\Gamma = 2.45$). Inset: velocity PDF for different ε at $\Gamma = 3.32$. The dashed curve is the Gaussian distribution.

onto the existence of magnetic confinement. This becomes very clear for $\varepsilon > 10^2$, as particles are strongly confined and move around equilibrium positions corresponding to the nodes of the hexagonal lattice.

For $\varepsilon \leq 30$ and after waiting long enough to define a normal diffusive regime, we extract from the MSD the particle diffusion coefficient D, computed as one fourth of the slope of the MSD (evaluated from $t+t_0 = 1\,\mathrm{s}$ until the end of the measurement). The corresponding fits are plotted as thick dashed lines in fig. 4, and the obtained values of D are shown in fig. 4(inset). Like E_c (fig. 2(a)), D as a function of ε is non-monotonous and decreases strongly for $\varepsilon \gtrsim 5$ (*i.e.*, $B_0 \gtrsim 70\,\mathrm{G}$), showing that magnetic repulsions oppose the displacements. It can also be noticed that D and E_c reach their respective maximum for values of ε of the same order of magnitude, when repulsive interactions are of the same order as kinetic agitation. Indeed, D can be roughly evaluated as the product of the root mean square velocity, which is directly related to E_c, by the mean free path, which should decrease with ϕ and ε as the magnetic confinement opposes the particle displacements. The evolutions of D and E_c are thus deeply connected.

Velocity statistics. – Structural modifications imply important changes on dynamics, especially on the particle trajectories and velocity distributions. In the inset of fig. 5, the probability density functions (PDF) of velocities (x-component) normalised by their standard deviation, v_x/σ_x with $\sigma_x \equiv \sqrt{\langle {v_x}^2 \rangle}$, are plotted at fixed Γ for different values of ε. They are compared to the Gaussian distribution expected for a perfect gas at thermal equilibrium. Identical results are found for v_y due to system isotropy in the central region. As predicted for an infinite system [2] and reported in other experiments [6–9], at $\varepsilon = 0$ the velocity distribution presents a deviation from the Gaussian. In fact, this behaviour is expected for out-of-equilibrium systems, as Gaussian distribution is predicted for equilibrium gases. The reported overpopulation of the high-velocity tails is characteristic of granular gases, although there is no simple argument to justify it [1]. As ε is increased, the PDF become progressively closer to the Gaussian until $\varepsilon \approx 10$ but then depart for higher values.

This behaviour is better depicted by plotting the flatness of the velocity distributions, defined as $F \equiv \langle (v_x - \langle v_x \rangle)^4 \rangle / \sigma_x^4$ and shown in fig. 5. For a purely Gaussian distribution F equals 3 and is larger for more spread distributions. A range of significantly low values of F can be defined for $4 < \varepsilon < 30$, where the granular gas can be considered as quasi-elastic. Indeed, energy exchanges between particles should occur mainly through magnetic repulsive interactions, which are dissipationless. Note that the lower bound in ε is fairly consistent with the value $\varepsilon = 2.89$ separating the usual granular gas regime and the one with negligible collisions (see fig. 3). For $\varepsilon > 30$, displacements become progressively constrained by magnetic repelling and the system can be seen as an assembly of confined particles [15]. F then increases with ε, highlighting a heterogeneity of velocities, as particles are individually more or less confined.

Conclusion. – We have studied the effect of tunable repulsive dipolar interactions on a quasi–two-dimensional granular gas. For fixed dimensionless accelerations Γ and in a low density regime ($\phi \approx 0.2$), we increased the magnetic field B_0. The rise of the ratio ε between magnetic interaction and kinetic agitation leads to a continuous phase transition from a dissipative granular gas state at $\varepsilon = 0$, to

a collisionless hexagonal nearly crystalline state at high ε. More interesting, in the intermediate range of ε, structural and dynamical properties of the magnetic granular gas display similar features to those expected for a molecular gas at thermal equilibrium (quasi-Gaussian velocity distributions and nearly flat pair correlation functions). This transition from a dissipative to a quasi-elastic granular gas, when B_0 is increased, comes from the decrease of the dissipative collision rate, which leads to the reduction of the total dissipation. Hence, the 2D granular gas is then closer to the quasi-elastic limit. We were thus able to produce a macroscopic system whose distance to the quasi-elastic limit could be precisely controlled through the applied magnetic field. We may also wonder how the results found here with repulsive dipolar interactions can be generalised for other interaction potentials, like the Coulombian one [22,23].

Future studies on this new system could be useful to validate theoretical works about out-of-equilibrium dissipative gases, by investigating velocity correlations and coupling with the forcing viewed as a thermal bath [9,33]. Another perspective is to apply a magnetic quench to the system, in order to try to solidify it into a disordered state, which could be analogous to a colloidal glass [34]. Moreover, for denser regimes and for high ε, we observe other complex disordered states. Our experimental system could indeed be used to mimic, at the macroscopic scale, geometric frustration [35,36] or topological defects [37] arising in various physical systems.

* * *

We thank J.-C. Bacri for providing the coils and for discussions, and P. Visco, L. Deike, L. Gordillo and T. Jamin for fruitful discussions. This work has been supported by Université Paris Diderot (BQR 2012, UFR Physique) and by ESA Topical Team on granular materials No. 4000103461.

REFERENCES

[1] Barrat A., Trizac E. and Ernst M. H., *J. Phys.: Condens. Matter*, **17** (2005) 99.
[2] van Noije T. P. C. and Ernst M. H., *Granular Matter*, **1** (1998) 57.
[3] Goldhirsch I. and Zanetti G., *Phys. Rev. Lett.*, **70** (1993) 1619.
[4] Moon S. J., Shattuck M. D. and Swift J. B., *Phys. Rev. E*, **64** (2001) 031303.
[5] Olafsen J. S. and Urbach J. S., *Phys. Rev. Lett.*, **81** (1998) 4369.
[6] Olafsen J. S. and Urbach J. S., *Phys. Rev. E*, **60** (1999) R2468.
[7] Losert W. *et al.*, *Chaos*, **9** (1999) 3.
[8] Reis P. M., Ingale R. A. and Shattuck M. D., *Phys. Rev. E*, **75** (2007) 051311.
[9] Puglisi A. *et al.*, *J. Chem. Phys.*, **136** (2012) 014704.
[10] Blair D. L. and Kudrolli A., *Phys. Rev. E*, **67** (2003) 021302.
[11] Stambaugh J., Lathrop D. P., Ott E. and Losert W., *Phys. Rev. E*, **68** (2003) 026207.
[12] Oyarte L., Gutiérrez P., Aumaître S. and Mujica N., *Phys. Rev. E*, **87** (2013) 022204.
[13] Laroche C. and Pétrélis F., *Eur. Phys. J. B*, **77** (2010) 489.
[14] Lopez D. and Pétrélis F., *Phys. Rev. Lett.*, **104** (2010) 158001.
[15] Schockmel J., Mersch E., Vandewalle N. and Lumay G., *Phys. Rev. E*, **87** (2013) 062201.
[16] Ghazali A. and Lévy J.-C. S., *Europhys. Lett.*, **74** (2006) 355.
[17] Dillman P., Maret G. and Keim P., *J. Phys.: Condens. Matter*, **24** (2012) 464118.
[18] Deutschländer S. *et al.*, *Phys. Rev. Lett.*, **111** (2013) 098301.
[19] Boyer F. and Falcon E., *Phys. Rev. Lett.*, **103** (2009) 144501.
[20] Coupier G., Guthmann C., Noat Y. and Saint-Jean M., *Phys. Rev. E*, **71** (2005) 046105.
[21] Kohlstedt K. *et al.*, *Phys. Rev. Lett.*, **95** (2005) 068001.
[22] Scheffler T. and Wolf D., *Granular Matter*, **4** (2002) 103.
[23] Müller M.-K. and Luding S., *Math. Model. Nat. Phenom.*, **6** (2011) 87.
[24] Shattuck M. D., *Particle tracking*, `gibbs.engr.ccny.cuny.edu/technical/Tracking/ChiTrack.php` (accessed: 2013-04-18).
[25] Crocker J. C. and Weeks E. R., *Particle tracking using idl*, `www.physics.emory.edu/faculty/weeks//idl/` (accessed: 2013-04-18).
[26] Blair D. and Dufresne E., *The matlab particle tracking code repository*, `www.physics.georgetown.edu/matlab/` (accessed: 2013-04-18).
[27] Jackson J., *Classical Electrodynamics*, 3rd edition (Wiley, New York) 1998.
[28] Prevost A., Melby P., Egolf D. A. and Urbach J. S., *Phys. Rev. E*, **70** (2004) 050301.
[29] Falcon E., Fauve S. and Laroche C., *Eur. Phys. J. B*, **9** (1999) 183.
[30] Falcon E. *et al.*, *Phys. Rev. Lett.*, **83** (1999) 440.
[31] Strandburg K. J., *Rev. Mod. Phys.*, **60** (1988) 161.
[32] Olafsen J. S. and Urbach J. S., *Phys. Rev. Lett.*, **95** (2005) 098002.
[33] Gradenigo G., Sarracino A., Villamaina D. and Puglisi A., *EPL*, **96** (2011) 14004.
[34] Pusey P. N. and van Megen W., *Nature*, **320** (1986) 27.
[35] Han Y. *et al.*, *Nature*, **456** (2008) 898.
[36] Shokef Y. and Lubensky T. C., *Phys. Rev. Lett.*, **102** (2009) 048303.
[37] Yao Z. and Olvera de la Cruz M., *Phys. Rev. Lett.*, **111** (2013) 115503.

4.5 Orientational order across the crystallization transition

Let us now present some first results of a work in the continuity of what we presented in this chapter, and which will lead to a more detailed characterization of the transition from a dissipative gas to a crystalline state.

If translational order is measured by the pair correlation function, $g(r)$, orientational order can be measured by means of a bond orientational order parameter. When one looks for the appearance of hexagonal order, *i.e.*, of a triangular lattice, it is relevant to use the 6-fold bond orientational order parameter, Q_6, locally defined for every particle j, as

$$Q_6^j = \frac{1}{n_k} \sum_{k=1}^{n_k} e^{6i\theta_{jk}}, \tag{4.1}$$

where n_k is the number of nearest neighbors of particle j, and θ_{jk} is the angle between the vector linking the center of particle j to the center of particle k, and an arbitrary fixed direction, for instance the one of the x-axis.

Considering the particle index, j, as implicit, we define ψ_6 as the complex modulus of Q_6, $\psi_6 = |Q_6|$, which equals 1 for a particle surrounded by 6 neighbors forming a regular hexagon; otherwise ψ_6 is smaller than 1. The quantity ψ_6 is therefore a relevant measure of the hexagonal order. Note that the complex phase of Q_6 indicates, for a perfect triangular lattice, the orientation of this lattice with respect to the chosen reference axis.

In Fig. 4.3(a, b, c) we show the Voronoi tesselation of snapshots from three representative experiments across the crystallization transition, for $\Gamma = 3.32$: $B_0 = 20.1\,\mathrm{G}$ ($\varepsilon = 0.894$; dissipative granular gas state), $B_0 = 208\,\mathrm{G}$ ($\varepsilon = 51.4$; collisionless state) and $B_0 = 436\,\mathrm{G}$ ($\varepsilon = 283$; crystalline state). The color code is relative to the value of ψ_6.

In the dissipative granular gas state, hexagonal order is weak but fluctuations of order parameter ψ_6 are large, as characterized by the probability density function (PDF) of ψ_6 shown in Fig. 4.3(d). Then, local density fluctuations are large, as the wide diversity of Voronoi cell sizes shows. In the collisionless state at $B_0 = 208\,\mathrm{G}$, particle spatial distribution is much more homogeneous and hexagonal order significantly increases, as shown by the shift of the PDF of ψ_6 towards higher values in Fig. 4.3(e). For the highest interaction strength tested here, with $B_0 = 436\,\mathrm{G}$, hexagonal order in the system is very high, as visible on the PDF of ψ_6 in Fig. 4.3(f) which presents a sharp, high-amplitude peak for the ψ_6 between 0.9 and 1. Yet, some local defects are clearly visible, as evidenced in Fig. 4.3(c) by the blue and yellow-green patches, which contribute to widening the PDF of ψ_6 towards smaller-than-1 values, as shown in Fig. 4.3(f).

In order to characterize the hexagonal order of the system at a given point of the parameter space (Γ, B_0), or equivalently, (Γ, ε), we use the ensemble-averaged value of ψ_6, which we denote $\langle\psi_6\rangle$. In Fig. 4.4 we show $\langle\psi_6\rangle$ as a function of ε (and as a function of B_0 in the inset), for the two set of experiments presented in this chapter. We find that $\langle\psi_6\rangle$ varies continuously from about 0.4 in the dissipative granular gas state to about 0.9 in the crystalline state, demonstrating that hexagonal order continuously increases as we increase the strength of the interactions. However, the fact that $\langle\psi_6\rangle$ does not converges towards 1 evidences the presence of defaults in the mostly triangular lattice, as visible in Fig. 4.3(c). The curves of $\langle\psi_6\rangle$ collapse very satisfyingly when plotted as a function of ε, which supports the choice of this parameter as being relevant for characterizing this transition.

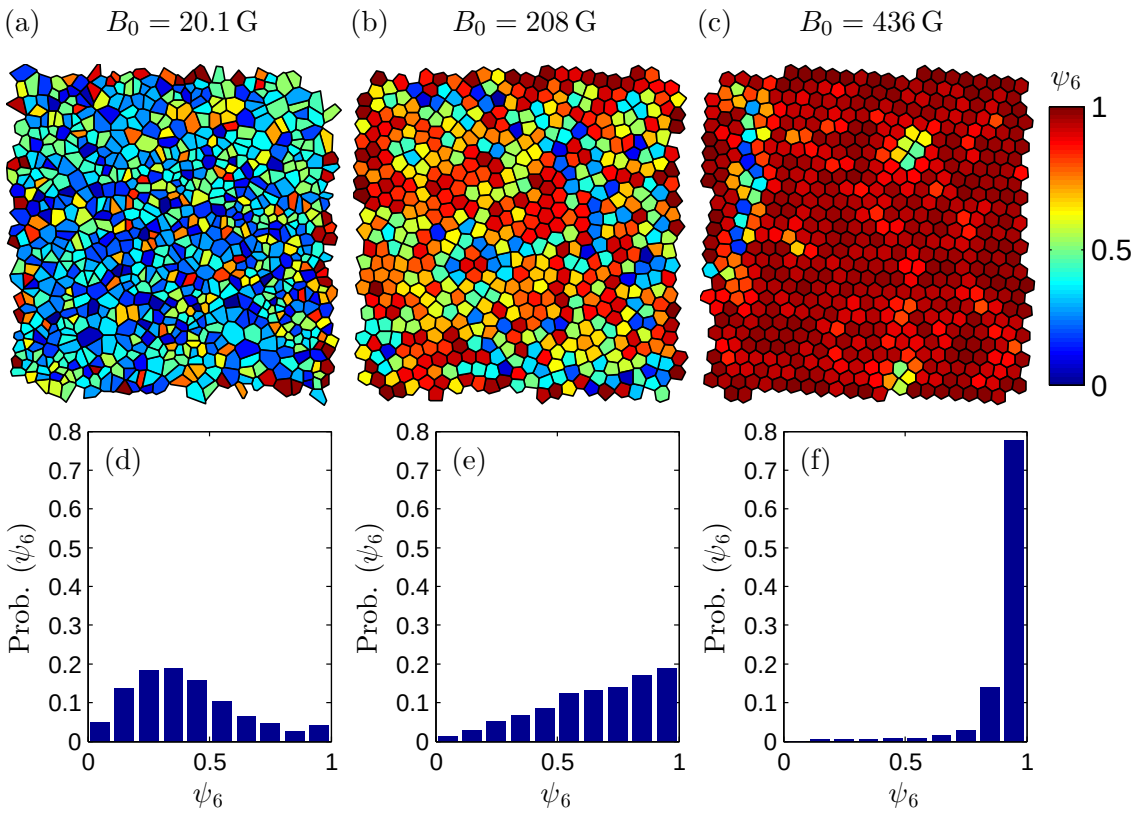

Figure 4.3 Orientational order across the crystallization transition. (a, b, c) Voronoi tesselation of snapshots from experiments with $\Gamma = 3.32$ and $B_0 = 20.1\,\mathrm{G}$, *i.e.*, $\varepsilon = 0.894$ (a), $B_0 = 208\,\mathrm{G}$, *i.e.*, $\varepsilon = 51.4$ (b) and $B_0 = 436\,\mathrm{G}$, *i.e.*, $\varepsilon = 283$ (c). The color code indicates the local value of the complex norm of the 6-fold bond orientational order parameter, $\psi_6 = |Q_6|$. (d, e, f) Probability density functions of ψ_6 relative to the experiments of diagrams (a, b, c).

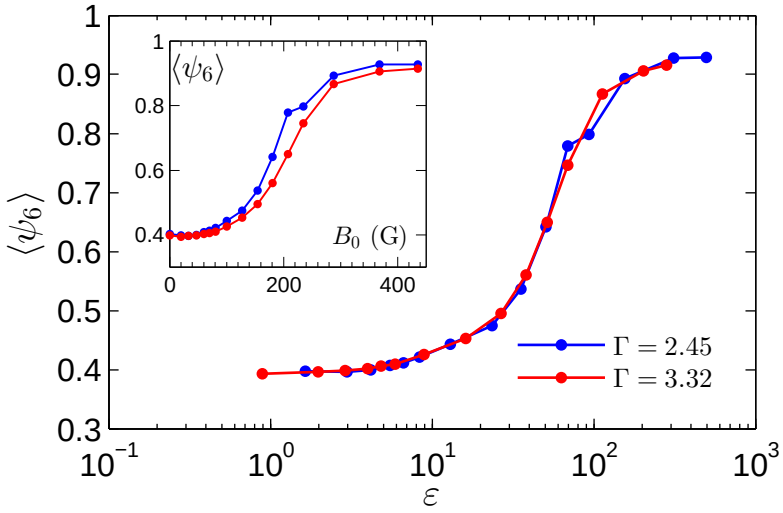

Figure 4.4 Ensemble averaged complex norm of the 6-fold bond orientational order parameter, $\langle\psi_6\rangle$, as a function of parameter $\varepsilon = E_m/E_c$ (inset: as a function of the magnetic field, B_0), for the two sets of experiments presented in this chapter ($\Gamma = 2.45$ and 3.32, B_0 varies). This order parameter increases continuously from about 0.4 to about 0.9, indicating a continuous ordering of the particles into a hexagonal lattice, and the presence of defects in this lattice even at high interaction strength.

Chapter 5

At high density, transition to a granular labyrinthine phase

Chapter 5 : At high density, transition to a granular labyrinthine phase

↑ back to contents

Chapter abstract

Labyrinthine patterns arise in two-dimensional physical systems subject to competing interactions, in fields ranging from solid-state physics to hydrodynamics. For systems of interacting particles, labyrinthine and stripe phases have been studied in the context of colloidal particles confined into a monolayer, both numerically by means of Monte Carlo simulations and experimentally using superparamagnetic particles. Here we report on the experimental observation of a labyrinthine phase in an out-of-equilibrium system constituted of macroscopic particles. Once sufficiently magnetized, they organize into short chains of particles in contact and randomly oriented. We characterize the transition from a granular gas state towards a solid-like labyrinthine phase, as a function of the ratio of the interaction strength to the kinetic agitation, ε. The spatial local structure is analyzed by means of particle tracking. Moreover, we explain the formation of these chains using a simple model.

5.1 Introduction

We encounter patterns in Nature every day: the stripes on a butterfly's wings, a wave-shaped cloud, the cracks on the bottom of a dried puddle. In chemistry, biology and fluid mechanics, but also in solid state physics and non-linear optics, patterns arise from out-of-equilibrium processes [91]. Alan Turing introduced, *via* his famous paper on reaction-diffusion patterns in 1952 [92], the analysis and the classification of spatio-temporal macroscopic patterns from the point of view of linear stability analysis: a pattern can be either stationary in time and periodic in space, or periodic in time and uniform in space, or periodic in both time and space (which is the case of the so-called Turing patterns). Here we focus on the former type of patterns: those with a spatial periodicity only.

Note that a *pattern* is defined by an ensemble of regions where the relevant order parameter takes identical values. Hence, in the context of patterns, a problem with *aligning or anti-aligning spins* is analogous to a problem of, respectively, *attracting and repulsive particles*. Therefore we will not distinguish the former from the latter, and we will always talk about attractive and repulsive interactions.

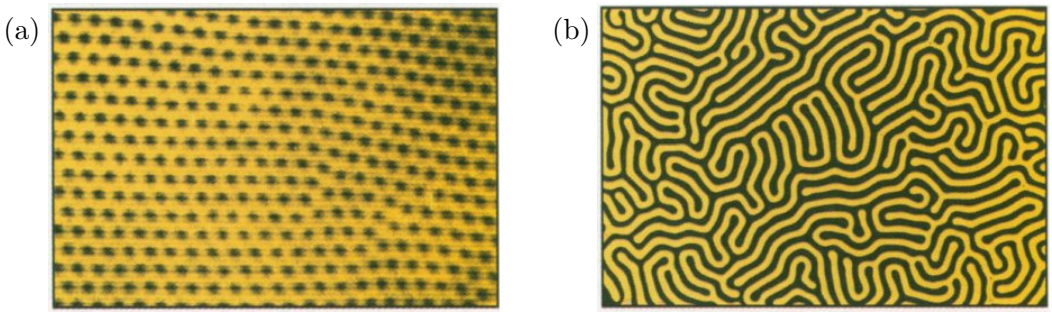

Figure 5.1 Ferrofluid (in dark) confined between two glass plates in a magnetic field normal to the fluid, exhibiting (a) a bubble state of period $\sim 4\mu$m, for a low filling fraction; and (b) a labyrinthine state of period ~ 1 cm, for a high filling fraction (adapted from [93]).

Crystal-like phases, such as the one we studied in our system at a low density ϕ and high interaction strength ε in Chapter 4, more generally called *bubble* phases when more than a single particle can be located at every node, are periodic in space. We show in Fig. 5.1(a) an example of a bubble phase obtained with a confined ferrofluid. Also periodic in space are *stripe* phases, *i.e.*, phases in which the pertinent order parameter varies periodically but in a preferred direction, generating parallel stripes. However, unlike bubble phases, in which one repulsive interaction dominates, stripe phases arise when two interactions with comparable strengths compete at different lengthscales [93, 94]. Stripes can be entangled, instead of being parallel. Then, one speaks of a *labyrinthine* phase, as illustrated in Fig. 5.1(b). The transitions between *bubble*, *stripe* and *labyrinthine* phases occur when the strength of the competing interactions and temperature vary [93, 95]. Let us now focus on labyrinthine phases, which arise in a wide variety of in- and out-of-equilibrium, two-dimensional physical and chemical systems.

Systems displaying labyrinthine phases and which can be considered continuous, that is, systems for which the typical stripe width is usually much larger than the inter-particle distance, are of various types. These include, among others, ferrimagnetic thin films [96, 97] (due to the competition between local exchange interactions and long-ranged dipolar interactions), amphiphilic monomolecular films, *i.e.*, Langmuir monolayers [98] (van der Waals forces *vs.* long-ranged dipolar interaction), ferrofluid drops [99] and biphasic ferrofluid-oil mixtures in Hele-Shaw cells [100] as illustrated in Fig. 5.1 (surface tension *vs.* long-ranged dipolar interactions), and granular-fluid suspensions in which air penetrates [101, 102] (effective surface tension *vs.* frictional stress). Seul and Andelman demonstrated that the phenomenology of these systems, that is, the choice between bubble and stripe phases, can be explained within the framework of modulated phases [93]. Even though these authors briefly mention a "buckling instability of stripe domains" leading to what we call here *labyrinthine* phases, it was not before the numerical work of Stoycheva and Singer [95] that the transition from stripe to labyrinthine phases was studied quantitatively. Using a model with competing short-range attraction and long-range repulsion, they demonstrated that this melting transition depends on both the ratio of the long-range to short-range interaction strengths, and on temperature. Finally, note that for systems whose particles are constrained on a lattice, such as spins in ultra-thin films, the structure of this lattice may influence the domain phases observed due to inherent geometrical frustration [94]. In fact, Han *et al.* demonstrated that the problem of frustrated spins on a triangular lattice can be mapped onto a problem of non-interacting particles packed on a triangular lattice and allowed to buckle in two positions (up or down), and they indeed observed labyrinthine patterns at low enough temperature [86, 85].

In contrast to the continuous systems mentioned above, labyrinthine patterns can be obtained with a typical width of a single particle diameter, as in [86, 85]. From diffusing particle simulations with short-range attraction and long-range repulsion, Haw obtained one-particle-wide labyrinthine phases, which evolved towards either a connected chain network or a connected aggregate network depending on the range and strength of the interactions [103]. Some Monte-Carlo simulations have even shown that one-particle-wide stripe and labyrinthine phases can be obtained with a purely repulsive potential, if it includes a soft shoulder at short distance, namely a *core-softened* potential [104, 105]. With such a potential, the alignment of particles into the chains constituting the labyrinthine phase near contact is more favored than a homogeneous liquid-like state, due to the repulsive forces from the surrounding particles. In particular, Malescio and Pellicane [104] demonstrated that the melting of parallel chains of particles (*i.e.*, stripes) into a labyrinthine phase occurs through a sharp temperature-controlled transition, as was also found for continuous systems by Stoycheva and Singer [95], where excessive energy fluctuations indicate strong spatial ordering rearrangements. Motivated by the numerical results on core-softened potentials, two-dimensional experiments have been performed with core-softened colloids. Two complementary studies, one experimental [106] and one numerical [65], have explored the phases obtained for the softest repulsive potential shoulder possible, *i.e.*, with a vanishing force at contact, and indeed obtained labyrinthine phases for high enough densities. In particular, a genetic algorithm approach has strongly suggested that stripe phases are ground states for labyrinthine phases [65].

5.2 Motivation

Labyrinthine phases in systems of interacting particles have only been realized experimentally once with core-softened colloids by Osterman *et al.* [106], with results consistent with their own simulations [65] and with the related numerical (Monte-Carlo) predictions [104, 105]. However, the latter models do not restrict the possibility of creating labyrinthine phases to colloids, but leave it accessible *a priori* to any system of particles interacting by a core-softened repulsive potential and agitated by an effective temperature for navigating the energy landscape. In particular, the question of the existence of labyrinthine phases for out-of-equilibrium systems remains open. One could expect results similar to thermal systems, but with a different dynamics.

In this chapter, our goal is twofold. First, demonstrating that such a labyrinthine phase can be obtained in an intrinsically out-of-equilibrium system of macroscopic particles, such as our magnetic granular gas, and quantitatively characterizing the transition that leads to it from a liquid-like state. Second, explaining simply but quantitatively the preference of the system for a labyrinthine rather than a crystalline configuration (like the one discussed in Chapter 4).

The work presented here is a logical step following Chapter 4. After having characterized the effects of an increasing interaction strength on the system dynamics and structural organization for low particle density, we perform an analogous investigation at a higher density, where the high-energy state is a *labyrinthine* phase.

5.3 Main results

The experimental setup that we use in this chapter is identical to the one in Chapter 4, except that now the particle area fraction is higher. A monolayer of soft ferromagnetic spheres 1 mm in diameter is vibrated to form a quasi-two-dimensional granular gas. In this chapter, we use $N_0 = 5000$ particles, yielding an expected particle area fraction $\phi_{\text{th}} = 0.485$. Under mechanical agitation ($\Gamma = 2.23$), particles undergo Brownian-like motion, but due to the dissipative nature of the collisions, the granular gas reaches a stationary out-of-equilibrium state. Immersed in a vertical external magnetic field B_0, the soft ferromagnetic spheres are magnetized and interact as induced dipoles. The gap size in these experiments, $e \sim 1.42\,a$, with a the particle diameter, is close to the specific value $e_x = a\,(\frac{1}{\sqrt{5}} + 1) \approx 1.45\,a$ (defined in Eq. 3.53). This makes the pair potential significantly softened for two *buckled* particles at contact, while it is normally repulsive elsewhere. As a result, when the magnetic field is increased, the granular gas solidifies into a labyrinthine phase composed of chains of a few particles in contact, as illustrated in Fig. 5.2 for three representative values of the magnetic field, B_0, and detailed below.

When increasing the applied magnetic field, in a first stage, we increase the effective elasticity of the particles' interactions, as described in Chapter 4 at a lower density. At this stage, all particles are free to move across the cell and the system looks like a gas [Fig. 5.2(a)]. Consequently, the fraction of particles in chains, φ, defined as the number of particles at contact divided by the total number of particles, equals zero, as shown in Fig. 5.3(a). At the same time, the pair correlation function has the expected spike at $r = a$ and ripple at $r = 2\,a$ [Fig. 5.3 (c)]. However, from $\varepsilon \approx 60$ (*i.e.*, $B_0 \approx 100\,\text{G}$), the behavior of this dense magnetic granular system is clearly different: first pairs of particles, then triplets and so on, aggregate, while unbounded particles move inbetween them, as illustrated in Fig. 5.2(b). Quantitatively, in the range of ε in which chains and free particles coexist, φ increases from 0 to 1 and the mean chain length, λ, from $1.6\,a$ to $2.6\,a$, as shown in Fig. 5.3(b), while a high-amplitude peak appears on the pair correlation function at $r \approx 0.9\,a$, proving the *buckled* structure of the chains illustrated in Fig. 5.3(c)(inset). Eventually, at an interaction strength $\varepsilon = 1000$, the whole system solidifies into a labyrinthine phase made of chains one-particle-wide, a few particle long and randomly oriented, as shown in Fig. 5.2(c). Then, increasing ε further does not cause any noticeable change. This is made

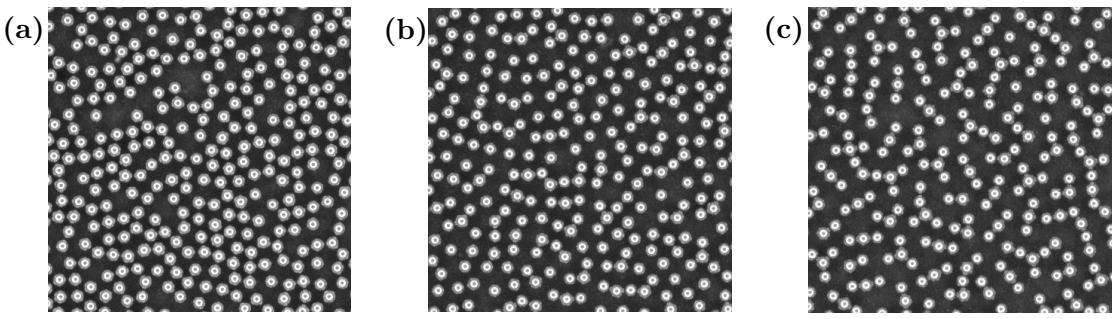

Figure 5.2 Transition to the granular labyrinthine phase. (a) Granular gas state with only free particles, at $B_0 = 20.5\,\text{G}$, *i.e.*, $\varepsilon = 6.23$; (b) State of coexistence of free particles and chains, at $B_0 = 161\,\text{G}$, *i.e.*, $\varepsilon = 126$; (c) Labyrinthine phase where almost all the particles are part of chains, at $B_0 = 188\,\text{G}$, *i.e.*, $\varepsilon = 4.62 \times 10^3$. The white rings are the reflection of the LED circular array on top of the particles and have a diameter about half of the particle diameter. The particles themselves are visible in gray.

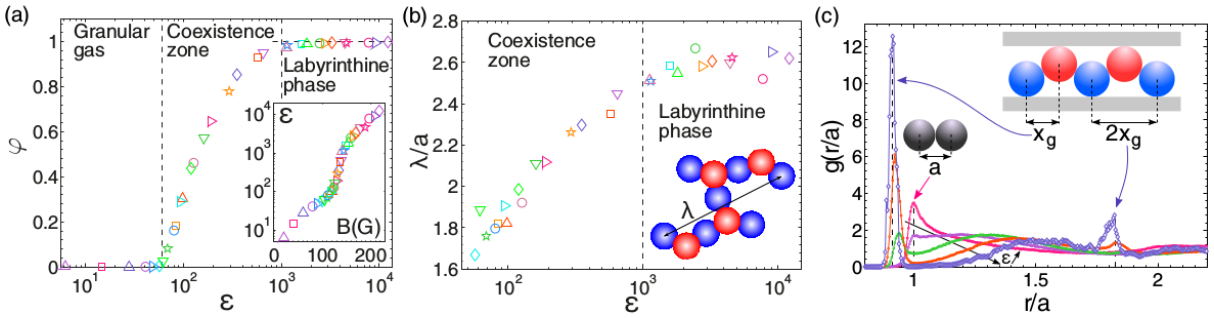

Figure 5.3 Characterizing the transition from a dissipative granular gas to a labyrinthine phase. (a) Fraction of particles in chains *vs.* control parameter $\varepsilon = E_m/E_c$ (inset: ε *vs.* applied magnetic field); (b) Dimensionless mean chain length, defined as the largest distance between two particles in a chain, *vs.* ε; (c) Pair correlation function at short distances for $\varepsilon = 14.7$ (red), 41.0 (purple), 68.9 (green), 127 (orange), and 649 (blue).

clear, one one hand, by the measures of φ and λ, which both saturate at the respective values they take at $\varepsilon = 1000$, and on the other hand, by $g(r)$, which displays for all $\varepsilon > 1000$ similar shapes characterized by a high-amplitude first peak and a secondary peak (these results are not shown here).

Now, how can we explain that the magnetic granular gas solidifies into a labyrinthine phase rather than into a crystalline state? We propose to answering this question using a simple model, which is valid when ε is high enough so that particles do not collide and the density is roughly homogeneous. We take a gap size of $e = 1.5\,a$. We consider six particles horizontally positioned at the nodes of a regular hexagon of side d equalling the node-to-node distance of a triangular lattice of particle area fraction ϕ, *i.e.*, $d = a\left[\pi/(2\sqrt{3}\phi)\right]^{1/2}$. These particles all remain fixed to the bottom plate. One test particle is linearly moved from the *central* position, at the center of the hexagon, to the *contact* with one of the two bottom particles, while always being in contact with the top plate. For different values of ϕ, we evaluate the energy landscape experienced by this particle. At $\phi = 0.5$, the central position is a local minimum of energy, while the global minimum is found at contact, thus the two particles preferentially stick together in the *buckled* configuration. Extending this argument to the whole system leads to the conclusion that at $\phi = 0.5$, the favored high-energy state is either a stripe or a labyrinthine phase. This conclusion also applies to $\phi = 0.6$ and higher area fractions, since then, the only minimum is found at contact. In contrast, at lower ϕ, such as 0.35 and 0.2, the global minimum of energy is reached when the test particle is at the central position. Therefore, at such area fractions, a crystal-like configuration is most favored. Finally, this simple model is consistent with the experimental results that we presented in this chapter and in Chapter 4.

5.4 Conclusion

We have demonstrated that a labyrinthine phase made of chains of particles can be obtained in a granular, out-of-equilibrium system of macroscopic particles, analogously to the labyrinthine phases observed in a colloidal system [106] and as predicted by Monte-Carlo simulations [104, 105]. In our granular gas, particles interact by anisotropic repulsive dipolar interactions and experience an agitation which enables them to explore the energy landscape. Through the

"solidification" of the granular gas into a labyrinthine phase, for which we use the fraction of particles in chains as an order parameter, the mean chain length significantly increases (*i.e.*, particles aggregate into nearly linear chains and not into round clusters) and a sharp peak of the pair correlation function grows at $r < a$ (*i.e.*, chains are *buckled* out of plane). Moreover, a simple model based on the comparison of the energies of particles in configurations corresponding, respectively, to a crystalline state and to a labyrinthine phase, enabled us to explain the system's preference for one state or the other depending on the particle area fraction.

In this chapter, we have not addressed the question of the dynamics of the granular labyrinthine phase, because we chose parameters that made relevant to consider it as stationary (relatively slow increase of the magnetic field and long waiting time $\tau_0 = 60\,\mathrm{s}$). Yet, as we are going to see in Chapter 6, the granular labyrinthine phase does undergo relaxation at long times, which is a phenomenon reminiscent of the slow dynamics of structural glasses [107, 108, 109]. Let us note that in the case of labyrinthine domain patterns in continuous systems, the analogy with glasses was also reported in an analysis of their globally disordered structure [97] and a study of their relaxation [110].

Finally, let us emphasize that, although the simple criterion of the variation of φ captures well the transition from a granular gas to a labyrinthine phase, it should fail to distinguish a parallel stripe phase [104, 65] from a labyrinthine phase. Topology and morphology would indeed have to be taken into account, like local orientational properties. Several approaches have been proposed to analyze or to model labyrinthine patterns, such as the introduction of a local wave vector [111], the computation of the wrinkledness [110], and the decomposition of the pattern into clusters of linear segments [97]. To our knowledge, the definition of an appropriate order parameter for labyrinthine patterns remains an open question.

Transition to a labyrinthine phase in a driven granular medium

Simon Merminod,* Timothée Jamin, Eric Falcon, and Michael Berhanu
Université Paris Diderot, Sorbonne Paris Cité, MSC, CNRS (UMR 7057), 75013 Paris, France
(Received 8 July 2015; revised manuscript received 9 November 2015; published 11 December 2015)

Labyrinthine patterns arise in two-dimensional physical systems submitted to competing interactions, in fields ranging from solid-state physics to hydrodynamics. For systems of interacting particles, labyrinthine and stripe phases were studied in the context of colloidal particles confined into a monolayer, both numerically by means of Monte Carlo simulations and experimentally using superparamagnetic particles. Here we report an experimental observation of a labyrinthine phase in an out-of-equilibrium system constituted of macroscopic particles. Once sufficiently magnetized, they organize into short chains of particles in contact and randomly orientated. We characterize the transition from a granular gas state towards a solid labyrinthine phase, as a function of the ratio of the interaction strength to the kinetic agitation. The spatial local structure is analyzed by means of accurate particle tracking. Moreover, we explain the formation of these chains using a simple model.

DOI: 10.1103/PhysRevE.92.062205 PACS number(s): 45.70.Qj, 05.65.+b, 75.50.Kj

I. INTRODUCTION

Labyrinthine phases are intriguing two-dimensional (2D) patterns occurring in various domains of physics, in equilibrium and out-of-equilibrium situations. Two distinct phases form at small-scale well-separated stripes, which are themselves entangled, leading to a complex large-scale pattern. These shapes were experimentally obtained for extremely varied 2D systems ranging from ferrimagnetic garnet films [1] in condensed matter, Langmuir monolayers [2] in soft matter, granular fluid suspensions in which air penetrates [3,4], ferrofluid drops [5] and biphasic ferrofluid-oil layers [6] in fluid mechanics, to chemical reaction-diffusion systems [7]. The common denominator of these systems is the competition between long-range repulsion and short-range attraction, which leads to the phenomenology of modulated phases [8]. Moreover, a wide range of ordering effects that lead to different patterns can also be related to the competition between interactions and geometrical frustration, as specifically shown for magnetic thin films [9].

By analogy with the phenomenology of these continuous systems, labyrinthine and stripe phases have been introduced for systems of particles. In particular, in the context of colloidal monolayers, several Monte Carlo simulations [10–13] and one molecular dynamics simulation [14] have been performed. It was shown that, to observe stripes and labyrinthine phases, a long-range repulsive potential is needed, together with a short-range attraction, which can be replaced by a core-softened potential [10,11]. Tuning geometrical frustration in noninteracting colloidal monolayers [13,15] leads also to stripe phases. Moreover, the only experimental observation of a labyrinthine phase in a colloidal system was obtained using superparamagnetic colloids under a magnetic field, inducing dipolar interactions [16]. Labyrinthine phases were indeed found as equilibrium states at a high enough density of micrometric spheres, in agreement with dedicated Monte Carlo simulations [12,16]. In contrast, similar labyrinthine or stripe phases have not been described in a macroscopic and out-of-equilibrium system whose particles can be individually identified.

Here, we report the observation of such a labyrinthine phase. A monolayer of soft ferromagnetic spheres 1 mm in diameter is vibrated to form a 2D granular gas [17–22]. Under mechanical agitation particles undergo a Brownian-like motion, but due to the dissipative nature of the collisions, the granular gas reaches a stationary out-of-equilibrium state. Then immersed in a vertical external magnetic field B, the soft ferromagnetic spheres are magnetized and interact with each other as induced dipoles. When the magnetic field is increased, the granular gas solidifies into a phase composed of chains of a few particles in contact, similar to the labyrinthine phase observed with colloids [16]. In contrast to this colloid study, which focuses on equilibrium states, the transition from gas to labyrinth is here clearly described, using accurate particle tracking. Finally, as a remark, we emphasize that the physical mechanisms at play in labyrinthine and stripe phases of interacting particles differ from those in chain and cluster phases reported in some interacting granular gases [23–25], despite visual similarities. Indeed, these phases are composed of head-to-tail dipoles and were observed when attractive behavior is dominant at a large scale, because permanent dipoles are considered [23,25] or because the hypothesis of a quasi-2D system is not verified [24].

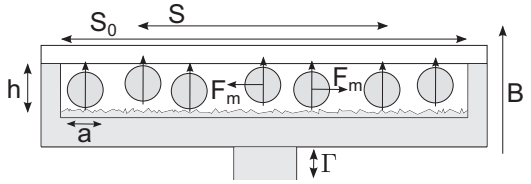

FIG. 1. Experimental setup. 5000 chromed steel spherical particles (diameter $a = 1$ mm and mass $m = 4.07$ mg) are vertically vibrated (acceleration $\Gamma = 21.9\ \mathrm{m \cdot s^{-2}}$) inside a horizontal, square aluminium cell (area $S_0 = 9 \times 9\ \mathrm{cm^2}$) with a rough bottom plate and a polycarbonate top lid (gap size $h = 1.5a$). In the presence of a vertical magnetic field B, particles repel each other with a force $\vec{F}_m$. The region of interest is of area $S = 5.7 \times 5.7\ \mathrm{cm^2}$.

*simon.merminod@univ-paris-diderot.fr

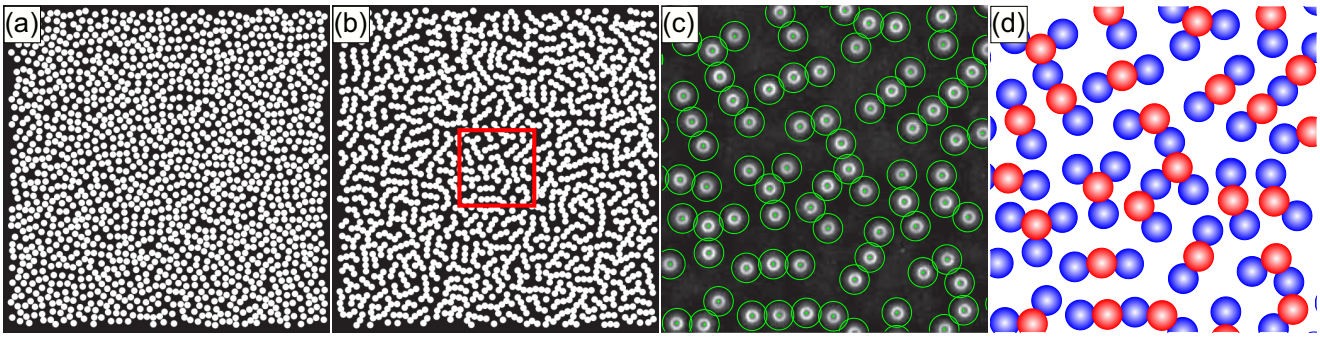

FIG. 2. (Color online) Top views of the system of particles. In (a) and (b), images of the spheres have been replaced by white disks of diameter a for better visualization, whereas (c) is from a direct image from the camera and (d) is the result of particle tracking. (a) Dissipative granular gas state at a moderate B (80 G). (b) Labyrinthine phase at a high B (170 G). The particles organize into an amorphous phase mostly composed of chains of a few particles. The region within the red square is enlarged in (c) and (d). (c) Thick circles are reflections of lighting on the spheres and appear smaller than the actual overlapping particle radii (thin circles). (d) Buckled chains (red spheres, top particles; blue spheres, bottom particles) mostly compose the amorphous phase.

II. FROM A GRANULAR GAS TOWARDS A LABYRINTHINE SOLID PHASE

The experimental setup is similar to the one used in [26]. Soft ferromagnetic spherical particles of diameter $a = 1$ mm are confined between two horizontal parallel plates separated by a gap of $h = 1.5a$ in order to form a monolayer as depicted in Fig. 1. Particles are vibrated vertically and are lit by an annular light-emitting diode (LED) array and imaged from the top by a fast camera through the transparent top plate. Particle center positions are tracked and their trajectories are reconstructed in the horizontal plane [21,27]. Interactions between particles are introduced by means of an external vertical magnetic field of amplitude B controlled by the experimentalist. Additional details on the experimental setup and protocol, and on the particle detection technique, are given in the Appendixes.

Magnetized soft ferromagnetic spheres behave as induced dipoles, whose magnetic moments are vertical and proportional to B. The interaction potential U_m of a particle located at a distance r and a polar angle θ from a second particle [28] reads in spherical coordinates [29], with μ_0 the vacuum permeability,

$$U_m(r,\theta) = -\frac{\pi}{16}\frac{B^2}{\mu_0}\frac{a^6}{r^3}(2\cos^2\theta - \sin^2\theta). \qquad (1)$$

Two spheres in the same horizontal ($\theta = \pi/2$) plane are thus repelling each other. Using this experimental method, macroscopic transitions were observed in 3D assemblies of magnetized soft-ferromagnetic particles [30,31]. Then the number of particles per surface unit is expressed by a dimensionless parameter, the area fraction $\phi = (N\pi a^2)/(4\,S)$, with N the number of particles tracked in the region of interest S. For a monolayer of particles, a high enough magnetic field, and a moderate area fraction ($\phi = 0.2$), the 2D granular gas solidifies into a hexagonal crystal [26], whose melting has been found to follow the Kosterlitz-Thouless-Halperin-Nelson-Young (KTHNY) scenario [32].

Here ϕ is increased to 0.5. For moderate values of the magnetic field B and continuous shaking, particles undergo a Brownian-like motion. At a given instant particle positions are random [Fig. 2(a)] and spheres exchange energy through dissipative collisions and magnetic interactions. We observe a 2D granular gas, whose properties are similar to those found at a lower area fraction [26]. Then by increasing B further, we observe that, despite the magnetic repulsion, small chains of two or three particles in contact start to form in the bulk of agitated particles. We remark also that the motions of the particles belonging to these chains are considerably restricted compared to those of free particles. At a higher magnetic field, the quasitotality of the particles are condensed into these chains [Fig. 2(b)]. At a large scale, the picture of the assembly of the system does not present an ordered structure. Thus, by increasing magnetic interactions, the system has been solidified in an amorphous state. Labyrinthine patterns were indeed described as globally disordered stripe domains [33]. Due to the presence of chains, the particle assembly presents striking similarities to the labyrinthine and stripe phases observed [16] and numerically predicted [10–14], for example, for 2D colloidal systems under thermal agitation and with dipolar repulsive magnetic interactions. Here, a transition from a granular gas phase to a labyrinthine phase for a macroscopic, out-of-equilibrium system is observed. This transition can also be visualized by applying a linearly increasing magnetic field from $B = 0$ G to $B = 200$ G (see video in Supplemental Material [34]). First, pairs aggregate, then triplets, and so on, homogeneously across the cell, until nearly motionless chains of various lengths occupy the whole cell, isolating the few remaining fluctuating particles from each other. We note also that, starting from the labyrinthine phase, the inverse transition is observed when the magnetic field is decreased. This shows that the system does not present any noticeable hysteresis.

By means of accurate particle tracking, chain morphology can now be quantitatively characterized. Chains are well separated due to the magnetic repulsion and can thus be considered as groups of more than one particle, according to a criterion of the contact distance. Moreover, chains appear mainly as linear objects because, most of the time, a particle inside a chain is in contact with two neighboring particles. Nevertheless, the relative orientations of the chains seem random. In the following, quantitative analysis of the small-scale structure reveals that chains correspond to a buckled

state of particles in contact [Fig. 2(c)]. A particle, once it is condensed in a chain, is in contact either with the top plate or with the bottom plate. Using slight differences in lighting for the two kinds of particles, our detection technique is able to provide the vertical position of the particles in the chains [as shown in the virtual image in Fig. 2(d)], which is coded as *up* (red spheres) or *down* (blue spheres). It can be noted that the particles at the tips of the chains are for the most part *down*, revealing an effect of gravity.

III. CHARACTERIZATION OF THE TRANSITION

Let us now quantitatively characterize the transition from a granular gas to the labyrinthine phase using the particle tracking data. The magnetic potential energy E_m and the horizontal kinetic energy E_c per particle can now be computed. From the interaction potential $U_m(r,\theta)$ defined in Eq. (1), the magnetic energy per particle is computed as the averaged summation over the pairs of the interaction potential of each pair,

$$E_m = \overline{\frac{1}{N_p}\sum_{i=1}^{N_p}\sum_{j=i+1}^{N_p} U_m(r_{ij},\theta_{ij})}, \qquad (2)$$

with N_p the number of particles involved in the calculation of E_m; r_{ij} and θ_{ij}, respectively, the distance and the polar angle between the two particles i and j; and $\overline{\cdot}$ the temporal average. The magnetic potential energy depends on the local configuration of the particles, and therefore it fluctuates in time. Its averaged value, E_m, is found to be proportional to B^2 [Fig. 3(a)]. The kinetic energy per particle is computed from velocity measurements,

$$E_c = \tfrac{1}{2}\, m\, \overline{\left(\langle v_x{}^2\rangle + \langle v_y{}^2\rangle\right)}, \qquad (3)$$

where m denotes the particle mass, v_x (respectively, v_y) the horizontal velocities in the x direction (y direction), and $\langle\cdot\rangle$ an ensemble average. E_c is a measure of the agitation in the system. When the magnetic field B is increased, in the first stage E_c grows [Fig. 3(b)]. Repulsive dipole-dipole interactions reduce the rate of dissipative collisions, which consequently increases E_c for a given shaking amplitude [26]. Once chains start to form, for $B \approx 100$ G, E_c drops significantly and nearly vanishes as the labyrinthine phase is formed for $B \approx 150$ G, illustrating the solidification process. For higher magnetic excitation values, the labyrinthine phase becomes less and less mobile as interactions strengthen and fluctuations are restrained.

Now, let us define the dimensionless control parameter $\varepsilon \equiv E_m/E_c$ [26], which is depicted as a function of B in the inset in Fig. 4(a). ε provides a measure of the competition between distance interactions and kinetic agitation. By analogy with an order parameter, the fraction of particles condensed in the chains φ is computed as the ratio of the number of particles belonging to a group of more than one particle to the total number of particles tracked in the region of interest. By plotting φ as a function of ε, as shown in Fig. 4(a), the transition is well depicted. For $\varepsilon < 60$, φ is nearly null in the granular gas phase, whereas for $\varepsilon > 1000$, φ is slightly smaller than 1, for the labyrinthine phase. The intermediate region of partial solidification corresponds to a coexistence zone between fluidized particles and particles condensed

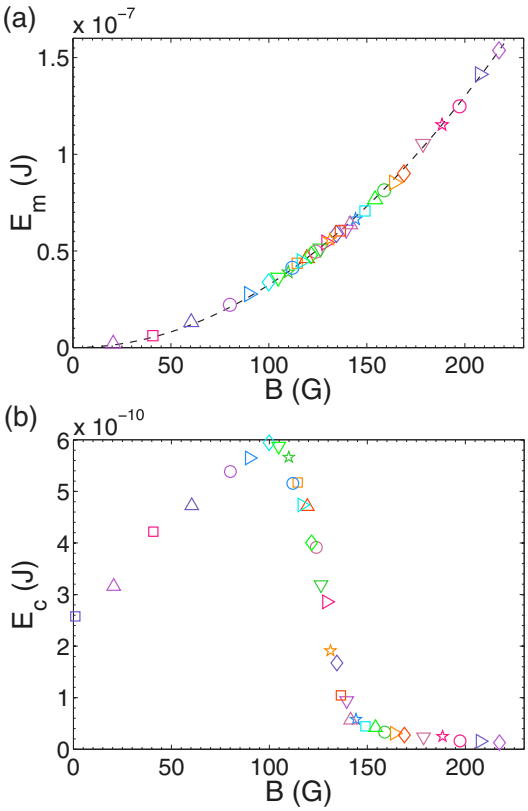

FIG. 3. (Color online) Potential magnetic energy and kinetic energy per particle. Each symbol corresponds to an independent experiment. (a) The potential magnetic energy is found to scale as B^2 (the dashed curve is a B^2 fit). (b) The kinetic energy, which measures agitation, plotted as a function of B. First, E_c increases due to the fluidizing effect of the magnetic interactions [26], then it suddenly drops towards 0 at the onset of solidification ($B \approx 100$ G).

in the chains. Let us emphasize that, although the simple criterion of the variation of φ captures well the transition from a granular gas to a labyrinthine phase, it should fail to distinguish a stripe phase from a labyrinthine phase. Topology and morphology would indeed have to be taken into account, like local orientational properties. Several approaches have been proposed to analyze or to model labyrinthine patterns, such as the introduction of a local wave vector [35], the computation of the wrinkledness [36], and the decomposition of the pattern into clusters of linear segments [33]. To our knowledge, the definition of an appropriate order parameter for labyrinthine patterns remains an open question.

Nonetheless, aiming at quantifying some of the directly observable morphological changes of the chains, we evaluate their mean length λ as a function of ε [Fig. 4(b)]. λ is defined as the average over all chains of the largest distance between particle centers inside a given chain. Starting from $1.6a$ at the formation of first chains, λ seems to saturate for the highest values of ε around $2.6a$. This suggests that competition between growing chains could limit their extension.

The pair correlation function, which is related to the probability of finding a particle center at a given distance from another particle center, provides information on the small-scale structure of the system. Before the transition, the particle

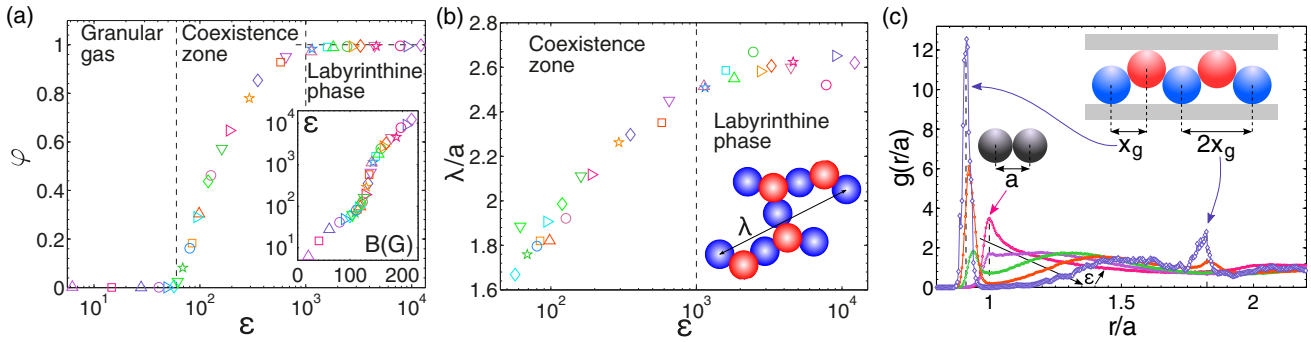

FIG. 4. (Color online) Characterizing the transition. Each symbol corresponds to an independent experiment. (a) The fraction of particles in chains φ as a function of the control parameter $\varepsilon = E_m/E_c$. It varies from about 0 in the dissipative state to 1 in the fully solidified state. The horizontal, dashed black line is a guide for the eye. Inset: ε as a function of B. (b) Adimensionalized mean chain length λ/a as a function of ε, with λ evaluated by computing the largest distance between particle centers inside a given chain. The value of λ averaged over the chains increases continuously with ε. If the averaging is weighted by the number of particles in the chains, the obtained values are larger by roughly 1 diameter unit, but the trend with ε is similar. (c) Evolution of the radial pair correlation function $g(r/a)$ for increasing values of ε (see arrow): $\varepsilon = 14.7$ (red), $\varepsilon = 41.0$ (purple), $\varepsilon = 68.9$ (green), $\varepsilon = 127$ (orange), and $\varepsilon = 649$ (blue). As the transition occurs, the $r = a$ peak of $g(r/a)$ drops down to 0, showing that the in-plane collision probability vanishes for high values of ε. In the meantime, another sharp peak appears at $r/a = x_g/a = 0.91$, which is the imprint of the buckled chains.

assembly evolves from a purely dissipative gas to an effectively more elastic gas [26]. Therefore, as Fig. 4(c) (red and purple lines) displays, the peak at the diameter value flattens while the effective elasticity rises. From the onset of solidification (green, orange, and blue lines), surprisingly, an extremely sharp peak grows from 0 at the distance value $r = x_g \approx 0.91a$, which is smaller than the particle diameter. This peak, which would be impossible to observe in purely 2D systems of hard spheres, reveals the internal structure of the chains. Here the gap size is indeed large enough so that partial overlaps of particles are allowed, leading to the formation of buckled particle chains in which particles are in contact with the top or bottom plate [see schematic in Fig. 4(c)]. Geometrical calculations yielding $x_g = \sqrt{2h\,a - h^2}$, one finds $h = 1.42$ mm, which corresponds to the announced gap of 1.5 mm diminished by the the roughness of the bottom plate. Moreover, in the labyrinthine phase (blue line), $g(r/a)$ also exhibits a shorter peak at the position $2x_g$, from the aligned second neighbors, showing the presence of linear chains. Between these two peaks, the zero probability at $x_g \lesssim r \lesssim 1.2a$ indicates the void spaces between the chains, while the nonvanishing probability for $1.2a \lesssim r \lesssim 2x_g$ stands for both nonaligned second neighbors in chains and particles from neighboring chains. The 3D effects related to the gap size h are thus essential to describe the small-scale structure of the labyrinthine phase. Therefore, we now discuss how three-dimensionality can explain the stability of the chains at a high enough area fraction.

IV. CHAIN FORMATION MECHANISM

At a low area fraction ($\phi = 0.2$ and lower), the stable state of the assembly of spheres in dipolar interaction was found to be a hexagonal crystal [26,32]. Why does the hexagonal structure now become unstable at a higher area fraction? How can we explain the formation of chains of particles in contact? In Fig. 5(a), we plot the 3D magnetic energetic landscape (in the vertical plane) for a sphere initially in the center of a hexagon of six neighboring particles, the projected horizontal distance between the particles being given geometrically by $d = a\sqrt{\pi/(2\sqrt{3}\phi)}$. Let us consider this central particle at $x = 0$ to be *up* [dashed circle in Fig. 5(a)] between six *down* neighbors, all at a distance d, and investigate its potential energy when it moves from $x = 0$ to the contact position for several values of ϕ [Fig. 5(b)]. Contact positions between spheres are local minima of potential energy, as the dipolar interaction aims to align spheres along a vertical axis. For $\phi = 0.2$, the central position is an absolute minimum of energy, in agreement with the expected stability of the hexagonal lattice. In contrast, when ϕ is increased, the energy barrier decreases and $E_m(0)$ augments relatively to $E_m(\pm d)$. For $\phi = 0.5$ contact positions become absolute minima, which can be reached by means of mechanical agitation. For $\phi = 0.6$, the central position is not even a minimum anymore. Therefore for $\phi = 0.5$ and above, we expect that the hexagonal structure is unstable, leading to local structures of spheres in contact like chains, despite the isotropic dipolar repulsion in a purely 2D system. This qualitative model explains the small-scale attraction leading to particle contacts, needed for the shaping and the stability of labyrinthine phases [8]. To improve the description, solid friction between the spheres and the top and bottom plates should be incorporated, as this may greatly stabilize the buckled chains. In thermal systems, similar predictions were obtained using Monte Carlo simulations [10–12]. In these examples and our system, the resultant of repulsive interactions of the assembly of particles over one acts as a magnetic pressure, favoring contact at a high enough particle density. Additionally, we note that buckled phases stabilized by pressure and friction can also appear in thin vibrated granular layers without magnetic interactions [37] if the density and gap size are sufficiently large [38]. Nevertheless, in the latter case, the structuring in separated chains is absent.

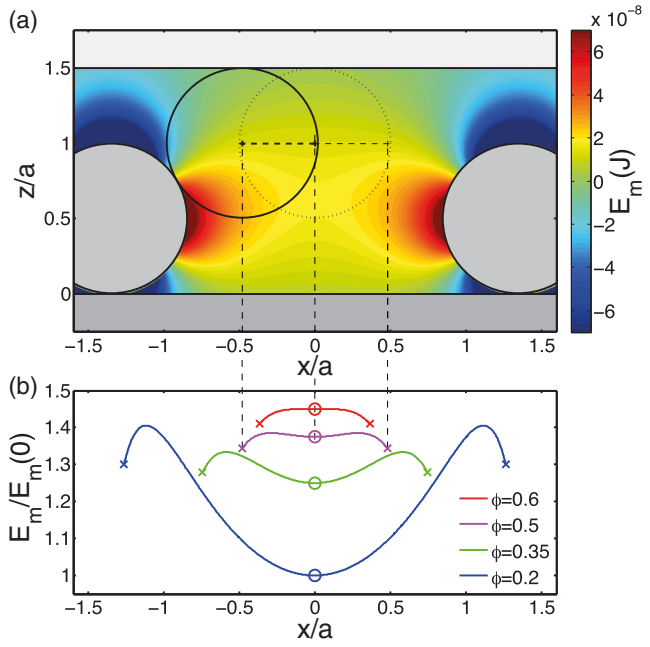

FIG. 5. (Color online) (a) The potential energy landscape E_m is computed for $\phi = 0.5$ and $B = 200$ G by averaging the pair potential U_m [see Eq. (1)] for six *down* neighbors forming a hexagon (four particles are out of the figure plane) and a central *up* particle moving along the x axis (dashed line). (b) The profile of E_m is plotted along this trajectory for four values of ϕ (curves have been rescaled and shifted vertically for clarity). The circles depict the initial central position and the crosses show the contact positions. From these graphs, for $\phi = 0.2$ and 0.35, hexagonal configurations are found to be stable, whereas for $\phi = 0.5$ and 0.6, the central particle in the presence of agitation should leave the position $x = 0$ to reach contact positions associated with buckled chains.

V. CONCLUSION

In this macroscopic and out-of-equilibrium model experiment, a labyrinthine phase is obtained by applying a magnetic field to a confined granular gas, by means of externally controlled dipolar interactions. We describe and quantitatively characterize the transition from a gas-like phase towards a globally disordered solid phase. It appears as a three-dimensional effect occurring in a quasi-two-dimensional system. The parameters setting the confinement, the gap h/a and the area fraction ϕ, are thus essential to explain the phase diagram of this granular medium, as also shown for colloidal and hard-sphere monolayers [12,16,39]. Although not presented here, after a fast increase in B, i.e., a magnetic quench, the labyrinthine phase exhibits a slow dynamics characterized by a slow evolution of its structural properties [40]. This aging phenomenon should thus be compared to the slow dynamics of structural glasses [41–43]. In the case of labyrinthine domain patterns arising in continuous systems, the analogy with glasses was also reported in an analysis of their globally disordered structure [33] and a study of their relaxation [36]. Finally, whereas the structure of the phases obtained in this macroscopic experiment resembles that of the phases found at thermal equilibrium in Monte Carlo simulations and colloidal monolayers [12,16,44], the kinetics of the transition described here is intrinsically an out-of-equilibrium process, which deserves further studies.

ACKNOWLEDGMENTS

The authors would like to thank Leonardo Gordillo, Jean-Claude Bacri, and Nicolas Vandewalle for discussions and Vincent Dupuis for performance of particle magnetization measurements. This work was supported by Université Paris Diderot and by the European Space Agency No. 4000103461CCN (Topical Team on granular materials).

APPENDIX A: POTENTIAL MAGNETIC ENERGY FOR TWO PARALLEL DIPOLES WITH FINITE MAGNETIC PERMEABILITY

For two ferromagnetic spheres of identical diameter a immersed in an unidirectional vertical magnetic field of intensity B and separated by a distance r, the potential energy of magnetic interaction reads in spherical coordinates as the interaction of two vertical magnetic dipoles [28],

$$U_m(r,\theta) = -\frac{\pi}{16}\frac{B^2}{\mu_0}\frac{a^6}{r^3}\left(\frac{\mu-\mu_0}{\mu+2\mu_0}\right)^2(2\cos^2\theta - \sin^2\theta), \tag{A1}$$

where θ is the polar angle between the two dipoles, $\mu_0 = 4\pi\,10^{-7}$ H $\cdot$ m^{-1} is the vacuum permeability, and μ is the intrinsic magnetic permeability of the sphere material. The induced magnetic fields of the neighboring particles are assumed negligible in front of the external magnetic field. For free-moving particles θ is taken equal to $\pi/2$, whereas for particles belonging to chains θ is computed from the measured vertical position of the particles (top or bottom). The magnetic potential energy per particle E_m is computed as an average of U_m over interacting pairs of particles [26] and in the limit of large μ. This approximation holds for soft and linear ferromagnetic materials [45], which is the case for our particles.

APPENDIX B: GENERATION OF THE VIBRATED AND INTERACTING SYSTEM OF PARTICLES

The particles are chromed alloy steel (AISI 52100) spheres of diameter $a = 1$ mm and of mass $m = 4.07 \times 10^{-3}$ g. Using a vibrating sample magnetometer, the magnetization of one particle was measured by V. Dupuis. The magnetic permeability μ verifies $122 < \mu/\mu_0 < \infty$ in the linear domain ($-2000\,\mathrm{G} < B < +2000\,\mathrm{G}$), and the remnant magnetic field B_r is below 12 G. The coercive field is small compared with the values of the magnetic field B used in our experiments. Within this range of B, the response to magnetic excitation is linear. The square aluminum cell (side, 9 cm long) containing these particles (see Fig. 1) is vertically driven by an electromagnetic shaker. The forcing is sinusoidal at the frequency $f_0 = 300$ Hz and the root mean square (RMS) acceleration of vibration is fixed at $\Gamma = 21.9\ \mathrm{m}\cdot\mathrm{s}^{-2} = 2.23g$ for all experiments, with g the gravity acceleration. This value corresponds to the upper limit of the linear response domain of the granular temperature $T_g = E_c/m$ as a function of Γ [21]. Two coils in Helmholtz configuration and current-controlled generate a nearly homogeneous magnetic field B across the cell (the measured variation is of 3%). Immersed in this magnetic field,

the particles are magnetized into induced dipoles vertically oriented (the particle rotation velocity is negligible compared with the speed of the magnetic domain rearrangements).

APPENDIX C: PARTICLE DETECTION

An annular LED array above the cell produces a high-contrast circular signal on the chromed particles, whose positions are recorded from above using a high-speed video camera at a high resolution (1152×1152 pixels at 780 Hz). The region of interest S is 5.7×5.7 cm^2 around the cell center (see Fig. 1). The particle diameter is about 20 pixels. For individual particle detection, we used a convolution-based least-squares fitting routine [21,46] completed by an intensity-weighted center detection algorithm (accuracy estimated as smaller than 0.3 pixel). Particle trajectories were reconstructed using a tracking algorithm [27,47].

APPENDIX D: EXPERIMENTAL PROTOCOL

The experimental protocol is fully automated for the sake of robustness. Every single experiment is noncorrelated with the others. The amplifiers of the electromagnetic shaker and of the Helmholtz coils are computer controlled via a data acquisition card. The experimental protocol routine is written in Matlab. It also proceeds to the dialogue with the camera, i.e., configuring and starting the video recordings, as well as to the recording of the data from the accelerometer and the Hall effect sensor. All experiments are performed according to the following protocol. First, the shaking is activated ($\Gamma = 21.9$ m $\cdot$ s^{-2}) while the magnetic field remains 0. The magnetic field is then linearly increased (the rising rate $\alpha_q \equiv \mathrm{d}B/\mathrm{d}t$ is kept fixed for all experiments) up to its higher plateau value B. Afterwards, a waiting time is respected prior to proceeding to the recordings. It is chosen along with the recording time length so as to reach the chosen mean aging time τ_w. In all the experiments presented here, $\alpha_q = 1$ G $\cdot$ s^{-1}, $\tau_w = 30$ s, and recordings last at least 2 s. Note that these two parameters, α_q and τ_w, have a noticeable influence on the nature of the labyrinthine state reached for high values of B, implying that a slow dynamics is at play.

For the 5000 particles introduced in the experiments, the area fraction evaluated on the cell is equal to 0.485. However, within the region of interest S, as the boundaries are not repulsive [26], ϕ decreases from 0.58 to 0.46 with B until $B \approx 80$ G. From the appearance of the first chains, ϕ remains nearly constant.

[1] M. Seul, L. Monar, L. O'Gorman, and R. Wolfe, Science **254**, 1616 (1991).
[2] M. Seul and M. J. Sammon, Phys. Rev. Lett. **64**, 1903 (1990).
[3] B. Sandnes, H. A. Knudsen, K. J. Måløy, and E. G. Flekkøy, Phys. Rev. Lett. **99**, 038001 (2007).
[4] B. Sandnes, E. G. Flekkøy, H. A. Knudsen, K. J. Måløy, and H. See, Nat. Commun. **2**, 288 (2011).
[5] A. Dickstein, S. Erramilli, R. E. Goldstein, D. P. Jackson, and S. A. Langer, Science **261**, 1012 (1993).
[6] F. Elias, C. Flament, J. C. Bacri, and S. Neveu, J. Phys. I France **7**, 711 (1997).
[7] K. J. Lee and H. L. Swinney, Phys. Rev. E **51**, 1899 (1995).
[8] M. Seul and D. Andelman, Science **267**, 476 (1995).
[9] K. De'Bell, A. B. MacIsaac, and J. Whitehead, Rev. Mod. Phys. **72**, 225 (2000).
[10] G. Malescio and G. Pellicane, Nat. Mater. **2**, 97 (2003).
[11] P. Camp, Phys. Rev. E **68**, 061506 (2003).
[12] J. Dobnikar, J. Fornleitner, and G. Kahl, J. Phys.: Condens. Matter **20**, 494220 (2008).
[13] Y. Shokef and T. C. Lubensky, Phys. Rev. Lett. **102**, 048303 (2009).
[14] M. D. Haw, Phys. Rev. E **81**, 031402 (2010).
[15] Y. Han, Y. Shokef, A. M. Alsayed, P. Yunker, T. C. Lubensky, and A. G. Yodh, Nature **456**, 898 (2008).
[16] N. Osterman, D. Babič, I. Poberaj, J. Dobnikar, and P. Ziherl, Phys. Rev. Lett. **99**, 248301 (2007).
[17] J. S. Olafsen and J. S. Urbach, Phys. Rev. Lett. **81**, 4369 (1998).
[18] J. S. Olafsen and J. S. Urbach, Phys. Rev. E **60**, R2468(R) (1999).
[19] W. Losert, D. G. W. Cooper, J. Delour, A. Kudrolli, and J. P. Gollub, Chaos **9**, 682 (1999).
[20] S. J. Moon, M. D. Shattuck, and J. B. Swift, Phys. Rev. E. **64**, 031303 (2001).
[21] P. M. Reis, R. A. Ingale, and M. D. Shattuck, Phys. Rev. E **75**, 051311 (2007).
[22] H. M. Jaeger, S. R. Nagel, and R. P. Behringer, Rev. Mod. Phys. **68**, 1259 (1996).
[23] D. L. Blair and A. Kudrolli, Phys. Rev. E **67**, 021302 (2003).
[24] A. Snezhko, I. S. Aranson, and W.-K. Kwok, Phys. Rev. Lett. **94**, 108002 (2005).
[25] L. Oyarte, P. Gutiérrez, S. Aumaître, and N. Mujica, Phys. Rev. E **87**, 022204 (2013).
[26] S. Merminod, M. Berhanu, and E. Falcon, Europhys. Lett. **106**, 44005 (2014).
[27] J. C. Crocker and D. G. Grier, J. Colloid Interface Sci. **179**, 298 (1996).
[28] J. D. Jackson, *Classical Electrodynamics*, 3rd ed. (Wiley, New York, 1998).
[29] See Appendix A for complements to the formula of U_m.
[30] C. Laroche and F. Pétrélis, Eur. Phys. J. B **77**, 489 (2010).
[31] D. Lopez and F. Pétrélis, Phys. Rev. Lett. **104**, 158001 (2010).
[32] J. Schockmel, E. Mersch, N. Vandewalle, and G. Lumay, Phys. Rev. E **87**, 062201 (2013).
[33] M. Seul, L. Monar, and L. O'Gorman, Philos. Mag. B **66**, 471 (1992).
[34] See Supplemental Material at http://link.aps.org/supplemental/10.1103/PhysRevE.92.062205 for a video of the transition.
[35] M. Le Berre, E. Ressayre, A. Tallet, Y. Pomeau, and L. Di Menza, Phys. Rev. E **66**, 026203 (2002).
[36] B. Reimann, R. Richter, and I. Rehberg, Phys. Rev. E **65**, 031504 (2002).

[37] P. Melby, F. V. Reyes, A. Prevost, R. Robertson, P. Kumar, D. A. Egolf, and J. S. Urbach, J. Phys.: Condens. Matter **17**, S2689 (2005).
[38] In our cell with $h = 1.5a$, the total number of particles should be larger than 9477 for such a buckled state to be observed [37].
[39] M. Schmidt and H. Löwen, Phys. Rev. E **55**, 7228 (1997).
[40] The slow dynamics reported in some attractive granular gases [23,25] results from a cluster growth process and should not be described as an aging phenomenon.
[41] J. Barrat and J. Hansen, *Basic Concepts for Simple and Complex Liquids* (Cambridge University Press, Cambridge, UK, 2003).
[42] G. L. Hunter and E. R. Weeks, Rep. Prog. Phys. **75**, 066501 (2012).
[43] F. H. Stillinger and P. G. Debenedetti, Annu. Rev. Condens. Matter Phys. **4**, 263 (2013).
[44] R. Messina, S. Aljawhari, L. Bécu, J. Schockmel, G. Lumay, and N. Vandewalle, Sci. Rep. **5**, 10348 (2015).
[45] A. Mehdizadeh, R. Mei, J. Klausner, and N. Rahmatian, Acta Mech. Sin. **26**, 921 (2010).
[46] M. D. Shattuck, Particle tracking. Available at: gibbs.engr.ccny.cuny.edu/technical/Tracking/ChiTrack.php; accessed 18 April 2013.
[47] J. C. Crocker and E. R. Weeks, Particle tracking using idl. Available at: www.physics.emory.edu/faculty/weeks/idl/; accessed: 18 April 2013.

5.5 Discussion of the validity of the energetic model

Here, we discuss the simple model presented in our *Physical Review E* article [2] and also explained in Section 5.3. We question the relevance of the choice of 6 neighbors, in the hexagonal configuration described above, and the validity of this approach itself, in particular in regard of the effect of the gap size on the potential interaction energies.

Let us first define the geometry of the problem we consider in this section. As in the article, we consider one test particle initially positioned at the origin of the (x, y) frame and touching the top plate [dashed black circle in Fig. 5.4(a, b)]. We move this particle to contact with its first neighbor along the x-axis, which is considered touching the bottom plate ($z = a/2$) and horizontally positioned at ($x = d, y = 0$), with d the node-to-node distance of a triangular lattice of particle area fraction ϕ, namely $d = a\left[\pi/(2\sqrt{3}\phi)\right]^{1/2}$. In Fig. 5.4(a, b), the test particle in its final position is represented by the plain black circle, and the first neighbor, by the blue circle.

Now, we consider a varying number of particles surrounding the test particle, n_v, placed at the nodes of a triangular lattice of side d, as shown in Fig. 5.4(a). All surrounding particles except the one at ($x = d, y = 0$) are taken at a mid-gap altitude, namely $z = e/2$. We consider the cases $n_v = 1, 6, 13, 29, 51, 79, 113$. For $n_v = 1$, only the particle at ($x = d, y = 0$) is considered; for $n_v = 6$, as in the article we consider the 6 particles at the nodes of a regular hexagon of side d surrounding the initial position of the test particle [innermost hexagon and blue circles in Fig. 5.4(a)]; for $n_v = 13$, we consider all the particles inside the first larger non-regular hexagon, whose particles are drawn in a darker shade of blue in Fig. 5.4(a), which includes the particles of the hexagon of $n_v = 6$; the case $n_v = 29$ includes all particles within the hexagon surrounding the ensemble of $n_v = 13$ particles; and so on for $n_v = 51, 79$, and 113.

As in Chapter 3, we denote $E_p^{\mathrm{mag}}(r_i, \theta_i)$ the magnetic energy of interaction of the test particle and neighboring particle i, where r_i (resp. θ_i) is the center-to-center distance (polar angle) between the test particle and particle i, as defined in Fig. 3.3. The formula of $E_p^{\mathrm{mag}}(r, \theta)$ is given in Eq. 3.42 (note that gravity here is not considered since the test particle remains at a fixed altitude, namely $z = e - a/2$). Note that $E_p^{\mathrm{mag}}(r, \theta)$ is denoted $U_m(r, \theta)$ in the article.

The total magnetic energy of interaction of the test particle when it has n_v neighbors, $E_p^{n=n_v}$, is the sum over the n_v neighbors of the magnetic energies $E_p^{\mathrm{mag}}(r_i, \theta_i)$, with $i = 1, ..., n_v$,

$$E_p^{n=n_v} = \sum_{i=1}^{n_v} E_p^{\mathrm{mag}}(r_i, \theta_i). \tag{5.1}$$

Let us now go back to the article. The approach that we presented in it is based on the local and global minima of magnetic energy of interaction for the test particle moving in the hexagon formed by the closer neighbors ($n_v = 6$). If this approach can be convincing for the gap size $e = 1.5\,a$ chosen for the discussion in the paper (FIG. 5 in the article), unfortunately, it does not explain the existence of a labyrinthine phase when the gap size, e, is smaller than the critical value, $e_x = a\,(1/\sqrt{5} + 1) \sim 1.45\,a$ (Eq. 3.53). Indeed, for $e < e_x$, the horizontal force between two particles in the *buckled* configuration, denoted F_x in Chapter 3, is repulsive and thus this configuration is not stable, as evidenced by the stability diagram in Fig. 3.8. In other words, the pair potential does not present any local minimum of energy at contact for $e < e_x$. We show as an example the pair potential, $E_p^{n=1}$, relative to the experiments presented in the article (gap size $e = 1.42\,a$ and particle area fraction $\phi = 0.47$), in Fig. 5.5(a) (black curve). Now considering the $n_v = 6$ first neighbors of the test particle, as in the article, yields $E_p^{n=6}$ [blue curve in Fig. 5.5(a)], which does not present a local minimum at contact either. Moreover, this

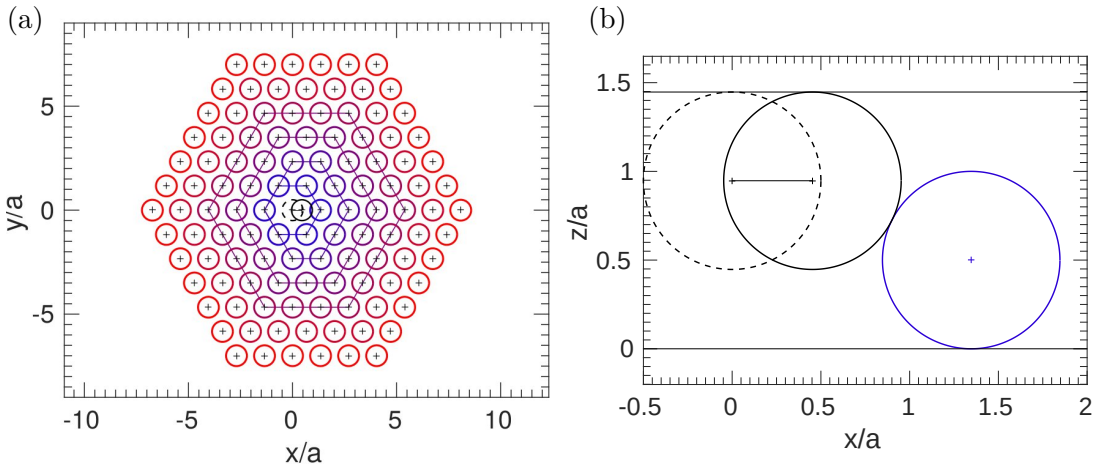

Figure 5.4 Geometry of the problem. (a) Top view. The colors from blue to red (and the hexagons drawn in grey lines) identify the outer limit of the ensembles of particles used for the computation of the magnetic energy (more details are given in the main text); (b) Side view. The test particle moves from the initial central position (dashed black circle) to contact position (plain black circle) with its first neighbor along the x-axis (plain blue circle). These schematics are draws on the example of $\phi = 0.5$ and gap size $e/a = 1.5$.

curve shows how the magnetic pressure from the surrounding particles decreases the potential energy barrier between the central and contact positions, relative to the energy at the initial position, $E_p^{n=6}(x = 0)$. The fact that neither of these curves presents a local minimum of energy at contact should prevent the formation of a labyrinthine phase, according to our simple model. However, we do observe such a phase, hence we should reconsider our reasoning.

To start with, we can question the choice of $n_v = 6$ particles for representing the total energy of interaction of the test particle. How is this energy changed when additional neighbors are considered? The curves of $E_p^{n=n_v}$ for $n_v = 13, 29, 51, 79$ and 113 are plotted in Fig. 5.5(b), for the particle area fraction measured at the transition in the experiments of this chapter, namely $\phi = 0.47$. We observe that the curve of $E_p^{n=6}$ is below the curves of $E_p^{n>6}$, and that its shape is slightly different from the others. In particular, the former seems to reach a plateau at contact, although this is not the case for the latter. This indicates that the asymmetry of the hexagonal configuration of the $n_v = 6$ neighbors, relative to the trajectory of the test particle, visibly modifies the shape of the energy landscape. For $n_v \geq 13$ this asymmetry is reduced and the shape of $E_p^{n>13}$ is much more similar to $E_p^{n=1}$, although the energy variations are reduced. This shows that the magnetic pressure from all surrounding particles acts as a mean field, when particles are distributed homogeneously around the test particle trajectory. Increasing further n_v, from 13 to 113, makes the curves of $E_p^{n=n_v}$ apparently converge towards a limit curve. This convergence indicates that the mean field effect from particles beyond the hexagon of $n_v = 113$ would have approximatively no effect on the test particle. This provides a relevant limit distance for the computation of the magnetic energy of interaction, namely approximatively $7\,a$. This result is close to $10\,a$, which is the distance that we use for our calculation of E_m, as explained in Section 2.2.3. More generally, we can say that the choice of $n_v = 6$ neighbors is not optimal for computing the energy landscape, and that replacing it by $n_v = 113$ seems satisfying.

As an other example, we take the gap size used in the experiments of Chapter 6, namely $e/a = 1.48$, the particle area fraction then measured at the transition, $\phi = 0.44$, and plot $E_p^{n=n_v}$ for $n_v = 6, 13, 29, 51, 79$ and 113 in Fig. 5.6. In this case, using $n_v = 6$ suggests that

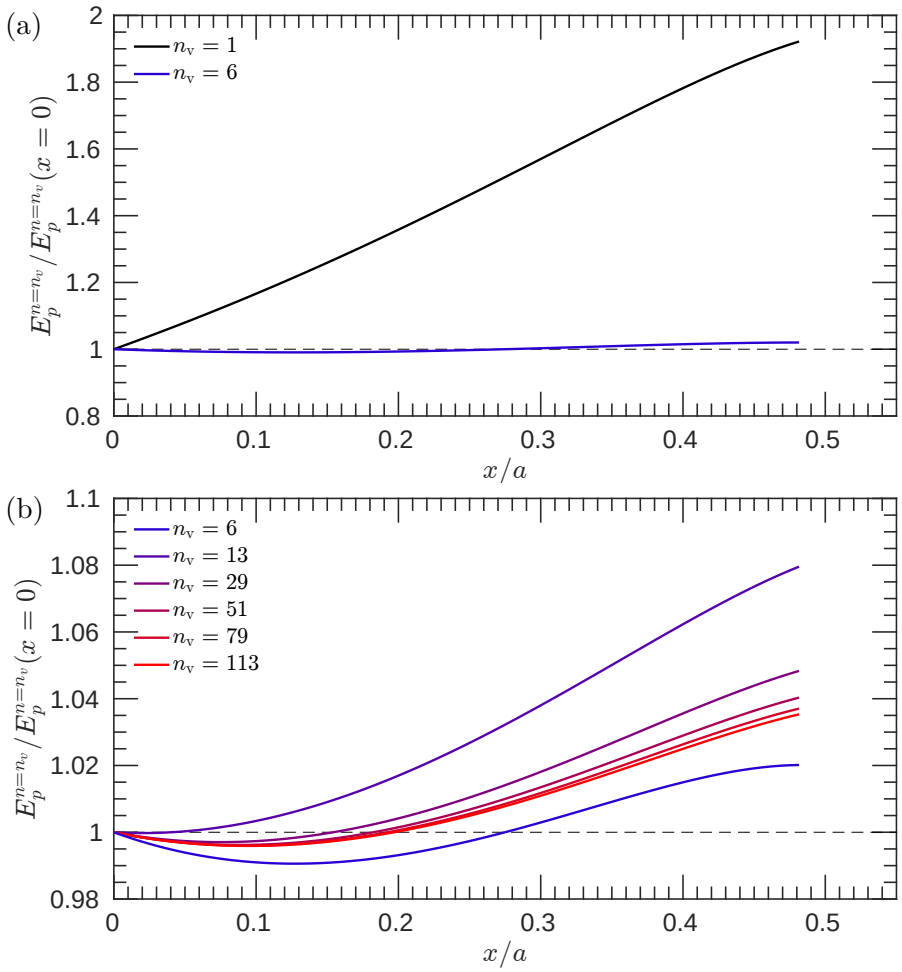

Figure 5.5 Potential energies of interaction, $E_p^{n=n_v}$, for $\phi = 0.47$ and $e/a = 1.42$, as in the article of this chapter. (a) $n_v = 1$ and 6; and (b) $n_v \geq 6$. The magnetic pressure from the neighbors acts as a mean field which reduces the relative variations on $E_p^{n=n_v}$ relative to the value at contact. In particular, (b) shows that typically $n_v = 113$ neighbors should be used to estimate the potential energy of interaction.

the potential is nearly purely attractive with a global minimum of energy at contact, while the curves of $n_v > 6$ show an attraction at short distances only, with a local minimum of energy at contact. This supports the choice of typically $n_v = 113$ particles for estimating the potential energies of interaction.

Let us also note that the existence of local minima of energy along the trajectories (*i.e.*, for $0 < x < a$), which we find on most curves in Fig. 5.5 and Fig. 5.6, is due to the fact that the first neighbor along the x-axis, drawn in blue in Fig. 5.4(b), is taken in contact with the bottom plate, unlike all the other neighbors, which are vertically taken at mid-gap. Indeed, this induces a breakup of the left-right symmetry in our problem.

Now, as the curve of $E_p^{n=113}$ in Fig. 5.5(b) makes clear, there is no local minimum of energy at contact when the gap size is $e/a = 1.42 < e_x/a$ (and $\phi = 0.47$). How can we explain the formation of chains in this experiments? We suggest that one should consider that friction plays an important role in the stabilization of the chains. Indeed, while the potential energy of interaction does not show any minimum at contact, this position may be stable anyway thanks

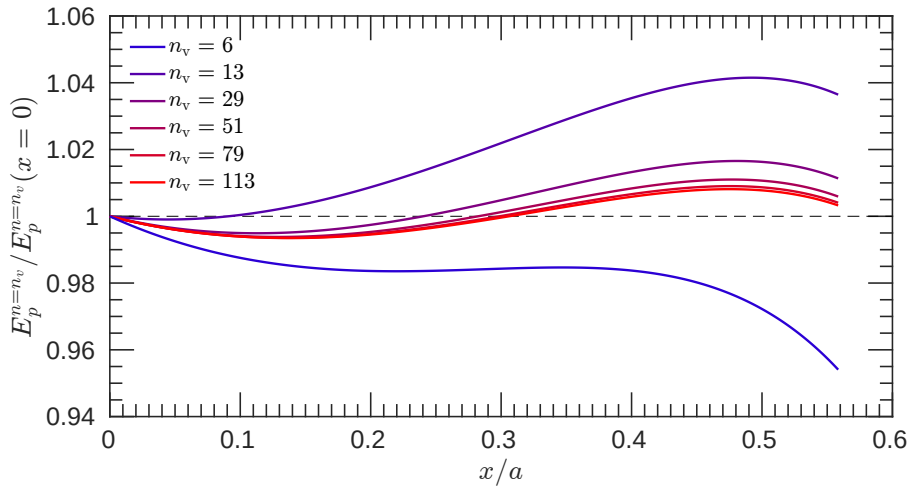

Figure 5.6 Potential energies of interaction, $E_p^{n=n_v}$, for $\phi = 0.44$ and $e/a = 1.48$, as in the experiments of Chapter 6.

to friction. Therefore, instead of considering *local* and *global* minimum of energy, it may be more relevant to consider the *barrier of energy* between the initial central position and the contact position, which we call ΔE_n and define as

$$\Delta E_n = \max\left[E_p^{n=113}(x>0)\right] - E_p^{n=113}(x=0), \tag{5.2}$$

if $E_p^{n=113}(x = x_{\max})$, with $x_{\max}$ the value of x at contact, is larger than the potential energy at the central position $E_p^{n=113}(x=0)$; else, *i.e.*, when $E_p^{n=113}(x = x_{\max}) < E_p^{n=113}(x=0)$, the particles attract each other and we consider ΔE_n as irrelevant. Although we have no final word on the question, we suggest that ΔE_n may be the relevant energy scale to compare with kinetic energy for understanding the chain formation process, as we discuss below.

Before this, let us study the effect of particle area fraction on the potential energies of interaction. In Fig. 5.7, we show the profiles of $E_p^{n=113}$ reduced by $E_p^{n=113}(x=0)$ for increasing area fractions, ϕ, and gap sizes of $e/a = 1.42$, as in the current chapter [Fig. 5.7(a)], $e/a = e_x/a$ [Fig. 5.7(b)], and $e/a = 1.48$, which corresponds to the experiments of Chapter 6 [Fig. 5.7(c)]. We find that at low density, typically $\phi = 0.2$, the energy landscape looks very similar to the pair potential; indeed then the effects from the neighbors are minimized. As we increase the particle are fraction, the intensity of the magnetic pressure from the neighbors augments. Then, the energy profile becomes more flat. Very interestingly, for all the gap values studied here, there exists a value of ϕ for which the interaction become *attractive*, although at lower ϕ it was *repulsive*. Then, there is no more energy barrier to overcome to go from the central position to the contact position.

We make this clear by plotting, in Fig. 5.8, the values of energy barriers, ΔE_n, as a function of the particle area fraction, ϕ, for the same three gap values. As could be qualitatively seen in Fig. 5.7, we find that the energy barrier ΔE_n decreases with ϕ, and vanishes from a value of ϕ proper to each gap value. Interestingly, for the experiments of this chapter, the mean kinetic energy per particle at the transition is about $E_c \sim 6 \times 10^{-10}$ J, and we find in Fig. 5.8(a) a corresponding energy barrier, *i.e.*, for $\phi = 0.47$, of $\Delta E_n \sim 2 \times 10^{-9}$ J, which is about three times higher but of the same order of magnitude. For the experiments of Chapter 6, for which $\phi \sim 0.44$, we measure at the transition $E_c \sim 4 \times 10^{-10}$ J, and we find in Fig. 5.8(c) $\Delta E_n \sim 4 \times 10^{-10}$ J too.

Then, the energy barrier ΔE_n is found of the same order of magnitude or even almost equal to the experimentally measured mean kinetic energy per particles at the transition to labyrinthine phase.

To summarize, the energy barrier ΔE_n, which we defined for $e < e_x$ (as long as the potential energy of interaction at contact is higher than at the central position), seems to be the relevant energy scale to be compared to the kinetic energy, and to discuss the transition from a collisionless state, like the crystalline state, to a phase with particles at contact, like the labyrinthine phase. We conclude that a proper theoretical study is needed for capturing the complete picture of the problem. Note that, in particular, considering vertical displacements in the trajectories of the test particle and of the other particles would be more realistic.

As a final word on this chapter, and supporting our explaination that labyrinthine phases can exist for gap size smaller than the critical value e_x, we show in Fig. 5.9 the results of experiments carried out for gap sizes ranging from $e/a = 1.28$ to $e/a = 1.78$, hence well below and well above the critical gap, with the circular cell. The fraction of particles in chains, φ, is plotted as a function of the magnetic field, B_0, for the 6 gap values. We observe that, whatever the gap size, we can always find a value of the applied magnetic field from which particles start to self-organize into chains.

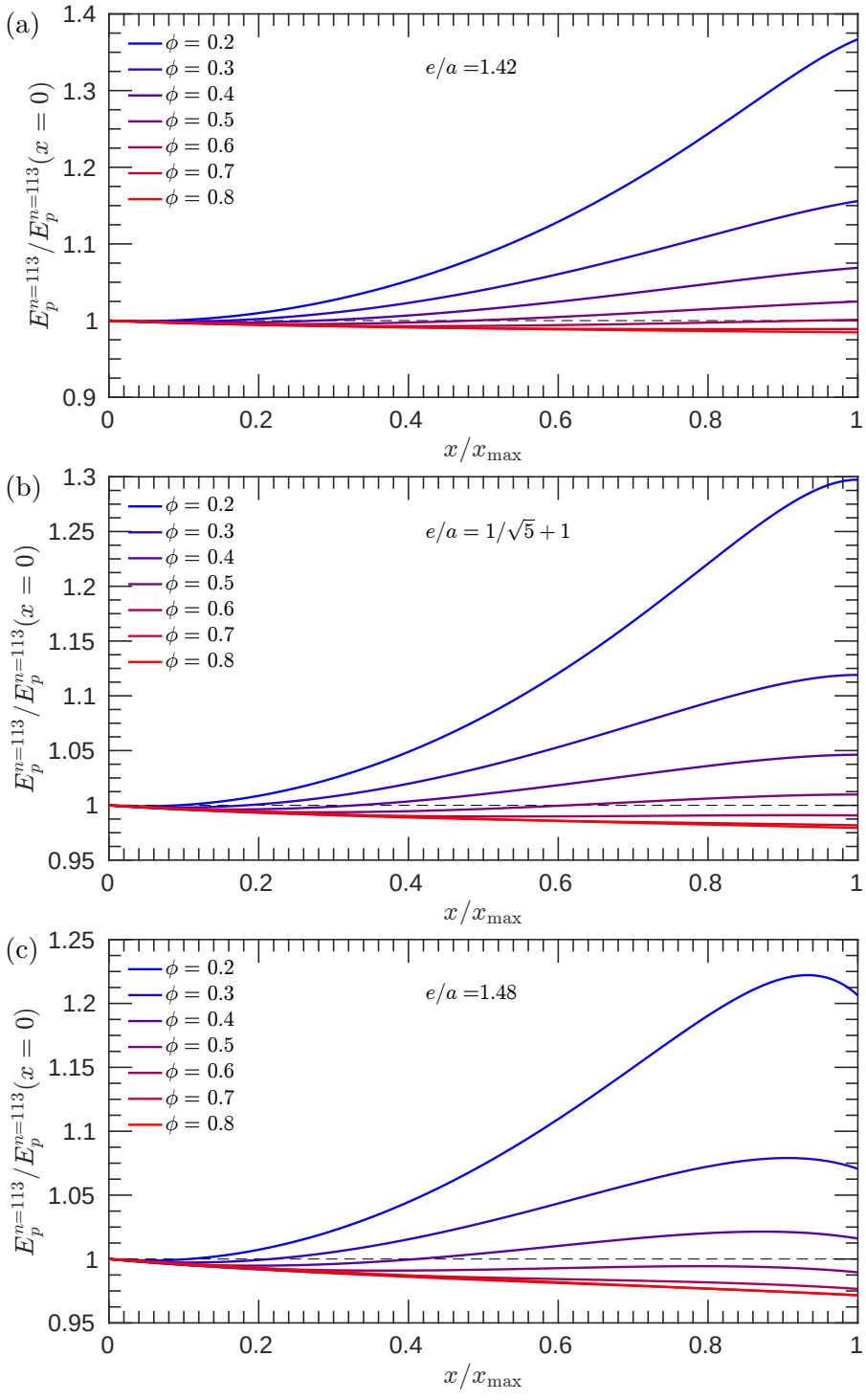

Figure 5.7 Profiles of potential magnetic energy computed with $n_v = 113$, $E_p^{n=113}$, reduced by $E_p^{n=113}(x = 0)$, as a function of the distance to the central position normalized by its value at contact, $x/x_{\max}$, for particle are fraction ϕ between 0.2 and 0.8, and for a gap size of (a) $e/a = 1.42$ (as in the experiments of the current chapter; (b) $e/a = 1/\sqrt{5} + 1$ (critical gap size; and (c) $e/a = 1.48$ (as in the experiments of Chapter 6). Whatever the shape of the potential at low ϕ, when ϕ is high enough, no more barrier exists between the central position and the contact position; the two particles are attracted towards each other.

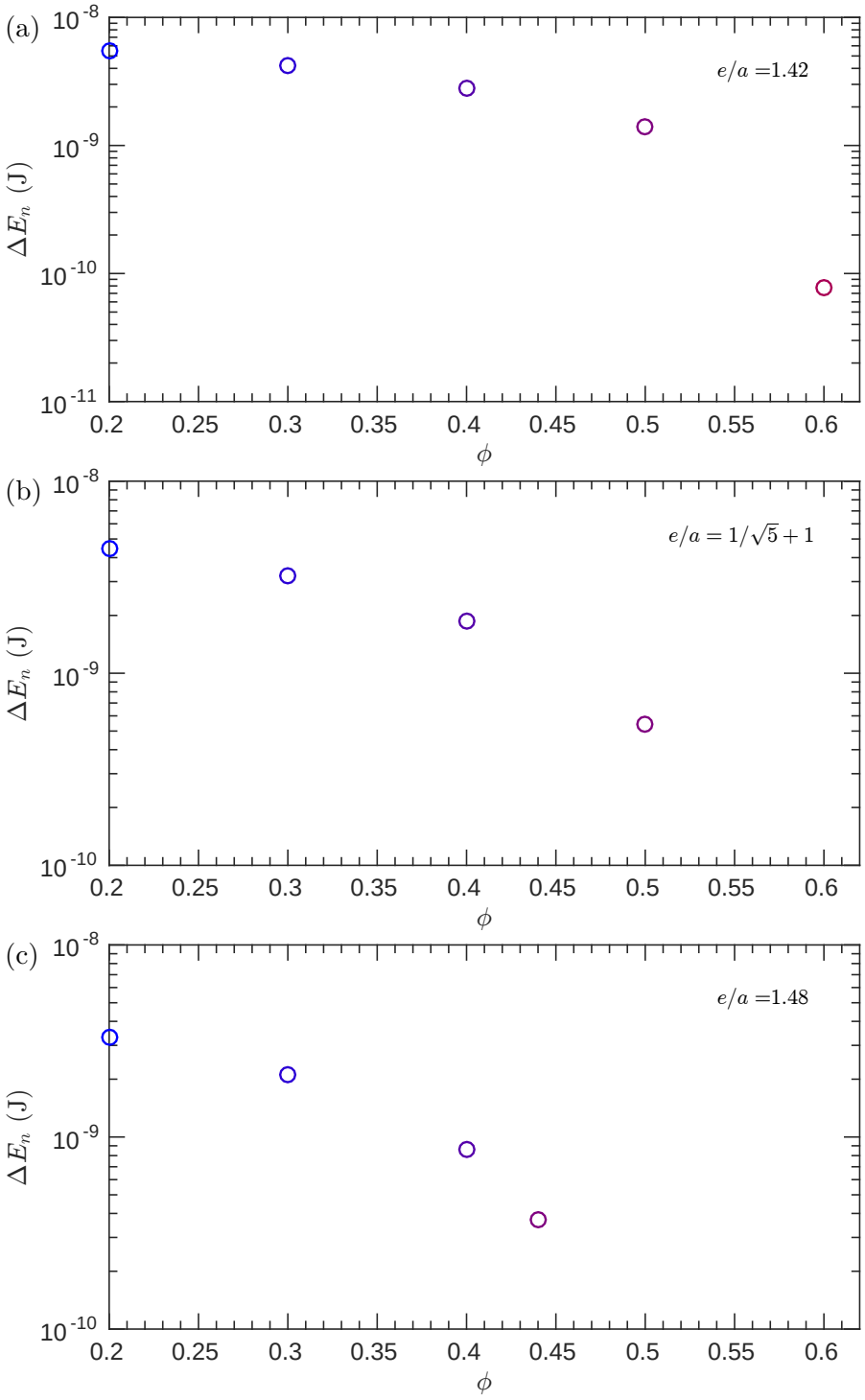

Figure 5.8 Barrier of potential energy between the central position and the contact position, ΔE_n, as a function of the particle area fraction, ϕ, for $B_0 = 100\,\mathrm{G}$ and for a gap size of (a) $e/a = 1.42$; (b) $e/a = 1/\sqrt{5}+1$; and (c) $e/a = 1.48$. When the potential energy at contact is larger than the potential energy at the central position, $\Delta E_n = \max\left[E_p^{n=113}(x>0)\right] - E_p^{n=113}(x=0)$; otherwise the particles attract each other and we consider ΔE_n as irrelevant. The energy barrier ΔE_n decreases with ϕ, until it vanishes for ϕ high enough, namely $\phi = 0.7$ (a), $\phi = 0.6$ (b), and $\phi = 0.5$ (c). The values of ΔE_n are found of the same order of magnitude than the values of mean kinetic energy in the related experiments, at the transition threshold, suggesting that ΔE_n is the relevant potential energy scale in the problem.

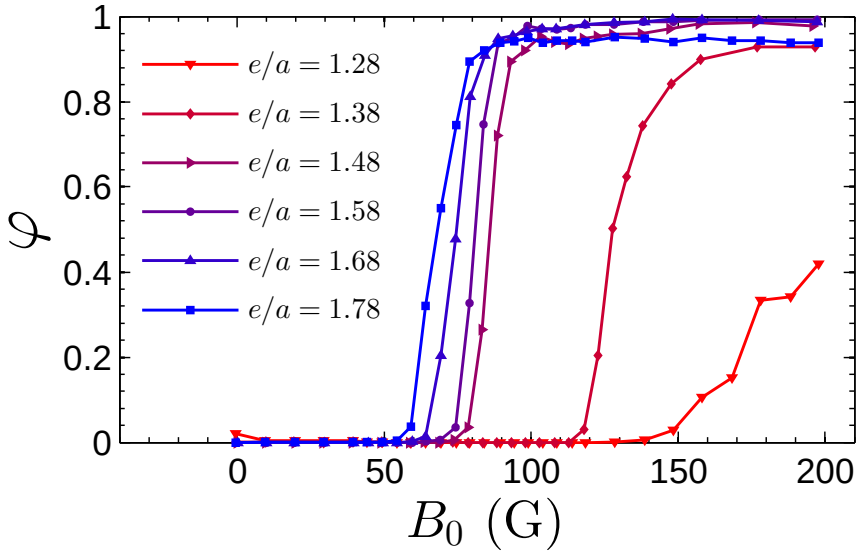

Figure 5.9 Creating chains even at very low gap sizes. Fraction of particles in chains, φ, as a function of B_0 for gap sizes ranging from $e = 1.28\,a$ to $e = 1.78\,a$, for $\phi \sim 0.36$, with the circular cell. Even though the critical values of B_0 at which the transition to the labyrinthine phase starts, *i.e.*, when $\varphi > 0$, increases as the gap size decreases, in all the experiments presented here, it is possible to make particle self-organize into chains.

Chapter 6

Temporal evolution of the labyrinthine phase

Chapter 6 : Temporal evolution of the labyrinthine phase

↑ back to contents

Chapter abstract

Labyrinthine phases are disordered, metastable states. As such, we can expect them to depend strongly on the processing pathway used to generate them, and to be unsteady states. Yet, surprisingly, only very few studies have focused on the time evolution of labyrinthine phases [103, 110], and most questions regarding this aspect remain unanswered. In this chapter, we demonstrate that a "magnetic quench" can be applied to the granular liquid-like state (mentioned in Chapter 4 and Chapter 5) to generate a highly disordered granular labyrinthine phase. We show that the relaxation of the latter involves different processes at short and at long times. We demonstrate that, at short times, free particles aggregate into mostly short, unbranched chains, and we detect no major chain rearrangements. In contrast, we show that at long times, nucleation continues much more slowly, and the dominant process is, for high enough values of the magnetic field, the rearrangement and the merging of chains into large, highly branched clusters; in other words, there is coarsening of the labyrinthine phase.

6.1 Introduction

Labyrinthine phases are disordered states: if in such phases a well-defined structure exists at short range, it disappears at long range. In thermal systems, disordered states are typically obtained by cooling a sample faster than nucleation can occur: then, particles do not have enough time to organize into a crystal, and a disordered structure is obtained. The resulting states, called

supercooled liquids, relax slowly through metastable states towards equilibrium: then, measured properties change with time [112]. Moreover, they display anomalously high viscosities and relaxation time scales, dynamical heterogeneities and caging effects. Analogous disordered states can be obtained in colloidal systems, where density plays the role of temperature in microscopic systems, that is, "supercooling" is then performed by abruptly increasing density [108]. In view of this, it is reasonable to ask: Do labyrinthine phases, which are disordered and can be made of microscopic constituents, colloids, or granular materials, display slow dynamics?

Surprisingly, if labyrinthine phases considered as steady states have been the subject of a large number of studies both on continuous systems and on systems of particles (see the introduction of Chapter 5), works devoted to the exploration of the time evolution of labyrinthine phases are scarce.

In fact, for systems with short-range attraction and long-range repulsion, we are only aware of two articles. Riemann *et al.* [110] obtained labyrinthine magnetic domain patterns in a ferrimagnetic garnet film initially magnetized, then rapidly subjected to a demagnetizing field. They characterized the dynamics of the relaxation of the pattern by means of a measure of the pattern borderline curvature, and found that it relaxes as a stretched exponential Kohlrausch-Williams-Watt law [113], which is a typical relaxation law for microscopically disordered systems exhibiting a slow dynamics.

More recently, Haw [103] studied numerically a system of particles with short-range attraction and long-range repulsion, using an algorithm of type molecular dynamics. The evolution of the number of clusters with numerical steps, which he considers analogous to real time, displays a slow logarithmic decay at long "times". Interpreting this logarithmic coarsening as arising from random walks of chains in the rough energy landscape created by their neighbors, he proposes viewing the aging labyrinthine phase as a "glass of chains".

6.2 Motivation

This suggests that relaxation occurs in labyrinthine phases in a way that may be analogous to relaxation in glassy systems. However, a more complete exploration of the aging process, based on the study of various relevant structural and dynamical quantities at both very short and very long times is still lacking. One idea would be to use colloids, which form labyrinthine phases very similar to those that we observe in our granular labyrinthine phase [106, 65], but this would require extremely accurate control over the density and temperature over long time scales. Moreover, quenching colloidal systems (*i.e.*, increasing the density fast) in a well-controlled manner is not easily done. Numerical simulations are confronted with the very rough nature of the potential energy landscape in which labyrinthine phases live, which makes exploring the long-time aging of such phases numerically too costly to be reliable, although it has been attempted by Haw [103]. Our granular system appears to be well fitted to the task: using a high-speed video camera for particle tracking, we can access particle positions and velocities, and hence both structural and dynamical properties, at any time from very short to very long. Most importantly, a crucial difference with colloidal systems is that thermal fluctuations are negligible in granular systems, which makes them much more easy to manipulate.

In this chapter, we aim at, first, evaluating the impact of a strong quench on the nature of the disorder in the resulting granular labyrinthine phase. Then, we will explore the time evolution of the structural and dynamical features of the labyrinthine phase, from the first moment after

the quench to very long times, by means of particle tracking. We will investigate separately each time scale associated with a particular process.

This chapter logically follows the work presented in Chapter 5: then, we did not address the question of the time evolution of the granular labyrinthine phase, which was relevant in the range of parameters then used; now, we go beyond this simplified picture and consider the granular labyrinthine phase more generally, as a disordered system which slowly relaxes.

6.3 A disordered system which slowly relaxes

In this section, we aim at finely characterizing the structure of the labyrinthine phases which we observe in our magnetic granular system, like those described in the previous chapter. To do this, we use both the pair correlation function, in real space, in order to estimate the range of order and the homogeneity of the system; and the structure factor, in Fourier space, for verifying the isotropy of the system. Moreover, we investigate how to tune the degree of disorder with respect to labyrinthine phases, in terms of the order parameter φ which we defined in the previous chapter as the fraction of particles in chains. Based on our conclusion on this point, we generate a highly disordered labyrinthine phase and introduce the slow relaxation processes that it undergoes from very short times, to very long times.

6.3.1 Spatial range of order, homogeneity and isotropy

One way to estimate the range of order in a system is *via* the pair correlation function, $g(r)$, by studying the way the amplitude of its maxima decays as a function of distance, r. If this amplitude decreases exponentially towards 0 at large distances, the system is said to be disordered; if the decay follows a power law, then the order is quasi-long-ranged; if the amplitude decreases to a constant value larger than 1 at large distances, the order is long-ranged. Moreover, if the system is homogeneous, the function $g(r)$ converges to 1.

In the previous chapter, we plotted in Fig. 5.3(c) $g(r)$ for multiple values of our control parameter, ε, across the transition. For the system in the labyrinthine phase (*i.e.*, in a state for which the fraction of particles in chains $\varphi \approx 1$), $g(r)$ mostly exhibited two peaks (blue curve in Fig. 5.3(c)): one at the distance separating two nearest neighbors in chains, which is smaller than one particle diameter due to chain buckling and which we called x_g, and a second one at twice that distance, accounting for the second nearest neighbors. No other peak was visible.

Here, our goal is to significantly improve this characterization on the example of a typical labyrinthine phase. Keeping in mind that labyrinthine phases are very robust metastable states, as explained by Seul and collaborators [96], we cannot hope to have the system rearrange quickly from one labyrinthine configuration to another. Instead –and this is the focus of Section 6.5 below– once formed, a labyrinthine phase slowly evolves across timescales, without any fast, major reconfiguration. Consequently, improving the structural characterization of labyrinthine phases requires accumulating measurements from a high number of experimental realizations performed with identical parameters, rather than from a single experiment during a long time (as was the case for studying the gas- and liquid-like states). This way, exploiting the variety of particle initial positions and velocities, we probe various metastable states while using identical experimental parameters (acceleration Γ, magnetic field B_0, magnetic quench rate α_q, aging time τ_{ag}, etc, as defined in Section 1.2.1). To achieve this, we perform several experiments for a

typical set of parameters leading to a labyrinthine phase: 50 independent runs, with $\Gamma \approx 2$ and $B_0 = 212\,\mathrm{G}$ (see Table 6.2), with the circular cell and a gap size $e = 1.48\,a$.

The resulting pair correlation function, averaged over the 50 realizations, is plotted in Fig. 6.1. The noise level is very low and four peaks clearly rise above it. The first peak is centered on the first-neighbor horizontal distance $r_1/a \equiv 0.88$, indicating the gap size of $e = a\,(1 + \sqrt{1 - r_1^2/a^2}) \approx 1.48\,a > e_x \approx 1.45\,a$ (see Eq. 3.53 for the value of e_x). The pair magnetic potential is thus core-softened with a local minimum at contact that stabilizes the particles aggregated into the buckled chains (see Chapter 3). Note that we use this gap size this gap size, $e = 1.48\,a$, with the circular cell, for all the experiments presented in this chapter. The 5 vertical grey lines in Fig. 6.1 mark the distance r_1/a and its four first multiples $2r_1/a$, $3r_1/a$, $4r_1/a$ and $5r_1/a$. Three secondary peaks of $g(r)$ are visible (and better visualized in the inset in log-scale) and match the values of the three first multiples of r_1/a, indicating a significant probability of finding linear chains a few particles long. However, the amplitude of these peaks decreases quickly and the peaks are no more distinguishable from the noise around $g(r) = 1$ after the third secondary peak. This shows that the spatial range of position-position correlations does not exceed 4 particle diameters. Moreover, the values of $g(r)$ are found higher in front of the secondary peaks than behind them. This comes from two contributions: the curvature of the chains, which makes same-chain n^{th}-neighbor particles closer than the distance nr_1/a, and the particles of neighboring chains. The latter significantly account for, in particular, the non-vanishing values of $g(r)$ between r_1/a and $2r_1/a$. Thus, the typical distance between two chains can be estimated at about $1.5\,a$. Finally, the pair correlation function can be considered flat with a value of 1 from $r/a \approx 4$, implying that the system appears homogeneous beyond that distance.

Let us remark that, even though labyrinthine phases in our system are long-range disordered as are structural glasses, at short distances, they are strongly ordered; this is the signature of the buckled chains, and in contrast to glasses which have the structure of a liquid.

Isotropy cannot be verified using the pair correlation function since it is an azimuthally averaged measure whose only variable is the center-to-center distance. To explore the orientational characteristics of our typical labyrinthine phases, we use the static structure factor, $S(\mathbf{k})$, which is the two-dimensional Fourier transform of the particle center positions,

$$S(\mathbf{k}) = \left\langle \frac{1}{N_p} \sum_{j=1}^{N_p} \sum_{k=1}^{N_p} \mathrm{e}^{-i\mathbf{k}(\mathbf{r}_j - \mathbf{r}_k)} \right\rangle \tag{6.1}$$

where $\mathbf{k} = k_x\,\mathbf{e}_x + k_y\,\mathbf{e}_y$ is the wavenumber in the horizontal plane, $\mathbf{r}_i$ and $\mathbf{r}_j$ are the positions of particles of indices i and j, N_p is the number of particles used in the computation, and $\langle\cdot\rangle$ denotes an ensemble average. We compute $S(\mathbf{k})$ using the same data set as for the pair correlation function plotted in Fig. 6.1.

Our measurements of the static structure factor $S(\mathbf{k})$ are presented in Fig. 6.2(a). An obvious feature of this plot is that it is invariant by rotation, implying that this labyrinthine phase is uniform in all directions of the plane (x, y), *i.e.*, it is isotropic. For instance, if the particles had been on a triangular lattice instead, that is, forming a crystal-like phase as in some of our experiments in Chapter 4, $S(\mathbf{k})$ would have six sharp maxima placed every $\pi/3$ on a circle (and secondary peaks for larger wave vectors) due to the strong orientational order.

In our case, we can average $S(\mathbf{k})$ over the angles to get the static structure factor, $S(k)$, where $k = |\mathbf{k}|$, without loss of information. The high-amplitude ring on the two-dimensional plot becomes a high-amplitude peak at $ka \approx 7.8$ for $S(k)$, as shown in Fig. 6.2(b). This peak is the

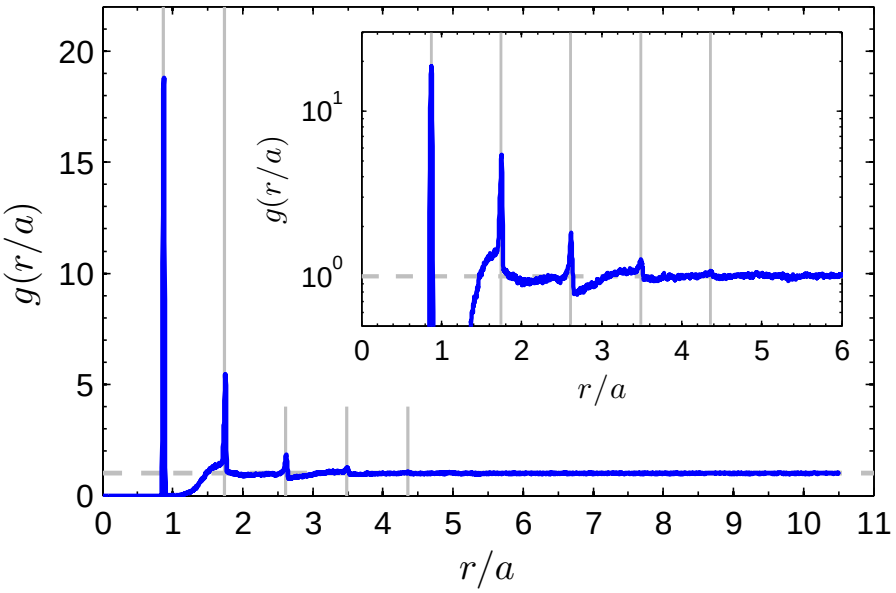

Figure 6.1 Pair correlation function of a typical labyrinthine phase, obtained from averaging over an ensemble of 50 experimental realizations with identical parameters (circular cell, gap size $e = 1.48\,a$, $B_0 = 212\,\mathrm{G}$ and $\Gamma \sim 2$; see Table 6.2 for other parameters). The first peak is at $r_1/a = 0.88$. The vertical grey lines are guides to the eye marking this value and its first four multiples nr_1/a, with $n = 2, ..., 5$. The horizontal dashed line at $g(r) = 1$ is also a guide to the eye. Inset: same plot in vertical log-scale for better visualizing the secondary maxima. We conclude that position-position correlations are negligible at distances larger than 4 particle diameters.

signature of the nearest neighbors in chains, *i.e.*, of the buckled pairs at contact. For decreasing wavelengths, $S(k)$ drops down to a lower plateau for ka = 4-6 (*i.e.*, wavelengths of 1-1.6 a), corresponding to both the second nearest neighbors in chains and to particles of neighboring chains. Even at shorter wavelengths, $S(k)$ further decreases towards zero. Structure is thus clearly visible from the particle scale up to the second- or third- nearest neighbors in chains, but then tends to disappear, as was observed above with the pair correlation function in Fig. 6.1.

The typical labyrinthine phase that we analyze here is therefore disordered, homogeneous and isotropic. We argue that these results can be generally extended to the ensemble of labyrinthine phases that we obtain with other parameters Γ (dimensionless acceleration), B_0 (transverse magnetic field), α_q (magnetic quenching rate) and τ_{ag} (post-quenching aging time), as long as they present a structure of chains apparently disordered in orientation and position. However, we do not perform systematic measurements like the one presented above (50 repeated runs), given the significant experimental and computational times required to do so.

6.3.2 Enhancing the aging process

In this chapter, our goal is to study the temporal evolution, or aging, of the granular labyrinthine phase, which is an unsteady, disordered state. A labyrinthine phase displaying a low probability of particle rearrangements on very long time scales is obviously not experimentally convenient to explore. Indeed, we are interested in generating a labyrinthine phase that is prone to evolving significantly over time scales accessible in the laboratory. We need, thus, to generate a state that is as disordered as possible with respect to the intermediate-time labyrinthine phase. This

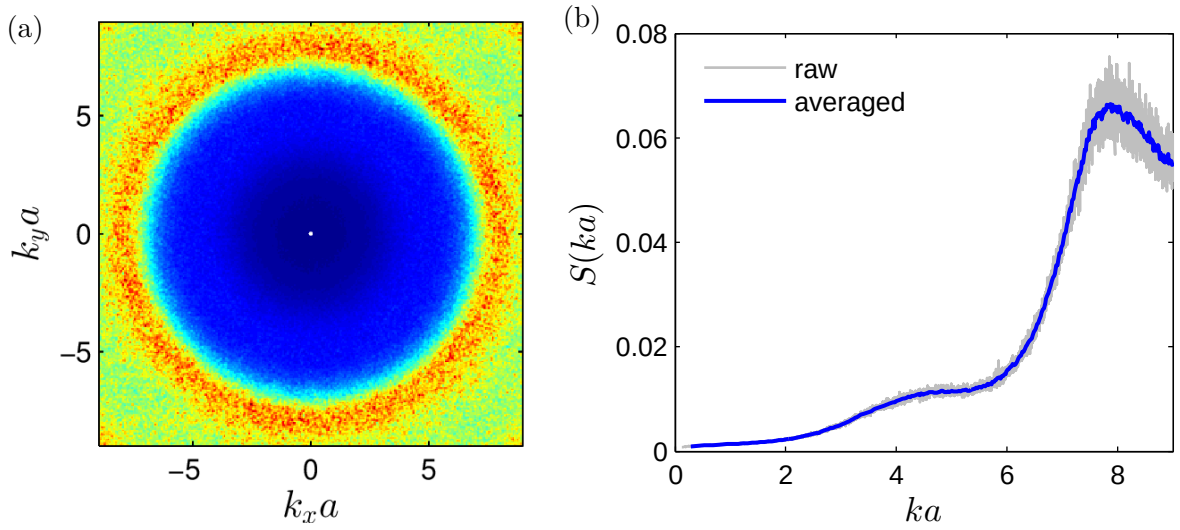

Figure 6.2 Static structure factor of a typical labyrinthine phase, obtained from averaging over an ensemble of 50 experimental realizations with identical parameters (circular cell, gap size $e = 1.48\,a$, $B_0 = 212\,\mathrm{G}$ and $\Gamma \sim 2$; see Table 6.2 for other parameters). (a) Two-dimensional static structure factor $S(\mathbf{k})$. The system is isotropic since $S(\mathbf{k})$ is invariant by rotation. (a) Angularly averaged structure factor, $S(k)$, with $k = |\mathbf{k}|$. The ridge near $ka = 8$ is the mark of the pairs at contact. Finite-size effects exclude wavelengths k such as $ka < \frac{2\pi}{57} \approx 0.1$ (the field of view of the camera is $57\,a \times 57\,a$).

disorder can be measured by the fraction of particles in chains, φ, which we introduced Chapter 5 as an order parameter for the transition from a liquid-like (*i.e.*, an "elastic" granular gas with no dissipative collisions, defined in Chapter 4) to a labyrinthine phase. Note, however, that φ could not be used to distinguish a parallel stripe phase from a disordered labyrinthine phase.

By analogy to a thermal quench in microscopic and colloidal systems, we achieve this goal by quenching the magnetic granular medium from a liquid-like state into a point of the parameter space where a labyrinthine phase is expected. Since $\varepsilon \equiv E_m/E_c$ is a control parameter for the transition from liquid-like to labyrinthine, performing a quench in our system can be realized by either decreasing fast agitation (by means of the dimensionless acceleration Γ) or by increasing fast magnetic interactions (by means of the transverse magnetic field B_0). With our experimental setup, we are restricted to values of Γ within the same order of magnitude, but we can access more than two orders of magnitude for B_0. Hence, instead of thermal-like quenches, we choose to perform *magnetic quenches* consisting of fast increases of the externally applied, vertical magnetic field, whose strength is measured by $\alpha_q \equiv \mathrm{d}B/\mathrm{d}t$. Let us remark that increasing pressure is also known to trigger glass formation [108]. In our system, an increase of B_0 increases also the pressure *via* the magnetic interactions between particles, as we explained in Section 3.3.3, and thus triggers the transition to a labyrinthine phase.

The protocol we use to perform these quenching tests is the following (see general schematic in Fig. 1.9). Mechanical agitation is fixed at $\Gamma = 2$ and remains unchanged for all experiments. First, the magnetic field is set to the plateau value $B_p = 85\,\mathrm{G}$ during 30 s, and the system forms a homogeneous liquid-like ("elastic") state. Second, the magnetic field is increased from this plateau up to $B_0 = 170\,\mathrm{G}$. Quenching rates $\alpha_q \equiv \mathrm{d}B/\mathrm{d}t$ ranging from $10^{-1}\,\mathrm{G/s}$ to $10^{3}\,\mathrm{G/s}$ are tested. We repeat 10 times the experiment for each value of α_q. We measure the fraction of particles in chains, φ, less than $10^{-2}\,\mathrm{s}$ after the magnetic field has reached its target value, B_0,

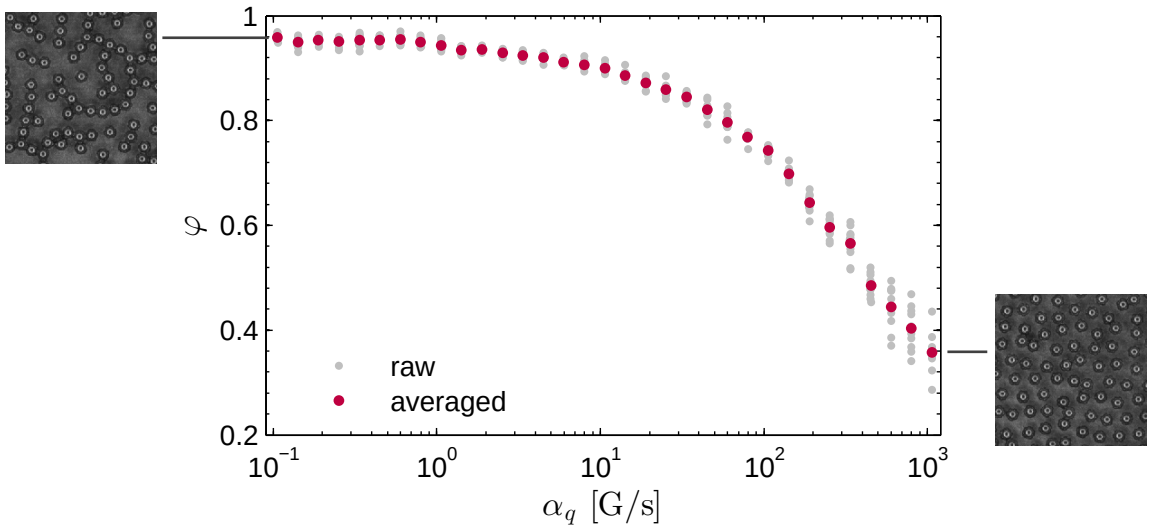

Figure 6.3 *Magnetically* quenching the system: Fraction of particles in chains just after applying an increase of magnetic field of strength $\alpha_q \equiv \mathrm{d}B/\mathrm{d}t$ from 85 G up to $B_0 = 170\,\mathrm{G}$ (circular cell, gap size $e = 1.48\,a$; see Table 6.2 for all parameters). Grey data points are raw data (10 repeated runs for each value of α_q), whose averaged values are the colored data points.

so as to probe the state of the system in its early stage. Note that the duration of the quench itself, *i.e.*, $\Delta B/\alpha_q$ (with $\Delta B = B_0 - B_p$), ranges from less than 0.1 s to more than 14 min, and during this time the system already rearranges.

Our results are presented in Fig. 6.3, which shows the fraction of particles in chains, φ, as a function of the quenching parameter, α_q. Note that the upper bound for α_q, which is of about 10^3 G/s, was chosen to make sure that the coils provided a non-delayed, linear response to the applied fast increase of electrical current (see Section 1.1.5). We find that when the quenching is weak, that is, when the magnetic field is increased slowly, φ takes values close to 1. As illustrated by the picture on the left of the graph, this corresponds to states in which almost all particles are in chains, while a few ones remain unbounded and oscillate between neighboring chains: with respect to φ, this is a very ordered state. As α_q is increased, however, φ drops down. Just after a sharp quench of 10^3 G/s, only one third of the particles are in chains, despite the fact that the magnetic field is high enough for all (or nearly all) the particles to solidify into a labyrinthine phase, as demonstrated with low values of α_q. The picture to the right of the graph shows a snapshot from one of the latter experiments, where most particles are free to move, although a few pairs and triplets are visible. In terms of φ, strong quenches generate very disordered states.

To conclude, the degree of order of the system, as measured by the labyrinthine order parameter φ and at very short times, can be adjusted *via* the magnetic quenching rate, α_q, which we use for driving the system from a liquid-like state into a labyrinthine phase, following an idea comparable to the way thermal quenching is used to turn a liquid into a glass. The higher α_q, the farther from the preferred labyrinthine state is the system. Therefore, strong quenches generate states which display dramatic changes in their structure and dynamics, both at short and long time scales. For the rest of this chapter, we use the highest value of quench presented here, namely $\alpha_q = 10^3\,\mathrm{G/s}$.

6.3.3 Relaxation following a strong quench

From now on, we report on experiments probing the relaxation, or *aging*, of the system after a strong quench at $\alpha_q = 10^3\,\mathrm{G/s}$ is applied. Mechanical excitation is kept fixed with a dimensionless acceleration $\Gamma = 2$, while the magnetic field reached at the end of the quench, B_0, is fixed to several different values between 105 G and 212 G. We choose these values to be from just above the critical B_0 for the transition from liquid-like to labyrinthine state for the current physical and geometrical parameters (circular cell with gap size $e = 1.48\,a$), namely about 95 G, as shown in Fig. 6.4 and further discussed below. The parameter against which we explore the structural and dynamical changes in the system is the *post-quenching aging time*, which we denote τ_{ag} and simply call *aging time*. We defined it in Chapter 1 as:

$$\tau_{\mathrm{ag}} = \tau_0 + \frac{\tau_{\mathrm{rec}}}{2}, \tag{6.2}$$

where τ_0 is the waiting time between the end of the magnetic quench and the start of the recordings, and τ_{rec} is the duration of the recordings (see general schematic in Fig. 1.9).

In Fig. 6.4 we plot the fraction of particles in chains, φ, against the magnetic field, B_0, for several aging times ranging from about $10^{-2}\,\mathrm{s}$ to $10^3\,\mathrm{s}$. These curves characterize the transition from a liquid-like to a labyrinthine phase similarly to the curve of φ *vs.* ε in Fig. 5.3(a), and can be considered as its generalization for a quenched system, in which aging is relevant. The transition here occurs around $B_0 = 95\,\mathrm{G}$. Non-vanishing values of φ below it are due to temporarily colliding pairs counted as chains, which occurs when we do not check the stability of the chains as explained in Section 2.2.1. Hence, this is a numerical artefact and φ should be zero below the transition. Above the critical magnetic field, φ increases towards 1 with B_0, but does so with a strong dependence over the aging time: near the transition, the larger τ_{ag}, the larger the increase of φ for a given increment in B_0. In other words, the transition to a labyrinthine phase seems to go from continuous to discontinuous when the aging time tends towards infinity. A question is then: Is this transition of first order? For now, we this as a perspective. Let us point of thet even if it were indeed of first order, no real discontinuity could be observed in our experiments due to the finite size of the system.

As a first approach of the *aging* process, we show in Fig. 6.5 and Fig. 6.6 virtual images of the system after a quench at rate $\alpha_q = 1.03 \times 10^3\,\mathrm{G/s}$, at increasing aging times and for an applied magnetic field $B_0 = 127\,\mathrm{G}$. These images are all from the same experiment, except for Fig. 6.6(d). The free particles are represented by the grey disks, and the particles "solidified" in chains, by the orange disks. The diameter of these disks is the one of a real particle, a.

The time evolution of the system at aging times τ_{ag} smaller than $4 \times 10^{-1}\,\mathrm{s}$ is represented in Fig. 6.5. Shortly after the quench, at $\tau_{\mathrm{ag}} = 7.7 \times 10^{-3}\,\mathrm{s}$, the greater part of the particles are free, and a few short chains are already formed, as shown in Fig. 6.5(a). As time passes, these chains do not break but grow, as shown in Fig. 6.5(b, c, d). At these short times, we observe the nucleation of free particle into chains, homogeneously across the system.

At times longer than $5 \times 10^{-1}\,\mathrm{s}$, most particles are part of chains, as can be seen in Fig. 6.6. The particles that are free at $\tau_{\mathrm{ag}} = 5.1 \times 10^{-1}\,\mathrm{s}$ [Fig. 6.6(a)] progressively join chains, and at very long times, just a few of them remain free, as visible in Fig. 6.6(d). At the same time, the morphology of the labyrinthine phase evolves from an ensemble of unbranched chains to a system of longer, more branched chains. Hence, the relaxation of the labyrinthine phase at long times is related to *coarsening*.

For a more systematic approach to the aging process of the granular labyrinthine phases, let us consider the order parameter φ and the mean kinetic energy per particle, E_c, over aging

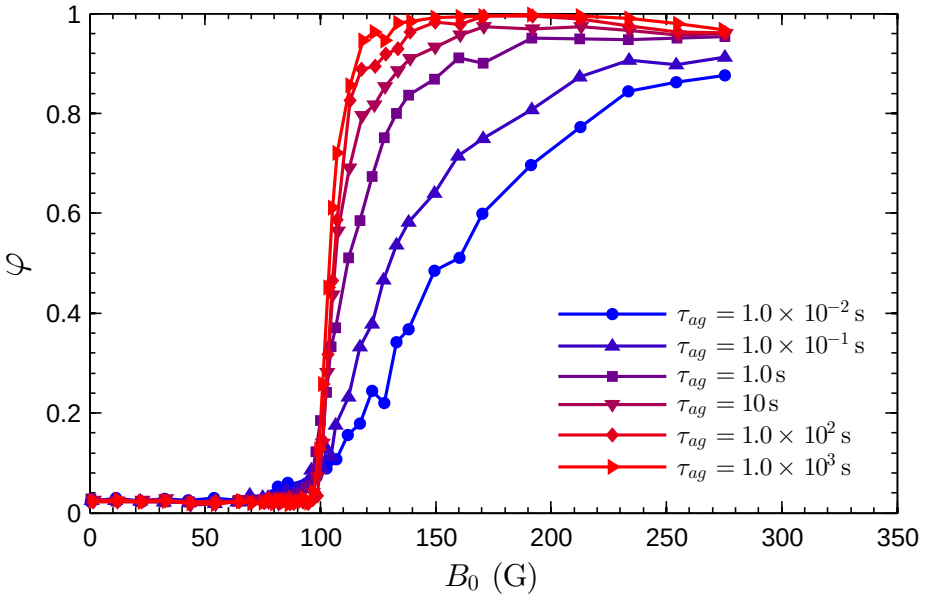

Figure 6.4 Transition from liquid-like to labyrinthine states as measured by the fraction of particles in chains, φ, for various aging times, $\tau_{\rm ag}$. The transition occurs around $B_0 = 95\,\mathrm{G}$. For $B_0 < 95\,\mathrm{G}$, $\varphi \sim 0$ since there are no stable chain. For $B_0 > 95\,\mathrm{G}$, φ strongly depends on $\tau_{\rm ag}$, which shows the evolution of the labyrinthine phase in time. The transition seems to go from continuous at short aging times, to discontinuous at long aging times.

times ranging from $10^{-3}\,\mathrm{s}$ to $10^{4}\,\mathrm{s}$. We plot φ and E_c against $\tau_{\rm ag}$ and for various values of B_0 in Fig. 6.7(a, b). These two observables provide a good picture of the structural and the dynamical states of the system. Note that travelling along an imaginary vertical line at a given B_0 in Fig. 6.4, from bottom to top, means travelling in aging time, and hence corresponds to following the curve of the corresponding B_0 in Fig.6.7(a) from left to right.

All the curves describing φ (respectively, E_c) have similar shapes: they display a plateau at very short times, then monotonically increase (respectively, decrease) with an inflexion point at intermediate times, and tend towards a limit value at long times. It clearly appears that the evolutions of φ and E_c are closely related, even though they remain distinguishable. This can be qualitatively explained as follows. When φ increases, by definition the number of free particles decreases. Moreover, these mobile particles are those who mostly contribute to E_c, the mean kinetic energy per particle, since the particles in chains are almost "frozen", *i.e.*, their displacements are extremely reduced compared to those of the free particles. Indeed, we recall that chains are buckled between the top and bottom plate and are almost static in the cell reference frame, thus injection of mechanical energy to the particles that compose them is highly inefficient. The velocity distribution functions (not shown here) also clearly display the coexistence of both mobile and almost immobile particles. To conclude, when the population of free particles drops down (*i.e.*, φ rises), the mean agitation in the system (*i.e.*, E_c) does so too.

At short times, we note that φ does not equal zero for any of the magnetic field values used here, reflecting the fact that at the start of the recordings, some chains are already formed. The values of the initial plateaus of φ increase with B_0 (*i.e.*, more chains are formed for higher B_0), and the same trend seems to qualitatively apply to the initial plateaus of E_c, although error bars are much larger. For longer times, kinetic energy measurements do order according to magnetic field values as φ does: the higher B_0, the higher φ and the lower E_c.

In the range of long aging times, the respective limit values of φ clearly indicate different limit states: for the two lower values of B_0, namely 105 G and 112 G, the fraction of particles in chains saturates below 1, which implies that some particles remain free between the chains constituting the rest of the system, although for all higher values of B_0, φ converges towards 1 and the whole system is "solidified". In the following, we refer to the former type of experiments as *type NC* experiments (for "non-converging to $\varphi = 1$", *i.e.*, for which there is phase coexistence in the limit $\tau \to \infty$) and the latter as *type C* experiments (for "converging to $\varphi = 1$"). Moreover, a specific magnetic field value emerges, $B_0 = 127\,\mathrm{G}$, which strictly speaking belongs to type C experiments, but for which φ converges to 1 in a time significantly larger than for other experiments. Hence in the following, we refer to this ensemble of experiments with $B_0 = 127\,\mathrm{G}$ as the *limit case*.

Finally, it appears that the system structure and dynamics behave in significantly different ways at short and long time scales, the inflection points of the curves marking a transition. At short aging times, the population of particles integrated in chains grows fast and the agitation drops simultaneously; this is what we focus on in the next section. Then, in Section 6.5, we will investigate the much slower relaxation that occurs at long times.

As a final remark, we would like to indicate that although experiments were easily reproducible when performed within short time intervals, some discrepancies appeared for data sets typically separated by a week, which we do not understand. For instance, the curve of $B_0 = 112\,\mathrm{G}$ clearly displays a discontinuity between $\tau_{\mathrm{ag}} = 3 \times 10^{-1}\,\mathrm{s}$ and $4 \times 10^{-1}\,\mathrm{s}$, which probably does not have any physical significance but in fact corresponds to, respectively, the final experiments of one data set, and the first experiments of another one. The error bars correspond to the standard deviation from ten repeated runs performed successively.

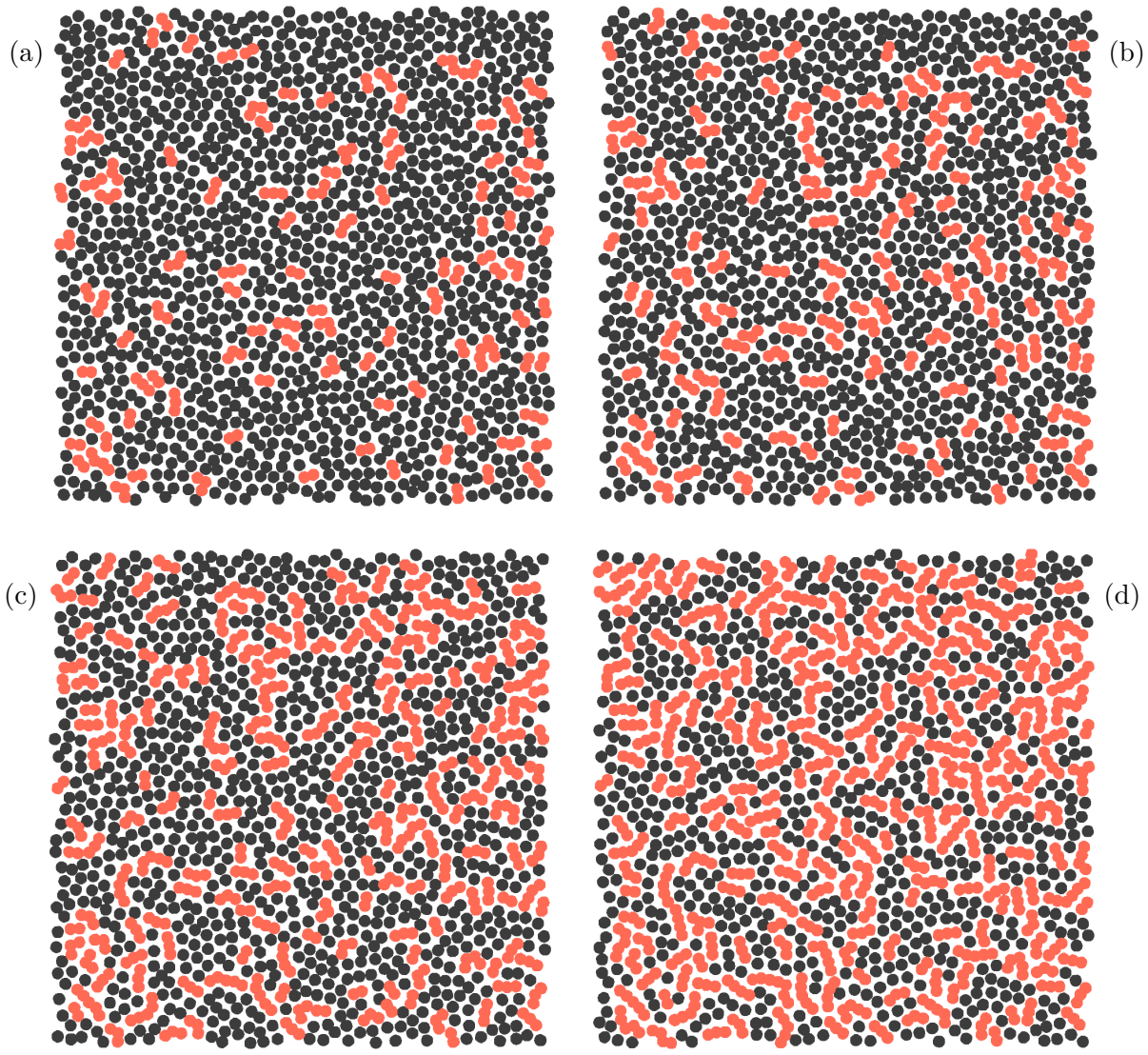

Figure 6.5 Short-time response of the magnetic granular gas to a magnetic quench at rate $\alpha_q = 1.03 \times 10^3\,\mathrm{G.s^{-1}}$, for a target magnetic field $B_0 = 127\,\mathrm{G}$ and an acceleration $\Gamma = 2.04$. The four images are from the same experiment and are taken at successive aging times. These times are smaller than the time at which the curve of φ in Fig. 6.7 shows an inflection point, namely near $4 \times 10^{-1}\,\mathrm{s}$. (a) $\tau_{\mathrm{ag}} = 7.7 \times 10^{-3}\,\mathrm{s}$, (b) $\tau_{\mathrm{ag}} = 3.7 \times 10^{-2}\,\mathrm{s}$, (c) $\tau_{\mathrm{ag}} = 1.0 \times 10^{-1}\,\mathrm{s}$, and (d) $\tau_{\mathrm{ag}} = 2.5 \times 10^{-1}\,\mathrm{s}$. Grey disks represent free particles, while orange disks show particles "solidified" in chains. The diameter of the disks is the real particle diameter, a. Clusters are detected by an algorithm mentioned in Section 2.2.1 and further examined in Section 6.4.1. At short times, free particles nucleate into mostly linear chains, homogeneously across the system.

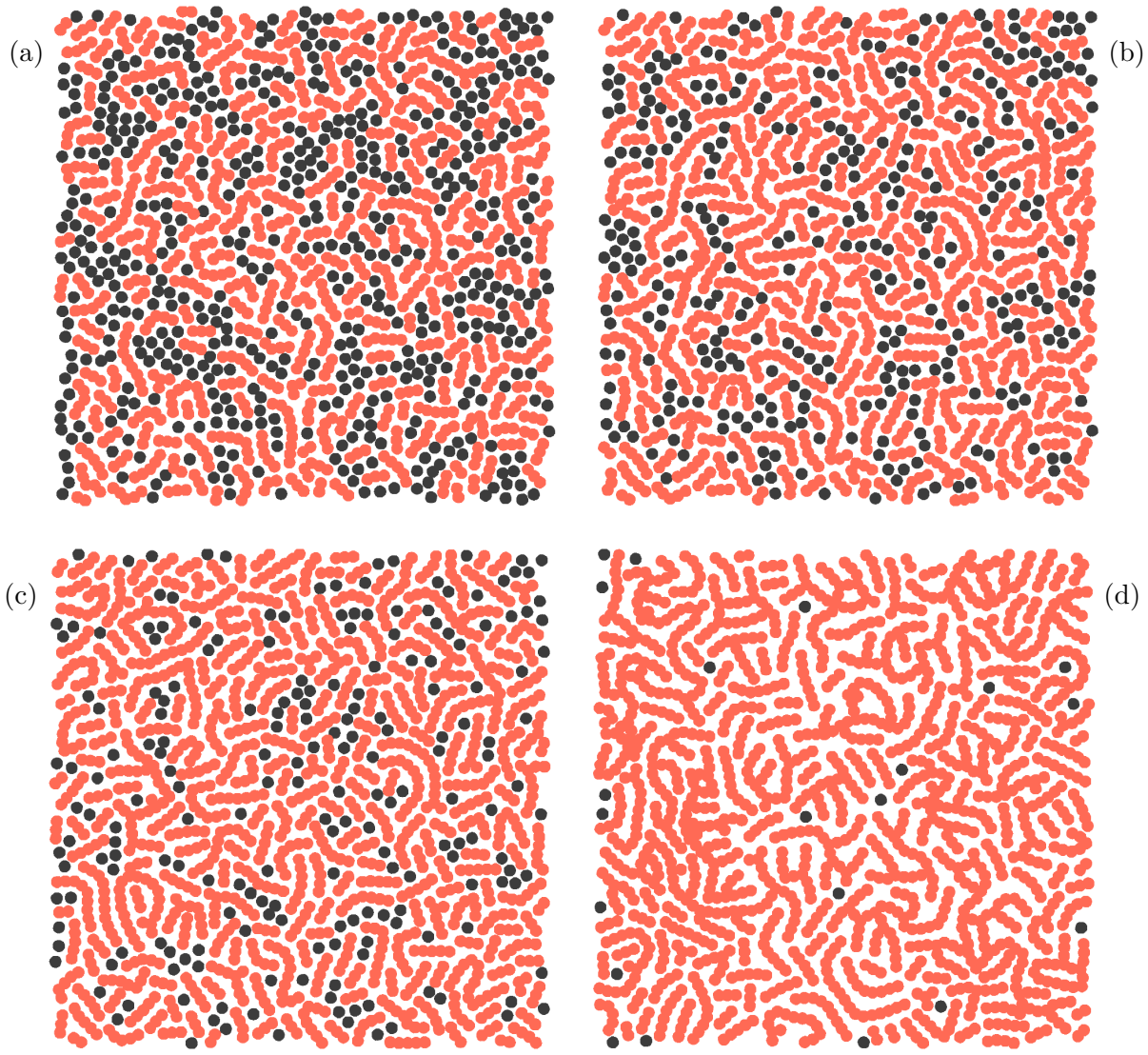

Figure 6.6 Long-time relaxation of the granular labyrinthine phase, after a magnetic quench at rate $\alpha_q = 1.03 \times 10^3\,\mathrm{G.s^{-1}}$, for a target magnetic field $B_0 = 127\,\mathrm{G}$ and an acceleration $\Gamma = 2.04$. The three first images are from the same experiment and are taken at successive aging times. The fourth image is from another set of experiments. The aging times are larger than the time at which the curve of φ in Fig. 6.7 shows an inflection point, namely near $4 \times 10^{-1}\,\mathrm{s}$. (a) $\tau_{\mathrm{ag}} = 5.1 \times 10^{-1}\,\mathrm{s}$, (b) $\tau_{\mathrm{ag}} = 2.0\,\mathrm{s}$, (c) $\tau_{\mathrm{ag}} = 10\,\mathrm{s}$, and (d) $\tau_{\mathrm{ag}} = 2.3 \times 10^3\,\mathrm{s}$. Grey disks represent free particles, while orange disks show particles "solidified" in chains. The diameter of the disks is the real particle diameter, a. At long times, free particles keep nucleating into chains, and the chains rearrange and merge, leading to a global coarsening of the labyrinthine phase.

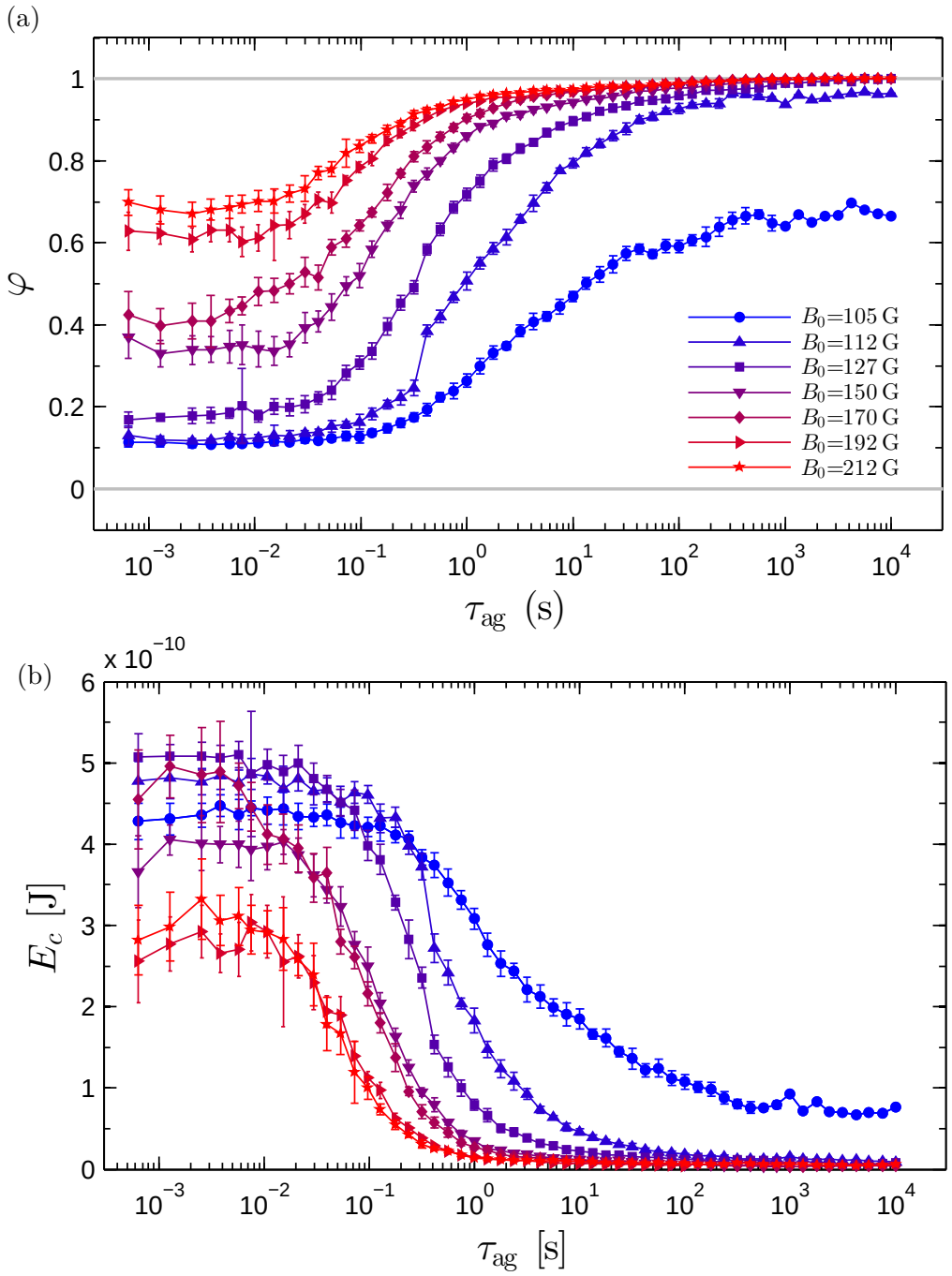

Figure 6.7 Relaxation of a labyrinthine phase. (a) Fraction of particles in chains, φ, and (b) kinetic energy per particle, E_c, *vs.* aging time, τ_{ag}, after a strong quench ($\alpha_q = 10^3$ G/s), for different target values of the magnetic field B_0. The grey horizontal lines in (a) indicate $\varphi = 0$ (no chains) and $\varphi = 1$ (only chains). For aging times $\tau_{ag} < 10^3$ s, every data point is obtained from averaging over ten repeated runs. Error bars represent the standard deviation of these repeated runs. For $\tau_{ag} \geq 10^3$ s, only one experiment was performed for each value of the aging time.

6.4 Steady nucleation at short times

Right after the magnetic quench, the fraction of particles in chains is very low compared to its long time values, as shown in Fig. 6.7(a), and particles are very agitated on average, as shown in Fig. 6.7(b). Such a state does not correspond to a preferred configuration and only exists as a result of the magnetic quench. Like a thermally quenched microscopic system, the granular system relaxes as it escapes from its quenched configurations towards more favored states, first quickly, and then more slowly. In this section we focus on the short time limit, that is, the range of times during which the fraction of particles in chains, φ, follows an accelerated increase, and which corresponds to an accelerated decrease of the mean kinetic energy per particle, E_c. The inflection points of the curves can be considered as the upper short time limit, for now, but we will give below a more quantitative estimate of this limit.

At these early times, free particles massively aggregate to form chains or to extend existing ones. Here we ask: Can we find universal laws describing the time evolution of, respectively, φ and E_c for all values of the magnetic field? What are the quantitative changes generated by the free particles' aggregation in terms of chain quantity and morphology (size, shape, etc.)?

Note that the answers to these questions, which we ask in the context of a *fixed* magnetic field B_0, should also be qualitatively valid concerning the aggregation of particles into chains *during the increase* of the magnetic field from B_1 to B_0.

6.4.1 Structure

Let us first focus on the structural changes affecting the system. We characterize them by means of the time evolution of the fraction of particles in chains, φ, which measures how advanced the state of the system is in the transition from liquid-like to the labyrinthine phase; but we also use some specific quantities giving a good picture of the morphology of the labyrinthine phase formed and of the chains that compose it, such as the total number of chains, the mean number of particles per chain, the distribution of sizes of the chains, and so on.

Fraction of particles in chains

In Section 6.3.3, we mentioned the visible similarity in general shape between the curves of the fraction of particles in chains, φ, for the values of magnetic field, B_0, used in the present experiments dedicated to the aging of the labyrinthine phase (from $B_0 = 105\,\mathrm{G}$ to $212\,\mathrm{G}$). Here we go further and demonstrate that there exists a universal law ("universal" here meaning "valid for any B_0") describing the time evolution of φ at short times.

During short times, φ increases from its initial plateau value up to an inflection point. The plateau value depends on B_0 and is defined by

$$\varphi_0(B_0) \equiv \lim_{\tau_{\mathrm{ag}} \to 0} \varphi(B_0; \tau_{\mathrm{ag}}). \tag{6.3}$$

Whatever the value of B_0, φ_0 is always non-vanishing: chains already exist for $\tau_{\mathrm{ag}} \to 0$. Indeed, as pointed out above, the magnetic quenching itself takes a finite time, namely $(B_0 - B_p)/\alpha_q$ (with $B_p = 85\,\mathrm{G}$ the magnetic field plateau value and $B_0 \in [105; 212]\,\mathrm{G}$ the magnetic field target value, as defined in Section 1.2.1), and during this time particles start to aggregate. Although the underlying process occurring during magnetic quenching is certainly interesting and deserves

further attention, we will not tackle it in this thesis and will focus instead on the aggregation process occurring for $\tau_{\text{ag}} > 0$, that is, once the magnetic field has reached its target value, B_0.

In practice, we take the values of $\varphi_0(B_0)$ as the average of $\varphi(B_0)$ between $\tau_{\text{ag}} = 1 \times 10^{-3}$ s and $\tau_{\text{ag}} = 4 \times 10^{-3}$ s. We estimate that this arbitrary choice correctly represents the very short time trends of the curves.

For the purpose of comparing the curves of φ at short aging times and for different magnetic field values, it is convenient to define a reduced fraction of particles in chains, φ_n, which equals 0 in the limit $\tau_{\text{ag}} \to 0$ for all B_0:

$$\varphi_n \equiv \frac{\varphi - \varphi_0}{1 - \varphi_0}. \tag{6.4}$$

Now, let us turn to searching for a universal behavior of $\varphi(B_0)$ at short times. As specified in Section 6.3, the gap size used for the experiments of this chapter is $e \approx 1.48\,a$ and corresponds to a long-distance repulsive and short-distance attractive pair potential, as we discussed in particular in Section 5.5. If this potential is modified by the presence of other particles which acts as a magnetic pressure, as defined in Section 3.3.3, its qualitative shape remains unchanged. In particular, the test particle must overcome a potential energy barrier for going from being free, to being part of a buckled chain.

In order to build a simple phenomenological model, we consider that particles can be either in the state "free" or in the state "chain". We assume that their kinetic energy enables them to jump over the potential energy barrier, that is, to switch from one state to the other, if it is large enough. Based on these assumptions, the time evolution of the probability for a particle to be part of a chain, P^{chain}, is the opposite of the time evolution of the probability for a particle to be free, P^{free}, and it is given by:

$$\frac{\mathrm{d}P^{\text{chain}}}{\mathrm{d}\tau_{\text{ag}}} = W_{\text{free}\to\text{chain}}\, P^{\text{free}} - W_{\text{chain}\to\text{free}}\, P^{\text{chain}}, \tag{6.5}$$

where $W_{\text{free}\to\text{chain}}$ and $W_{\text{chain}\to\text{free}}$ are, respectively, the probability that a particle become part of a chain when it was free, and the probability that a particle become free when it was in a chain, in the long time limit.

It is important to note that friction probably plays an important role in stabilizing the chains, as mentioned in Section 5.5. Indeed, given that chains are buckled between the lid and the bottom plate, particle-particle, particle-lid and particle-bottom surface friction effects should not be neglected. Qualitatively, friction probably acts as if the short-distance attractive potential well was much deeper, making it harder for a trapped particle to escape. Additionally, as mentioned previously, particles inside buckled chains are very inefficiently provided energy by the cell vibration since they are immobile in the cell reference frame, and as a consequence, their kinetic energy is very low. Finally, the amount of energy required for particles trapped at contact to escape and become free again is most probably much greater than their kinetic energy in the "chain" state. This idea is supported by the experimental observation that chains of particles, once formed, almost never break apart. Hence, it seems relevant to consider the nucleation of free particles in chains as an irreversible process, *i.e.*, we estimate relevant to assume $W_{\text{chain}\to\text{free}} = 0$. Additionally using the relation $P^{\text{free}} = 1 - P^{\text{chain}}$, and the fact that the probability that a particle is part of a chain equals the measured fraction of particles in chains,

i.e., $P^{\text{chain}} = \varphi$, we can rewrite Eq. 6.5 as:

$$\frac{\mathrm{d}\varphi}{\mathrm{d}\tau_{\text{ag}}} = W_{\text{free}\to\text{chain}}\,(1-\varphi). \tag{6.6}$$

The probability $W_{\text{free}\to\text{chain}}$ is related to the ratio of the height of the potential energy barrier between the state "free" and the contact position, to the kinetic energy of the free particles. It certainly depends on the applied magnetic field B_0, and also possibly presents a dependence over time arising from geometrical rearrangements of the particles in the system. For now, we assume that $W_{\text{free}\to\text{chain}}$ varies sufficiently slowly with the aging time so that we can consider it as time-invariant in the range of τ_{ag} considered in this section. Therefore, the solution of Eq. 6.6 at short times is an exponential with a characteristic time

$$\tau^c_{\text{ag}}(B_0) \equiv W^{-1}_{\text{free}\to\text{chain}}(B_0), \tag{6.7}$$

which writes

$$\varphi(\tau_{\text{ag}}; B_0) = 1 - (1-\varphi_0)\,\exp\left(-\frac{\tau_{\text{ag}}}{\tau^c_{\text{ag}}}\right), \tag{6.8}$$

where φ_0 is the short-time limit of φ defined in Eq. 6.3.

Note that the characteristic time τ^c_{ag} is the typical time for free particles to jump over the potential energy barrier and go from the state "free" to the state "chain". As such, we call it *characteristic time of nucleation*.

Now re-writing Eq. 6.8 for the reduced fraction of particles in chains, φ_n, we have at short times:

$$\varphi_n(\tau_{\text{ag}}) = 1 - \exp\left(-\frac{\tau_{\text{ag}}}{\tau^c_{\text{ag}}}\right). \tag{6.9}$$

In Fig. 6.8(a), we show φ_n as a function of the aging time, τ_{ag}, along with the best fits of φ_n by Eq. 6.9. We obtain the characteristic nucleation times, $\tau^c_{\text{ag}}(B_0)$, shown in the inset. Note that the quality of the fits and the resulting error bars are directly related to the arbitrary choice of the range of τ_{ag} used for performing the fits. The ones we used are reported in Table 6.1, along with the values obtained for τ^c_{ag}. In particular, for $B_0 = 112\,\text{G}$ (blue up-pointing triangles in Fig. 6.8), we only used the time preceding the gap between the two sets of data, *i.e.*, $\tau_{\text{ag}} < 4\times10^{-1}\,\text{s}$.

As shown in Fig. 6.8(a)-(inset), we find that τ^c_{ag} decreases faster than exponentially with B_0. It may be counterintuitive that nucleation is accelerated by higher magnetic field, since increasing the magnetic field decreases particle agitation, as shown in Fig. 6.7(b), and increases the height of the pair potential energy barrier. However, increasing B_0 also increases the magnetic pressure exerted by the neighboring particles on the test particle, which in turn decreases the height of the *real* (and not *pair*) potential energy barrier, hence justifying the decrease of τ^c_{ag} with B_0. Note that the uncertainty on our estimates of τ^c_{ag} dramatically increases with B_0. This comes from the dispersion in the raw data for φ, which is much smaller for the three lower values of B_0 than for the others, as attested by the error bars in Fig. 6.7(a).

Each characteristic nucleation time $\tau^c_{\text{ag}}(B_0)$ is a relevant time scale for the set of experiments performed with the magnetic field B_0. Indeed, by rescaling the aging time, τ_{ag}, by $\tau^c_{\text{ag}}(B_0)$ for each set of experiments, we make all curves of $\varphi_n(B_0)$ satisfyingly collapse on a master curve, as shown in Fig. 6.8(b). A good agreement with the exponential fit of Eq. 6.9 (thick black line in Fig. 6.8(b)) is obtained for times $\tau_{\text{ag}}/\tau^c_{\text{ag}} \lesssim 5\times10^{-1}$, except for $B_0 = 105\,\text{G}$ (blue circles), which departs from the master curve at earlier times. For the experiments with $B_0 = 105\,\text{G}$, the

fraction of free particles that aggregate is so low that the nucleation process relevant at short times is shortened compared with the other experiments.

The dispersion of the data points with respect to the exponential fit is made more clear in the inset in Fig. 6.8(b), which represents the same measures as the main plot but in log-log scale. This confirms that dispersion seems acceptable for $\tau_{\mathrm{ag}}/\tau_{\mathrm{ag}}^{c} \lesssim 5 \times 10^{-1}$.

At longer aging times, however, all curves separate from the exponential fit and increase much more slowly towards 1. This implies that in this time range, the assumption of a non-time-dependent characteristic nucleation time, which is what we assumed above to obtain Eq. 6.9, breaks down: τ_{ag}^{c} then not only depends on B_0, but also on τ_{ag}. In other words, if the nucleation process can be considered as *steady* at times $\tau_{\mathrm{ag}}/\tau_{\mathrm{ag}}^{c} \lesssim 5 \times 10^{-1}$, it becomes *unsteady* at longer times. This enables us to quantitatively define the upper limit of the *short times* as being the dimensionless time $\tau_{\mathrm{ag}}/\tau_{\mathrm{ag}}^{c} = 5 \times 10^{-1}$. Beyond that time, *i.e.*, at *long times*, the greater part of the particles are part of chains, the dynamics slows down and the processes that are then relevant clearly differ from steady nucleation; this is the focus of Section 6.5.

Morphology of the chains

At short times, the labyrinthine phase sets up from a state with a significant fraction of free particles, which progressively nucleate into chains [Fig. 6.7(a)]. In the previous section, we identified the characteristic nucleation times, $\tau_{\mathrm{ag}}^{c}(B_0)$, which indicate the time at which about two thirds of the particles which were free in the limit $\tau_{\mathrm{ag}} \to 0$ belong to the labyrinthine phase [Fig. 6.8(a)-(inset)]. Now we ask: What is the morphology of the chains as they form during this nucleation process? Are they short or extended? Are they straight or bent? Do they have branching points?

To answer these questions, we designed an algorithm identifying independently every particle in every chain, so that we can measure a variety of their morphological properties. Aiming at obtaining statistics with as little bias as possible, we exclude from our measurements the chains intersecting with at least one of the boundaries of the region of interest, because information about such chains is irreversibly lost. Moreover, to not exclude them would artificially increase the shortest chain population, with no certainty that they are representative of that population. Of course, such a method has a related drawback: if chains become long enough so that the number of excluded chains is not negligible compared with the number of those accepted by the algorithm, then statistics become significantly biased for the long chains.

In order to evaluate the validity of our method, we measure the total number of particles accepted by the algorithm, N_{all}, which is the sum of both free and in-chain particles, as shown in Fig. 6.9. Since, generally, chains grow while the labyrinthine phase sets up, N_{all} is expected to follow a decreasing trend. For now, we focus only on the part of the curves at short times, *i.e.*, on dimensionless times $\tau_{\mathrm{ag}}/\tau_{\mathrm{ag}}^{c} < 5 \times 10^{-1}$. As Fig. 6.9(a) shows for type NC experiments (*i.e.*, experiments for which "solidification" is not complete even at long times) and Fig. 6.9(b)

B_0 (G)	105	112	127	150	170	192	212
${\tau_{\mathrm{ag}}}^{i}$ (s)	1×10^{-3}	1×10^{-3}	1×10^{-3}	1×10^{-3}	1×10^{-2}	1×10^{-3}	1×10^{-3}
${\tau_{\mathrm{ag}}}^{f}$ (s)	8×10^{-1}	4×10^{-1}	6×10^{-1}	9×10^{-2}	7×10^{-2}	1×10^{-1}	8×10^{-2}
τ_{ag}^{c} (s)	4.5	2.0	6.5×10^{-1}	2.7×10^{-1}	2.0×10^{-1}	1.6×10^{-1}	1.2×10^{-1}

Table 6.1 Lower and upper aging time boundaries used for performing the exponential fits of φ_n given by Eq. 6.9 and plotted in Fig. 6.8, τ_{ag}^{i} and τ_{ag}^{f}; and resulting characteristic nucleation times, τ_{ag}^{c}.

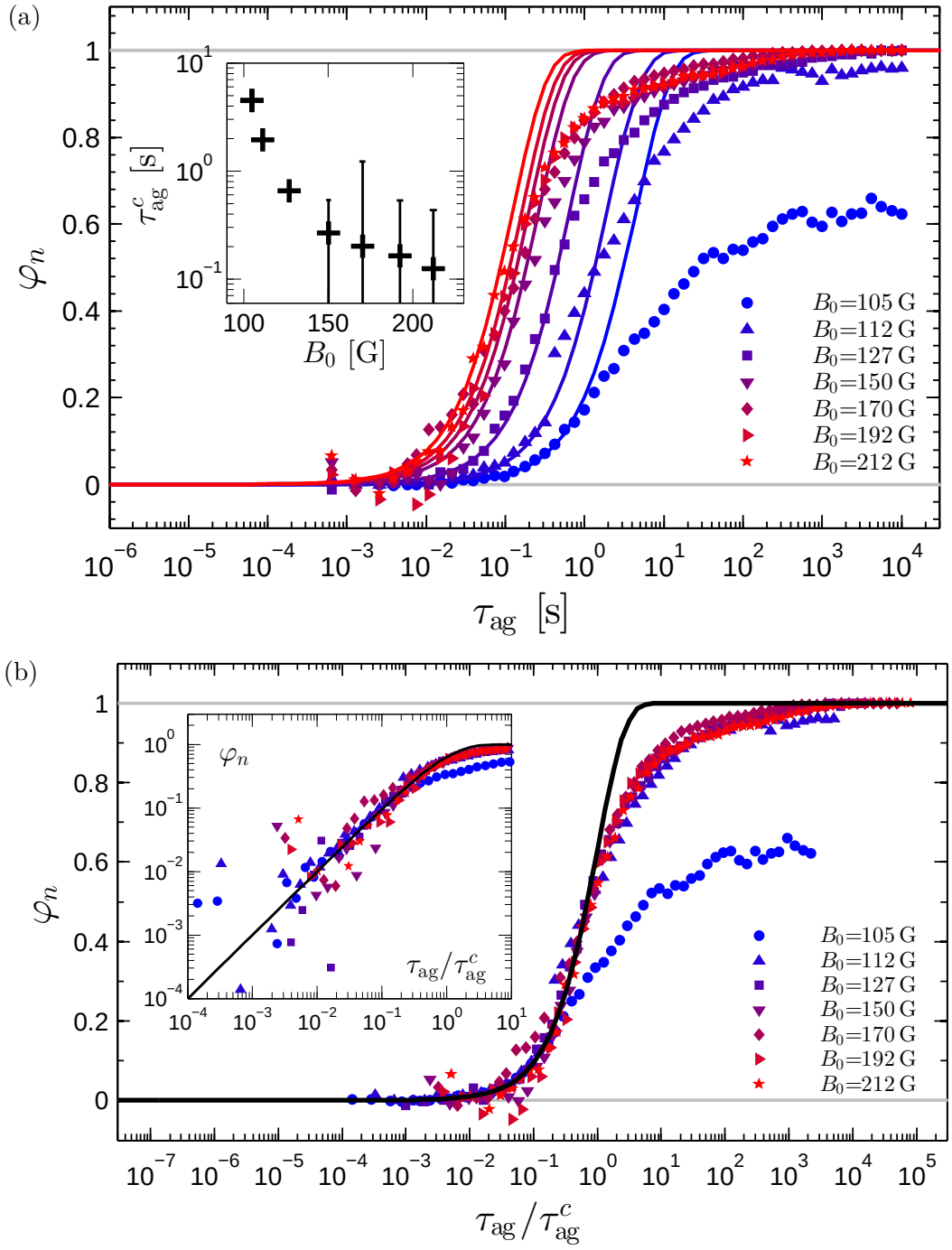

Figure 6.8 Reduced fraction of particles in chains, φ_n, defined in Eq. 6.4, and characteristic nucleation times $\tau^c_{ag}(B_0)$. (a) φ_n as a function of τ_{ag}. The full lines are fits from Eq. 6.9, which provide the characteristic nucleation times $\tau^c_{ag}(B_0)$ (plotted in inset against B_0). (b) φ_n as a function of the dimensionless aging time, τ_{ag}/τ^c_{ag}. For $\tau_{ag}/\tau^c_{ag} \lesssim 5 \times 10^{-1}$, all curves collapse on a master curve which is well fitted by the exponential defined in Eq. 6.9. This is the *steady nucleation process*. For $\tau_{ag}/\tau^c_{ag} \gtrsim 5 \times 10^{-1}$, the characteristic nucleation times are time-dependent and the exponential fit is irrelevant. Inset: same data plotted in log-log scale.

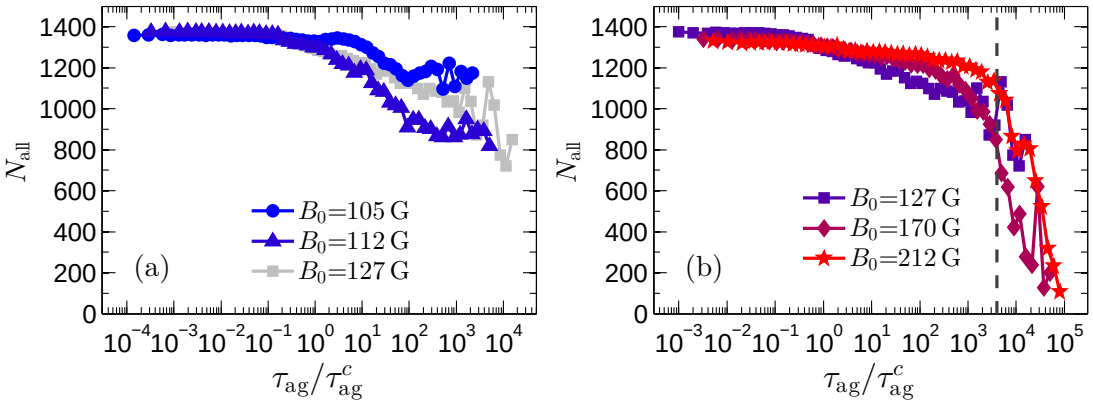

Figure 6.9 Total number of particles, $N_{\rm all}$, *i.e.*, number of free particles plus number of particles in chains, accepted by the algorithm analyzing the chains, for (a) experiments of type NC, *i.e.*, experiments for which "solidification" is not complete even at long times; and for (b) examples of experiments of type C, *i.e.*, experiments for which "solidification" is complete at long times. The vertical black dashed line in (b) indicates the limit of validity of the algorithm (see Section 6.5) past which $N_{\rm all}$ drops down anomalously; this is a numerical artefact.

shows for type C experiments (*i.e.*, experiments for which "solidification" is complete at long times), $N_{\rm all}$ is almost constant at short times whatever the value of B_0. Note that the *limit case* (*i.e.*, the set of experiments with $B_0 = 127\,\mathrm{G}$ and for which "solidification" takes the longest time) appears on both plots in Fig. 6.9 (and in the following figures) because, as we will see, it shares features of both type NC and type C experiments. To conclude, the algorithm does not seem to exclude an excessive number of particles at short times. This observation clearly does not hold at long times anymore, as we will discuss in the next section.

Let us now focus on the morphological characteristics of the chains constituting the labyrinthine phase which forms at short times. The mean *number of chains* accepted by the algorithm, which we denote N_c, provides a general picture of the state. We are also interested in the mean number of particles per chain, which we call here mean *chain size*, n_c, mean chain linear extension, or mean *chain length*, λ_c, and mean fraction of particles in a chain with 3 neighbors, or mean *chain connectivity*, κ_3.

More precisely, N_c, n_c, λ_c and κ_3 are averaged over a few frames and over experimental realizations, and additionally, n_c and λ_c are averaged over the clusters:

$$N_c = \left\langle N_c^t \right\rangle \tag{6.10}$$

$$n_c = \left\langle \frac{1}{N_c^t} \sum_{i=1}^{N_c^t} n_c^1(i) \right\rangle \tag{6.11}$$

$$\lambda_c = \left\langle \frac{1}{N_c^t} \sum_{i=1}^{N_c^t} \lambda_p^1(i) \right\rangle \tag{6.12}$$

$$\kappa_3 = \left\langle \frac{N_3^t}{\sum_{i=1}^{N_c^t} n_c^1(i)} \right\rangle \tag{6.13}$$

where $\langle\cdot\rangle$ denotes the average over a few frames and over repeated experiments, N_c^t is the number of chains at time t, $n_c^1(i)$ [resp., $\lambda_c^1(i)$] is the number of particles (the longest distance between two particles) in the chain of index i at time t, and N_3^t is the number of particles with three

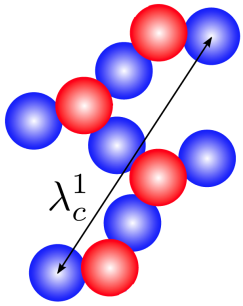

Figure 6.10 Virtual representation of a non-straight, branched chain with indication of the longest distance between two particles in this chain, λ_c^1. All chains are buckled between the cell lid and the bottom plate. Here, particles in contact with the bottom plate are represented in blue, while those in contact with the cell lid, in red. The mean chain length, λ_c, is defined by Eq. 6.12 as the average of λ_c^1 over the ensemble of chains at a given time, over a very short time window, and over repeated experiments.

neighbors at time t. Note that $\sum_{i=1}^{N_c^t} n_c^1(i)$ is the total number of particles in chains at time t. We illustrate the calculation of λ_c^1 for a random chain in Fig. 6.10.

On Fig. 6.11 we represent N_c, n_c, λ_c and κ_3 for experiments of type NC (left column) and for experiments of type C (right column). The limit case appears in both columns. As for Fig. 6.9, we focus for now on the short times, *i.e.*, $\tau_{\rm ag}/\tau_{\rm ag}^c < 5 \times 10^{-1}$.

In this range of time, the mean number of clusters, N_c, displays trends similar to those of φ [see Fig. 6.7(a)] for both type NC [Fig. 6.11(a)] and type C [Fig. 6.11(b)] experiments: plateaus at $\tau_{\rm ag} \to 0$ are followed by increases, whose respective values and rates are ordered according to B_0. Therefore, φ and N_c are directly related, which implies that mostly short chains grow at short times. If this were not the case, that is, if long chains prevailed, the increases of N_c would be much slowed down compared to that of φ.

The time evolution of the mean cluster size, n_c, provides insight on the kinetics of the nucleation process. As shown in Fig. 6.11(c), for type NC experiments as well as for the limit case, increases in n_c occur from a common plateau at $n_c = 2$, simultaneously at dimensionless time $\tau_{\rm ag}/\tau_{\rm ag}^c \sim 10^{-2}$, and with a very similar increase rate. In contrast, in type C experiments, n_c curves start from slightly higher plateaus and increase all the more slowly as B_0 is increased, as shown in Fig. 6.11(d). Note that the values of the plateaus at $\tau_{\rm ag} \to 0$, ranging from $n_c = 2$ to $n_c = 3$, suggest that pairs are initially the dominant population in type NC experiments, but that chains are already longer for type C experiments. Moreover, it is remarkable that, below the limit case $B_0 = 127\,\mathrm{G}$, chain growth is simultaneous whatever B_0, while for higher magnetic fields, it is all the more delayed as B_0 is increased.

These observations are echoed by our results on the mean chain length, λ_c, which measures the largest extension of the chains, as defined in Eq. 6.12 and illustrated in Fig. 6.10. The dimensionless chain length λ_c/a and chain size n_c equal each other but for a constant $+1$ when chains are composed of aligned particles. For chains that are curved or branched, λ_c grows more slowly than n_c. In type NC experiments, as shown in Fig. 6.11(e), λ_c qualitatively follows the trend drawn by n_c. But they differ quantitatively: when n_c increases from 2 to 4 (during the short times), λ_c/a only increases from 1 to 2, which reveals that the chains being formed are either branched, or curved, or both. For type C experiments, the increases of λ_c are too small for us to draw a conclusion, as shown in Fig. 6.11(f).

We measure the quantity of branching using of κ_3, the chain connectivity. Let us recall that

κ_3 is the ratio of the number of particles having 3 neighbors to the total number of particles in chains, as defined in Eq. 6.13. Again, the two types of experiments are different from each other: as shown in Fig. 6.11(g), connectivity sharply increases for type NC experiments from 0, simultaneously at a time of about $\tau_{ag}/\tau_{ag}^c = 10^{-1}$ and past the short time limit, while for experiments of type C, branching essentially does not occur at short times, as shown in Fig. 6.11(h). Hence, at short times, connectivity either increases simultaneously and sharply (B_0 below the limit case), or it remains zero (B_0 larger than the limit case).

In a nutshell, at short times: first, the total number of chains, N_{all}, increases in response to the increase of φ, suggesting that mostly short chains are formed. This is confirmed by the slowly increasing mean chain size, n_c, whatever B_0; second, for experiments of type NC and for the limit case, chains grow simultaneously and at similar rates, which occurs in parallel with a strong branching; third, in experiments of type C, chains are initially larger but they grow slowly and at a decreasing rate as B_0 increases, and they are essentially not branched.

At this stage, it is tempting to go beyond the general picture given by cluster-averaged quantities such as n_c or λ_c and have a look at the distributions of the measures averaged to produced them, like the individual numbers of particles in a chain, n_c^1, or the individual chain lengths, λ_c^1. By doing so, we can estimate the exchange fluxes between the different populations of sizes of chains. The mean number of particles per chain, n_c, provides the most straightforward piece of information for characterizing the chains: therefore we will analyze n_c instead of λ_c. We now investigate the time evolution of the probabilities of finding n-particle-long chains (with $n = n_c^1 \geq 2$) among all the chains, which we simply call *populations* of n-particle-long chains. Note that these populations are "relative" to the others, and their values are between 0 and 1.

In Fig. 6.12 are plotted the populations of 2-, 3-, 4-, 5- and more-than-5-particle-long chains (respectively, from top to bottom). As in Fig. 6.11, the left column is dedicated to type NC experiments, and the right column to type C experiments. We observe, again, a marked distinction between the two types.

For type NC experiments (limit case $B_0 = 127\,\mathrm{G}$ included), right after the magnetic quench, the population of chains is almost solely composed of pairs [Fig. 6.12(a)]. This population then decreases and approaches extinction (10 % of the total) when $\tau_{ag}/\tau_{ag}^c = 5\times10^{-1}$. Simultaneously, longer chains replace them, among which trimers are by far the most represented [Fig. 6.12(c)]: more than 60 % of all chains are trimers at the end of short times. The population of 4-particle-long chains starts growing shortly after that of trimers, but the amplitude of this increase is quite small [Fig. 6.12(e)]. In contrast, the population of 5-particle-long chains grows after an even longer time delay at a rate which apparently does not depend on B_0, but whose maximum does increase with B_0. The longer chains grow from an even longer time ($\tau_{ag}/\tau_{ag}^c \sim 10^{-1}$) and as such, become non-zero only at the very end of the short times [Fig. 6.12(i)].

Experiments of type C (limit case $B_0 = 127\,\mathrm{G}$ excluded) display much different initial composition and time evolution of their populations. Indeed, for $\tau_{ag} \to 0$, pairs only account for half of the chains [Fig. 6.12(b)], trimers for one third [Fig. 6.12(d)] and 4- and 5-particle-long chains [Fig. 6.12(f, h)] for the rest. As for type NC experiments, longer chains do not exist at very short times [Fig. 6.12(j)]. However, in contrast with experiments of type NC, here there is no abrupt change of behavior in any of these populations: the population of pairs decreases steadily and all the more slowly as B_0 increases, the population of trimers is roughly stable, the population of 4-particle-long chains very slowly increases, the population of 5-particle-long chains increases steadily but all the more slowly as B_0 increases, and the longer chain population remain negligible (below 5 %).

Finally, at short times and for both types of experiments, we observe, as suggested by the

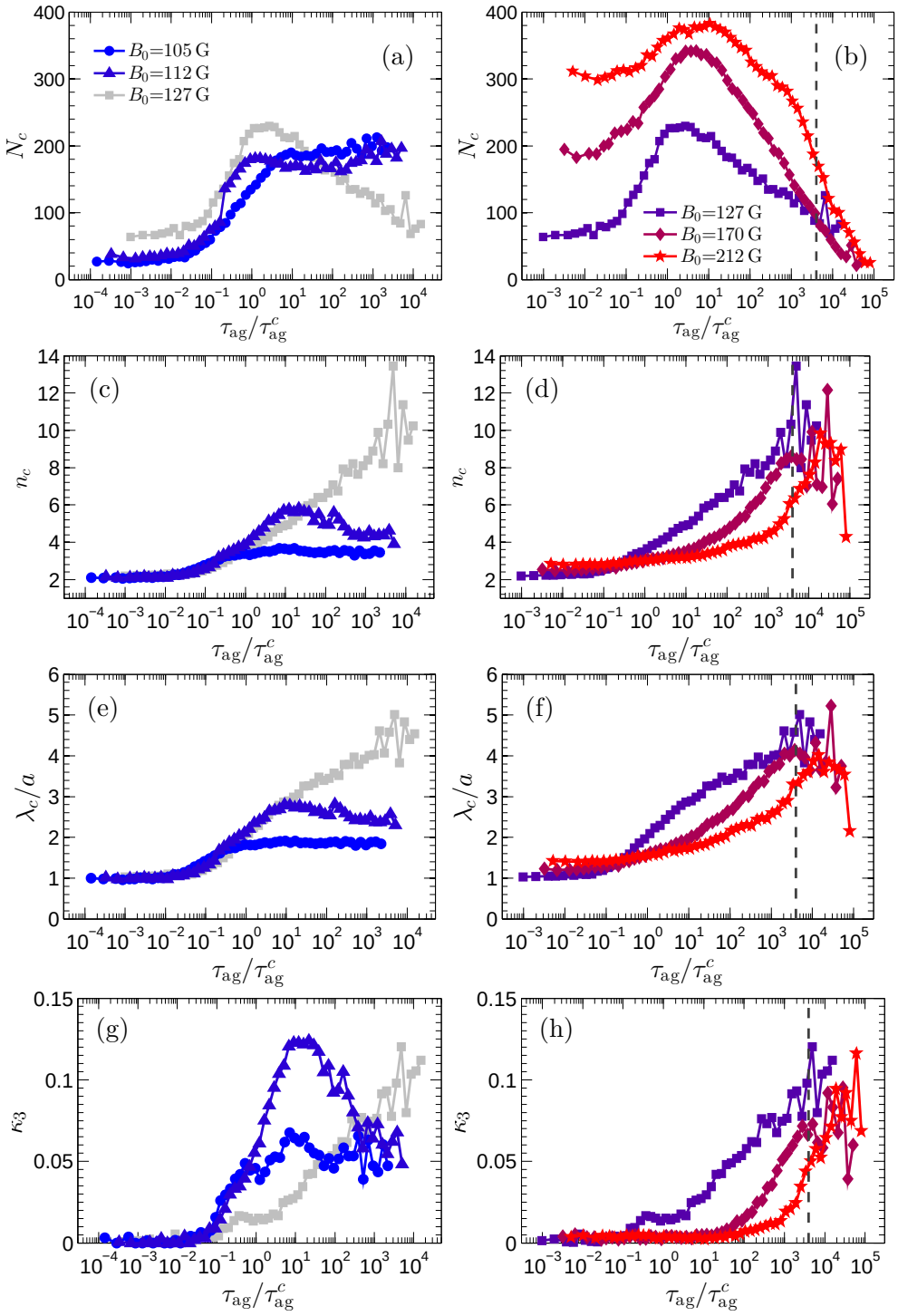

Figure 6.11 Chain morphology characterization for type NC experiments (left column) and for type C experiments (right column). (a, b) Number of chains accepted by the algorithm, N_c; (c, d) Mean number of particles per chain, or mean *chain size*, n_c; (e, f) Mean nondimensional chain linear extension, or mean nondimensional *chain length*, λ_c/a; (g, h) Mean fraction of particles in a chain with three neighbors, or mean *chain connectivity*, κ_3. The vertical black dashed line in (b, d, f, h) indicates the limit of validity of the algorithm, as defined from Fig. 6.9.

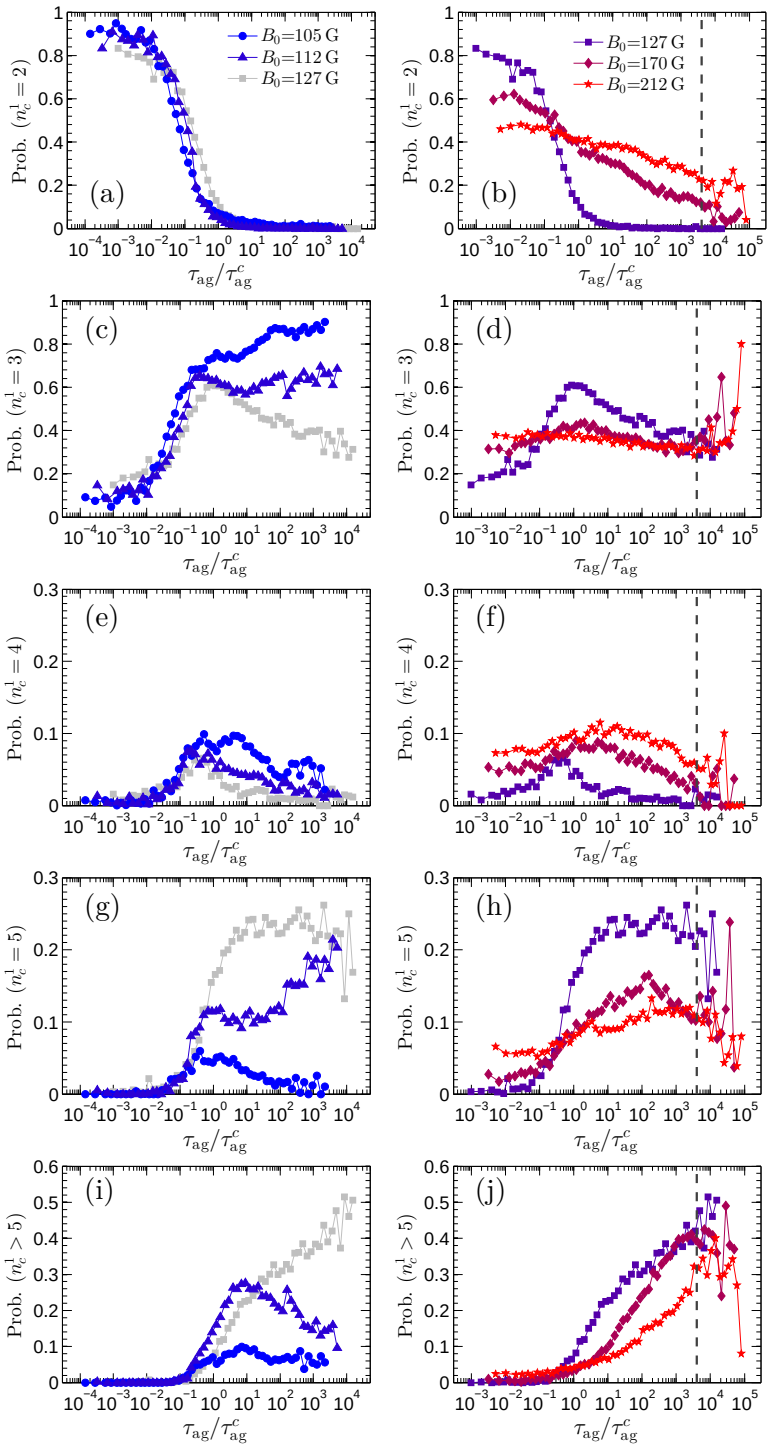

Figure 6.12 Probability, or relative *population*, of n-particle-long chains ($n = n_c^1 > 2$) for type NC experiments (left column) and type C experiments (right column). (a, b) Population of pairs; (c, d) Population of trimers; (e, f) Population of 4-particle-long chains; (g, h) Population of 5-particle-long chains; (i, j) Population of more-than-5-particle-long chains. The vertical black dashed line in (b, d, f, h) indicates the limit of validity of the algorithm, as defined from Fig. 6.9.

measures of N_c, n_c and λ_c in Fig. 6.11, that the most represented populations of chains are those of pairs and trimers. For type NC experiments (limit case included), the growth of chains is hierarchical: pairs and free particles associate to become trimers, which themselves grow a short time afterwards into 4-particle-long chains, which later form 5-particle-long chains, and so on. The time at which trimers start to develop, namely $\tau_{\mathrm{ag}}/\tau^c_{\mathrm{ag}} \sim 10^{-2}$, corresponds to the start of the increase of n_c and λ_c. Moreover, the sharp increase of more-than-5-particle-long chains occurs simultaneously with the increase of κ_3, which reveals the branched nature of these long chains. For type C experiments (limit case excluded), hierarchical growth is less obvious since exchanges between the different populations are not clear. However, the observed slowing down of the decrease (resp., increase) of the population of pairs (of 5-particle-long chains) with B_0, is representative of the slowing down of the growth of n_c and λ with B_0. As a final note, it is remarkable that the growing and branching rates evolve at short times in the same way as the characteristic time of nucleation, τ^c_{ag}, *i.e.*, they decrease with B_0, which means that if a higher magnetic field favors quick short chain nucleation, it also slows down the development of these chains into larger, branched clusters.

6.4.2 Dynamics

Let us now focus on the dynamical aspects of steady nucleation, at short times. We consider, first, the mean kinetic energy of the particles, and then the mean square displacement of the particles. These two quantities are averaged, in particular, over the ensemble of particles present on each frame, which means that the contributions from free and in-chain particles are not distinguished.

Mean kinetic energy per particle

In Fig. 6.7, we plotted the mean kinetic energy per particle, E_c, as a function of the aging time, τ_{ag}. We observed that the general shape of the curves of E_c is similar to the one of the curves of φ. In fact, we can quantitatively relate E_c and φ from the idea mentioned in Section 6.3.3, that because particles in the buckled chains are mostly immobile in the cell reference frame, the greater contribution to E_c comes from the free particles. Let us denote $E^1_c(i)$ the amount of kinetic energy carried by the single particle of index i. This quantity depends *a priori* on each particle and on time.

In order to evaluate how $E^1_c(i)$ depends on the particle, let us go back to Chapter 4. We have shown there that, from a high enough magnetic field, the mean kinetic energy of the free particles decreases with B_0, B_0 being then a measure of the confinement strength [see Fig. 2(a) in our EPL article [1], for $B_0 > 80\,\mathrm{G}$]; hence $E^1_c(i)$ decreases with the confinement strength. Now, for a fixed magnetic field, confinement decreases when the mean distance between particles increases. In the present experiments, the use of a plateau of magnetic field at $B_p = 85\,\mathrm{G}$ before the magnetic quench, as explained in Section 1.2.1, ensures that free particles all have similar nearest-neighbor distances, at least at short times. Consequently, we can consider that all free particles carry the same amount of kinetic energy, which we simply denote E^1_c.

Moreover, as shown in Fig. 6.13, the mean distance between free particles and their neighbors, which is a measure of their confinement, remains essentially unchanged before $\tau_{\mathrm{ag}}/\tau^c_{\mathrm{ag}} = 5\times10^{-1}$. During short times, the confinement of free particles can be considered fixed, and thus it is relevant to take E^1_c as fixed too.

By denoting $N_s(\tau_{\mathrm{ag}})$ the number of free particles at aging time τ_{ag}, the mean kinetic energy then can be expressed as

$$E_c \approx N_s(\tau_{\mathrm{ag}})\, E^1_c, \tag{6.14}$$

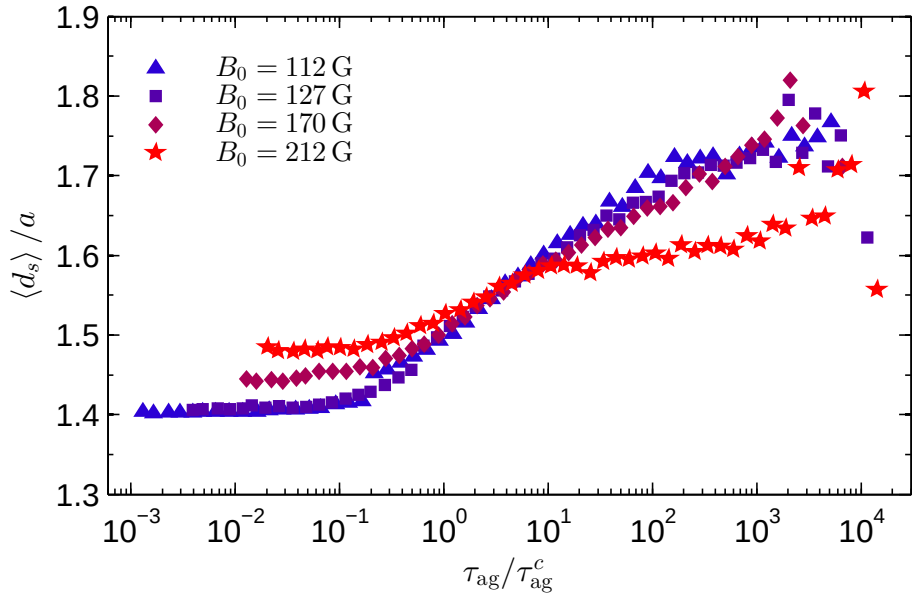

Figure 6.13 Mean distance between a free particle and its neighbors, $\langle d_s \rangle$, as measured from Delaunay tesselation, as a function of the dimensionless aging time $\tau_{\rm ag}/\tau^c_{\rm ag}$. This is a measure of the confinement of the free particles. At short times, *i.e.*, $\tau_{\rm ag}/\tau^c_{\rm ag} < 5 \times 10^{-1}$, confinement is approximately constant, but at long times, *i.e.*, $\tau_{\rm ag}/\tau^c_{\rm ag} > 5 \times 10^{-1}$, it decreases.

where $N_s = N^R_{\rm all}\,(1-\varphi)$, $N^R_{\rm all}$ being the real total number of particles (to distinguish from the total number of particles in the algorithm, $N_{\rm all}$, plotted on Fig. 6.9). Using the expression for φ given in Eq. 6.8 therefore yields

$$E_c \approx N_{\rm all}\,(1-\varphi_0)\,e^{-\tau_{\rm ag}/\tau^c_{\rm ag}}\,E^1_c. \tag{6.15}$$

Based on the above assumptions, the plateaus of kinetic energy in the limit $\tau_{\rm ag} \to 0$, namely

$$E^0_c(B_0) \equiv \lim_{\tau_{\rm ag}\to 0} E_c(B_0;\tau_{\rm ag}), \tag{6.16}$$

are simply related to the plateaus of the fraction of particles in chains, φ_0 (defined in Eq. 6.3), through $E^0_c \approx N^R_{\rm all}\,(1-\varphi_0)\,E^1_c$. This yields the approximated form of the mean kinetic energy per particle normalized by its value at short times,

$$\frac{E_c}{E^0_c} = e^{-\tau_{\rm ag}/\tau^c_{\rm ag}}. \tag{6.17}$$

In Fig. 6.14 is shown E_c/E^0_c as a function of the dimensionless aging time, $\tau_{\rm ag}/\tau^c_{\rm ag}$. As for φ_n in Fig. 6.8(b), the data points of E_c/E^0_c from all experiments satisfyingly collapse on a master curve at short times. We test our estimate of E_c at short times, namely Eq. 6.17, by comparing the exponential prediction (thick black curve in Fig. 6.14) with our experimental results. As we can see on the main plot, and better visualize in the inset in log-log scale, the exponential fit is suited to the master curve at short times, although it is not as satisfying as Eq. 6.9 is for representing φ_n: Eq. 6.17 slightly overestimates the kinetic energy. It may be possible to improve our estimate of E_c by taking into consideration that free particles are not exactly confined all with the same strength (*i.e.*, the E^1_c's are not all equal), and that confinement is not strictly

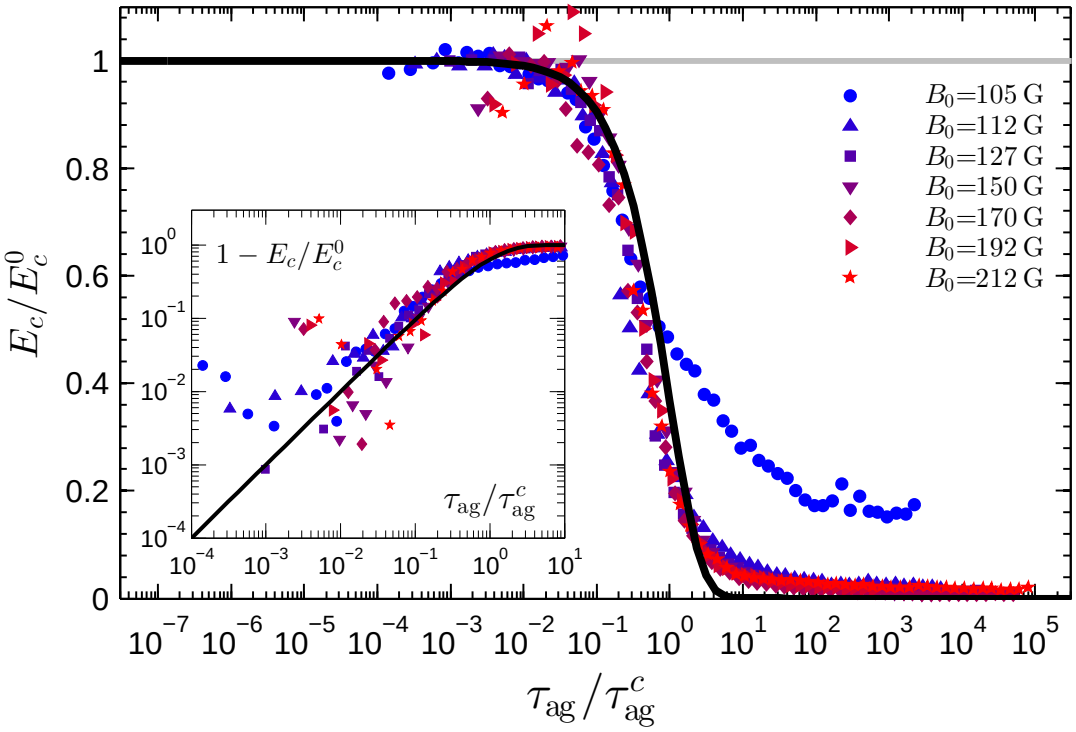

Figure 6.14 Mean kinetic energy per particle, E_c, divided by its plateau values at very short aging times, $E_c^0(B_0)$, as a function of the dimensionless aging time, τ_{ag}/τ_{ag}^c. All curves satisfyingly collapse on a master curve, except for the set of experiments with $B_0 = 105\,\mathrm{G}$, which departs from the master curve at the end of short times. The thick black curve represents the exponential decay predicted in Eq. 6.17. It is shifted with respect to the experimental data, but has a shape that matches them well. Inset: $1 - E_c/E_c^0$ as a function of τ_{ag}/τ_{ag}^c in log-log scale.

constant for all short times (*i.e.*, the E_c^1's are time-dependent).

Mean square displacements

Another way to characterize the dynamics is to measure the amount of space explored by the particles during a given time. This can be achieved by measuring the mean square displacement (MSD) of the particles, which we denote $\langle r^2 \rangle$ and which is defined as:

$$\langle r^2(t) \rangle = \left\langle \frac{1}{N_p^t} \sum_{i=1}^{N_p^t} |\mathbf{r}_i(t - \tau_0) - \mathbf{r}_i(\tau_0)|^2 \right\rangle, \tag{6.18}$$

where $\langle \cdot \rangle$ denotes an ensemble average, time t is larger than τ_0, the time at which the recordings are started, as defined in Section 1.2.1, $t - \tau_0$ is called the *delay time*, N_p^t is the number of particles at time t, and $\mathbf{r}_i(t)$ is the position of particle i at time t.

The MSD of particles undergoing a ballistic motion increases as the square of the delay time:

$$\langle r^2 \rangle \propto (t - \tau_0)^2, \tag{6.19}$$

while for Brownian particles confined in two dimensions, the MSD is related to the delay time

by a linear relation implying a *coefficient of diffusion*, or diffusivity, D, as

$$\langle r^2 \rangle = 4D(t - \tau_0), \tag{6.20}$$

a formula which directly comes from the central limit theorem and the Markovian nature of the underlying stochastic process.

For systems of particles with either broad displacement distributions or long-range correlations, the diffusion is anomalous and does not follow Eq. 6.20 [114]. In this case, the linear relationship between the MSD and the delay time in Eq. 6.20 is modified into the non-linear relationship:

$$\langle r^2 \rangle = 4D_\alpha(t - \tau_0)^\alpha, \tag{6.21}$$

where α is an *anomalous diffusion exponent* and D_α is a *generalized coefficient of diffusion*. The motion is characterized as *superdiffusive* if $\alpha > 1$, which is for example the case of Richardson turbulent diffusion, transport in micelle systems and bacterial motion; and it is called *subdiffusive* if $0 < \alpha < 1$, which corresponds for instance to the reptation dynamics in polymeric systems, transport on fractal geometries, and the dynamics of a bead in a polymeric network [114], and more generally to situations where particles can get randomly trapped.

Here, we study the MSD of particles in the set of experiments with $B_0 = 170\,\mathrm{G}$, which is representative of type C experiments, because it has an intermediate characteristic nucleation time [see Fig. 6.8(a)-(inset)]. We use an acceleration $\Gamma = 2$ and a magnetic quenching rate $\alpha_q = 10^3\,\mathrm{G.s^{-1}}$ so that our results are directly comparable with the other experiments of this chapter.

Let us remark that if MSD recordings starting at a time τ_0 provide a picture of the dynamics of the system as it evolves *from the state it was in* at time τ_0, they do not represent the dynamics of the state of the system *around* time τ_0. In our experiments, we use starting times τ_0 shorter than, or of the order of magnitude of, the characteristic nucleation time $\tau^c_{\mathrm{ag}}(B_0 = 170\,\mathrm{G}) \approx 2.0 \times 10^{-1}\,\mathrm{s}$ [see Fig. 6.8(a), inset], so as to explore the displacements of particles originating from states belonging to the short aging time regime.

Our measurements of the MSD as a function of the delay time, $t - \tau_0$, are presented in Fig. 6.15. For delay times shorter than $t - \tau_0 = 10^{-2}\,\mathrm{s}$, particles undergo a ballistic motion whatever the starting time τ_0 (slope 2 in the log-log plot corresponding to Eq. 6.19). In such a time range, particles behave as projectiles whose kinetic energy is obtained from collisions with the bottom plate. This ballistic motion is arrested, however, by the interaction with a neighboring particle: either the two particles repel each other and hence reverse or deflect each other's trajectories, or they aggregate to form a pair or extend an already existing chain. This type of event occurs at delay times $t - \tau_0 \approx 3 \times 10^{-2}\,\mathrm{s}$ and corresponds to an inflection point in the MSD. For longer delay times, two types of behaviors emerge: for very short starting times $\tau_0 < 5 \times 10^{-2}\,\mathrm{s}$, the MSD increases monotonically according to an anomalous diffusion law with exponents smaller than 1/4, while for longer starting times $\tau_0 > 5 \times 10^{-2}\,\mathrm{s}$, a temporary saturation of the MSD, which is the hallmark of caging effects [43, 115, 116, 117], is followed by an anomalous diffusion regime with exponent $\alpha \approx 1/2$.

Note that the "age" of the system when caging arises, namely the sum of the starting time of the first experiment displaying an intermediate plateau ($\tau_0 = 5.62 \times 10^{-2}\,\mathrm{s}$) and of the delay time at which the plateau appears ($t - \tau_0 \approx 4 \times 10^{-2}\,\mathrm{s}$), is $t_c \approx 10^{-1}\,\mathrm{s}$. Now, Table 6.1 provides $\tau^c_{\mathrm{ag}}(B_0 = 170\,\mathrm{G}) = 2.0 \times 10^{-1}\,\mathrm{s}$, hence $t_c/\tau^c_{\mathrm{ag}} \approx 1/2$. Therefore caging arises at a dimensionless time $t_c/\tau^c_{\mathrm{ag}} \approx 5 \times 10^{-1}$, *i.e.*, at the end of steady nucleation. We can interpret this result as follows: a significant fraction of free particles nucleates during steady nucleation, which leads

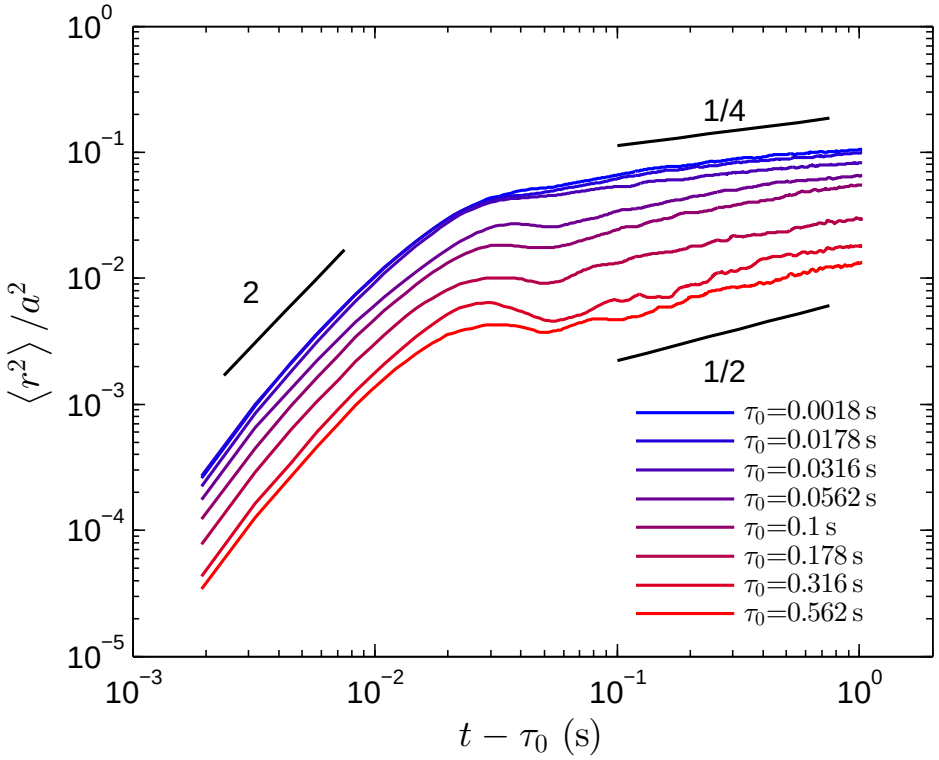

Figure 6.15 Mean square displacements, non-dimensionalized by the particle diameter, for $B_0 = 170\,\mathrm{G}$. The time τ_0 is the time from which MSD measurements are performed, and $t-\tau_0$ is the delay time. As for glassy systems, the caging effect arises: the MSD temporarily saturates between the ballistic regime at very short times and the subdiffusive regime at longer times.

to a decrease of the confinement of the remaining free particles, as shown in Fig. 6.13, hence making the causing effect. Then, the remaining free particles are caged for some time before they nucleate in turn.

To summarize, at all times the initial motion of particles is ballistic, inside a cage, then nucleation occurs either without ($\tau_0 < 5 \times 10^{-2}\,\mathrm{s}$) or with the occurrence of a caging effect ($\tau_0 > 5 \times 10^{-2}\,\mathrm{s}$). The subsequent motion at longer times is subdiffusive, with an anomalous exponent increasing from below 1/4 towards 1/2 with τ_0.

6.4.3 Partial conclusion for short times

In this section, we studied the formation of the labyrinthine phase at short times, after a sharp magnetic quench is applied to the system in a liquid-like ("elastic") phase. Right after the quench, the system is composed of coexisting free particles and chains, the fraction of free particles decreasing with the magnetic field.

We interpreted the chain growth as an irreversible, *steady nucleation* process, which corresponds to an exponential increase of the fraction of particles in chains. For each value of the magnetic field, we measured a characteristic nucleation time, which we used as the relevant time scale for non-dimensionalizing the aging time. Mostly based on the hypothesis of weak structural rearrangements, we estimated the mean kinetic energy per particle to be decreasing exponentially.

We demonstrated that after the quench, chains in type NC experiments (those which do not fully "solidify" at long times, limit case $B_0 = 127\,\mathrm{G}$ included) are mostly pairs, which serve

as a basis for a subsequent hierarchical growth, itself corresponding to quick chain growth and branching, simultaneously for all experiments. In contrast, longer chains already exist after the quench for type C experiments (those which fully "solidify" at long times, limit case $B_0 = 127\,\mathrm{G}$ excluded), which have growth rates that decrease as B_0 increases, and essentially no branching.

Using the mean square displacements on the example of $B_0 = 170\,\mathrm{G}$, we shed the light on the caging effect arising at the end of steady nucleation, and connected it to the simultaneous loosening of the confinement of the remaining free particles. This confirmed that steady nucleation ends at a dimensionless time of about $\tau_{\mathrm{ag}}/\tau_{\mathrm{ag}}^{c} = 5 \times 10^{-1}$.

An exciting perspective is to view the irreversible nucleation process that we analyzed in this section as analogous to a transition from an agitated state to an absorbing state. An absorbing state is a particular out-of-equilibrium state that can be reached by the dynamics of the particles but cannot be left, and which is characterized by total freezing of the relevant degree of freedom of the particles [118, 119]. In such a state, fluctuations are completely absent. Hence, the irreversible nature of the transition that we observe in our system from the "free", agitated state into the "chain" state, in which particles are essentially "frozen", makes encouraging to use our system for testing a certain type of transition to an absorbing phase. Future work in this direction should include, in particular, a more complete analysis of the characteristic nucleation times and of the spatial correlations between the chains.

6.5 Coarsening of the labyrinthine phase at long times

In Section 6.4, we characterized the development of the chains constituting the granular labyrinthine phase right after the magnetic quench. We found that, generally speaking, the nucleation of free particles into chains is such that the growth of the chains is hierarchical (*i.e.*, from pairs to trimers to 4-particle-long chains, and so on), and that pairs and trimers constitute the vast majority of the chains. We identified at short times a *characteristic nucleation time* for each value of the magnetic field, $\tau_{\mathrm{ag}}^{c}(B_0)$, which proved to be the relevant time scale as long as structural rearrangements are negligible.

Yet, at the end of the short times, *i.e.*, around $\tau_{\mathrm{ag}}/\tau_{\mathrm{ag}}^{c} \sim 5 \times 10^{-1}$, there remain a number of free particles that have not nucleated yet, but which will do so at *long times*, *i.e.*, for $\tau_{\mathrm{ag}}/\tau_{\mathrm{ag}}^{c} > 5 \times 10^{-1}$. Nucleation hence continues, even though in a different way. Moreover, given that the time scales in this section are much larger than in Section 6.4, processes much slower than free particle nucleation, such as chain motion, become relevant. Indeed, already at the end of the short times, we identified for type NC experiments a sharp increase of the connectivity associated with the growth of long chains: some chains have moved and connected with each other. Therefore at long times chain rearrangements can play a major role.

Thus we ask: What are the characteristics of this new long time regime, where free particle nucleation meets chain rearrangements?

6.5.1 Structure

At the end of steady nucleation, about half of the particles that were free at the end of the magnetic quench have nucleated into chains. How fast does the remaining half nucleate at long times? Moreover, this continuing nucleation is associated with structural changes, in particular

with a decrease of free particle confinement. Can we relate these changes to the appearance of specific morphological features?

Fraction of particles in chains

In order to highlight the long time convergence (resp., divergence) of the fraction of particles in chains towards (from) 1 for type C (type NC) experiments, we show $1-\varphi_n$ on a log-log scale in Fig. 6.16. In this way, the short time changes of φ_n, which we studied in Section 6.4, are mostly invisible.

As shown in Fig. 6.8(b) (in Section 6.4), at the limit of validity of steady nucleation, that is, around $\tau_{\mathrm{ag}}/\tau_{\mathrm{ag}} \sim 5\times10^{-1}$, the increase of φ_n significantly slows down compared to the proposed exponential growth. This change of behavior is made even more obvious in Fig. 6.16: all curves of $1-\varphi_n$ (except for the lowest magnetic field $B_0 = 105\,\mathrm{G}$) are deflected downwards from $\tau_{\mathrm{ag}}/\tau_{\mathrm{ag}} \sim 5\times10^{-1}$, not as an exponential, but as a power law of exponent $-1/2$, over two decades of dimensionless time. This power law decay characterizes the continuing nucleation occurring at long times, and it can be explained by a characteristic time of nucleation varying as $(1-\varphi_n)^2$ [120]. As this process occurs, the fraction of free particles is divided by 10, reaching a value of a few percent at around $\tau_{\mathrm{ag}}/\tau^c_{\mathrm{ag}} = 10^2$, that is, fifty or so free particles. Beyond that time, the accelerated decrease of $1-\varphi_n$ most probably arises from finite-size effects; indeed, the number of free particles being finite, $1-\varphi_n$ must diverge towards $-\infty$ within a finite time. Note that our accuracy on $1-\varphi_n$ corresponds to a single remaining free particle, *i.e.*, $1-\varphi_n \sim 10^{-3}$, and is indicated by the horizontal black dashed line in Fig. 6.16. Note also that for experiments of type NC, no divergence is observed since, by definition, for them the fraction of particles in chains does not reach 1.

To conclude, the continuing nucleation process that occurs at long times is very slow compared to *steady nucleation* at short times and is characterized by an increase of the fraction of particles in chains, φ, as the square root of the dimensionless time, $\tau_{\mathrm{ag}}/\tau^c_{\mathrm{ag}}$.

Chain morphology

In order to characterize the structural changes affecting the labyrinthine phase at long times, let us now turn to chain statistics. Note that in this paragraph, we use Fig. 6.9, Fig. 6.11 and Fig. 6.12, which are plotted in Section 6.4.

Our algorithm, as mentioned in Section 6.4, excludes clusters that intersect with the image boundaries. As shown in Fig. 6.9, the very slow decrease at short times of the total number of accepted particles, N_{all}, is followed by an accelerated drop from $\tau_{\mathrm{ag}}/\tau^c_{\mathrm{ag}} \sim 5\times10^{-1}$. For type NC experiments [Fig. 6.9(a)], this decrease saturates at times around $\tau_{\mathrm{ag}}/\tau^c_{\mathrm{ag}} = 10^2$. In contrast, for type C experiments [Fig. 6.9(b)], the decrease is more moderate until $\tau_{\mathrm{ag}}/\tau^c_{\mathrm{ag}} = 10^2$-$10^3$, but then N_{all} dramatically drops down towards 0. The limit case $B_0 = 127\,\mathrm{G}$ has an intermediate behavior: marked, steady decrease for all $\tau_{\mathrm{ag}}/\tau^c_{\mathrm{ag}} > 5\times10^{-1}$, but no divergence at very long times.

It is essential to understand the meaning of the huge drops of N_{all} for type C experiments: then, the greatest part of the particles found in the region of interest are excluded from our analysis of the chains, which, in turn, significantly biases it. We concede that the trick that we used in our algorithm backfires here: it becomes irrelevant when the chance that a cluster intersects the image boundaries becomes too large. Evaluating such a limit of validity is, however, not an easy task since it depends on the time evolution of the populations of chains of different sizes. Here, we consider our results as trustworthy until the decrease of N_{all} appears to be too fast to be likely to arise from a physical mechanism, a guess which will be validated *a posteriori*

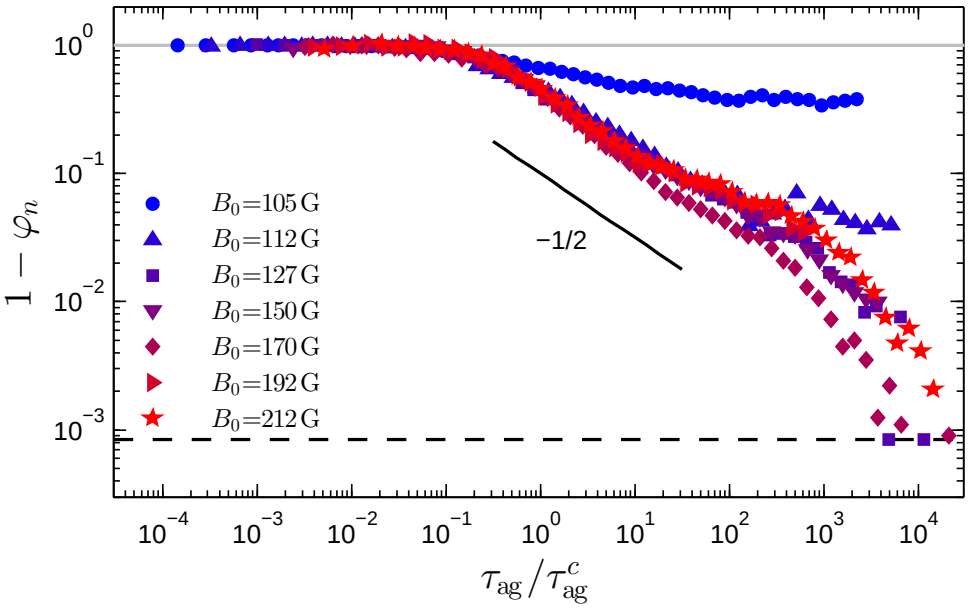

Figure 6.16 Shifted opposite of the reduced fraction of particles in chains, $1-\varphi_n$, with emphasis on the long time behavior, as a function of the dimensionless aging time, τ_{ag}/τ^c_{ag}. From the times at which the exponential fit given in Eq. 6.9 fails to describe the curves (*i.e.*, $\tau_{ag}/\tau^c_{ag} \sim 5\times10^{-1}$), $1-\varphi_n$ decreases as a power law with exponent $-1/2$ over two decades of time, for all experiments except for $B_0 = 105$ G. The accelerated decrease of $1-\varphi_n$ at very long times is most probably due to the finite number of particles. The horizontal black dashed line shows our experimental resolution on $1-\varphi_n$, which is relative to detecting one single free particle. The horizontal grey line indicates $1-\varphi_n = 1$.

by our measurements of the mean chain size, n_c, as explained below. Based on our results with $B_0 = 170$ G, we choose as an indicative limit of validity the value $\tau_{ag}/\tau^c_{ag} = 4\times10^3$ (note that this value may be adjusted for every value of B_0). We indicate it by the vertical black dashed line in Fig. 6.9(b), as well as in Fig. 6.11 (right column) and in Fig. 6.12 (right column). Note that it may be possible to balance this drawback from a study of how the probability of excluding a chain varies with its size, curvature, etc., but this is a complex question that we do not tackle here.

In Fig. 6.11 (in Section 6.4), we plotted the mean total number of clusters accepted by the algorithm, N_c, the mean chain size n_c, the mean chain length λ_c and the mean chain connectivity κ_3, at all times. Here, we focus on the long time limit, *i.e.*, one times such that $\tau_{ag}/\tau^c_{ag} > 5\times10^{-1}$.

In this time range, the total number of clusters, N_c, does not behave similarly to φ as it does at short times. Indeed, for type NC experiments, N_c temporarily saturates and then only very slowly increases: almost all the clusters are formed during steady nucleation, at short times [Fig. 6.11(a)]. For type C experiments, the dramatic and continued decrease of N_c from the end of steady nucleation can only mean that chains massively merge into larger clusters [Fig. 6.11(b)]. Indeed, this decrease cannot be attributed to the exclusion of clusters by the algorithm before times near the limit of validity defined above, which is represented by the vertical black dashed line in Fig. 6.11(b).

The study of the mean chain size, n_c, reveals a surprising result: for experiments of type NC [Fig. 6.11(c)], while n_c for $B_0 = 105$ G simply saturates, it clearly decreases for $B_0 = 112$ G. The latter result is more unexpected since, exclusion of clusters by the algorithm being negligible at this stage, this means that some of the chains formed at short times split up into shorter

chains: hence chain formation is not irreversible. As shown in [Fig. 6.11(d)], the picture is totally different for experiments of type C: n_c only increases. More precisely, n_c for $B_0 = 127\,\mathrm{G}$ follows a very steady increase, while for $B_0 = 170\,\mathrm{G}$ and $212\,\mathrm{G}$, it goes from slow to accelerated at dimensionless times of about, respectively, 10^2 and 10^3: the higher B_0, the more delayed and the sharper is the late-time increase of n_c. It is not possible, unfortunately, to arrive at possible asymptotic values of n_c at very long times, due to both noise in the measurements (experiments are not repeated for $\tau_{\mathrm{ag}} \geq 10^4\,\mathrm{s}$) and the limit of validity of our algorithm.

As shown in Fig. 6.11(e, f), the behavior of the mean chain length, λ_c, leads to the same comments as in the short time limit: trends of λ_c are similar to those of n_c, but increases are much slower than they should be if the chains were straight and unbranched. For the limit case $B_0 = 127\,\mathrm{G}$, we possibly detect a saturation of λ_c at very long times, as is the case for type NC experiments, but we cannot make a firm conclusion from the present data set.

The measures of the mean chain connectivity, or fraction of particles in chains with three neighbors, κ_3, are far from being as trivial in the long time range as they were in the steady nucleation regime, in which κ_3 was essentially zero. At long times, κ_3 quickly saturates for $B_0 = 105\,\mathrm{G}$, but rises high for $B_0 = 112\,\mathrm{G}$ before it drops down to reach around 5 % [Fig. 6.11(g)]. This local maximum of κ_3 seems to correspond to the local maximum of n_c and λ_c, suggesting that the chains that split do so at branching points. Note that such splitting event seems to occur only when free particles coexist with chains. For type C experiments [Fig. 6.11(h)], κ_3 follows the same trend as n_c: it increases with a delay and a sharpness all the more high as B_0 is increased.

Finally, at long times, for type NC experiments, just a few more chains are formed. They do not undergo dramatic morphological changes, except for $B_0 = 112\,\mathrm{G}$, where their mean chain size and length temporarily decrease in parallel with a burst of connectivity. For type C experiments, the number of chains rapidly drops as chains merge into larger, more branched clusters. For these experiments, chain growth and increase of connectivity are accelerated by a magnetic field as low as possible above the limit case $B_0 = 127\,\mathrm{G}$. Note that this limit case shares at long times the morphological features of type C experiments, and not those of type NC experiments as it did at short times.

The time evolution of the populations of chains 2-, 3-, 4-, 5- and more-than-5-particles-long is plotted in Fig. 6.12 (in Section 6.4). We keep focusing on times such that $\tau_{\mathrm{ag}}/\tau_{\mathrm{ag}}^c > 5 \times 10^{-1}$.

For type NC experiments, there are essentially no more pairs at long times [Fig. 6.12(a)]. The population of trimers is dominant [Fig. 6.12(c)], but leaves all the more room to 5- and more-than-5- particle-long chains as B_0 approaches its limit case value, namely 127 G [Fig. 6.12(e, g)]. This echoes the behaviors of n_c and λ_c in Fig. 6.11(c, e), whose long-time limits increase with B_0. Moreover, the absence of pairs means than free particles do not aggregate to create pairs anymore, hence contributing to keeping N_c constant. The population of 4-particle-long chains is very low at very long times.

For type C experiments, the decrease of the populations of pairs [Fig. 6.12(b)] and 4-particle-long chains [Fig. 6.12(f)], the stabilization of the trimers [Fig. 6.12(d)], and the increase of the populations of 5- and more-than-5-particle-long chains [Fig. 6.12(h, j)], are all the more enhanced and less delayed as the magnetic field is close to its limit case value, 127 G. In particular, the delays in the increases of 5- and more-than-5-particle-long chains reflect the delays of the increases of the chain size, n_c, and length, λ_c.

Moreover, for all experiments, the similarities between the time evolution of the cumulated population of 5- and more-than-5-particle-long chains (which we do not show explicitly) and of the mean chain connectivity [Fig. 6.11(g, h)] strongly suggest that these long chains are highly

branched.

Let us point out that, for all experiments, chains with an even number of particles are much less present than chains with an odd number of particles. We can see two main reasons for this. First, gravity (and maybe friction too) favors chains with their end particles being *down* (*i.e.*, touching the bottom plate), which is the case at both ends for trimers and (unbranched) 5-particle-long chains, but only at one end of pairs and (unbranched) 4-particle-long chains. The former ones are thus more stable. Second, chains with one end *up* (*i.e.*, touching the top lid), *e.g.*, pairs and (unbranched) 4-particle-long chains, can easily attach to any other end that is *down*, the latter being easily found since in a large majority; this can only result in a decrease of the population of even chains. Note also that the attachment of one *down* (resp. *up*) end to an intermediate *up* (*down*) particle is possible too, when one chain approaches the other perpendicularly, and this results in a new branching point, *i.e.*, in increasing the connectivity, κ_3.

As a last remark, we would like to stress the very particular role of the limit case, $B_0 = 127\,\mathrm{G}$, between type NC experiments, that evolve quickly but eventually have mostly short chains, and type C experiments, that evolve with delays (increased by B_0) towards states with large chains: setting the magnetic field to $B_0 = 127\,\mathrm{G}$ enables the quick formation of long chains.

6.5.2 Dynamics

As the system relaxes, free particles keep nucleating, even though more slowly than at short times, and at the same time chains move to change configuration and possibly merge. These structural changes are associated with changes in the dynamics of the system. Now we investigate the time evolution of the mean kinetic energy per particle and of the mean square displacement of the particles. As we will see, at long times, it is relevant to compute coefficients of diffusion, which are a measure of the mobility of the particles.

Mean kinetic energy per particle

In Section 6.4 we introduced the dynamical aspects of steady nucleation using the mean kinetic energy per particle, divided by its value in the limit $\tau_{\mathrm{ag}} \to 0$, E_c/E_c^0 (Fig. 6.14). We found the decrease of E_c/E_c^0 during steady nucleation to be exponential.

Here, in order to study the long-time aging of the labyrinthine phase, we represent E_c/E_c^0 on a log-log scale, in Fig. 6.17. As for $1-\varphi_n$ in Fig. 6.16, the short time changes are flattened and we observe a power-law decay of E_c/E_c^0, between about $\tau_{\mathrm{ag}}/\tau_{\mathrm{ag}}^c \sim 3\times10^{-1}$ and 3×10^{1}. We estimate the exponent of the decay between $-3/4$ and -1 for experiments of type C and the limit case $B_0 = 127\,\mathrm{G}$, but closer to $-1/2$ for $B_0 = 112\,\mathrm{G}$. The decrease of E_c is thus faster than the increase of φ for experiments of type C and the limit case, which is due to the fact that E_c is obtained from an average over all particles, and not only over the free particles. For $B_0 = 112\,\mathrm{G}$, this effect is less pronounced because more particles remain free at long times.

An interesting feature of the curve of E_c/E_c^0 lies at very long times. Then, particles are all part of chains for experiments of type C (in particular for $B_0 = 170\,\mathrm{G}$ and $212\,\mathrm{G}$, as demonstrated by the vanishing values of $1-\varphi_n$ beyond $\tau_{\mathrm{ag}}/\tau_{\mathrm{ag}}^c \sim 10^4$, in Fig. 6.16) hence the measured mean kinetic energy is the mean kinetic energy of the particles in chains. This shows that, qualitatively, a particle in a chain has a mean kinetic energy of about $1/100^{\mathrm{th}}$ of that of a free particle right after the quench.

To summarize, mean agitation decreases sharply as more and more free particles nucleate into chains, but it clearly remains non-vanishing and experimentally measurable even when chains occupy the whole system at very long times.

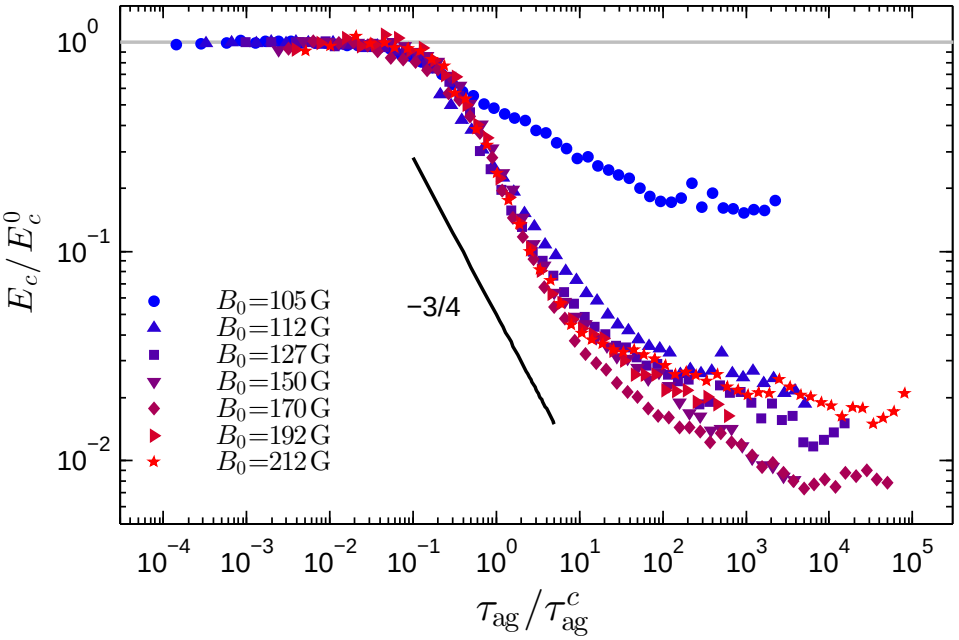

Figure 6.17 Mean kinetic energy per particle, E_c, divided by its plateau value at very short aging times, $E_c^0(B_0)$, with emphasis on the long time behavior, as a function of the dimensionless aging time, τ_{ag}/τ_{ag}^c. E_c/E_c^0 decreases as a power law of time with an exponent between $-3/4$ and -1 for $B_0 \geq 127\,\mathrm{G}$ (and closer to $-1/2$ for $B_0 = 112\,\mathrm{G}$), in the same time range than $1-\varphi_n$ decreases as a power law of time with an exponent $-1/2$, as shown in Fig. 6.16. The very long time values of E_c/E_c^0 show that the agitation of a nucleated particle is about $1/100^{\text{th}}$ of that of a free particle right after the quench. The horizontal grey line indicates $E_c/E_c^0 = 1$.

Mean square displacements

Since even particles in chains are agitated, chains can move: collective motion can arise from individual particle (low) agitation due to the strong interactions between the particles inside chains. In fact, chain motion does occur from the end of short times and across long times and has as a consequence the development of larger and more branched chains by the merging of shorter chains, as we have seen from the time evolution of the morphological characteristics of the chains, from Fig. 6.11 and Fig. 6.12.

The mean square displacement (MSD) of the particles indicates how far they have moved between starting time τ_0 and time t. We measure the MSD for experiments with an acceleration $\Gamma = 2$, a quenching rate $\alpha_q = 10^3\,\mathrm{G/s}$, and a magnetic field $B = 170\,\mathrm{G}$ (as in Section 6.4), with starting times ranging from just before the end of steady nucleation, which occurs around $\tau_{ag}/\tau_{ag}^c = 5 \times 10^{-1}$, until the longest aging times that we can reach, namely $\tau_{ag} = 10^4\,\mathrm{s}$.

Note that when the starting time, τ_0, is much larger than the duration of the recordings of the MSD, the distinction between τ_0 and the age of the system at the end of these recordings (1 s later) is irrelevant: the MSD measurement then provides a good picture of the system at age τ_0. This is the case for most of our MSD measurements in the long time limit, shown in Fig. 6.18.

A ballistic regime (curves of slope 2 in the log-log plot) is visible for all starting times until $\tau_0 \sim 100\,\mathrm{s}$. The ballistic regime shows the presence of a significant number of free particles, since particles in chains are strongly "attached" to each other due to magnetic interactions and

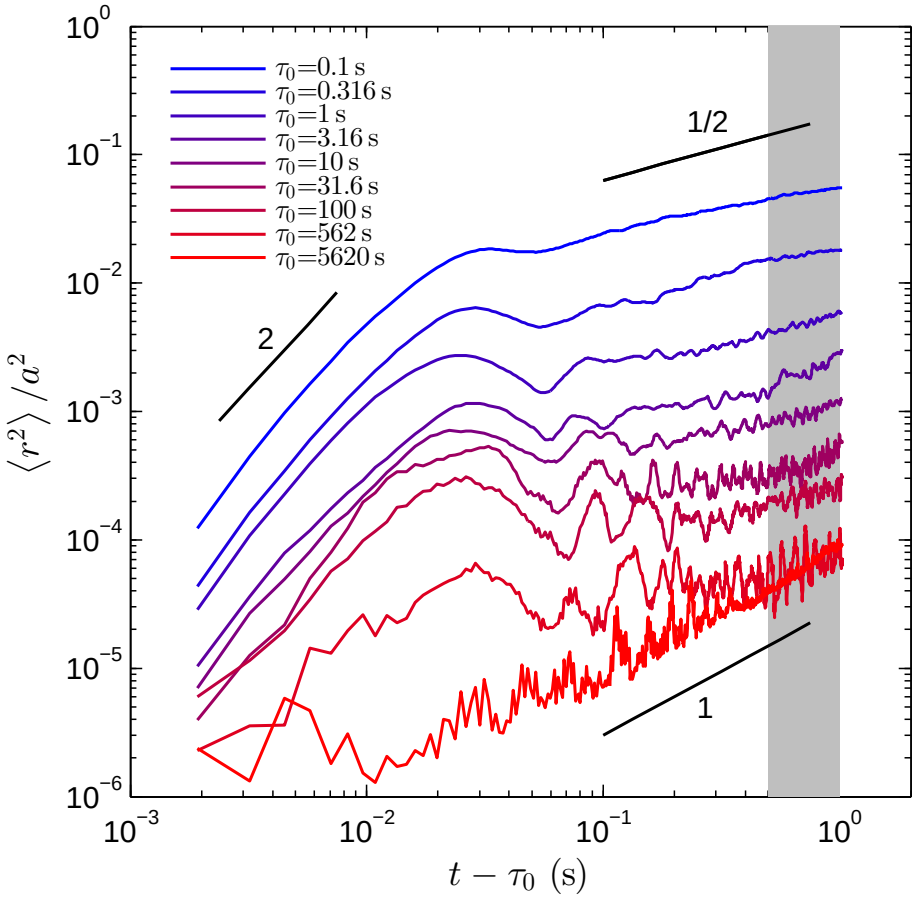

Figure 6.18 Mean square displacement non-dimensionalized by the particle diameter, $\langle r^2 \rangle / a$, for $B_0 = 170\,\mathrm{G}$. Time τ_0 is the starting time for the MSD recordings, and $t - \tau_0$ is the delay time. Caging effects tend to disappear as free particles become scarce ($\tau_{\mathrm{ag}}/\tau_{\mathrm{ag}}^c \sim 10^2$), and the long time motion goes from subdiffusive with an anomalous diffusion exponent $\alpha \sim 1/2$, to diffusive from $\tau_0 \sim 10^3\,\mathrm{s}$. To compute coefficients of anomalous diffusion, shown in Fig. 6.19, we use the data points of the MSD between $t - \tau_0 = 0.5\,\mathrm{s}$ and $1\,\mathrm{s}$, a time range indicated by the grey shading.

friction, and certainly do no undergo a ballistic motion. Using Fig. 6.16, we estimate that only a few percent of all particles are left free by times $\tau_0 \sim 100\,\mathrm{s}$. The ballistic regime is associated with a caging effect (temporary saturation of the MSD), as discussed in Section 6.4, which is itself followed by a subdiffusive regime of anomalous exponent close to 1/2 (slope 1/2 in the log-log plot).

At larger starting times, the ballistic motion progressively dies off, as the motion tends to become diffusive only (slope 1 in the log-log plot), at all delay times studied here. At these very long times, free particles essentially disappear and there only remain particles in chains. This result suggests that particles in chains diffuse on scales of $(10^{-5}\,a^2)^{1/2} \approx 3 \times 10^{-3}\,a$, with a the particle diameter, which remains within our detection range according to our estimate of detection accuracy: $\delta \sim 5 \times 10^{-4}\,a$, as given by Eq. 2.25.

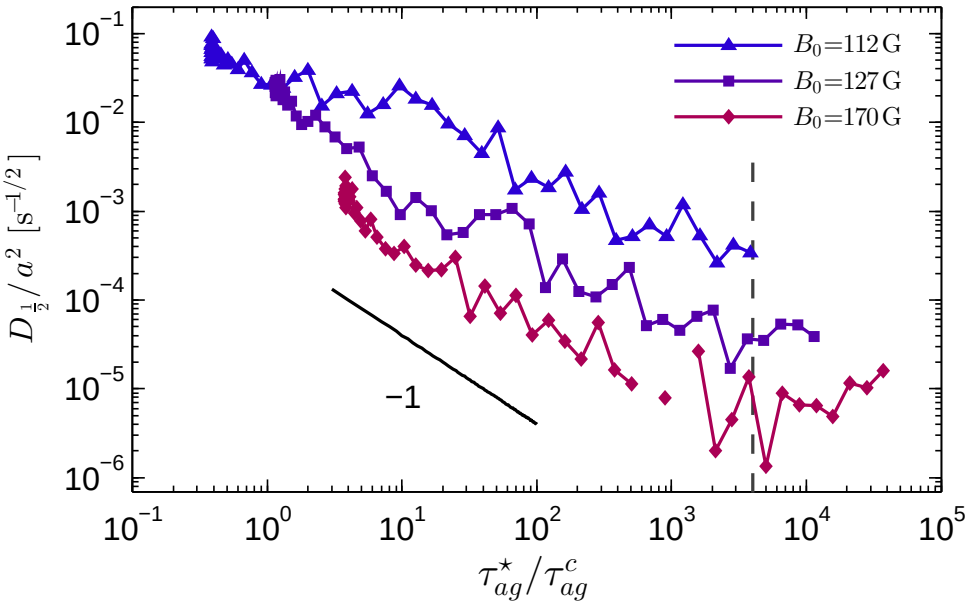

Figure 6.19 Generalized coefficients of diffusion, $D_{\frac{1}{2}}$, as a function of the dimensionless modified aging time, $\tau^\star_{\rm ag}/\tau^c_{\rm ag}$. The coefficients $D_{\frac{1}{2}}$ are obtained from fits of the mean square displacements between $t-\tau_0 = 0.5\,$s and 1 s, according to the equation of anomalous diffusion, namely Eq. 6.21, with exponent $\alpha = 1/2$. The modified aging time is defined as $\tau^\star_{\rm ag} = \tau_0 + \bar{\tau}_{\rm MSD}$, with $\bar{\tau}_{\rm MSD} = 0.75\,$s the mean delay time of the MSD data used in the computation of $D_{\frac{1}{2}}$. For all types of experiments (*i.e.*, type NC with $B_0 = 112\,$G, limit case with $B_0 = 127\,$G, and type C with $B_0 = 170\,$G), the coefficients $D_{\frac{1}{2}}$ decay as the inverse of time, until they each reach a plateau from $\tau^\star_{\rm ag}/\tau^c_{\rm ag} \sim 4\times10^3\,$s (at least for $B_0 = 127\,$G and 170 G), a time indicated by the vertical black dashed line.

Generalized coefficients of diffusion

The subdiffusive motion of particles at long delay times, which we almost always observe in our experiments (in Fig. 6.18, but also in Fig. 6.15 at shorter times), is not only characterized by an anomalous diffusion exponent, α, but also by a generalized coefficient of diffusion, D_α. Indeed, let us recall here Eq. 6.21, which is the nonlinear relation between the MSD, $\langle r^2\rangle$, and the delay time, $t-\tau_0$, using α and D_α:

$$\langle r^2\rangle = 4D_\alpha (t-\tau_0)^\alpha. \tag{6.22}$$

In our experiments with $B_0 = 170\,$G, we found for starting times larger than $\tau_0 = 1\,$s that α takes values close to 1/2, as shown in Fig. 6.18 (except for the largest τ_0). We therefore compute generalized coefficients of diffusion from fits of the MSD plotted in Fig. 6.18, between delay times $t-\tau_0 = 0.5\,$s and 1 s (vertical black dashed lines in Fig. 6.18), using the anomalous diffusion equation with $\alpha = 1/2$, that is, $\langle r^2\rangle = 4D_{\frac{1}{2}}(t-\tau_0)^{1/2}$.

This provides the coefficients $D_{\frac{1}{2}}$ as a function of the starting times τ_0. However, we find more relevant to use as time, the mean aging time associated with the computation of $D_{\frac{1}{2}}$, which we call *modified aging time*, $\tau^\star_{\rm ag}$, and which we define by

$$\tau^\star_{\rm ag} \equiv \tau_0 + \bar{\tau}_{\rm MSD}, \tag{6.23}$$

where $\bar{\tau}_{\rm MSD} = (0.5+1)/2\,{\rm s} = 0.75\,$s is the mean delay time associated with the computation of $D_{\frac{1}{2}}$.

In Fig. 6.19, we show as a function of $\tau^{\star}_{\mathrm{ag}}/\tau^{c}_{\mathrm{ag}}$ the coefficients $D_{\frac{1}{2}}$ that we obtain from the experiments with $B_0 = 170\,\mathrm{G}$ at long times (Fig. 6.18), but also at short times (Fig. 6.15), and additionally from experiments at $B_0 = 112\,\mathrm{G}$ and $127\,\mathrm{G}$, whose MSD measurements we do not present here. Note that we make the choice of $\alpha = 1/2$ because it appears to be the one best adapted to compare this large ensemble of experiments, even though it is not always the best choice for each individual experiment. Note also that we choose each of the values of B_0, namely $112\,\mathrm{G}$, $127\,\mathrm{G}$ and $170\,\mathrm{G}$, so that they are representative of the different types of experiments identified in Section 6.3.3: respectively, type NC, limit case, and type C.

As shown in Fig. 6.19, we find that for all three values of the magnetic field tested here, the coefficients $D_{\frac{1}{2}}$ decrease as the inverse of the dimensionless modified aging time $\tau^{\star}_{\mathrm{ag}}/\tau^{c}_{\mathrm{ag}}$, over 2-3 decades of time. At a fixed time, the values of $D_{\frac{1}{2}}/a^2$ are decreased as B_0 is increased, which is reminiscent of the populations of free particles in the different systems at a fixed time: φ increases as B_0 is increased. All decreases apparently stop at distinct plateau values at around the same time, namely at $\tau^{\star}_{\mathrm{ag}}/\tau^{c}_{\mathrm{ag}} \sim 4 \times 10^3$. At such times, φ has reached its long time limit value, as shown in Fig. 6.16: either finite ($B_0 = 112\,\mathrm{G}$, type NC experiment) or vanishing ($B_0 = 127\,\mathrm{G}$ and $170\,\mathrm{G}$, resp. limit case and type C experiment). For the latter, all particles have nucleated into chains, hence the coefficients $D_{\frac{1}{2}}$ that we measure are relative to the diffusivity of the chains themselves. The values of these plateaus decrease with B_0, showing that chains are less mobile when B_0 is increased.

Note that we also tested $\alpha = 1/4$ and $\alpha = 1$ for computing the generalized coefficients of diffusion. We found that, if quantitatively the values of D_α depend on α, the trends are comparable to the results with $\alpha = 1/2$ presented in Fig. 6.19.

6.5.3 Partial conclusion for long times

In this section, we explored how the labyrinthine phase obtained at the end of *steady nucleation* (*i.e.*, $\tau_{\mathrm{ag}}/\tau^{c}_{\mathrm{ag}} \sim 5 \times 10^{-1}$) relaxes at long times, through both structural and dynamical analyses. The timescales involved here are large enough for observing chain rearrangements, which can be thought of as collective motion occurring much more slowly than single-particle displacements.

We demonstrated that the fraction of particles in chains, φ, grows towards 1 as the square root of time from the end of steady nucleation. We saw that this continuing nucleation process mostly leads to extending existing chains, instead of creating new pairs. In addition, we observed chain rearrangements, sometimes massive enough to lead to dramatic changes of the labyrinthine phase morphology. In type NC experiments (for which there is no long-time full "solidification"), morphological changes are weak: the number of chains, N_c, mean chain size, n_c, length, λ_c, and connectivity, κ_3, in the limit $\tau_{\mathrm{ag}} \to +\infty$ all take similar values than at the end of steady nucleation (although we noticed a temporary burst of connectivity and size). Then, trimers are the most common, but the proportions of 5- and more-than-5-particle-long chains increase as B_0 approaches the limit case value, $B_0 = 127\,\mathrm{G}$. In type C experiments (for which there is long-time full "solidification"), the labyrinthine phase undergoes *coarsening*: chains merge massively as the system ages, and their size, length and connectivity increase all the more quickly as B_0 approaches the limit case value, $127\,\mathrm{G}$; however, their long-time values seem similar. In these experiments, 5-particle-long chains are more numerous, and longer chains form more quickly, as B_0 approaches the limit case value. In both type NC and type C experiments, chains containing an even number of particles progressively give way to chains with an odd number of particles, most probably due to gravity, but also because the merging of the former with the latter is energetically favored.

We also characterized the "freezing" of the labyrinthine phase as it ages. For all types of

experiments, we have shown that, first, the mean kinetic energy per particle, E_c, decreases as a power law in parallel to the power law increase of φ; and second, that the generalized coefficients of diffusion obtained in subdiffusive regimes decrease as the inverse of the age of the labyrinthine phase, which characterizes the dramatic *slowing down* of its dynamics as it ages.

Finally, at long times, the granular labyrinthine phase for type C experiments is like a disordered system that undergoes coarsening through slow relaxation, and as such is comparable to glassy systems, which also approach equilibrium slowly [103]. In both cases, a metastable state evolves into another metastable state due to agitation and so on, as the system moves towards the global minimum of energy of its multi-dimensional energy landscape (*i.e.*, equilibrium in glassy systems) [121, 122]. Each jump corresponds to a rearrangement event, which in our system consists of the motion of increasingly larger chains, and in glassy systems of large-scale cooperative motion.

However, unlike in glassy systems, in our system there are two distinct populations of particles, namely free and nucleated; caging effects are only relevant for the free particles, and not for those in the slowly rearranging chains; the dramatic slowdown of the dynamics measured by the generalized coefficients of diffusion is most probably due to the freezing of the free particles and not due to the decreasing mobility of chains (indeed when $\varphi \sim 1$, $D_{\frac{1}{2}}$ reaches a plateau value); and the long-time state is, for the granular labyrinthine phase, intrinsically out-of-equilibrium due to the nature of this system.

Yet, motivated by the similarities in the nature of the structural rearrangements that occur in the aging granular labyrinthine phase and in thermal glassy systems, we will further investigate our system's relaxation time- and length-scales, and characterize the dynamical heterogeneities it displays because of chain-rearrangement events.

6.6 Conclusion

In this chapter, we explored the time evolution of the granular labyrinthine phase introduced in Chapter 5, from its emergence at extremely short times, to its aging at very long times.

We started by characterizing the effects of a "magnetic quench", *i.e.*, a rapid increase in the vertical magnetic field, on the obtained labyrinthine phase. We concluded that the stronger the quench, the more disordered and hence the farther from its long-time state is the granular labyrinthine phase. Aiming at obtaining the labyrinthine phase that is as prone to evolving with time as possible, we decided to use a very strong magnetic quench.

We found that the time evolution of the quenched granular labyrinthine phase can be separated into two main phases: at short times, *steady nucleation*, and at long times a continuing nucleation process and chain rearrangements simultaneously, leading to a *coarsening* of the labyrinthine phase.

Steady nucleation refers to the irreversible process of aggregation of free particles into chains, right after the quench. Then, we found that nucleation is accelerated by increasing the magnetic field B_0. For experiments of type NC, chains grow quickly and develop little branching simultaneously for all B_0, while for experiments of type C the system does not undergo significant morphological changes. We concluded that this system, in the future, could be used for testing a particular type of transition from an agitated state into an absorbing phase, between the "free" and the "chain" states of our granular particles.

At long times, the labyrinthine phase coarsens in type C experiments: the remaining free particles continue nucleating, but much more slowly, and at the same time chains rearrange in

a relaxation process that implies massive chain merging events and hence marked chain growth and branching development. In type NC experiments, changes during relaxation are minor. Our results show that strong analogies exist between the aging of the labyrinthine phase and aging in thermal glassy systems, hence we see perspective in pushing further investigation in this direction by using tools specific to the study of slowly relaxing disordered systems.

Aside from these analogies, we have shown that labyrinthine phases are systems that are very rich on their own. Indeed, they constitute a novel class of disordered systems which undergo slow relaxation, with a wide variety of processes that can occur in a coupled manner, like chain rearrangements and merging in parallel with a slow nucleation process.

Finally, our results are in qualitative agreement with the work of Riemann *et al.* [110] on ferrimagnetic garnet films and with the simulations of Haw [103]: labyrinthine phases slowly relax at long times, which is reminiscent of glassy systems. This conclusion seems, however, in disagreement with the suggestion of Dobnikar *et al.* [65] that labyrinthine phases –for them, made of colloids, but very much analogous to the one we studied here– may be equilibrium phases, and thus stationary states. Hence this suggests investigating the possible time dependence of their colloidal labyrinthine phase, in order to compare with our results on the granular labyrinthine phase and with microscopic glassy systems.

To conclude this chapter, let us propose another possible approach for studying the relaxation of the granular labyrinthine phase. As we have seen, its relaxation is generally slow due to strong confinement making it hard for the system to reorganize. In order to accelerate relaxation, one could use a magnetic field oscillating between a target value and a lower value, instead of a being fixed at this target value. Through such an "annealing" process, confinement would be periodically decreased, then reconfiguration events favored and relaxation accelerated, as used for instance by Riemann *et al.* [110]. Such a method would be particularly relevant in the search of a long-time limit state of the granular labyrinthine phase. Can the system reach a state of parallel stripes? Or is this state inaccessible, as suggested for similar colloidal labyrinthine phases [65]?

Figure	Γ	B_0 (G)	α_q (G.s^{-1})	τ_{ag} (s)	n_{pic}	f_{acq} (Hz)	*iter*
6.1, 6.2	2.02 ± 0.01	212 ± 1	10.6 ± 0.01	15	40	4	50
6.3	2.03 ± 0.02	171 ± 1	*var.*	0.9×10^{-2}	10	780	10
6.4	2.06 ± 0.03	*var.*	$(1.08 \pm 0.02) \times 10^3$	*mult.*	≤ 17	780	1
6.7, 6.8, 6.9, 6.11, 6.12, 6.13, 6.14, 6.16, 6.17	2.03 ± 0.02	*mult.*	$(1.07 \pm 0.01) \times 10^3$	*var.*	*var.*	780	10 (or 1)
6.15, 6.18	2.01 ± 0.01	171 ± 1	$(1.07 \pm 0.01) \times 10^3$	*mult.*	800	780	1
6.19	2.01 ± 0.01	*mult.*	$(1.07 \pm 0.01) \times 10^3$	*var.*	50	780	1

Table 6.2 Experimental parameters for the figures of Chapter 6. Γ is the dimensionless acceleration defined in Eq. 1.10; B_0 is the applied transverse magnetic field; $\alpha_q = \mathrm{d}B/\mathrm{d}t$ is the quenching parameter; τ_{ag} is the post-quenching aging time defined in Section 1.2.1; n_{pic} is the number of pictures recorded; f_{acq} is the acquisition frequency; and *iter* is the number of repeated experiments with the identical parameters. The errors indicated correspond to the standard deviation of the measurements. The entry *var.* (resp., *mult.*) indicates that the quantity is the main variable (a variable for which multiple values are taken) for the experiments. All experiments are performed using the circular cell with a gap size $e = 1.48\,a$.

Conclusion

Conclusion and perspective

In this thesis, we have studied the self-organization properties of a quasi-two-dimensional ensemble of vibrated magnetic granular particles. We have shown that either ordered or slowly relaxing disordered states can be generated by tuning the applied magnetic field.

In Chapter 4, we presented the first experimental realization of a quasi-two-dimensional granular gas whose typical out-of-equilibrium and dissipative properties are progressively replaced by those of a molecular gas at thermal equilibrium, by tuning an external field. We achieved this with a granular gas composed of soft-ferromagnetic balls vibrated at a fixed strength and immersed in an external vertical magnetic field. The particle area fraction was about 20 %. By increasing the magnetic field, we increased the ratio of the magnetic repulsive interaction to the mechanical agitation strength, ε. A moderate increase of ε decreased the collision rate and thus the energy dissipated in particle-particle collisions, bringing the granular gas closer to the quasi-elastic limit. By further increasing ε, we observed a continuous phase transition to a collisionless, nearly crystalline phase, already reported in [26].

In Chapter 5, we demonstrated that a disordered labyrinthine phase made of discrete particles can be generated in a macroscopic and out-of-equilibrium model experiment, and, for the first time, we characterized the transition that leads to it from a liquid-like state by means of particle tracking. For this, we used the same quasi-two-dimensional granular gas as in Chapter 4 but at a higher particle area fraction, namely about 50 %. By increasing the applied magnetic field, we made the system undergo a transition from a dissipative gas state, to a state of coexisting chains of particles and free particles, to a labyrinthine phase almost only composed of these chains. The stability of the latter, which are buckled and confined between the top and bottom plates, is a three-dimensional effect. The parameter setting the vertical confinement, namely the gap size, is then essential to explain the different phases of this granular medium, as has also been shown for colloidal systems [65, 106]. Even though, if the structure of the phases obtained in this macroscopic experiment resembles that of the phases found in thermal equilibrium in Monte-Carlo simulations and colloidal monolayers [65, 106, 104], the kinetics of the transition described in this chapter is intrinsically an out-of-equilibrium process, as we saw in Chapter 6.

In Chapter 6, we showed that the granular labyrinthine phase is a disordered metastable state which undergoes slow relaxation. We saw that, shortly after a strong magnetic quench, this highly disordered structure arises from a nucleation process that occurs homogeneously across the system. We further observed that, once the timescale of observation becomes of the order of the timescale of chain displacements, slow chain rearrangements become apparent. This leads to a coarsening of the labyrinthine phase, along with a dramatic slowing down of its dynamics, which makes it tempting to call it a "glass of chains" [103]. Our results corroborate the two existing studies on the long-time evolution of a labyrinthine phase, namely in a thermal system [110] and in numerical simulations [103], and strongly question the view that labyrinthine phases as stationary, or even equilibrium states [65].

To summarize, we have seen that adding dipolar magnetic interactions between the particles

of a granular gas leads to self-organization phenomena that had not been previously observed in such a macroscopic and out-of-equilibrium model system. We are not only able to tune the distance of a dissipative granular gas to the quasi-elastic limit by controlling these interactions, but also to study the transitions to a collisionless crystalline state and a labyrinthine phase made of chains of macroscopic particles at contact, both of which have counterparts in microscopic systems. We have also identified the key role of the protocol in designing disordered labyrinthine phases with different structural and dynamical properties.

The strong analogies between our interacting granular gas and some colloidal systems, despite the dissipative nature of the collisions between grains and grain-plate friction, suggest that advances in these two fields can benefit each other. More generally, we hope that these results will motivate the exploration of granular gases with distance interactions as macroscopic model systems for self-organization phenomena in interacting many-body systems.

In Chapter 4, Chapter 5 and Chapter 6, we proposed a few possible lines of research, to which we would like to add the following ones.

One exciting question is: What more can we learn from a detailed analysis in Fourier space of the transition from a liquid-like to a crystalline state described in Chapter 4? In particular, to what extent is this transition analogous to two-dimensional crystal melting as described by the Kosterlitz-Thouless-Halpering-Nelson-Young (KTHNY) scenario [123]? An experimental confirmation for the KTHNY theory has been reported with a colloidal model system with repulsive magnetic dipole–dipole interactions [124]. Moreover, the work of Schockmel *et al.* [26], on a granular system similar to ours, supports this analogy too and shows the existence of two successive steps. To tackle this question more completely, we have ongoing collaborative work with Gustavo Castillo from Universidad de Chile (previously from ENS Paris). Our idea is to analyze the two successive second-order transitions that occur during crystallization, and possibly to show critical behavior near these transitions (divergence of the relevant quantities as power laws). Moreover, studying velocity correlations in Fourier space enables us to track propagating waves, which can be seen as analogous to phonons. The behavior of these correlations at large scale provides us with a "speed of sound" related to the elastic constants of the lattice [125], and for which the KTHNY theory predicts values for both transitions.

Finally, there is now a need to bridge the gap between the different phases observed in our experiments, that is, to build up the full phase diagram of the magnetic granular gas. However, the parameter space is extremely large. In Chapter 4 and Chapter 5, we studied the transitions to crystalline and labyrinthine phases for two densities ϕ, fixed gap size e and shaking strength Γ, and only the magnetic field B_0 was varied. There are also a number of parameters other than ϕ, e, B_0 and Γ than may be relevant, including those of the processing pathway (*e.g.*, rate of increase of the magnetic field, aging time, etc.), friction and restitution coefficients, and bead physical properties (magnetic permeability, mass, diameter, etc.). What are the phases found in the regions of parameter space that we have not explored yet? Experiments on colloidal systems by Osterman *et al.* [106], in particular, give insight on the variety of phases that we could observe. Indeed, even though dissipative collisions and friction in our system may lead to novel phases, many of the parameters relevant in our experiments are also relevant for colloidal systems. For example, a collisionless square ordered phase at low density is obtained in [106], which differs from the hexagonal crystalline phase that we described in Chapter 4. Such a state exists when, although chain formation does not occur, interactions are too strong for the hexagonally ordered phase to be stable. Indeed, a square lattice enables reducing the magnetic forces by distortion without geometrical frustration (particles are then alternatively in contact with

the bottom and top plate), which is impossible to achieve in a triangular lattice.

In order to thoroughly explore the parameter space of the magnetic granular gas (particle area fraction, applied magnetic field, gap size, etc.), we are currently working in collaboration with Eric Opsomer and Nicolas Vandewalle from University of Liège, Belgium, on molecular dynamics simulations of this system. So far, we have simulated a system of particles with mass, size and permeability identical to those used in the experiments, in a square cell of side 25 mm. The roughness of the bottom plate is not physically represented but is accounted for by randomly scattering the particles after a particle-plate collision, a process for which we adjusted the parameters so as to obtain particle velocity distributions that match the experimental ones. We have successfully checked for a particle density $\phi \sim 0.2$ that the results of the simulations quantitatively match those of the experiments across the "crystallization" transition when we increase B_0.

With these simulations, we have so far explored the phases of the magnetic granular gas, on one hand for a fixed gap size of $e/a = 1.5$, in the plane (ϕ, B_0), as shown in Fig. 7.1, and on the other hand for a fixed magnetic field $B_0 = 400\,\mathrm{G}$, in the plane (ϕ, e), as shown in Fig. 7.2. In Fig. 7.1, classical dissipative granular gas states are found along the row at $B_0 = 0\,\mathrm{G}$ and for increasing ϕ; the transition from a dissipative gas to a hexagonal crystalline state, as in Chapter 4, along the column at $\phi = 0.2$ and for increasing B_0; and the transition from dissipative gas to labyrinthine phase, as in Chapter 5, along the column at $\phi = 0.5$ and for increasing B_0. The different states observed in the simulations are in good agreement with those observed in the experiments, and generalize the picture that has emerged from the latter. Fig. 7.2 gives an idea of the extremely wide variety of morphologies that can be accessed by varying the gap size e/a. In particular, phases with square ordered regions resembling those in colloidal systems [106] are found for $e/a = 1.3$ and $\phi \gtrsim 0.5$. For gap size $e/a \geq 1.5$, we obtain a labyrinthine phase whose morphology strongly differs from one gap size value to an other. Specifically, when particles can almost totally overlap, with $e/a = 1.9$, preferential directions of alignment of the short chains appear, making these phases differ from the disordered labyrinthine phases that we have studied in this thesis.

To conclude, these numerical simulations provide results that not only corroborate the experimental results presented in this thesis, but also challenge us to explain the large variety of phases found in the different regions of parameter space. In the future, we will use them to further explore the multi-dimensional phase space of the granular gas and to guide new experiments. These simulations also offer the possibility to test the effects of other types of interaction potentials, or of the influence of gravity, on the self-organization properties of this macroscopic model system, which opens additional exciting perspectives.

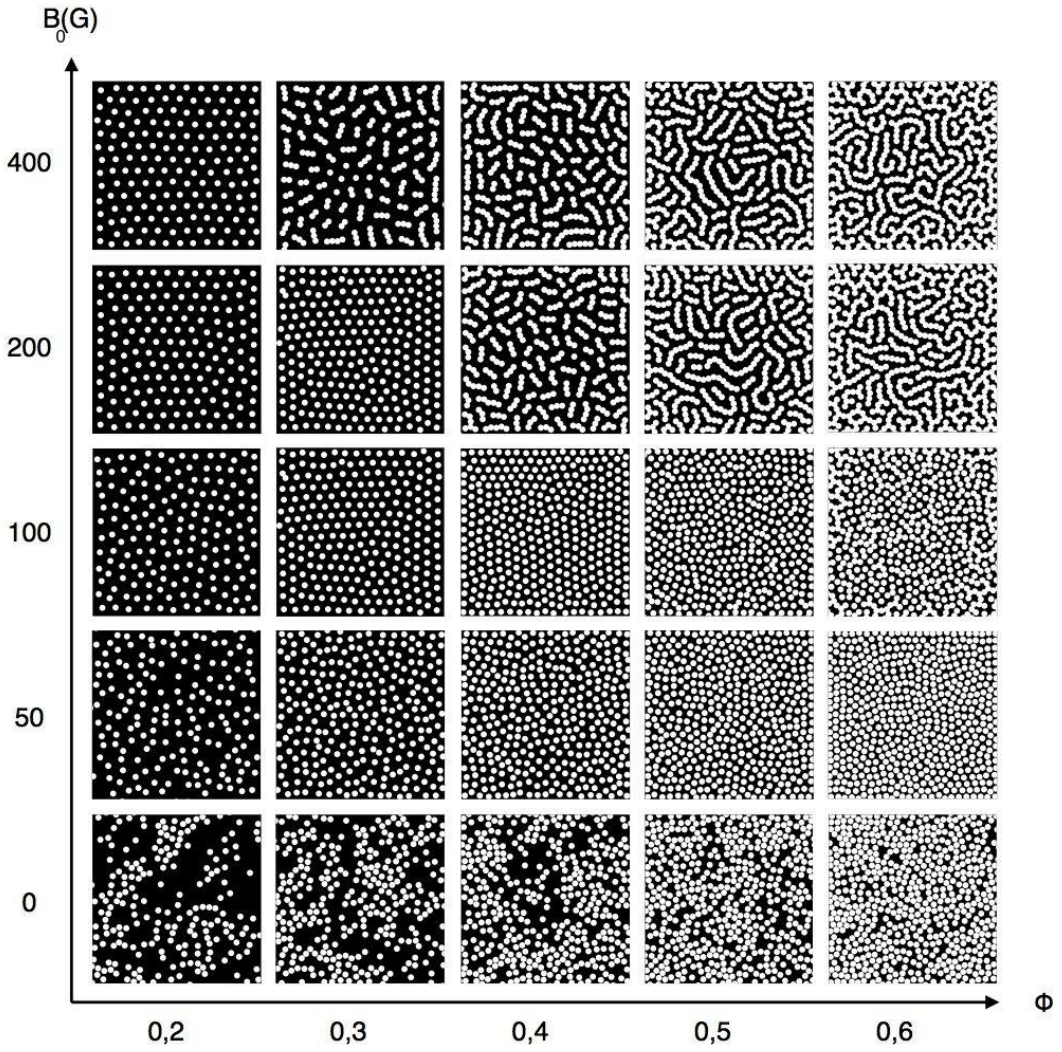

Figure 7.1 Phase diagram of the magnetic granular gas obtained from molecular dynamics simulations, when the particle area fraction, ϕ, and the applied magnetic field, B_0, are varied. The gap size is $e = 1.5\,a$. In particular, dissipative granular gas states are found along the row with $B_0 = 0\,\mathrm{G}$, while the transition from dissipative granular gas to crystalline state (resp., to labyrinthine phase), studied in Chapter 4 (Chapter 5), is observed along the column at $\phi = 0.2$ ($\phi = 0.5$).

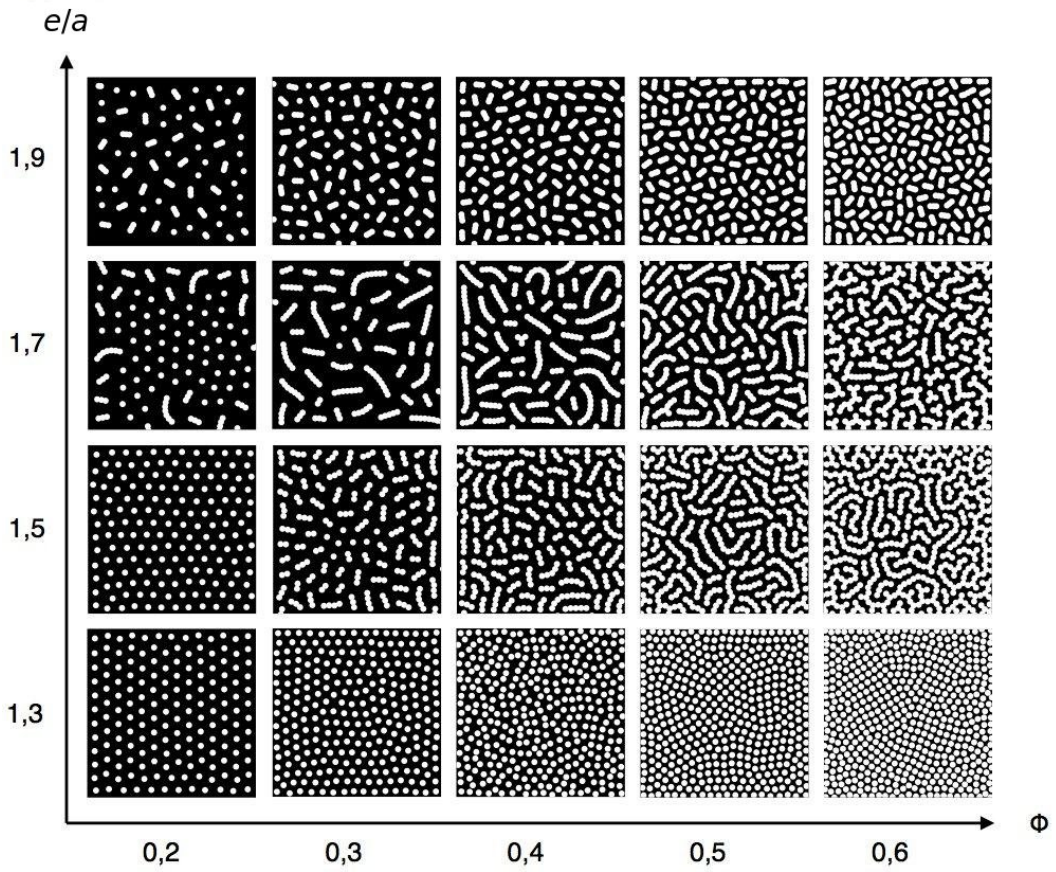

Figure 7.2 Phase diagram of the magnetic granular gas obtained from molecular dynamics simulations, when the particle area fraction, ϕ, and the gap size, e, are varied. The applied magnetic field is $B_0 = 400\,\mathrm{G}$. The morphologies of the phases strongly depend on the gap size value. Contactless ordered phases are observed for $e/a = 1.3$, while phases mostly composed of chains occupy the region $e \geq 1.5$. The disordered nature of the labyrinthine phase discussed in Chapter 5 and Chapter 6 seems to be partially lost for large gap sizes, like $e/a = 1.9$, where chains clearly display preferential orientations.

Appendix A

Kinetics of a granular system

Appendix A: Kinetics of a granular system

↑ back to contents

Abstract

If describing the collisions between two grains is the first stone for understanding the kinetics of an ensemble of colliding granular particles, the collective properties of such a system are obtained using statistical tools. Here, we explore two types of granular systems: first, in a transient state, once the injection of energy is stopped, and second, with a homogeneous and continuous input of mechanical energy. We aim at writing a constitutive equation and at characterizing the velocity distributions in both cases. Most of what follows is inspired from the reference book of Brilliantov and Pöschel [7] and of an article of van Noije and Ernst [38].

1 Homogeneous cooling granular fluid

Let us consider an ensemble of N identical granular particles of a mass m and a radius σ, in a space of dimension d. Initially, these particles are agitated and thus constitute a granular fluid. However, since collisions are dissipative, the system cools down at each collision. We study the evolution of this system in the phase space.

1.1 Definitions

The single particle distribution function $f(\mathbf{r}, \mathbf{v}, t)$ describes the probability of finding a particle at the position $\mathbf{r}$ and with the velocity $\mathbf{v}$ at time t:

$$f(\mathbf{r}, \mathbf{v}, t) = \sum_{i=1}^{N} \langle \delta(\mathbf{r}_i(t) - \mathbf{r}) \delta(\mathbf{v}_i(t) - \mathbf{v}) \rangle \tag{A.1}$$

where $(\mathbf{r}_i(t), \mathbf{v}_i(t))$ is the location of particle i at time t in the phase space. Moreover, the integral of f over the full phase space equals the total number of particles:

$$\int f(\mathbf{r}, \mathbf{v}, t) \, \mathrm{d}\mathbf{r} \, \mathrm{d}\mathbf{v} = N. \tag{A.2}$$

We focus here on the case of a homogeneous system, which allows us to rule out the space dependence of f. From this assumption, we can relate the moments of f with certain macroscopic properties of the granular gas, namely with its *number density*, n, its *flow velocity* $\langle \mathbf{v} \rangle$ (which vanishes here), and its *granular temperature*, T:

$$\int f(\mathbf{v}, t)\, \mathrm{d}\mathbf{v} = n \tag{A.3}$$

$$\int \mathbf{v} f(\mathbf{v}, t)\, \mathrm{d}\mathbf{v} = n \langle \mathbf{v} \rangle = 0 \tag{A.4}$$

$$\int \frac{1}{2} m v^2 f(\mathbf{v}, t)\, \mathrm{d}\mathbf{v} = n \left\langle \frac{1}{2} m v^2 \right\rangle = \frac{d}{2} n T(t). \tag{A.5}$$

where the angle brackets denote an ensemble average.

We used here the term *granular temperature*, in analogy with the temperature in the theory of molecular gases, which we defined as the average kinetic energy of the grains. Following this analogy, we can define a *thermal-like velocity*, v_0, such as

$$T(t) = \frac{1}{2} m v_0^2(t). \tag{A.6}$$

Note that for $d = 2$, first, v_0 equals the standard deviation of the velocity distribution, and second, Eq. A.5 simplifies into the expression of the *two-dimensional granular temperature*, which we denote T_g,

$$T_g(t) = \frac{1}{2} m \left\langle v^2 \right\rangle. \tag{A.7}$$

1.2 Enskog-Boltmann equation

Very generally, the evolution of the homogeneous distribution $f(\mathbf{v}, t)$ with respect to time can be seen as resulting from three contributions: the influence of external forces on the particles, the (self-)diffusion of the particles, and the contribution of the collisions between particles. Hence we can write the general equation

$$\frac{\partial f}{\partial t} = \left(\frac{\partial f}{\partial t} \right)_{\text{ext.}} + \left(\frac{\partial f}{\partial t} \right)_{\text{diff.}} + \left(\frac{\partial f}{\partial t} \right)_{\text{coll.}} \tag{A.8}$$

which becomes, in the absence of external forces and in the homogeneous case, *i.e.*, when the first and second terms of the RHS vanish,

$$\frac{\partial f}{\partial t} = \left(\frac{\partial f}{\partial t} \right)_{\text{coll.}}. \tag{A.9}$$

In other words, under these assumptions, the probability at time t of finding a particle with a velocity comprised between $\mathbf{v}$ and $\mathbf{v} + \mathrm{d}\mathbf{v}$ is solely modified by the effects of collisions. The collisions involving particles whose velocities are comprised in the interval $[\mathbf{v}, \mathbf{v} + \mathrm{d}\mathbf{v}]$, or *direct* collisions, mostly drive these particles into another velocity interval and hence correspond to a loss in the RHS of Eq. A.9 ; while *inverse* collisions involve particles whose velocities are initially outside the interval $[\mathbf{v}, \mathbf{v} + \mathrm{d}\mathbf{v}]$, but end up being inside it, hence contributing as a gain.

The complete calculation of the RHS of Eq. A.9, *i.e.*, the collision term, is done for example in [7]. To make a long story short, the starting point of this calculation is the relationship between the incoming velocities ($\mathbf{v}_1$ and $\mathbf{v}_2$) and outgoing velocities ($\mathbf{v}_1{}'$ and $\mathbf{v}_2{}'$) for two

colliding identical particles 1 and 2,

$$\begin{cases} \mathbf{v}_1{}' = \mathbf{v}_1 - \dfrac{1}{2}(1+\epsilon)(\mathbf{v}_{12}\cdot\mathbf{e}_{12})\,\mathbf{e}_{12} \\ \mathbf{v}_2{}' = \mathbf{v}_2 + \dfrac{1}{2}(1+\epsilon)(\mathbf{v}_{12}\cdot\mathbf{e}_{12})\,\mathbf{e}_{12} \end{cases} \tag{A.10}$$

where ϵ is the *coefficient of restitution* and $\mathbf{e}_{12}$ is the unit vector linking the center of particle 1 to the center of particle 2.

From this, one can count the number of particles entering and exiting the volume of the phase space where particles have velocities comprised in the range $[\mathbf{v}, \mathbf{v}+\mathrm{d}\mathbf{v}]$, as described above. The gain and loss contributions of, respectively, the inverse and direct collisions, to the collision term of Eq. A.9, can be written in the form of a bilinear collision operator, $I[f,f]$, called *collision integral*. We will not make it explicit here, but will instead focus on the resulting formulation of Eq. A.9, which is called the *Boltzmann equation* of a homogeneously cooling granular gas:

$$\frac{\partial f}{\partial t}(\mathbf{v}_1, t) = I[f,f]. \tag{A.11}$$

This equation is actually based on the strong hypothesis of "molecular chaos" stating that the velocities of two colliding particles are not correlated with each other. However, although this hypothesis is relevant for ideal molecular gases, it has been shown both experimentally and numerically that it does not properly fits to granular gases, even in the dilute case [20, 83, 126]. To tackle this problem, David Enskog had the idea of taking into account finite-size effects, which increase collision frequency by comparison with a system of point-like particles [127]. Further developing this original idea led to the *Enskog-Boltzmann equation* for the homogeneously cooling granular gas [128]:

$$\frac{\partial f}{\partial t}(\mathbf{v}_1, t) = g_\sigma(n)\, I[f,f] \tag{A.12}$$

where $g_\sigma(n)$, called the *Enskog factor*, is the contact value of the pair correlation of hard spheres at density n. Note that for the three-dimensional case, Carnahan and Starling [129] proposed an expression of $g_\sigma(n)$ for hard sphere fluids at equilibrium, which is valid for a large density n,

$$g_\sigma(n) = \frac{2-\phi}{2(1-\phi)^3} \tag{A.13}$$

where ϕ is the packing fraction, that is $\phi = \frac{1}{6}\pi n\sigma^3$, and whose expression in two dimensions is [44, 69]:

$$g_\sigma^{\mathrm{2D}}(n) = \frac{1-7\phi/16}{(1-\phi)^2}. \tag{A.14}$$

1.3 High-energy tails in the homogeneous cooling state

As demonstrated by Goldshtein and Shapiro [130], the Enskog-Boltzmann equation (*i.e.*, Eq. A.12) admits an isotropic scaling solution, $\tilde{f}$, involving the thermal velocity defined by Eq. A.6:

$$f(\mathbf{v}, t) = \frac{n}{v_0^2(t)}\tilde{f}\left(\frac{v}{v_0(t)}\right). \tag{A.15}$$

In Eq. A.5, we introduced the *granular temperature*, T, in analogy with the *thermodynamic temperature*. Even though, since collisions between grains are inelastic, one can expect the velocity distribution function (VDF) of a granular gas to deviate from the VDF of a molecular

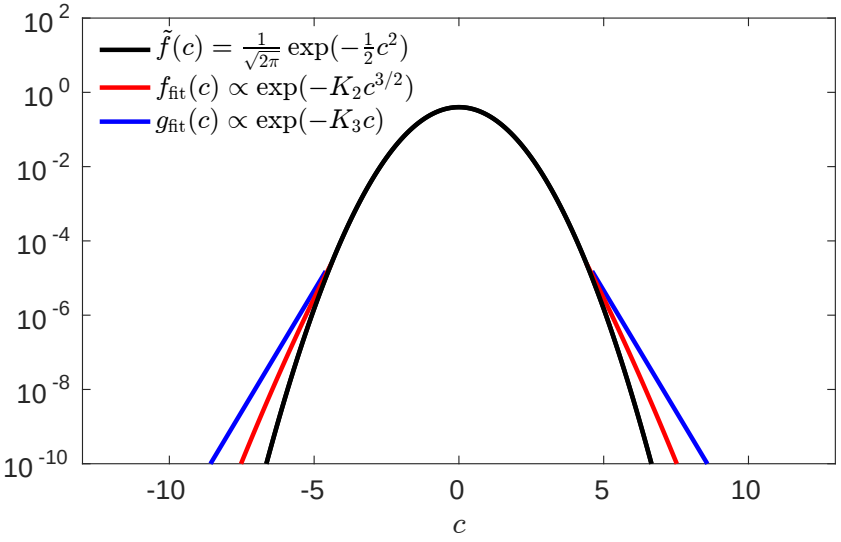

Figure A.1 Gaussian velocity density function (VDF) and sketches of exponential and stretched exponential high-energy velocity tails. Black curve: Gaussian VDF with zero mean and a standard deviation of 1; Red curves: sketches of portions of a stretched exponential (prop. factor 10, $K_2 = 1$) for $|c| > 5$; Blue lines: sketches of portions of an exponential (prop. factor 50, $K_3 = 3$) for $|c| > 5$. Note that in experiments, measuring velocities such as $c > 5$ is rare enough so that measures of the VDF smaller than 10^{-4} are significantly noisy. It is therefore hard to compare experimental results with these analytical predictions for $|c| > 5$.

gas, namely, the Maxwell-Boltzmann distribution:

$$f_{\text{MB}}(\mathbf{v}) = \left(\frac{m}{2\pi kT}\right)^{3/2} \exp\left(-\frac{mv^2}{2kT}\right). \tag{A.16}$$

Investigating the shape of the high-energy tails of the VDF, that is, for $c = \frac{|\mathbf{v}|}{v_0(t)} \gg 1$, Esipov and Pöschel demonstrated [37] that the scaled distribution function has the form

$$\tilde{f}(c) \propto \exp(-A\, c), \tag{A.17}$$

where A is a constant. This means that the high-energy tails of homogeneously cooling granular gases are overpopulated compared to Maxwell-Boltzmann's VDF, which are proportional to $\exp(-Bc^2)$, with B a constant. We give a graphical representation of this overpopulation in Fig. A.1, where we have plotted the normalized Gaussian distribution (in black) along with a sketch of a high-energy exponential tail (in blue), $g_{\text{fit}}(c) \propto \exp(-K_3 c)$ (with $K_3 = 3$ and a proportionality factor of 50).

2 Uniformly heated granular fluid

When a horizontal monolayer of granular particles is fluidized by vertical vibrations of the plate it reposes on, grains are mechanically agitated and energy input is homogeneous across the system, that is, all grains receive on average the same amount of mechanical energy. Such a system is called a *uniformly heated granular fluid*. In the absence of external magnetic field, the

quasi-two-dimensional granular gas presented in this thesis is such a fluid.

2.1 Modified Enskog-Boltzmann equation

In the uniformly heated case, we can model the evolution of the velocity of particle i, $\mathbf{v}_i$, by the stochastic equation:

$$\frac{\mathrm{d}\mathbf{v}_i}{\mathrm{d}t} = \frac{\mathbf{F}_i}{m} + \hat{\boldsymbol{\xi}}_i \tag{A.18}$$

with $\mathbf{F}_i$ the force due to inter-particles collisions and $\hat{\boldsymbol{\xi}}_i$ the random acceleration due to external forcing. We assume that $\hat{\boldsymbol{\xi}}_i$ is a Gaussian white noise of strength ξ_0^2 and uncorrelated for different particles:

$$\left\langle \hat{\xi}_{i\alpha}(t)\, \hat{\xi}_{j\beta}(t') \right\rangle = \xi_0^2 \delta_{ij} \delta_{\alpha\beta} \delta(t - t') \tag{A.19}$$

where δ is the Kronecker symbol, α and β represent dimensions, t and t' two times, and the angular bracket an ensemble average. This description is valid as long as the system is thermodynamically large (*i.e.*, $N \to \infty$), and that the time between random kicks is small compared to the mean free time of the equivalent homogeneously cooling state.

In order to account for the *heating* due to the random kicks modelled through the $\hat{\boldsymbol{\xi}}_i$'s in Eq. A.18, the Enskog-Boltzmann equation for the homogeneous single particle distribution function $f(\mathbf{v}, t)$, given in Eq. A.12, is corrected with a Fokker-Planck diffusion term, as demonstrated by van Kampen [131]:

$$\frac{\partial f}{\partial t}(\mathbf{v}_1, t) = g_\sigma(n)\, I[f, f] + \frac{\xi_0^2}{2} \left(\frac{\partial}{\partial \mathbf{v}_1} \right)^2 f(\mathbf{v}_1, t). \tag{A.20}$$

In this equation, interestingly, the diffusion coefficient ξ_0^2 for the velocities is proportional to the rate of energy input $\frac{d}{2}\xi_0^2$ per unit mass, and even equals it in two dimensions. Note also that this additional Fokker-Planck diffusion term does not correspond to the contribution of an external force $\mathbf{F}_{\mathrm{ext}}$, which would have led instead to a new term $\mathbf{F}_{\mathrm{ext}} \cdot \boldsymbol{\nabla}_{v_1} f$ in the LHS of the Enskog-Boltzmann equation.

2.2 High-energy velocity tails for the uniformly heated granular fluid

When heating exactly balances the dissipation of energy due to inelastic collisions, the particle distribution function is stationary and the granular temperature is a constant. In order to find a stationary solution to the modified Enskog-Boltzmann equation (Eq. A.20), Van Noije and Ernst [38] used a scaled stationary distribution function $\tilde{f}$ in a similar fashion to what Goldshtein and Shapiro did in the homogeneous cooling case:

$$f(\mathbf{v}) = \frac{n}{v_0^2} \tilde{f}\left(\frac{v}{v_0} \right). \tag{A.21}$$

Injecting this stationary particle distribution function in Eq. A.20 and denoting $\mathbf{c}_1 = \mathbf{v}_1 / v_0$ a scaled velocity yields:

$$\tilde{I}[\tilde{f}, \tilde{f}] + \frac{\xi_0^2}{2 v_0^3 g_\sigma(n) n \sigma} \left(\frac{\partial}{\partial \mathbf{c}_1} \right)^2 \tilde{f}(c_1) = 0, \tag{A.22}$$

where $\tilde{I}[\tilde{f}, \tilde{f}]$ is the dimensionless form of the collision integral. The authors further show that

inserting solutions of the form

$$\tilde{f}(c) \propto \exp(-Ac^{\beta}) \tag{A.23}$$

in Eq. A.22, with A a constant, yields for large rescaled velocities $c \gg 1$,

$$\beta = \frac{3}{2}. \tag{A.24}$$

This result implies that in the uniformly heated case, granular gases display VDF high-energy tails that are overpopulated in comparison with molecular gases (Gaussian VDF), while being underpopulated relative to homogeneously cooling granular gases (exponential high-energy VDF tails). Stretched exponential VDF tails with exponent $\beta = 3/2$ are sketched in Fig. A.1 (in red). It is important to remark that, as stressed by Barrat and Trizac [39], one has to be careful when comparing experimental results with this theoretical prediction, since the condition $c \gg 1$ is rarely, if ever, verified using experimental data. Indeed, detecting a statistically significant quantity of events with velocities of about 10 times (or even 5 times) the thermal-like velocity is experimentally very hard to achieve. Hence, overpopulated VDF high-energy tails in experiments for $c \not\gg 1$ cannot be related to the present theory. However, considering velocity-dependant coefficients of restitution in numerical simulations seemed to be the answer to the question, since then, VDF from numerical simulations satisfyingly reproduce the experimental VDF [34, 132].

Bibliography

[1] S. Merminod, M. Berhanu and E. Falcon, Transition from a dissipative to a quasi-elastic system of particles with tunable repulsive interactions. *EPL*, 2014, vol. 106, page 44005. Cited on pages 3, 22, 89 and 145.

[2] S. Merminod, T. Jamin, E. Falcon and M. Berhanu, Transition to a labyrinthine phase in a driven granular medium. *Physical Review E*, 2015, vol. 92, page 062205. Cited on pages 3, 22 and 113.

[3] B. Andreotti, Y. Forterre and O. Pouliquen. *Granular Media: Between Fluid and Solid*. Cambridge, England, Cambridge University Press, 2013. Cited on pages 17, 64 and 82.

[4] I. S. Aranson and L. S. Tsimring, Patterns and collective behavior in granular media: Theoretical concepts. *Reviews of Modern Physics*, 2006, vol. 78, num. 2, pages 641–692. Cited on pages 18 and 19.

[5] H. Jaeger, S. Nagel and R. Behringer, Granular solids, liquids, and gases. *Reviews of Modern Physics*, 1996, vol. 68, num. 4, pages 1259–1273. Cited on page 19.

[6] S. Ogawa. Multitemperature theory of granular materials. *In* S. C. Cowin and M. Satake, editors. *Proceedings of the U.S.–Japan Seminar on Continuum Mechanical and Statistical Approaches in the Mechanics of Granular Materials*, Tokyo, 1978. Cited on page 18.

[7] N. V. Brilliantov and T. Poschel. *Kinetic Theory of Granular Gases*. Oxford, England, Oxford University Press, 2004. Cited on pages 18, 19, 64, 82, 172 and 173.

[8] C. K. K. Lun, S. B. Savage, D. J. Jeffrey and N. Chepurniy, Kinetic theories for granular flow: inelastic particles in Couette flow and slightly inelastic particles in a general flowfield. *Journal of Fluid Mechanics*, 1984, vol. 140, pages 223–256. Cited on page 19.

[9] K. K. Rao and P. R. Nott. *An introduction to granular flow*. Cambridge series in chemical engineering. New York, USA, Cambridge University Press, 2008. Cited on page 19.

[10] N. Mujica and R. Soto. Dynamics of Noncohesive Confined Granular Media. *In* J. Klapp, L. Sigalotti, A. Medina, A. López and G. Ruiz-Chavarría, editors. *Recent Advances in Fluid Dynamics with Environmental Applications*, pages 445–463. Springer, 2016. Cited on page 19.

[11] E. Falcon, S. Fauve and C. Laroche, Cluster formation, pressure and density measurements in a granular medium fluidized by vibrations. *European Physical Journal B*, 1999, vol. 9, pages 183–186. Cited on page 19.

[12] E. FALCON, R. WUNENBURGER, P. ÉVESQUE, S. FAUVE, C. CHABOT, Y. GARRABOS and D. BEYSENS, Cluster Formation in a Granular Medium Fluidized by Vibrations in Low Gravity. *Physical Review Letters*, 1999, vol. 83, num. 2, pages 440–443. Cited on page 19.

[13] E. OPSOMER, F. LUDEWIG and N. VANDEWALLE, Phase transitions in vibrated granular systems in microgravity. *Physical Review E*, 2011, vol. 84, num. 5, page 051306. Cited on page 19.

[14] E. OPSOMER, N. VANDEWALLE, M. NOIRHOMME and F. LUDEWIG, Clustering and segregation in driven granular fluids. *European Physical Journal E*, 2014, vol. 37, page 115. Cited on page 19.

[15] R. D. WILDMAN and D. J. PARKER, Coexistence of Two Granular Temperatures in Binary Vibrofluidized Beds. *Physical Review Letters*, 2002, vol. 88, num. 6, page 064301. Cited on page 19.

[16] J. S. OLAFSEN and J. S. URBACH, Clustering, Order, and Collapse in a Driven Granular Monolayer. *Physical Review Letters*, 1998, vol. 81, num. 20, pages 4369–4272. Cited on pages 19, 20, 84 and 87.

[17] W. LOSERT, D. G. W. COOPER, J. DELOUR, A. KUDROLLI and J. P. GOLLUB, Velocity statistics in excited granular media. *Chaos*, 1999, vol. 9, num. 2, pages 682—-690. Cited on pages 19, 20, 84 and 87.

[18] F. ROUYER and N. MENON, Velocity fluctuations in a homogeneous 2D granular gas in steady state. *Physical Review Letters*, 2000, vol. 85, num. 17, pages 3676–3679. Cited on pages 19 and 20.

[19] D. L. BLAIR and A. KURDOLLI, Velocity correlations in dense granular gases. *Physical Review E*, 2001, vol. 64, page 050301(R). Cited on pages 19 and 20.

[20] A. PREVOST, D. A. EGOLF and J. S. URBACH, Forcing and velocity correlations in a vibrated granular monolayer. *Physical review letters*, 2002, vol. 89, num. 8, page 084301. Cited on pages 19 and 174.

[21] D. L. BLAIR and A. KUDROLLI, Clustering transitions in vibrofluidized magnetized granular materials. *Physical Review E*, 2003, vol. 67, num. 2, page 021302. Cited on pages 19, 21, 27 and 85.

[22] A. PREVOST, P. MELBY, D. A. EGOLF and J. S. URBACH, Nonequilibrium two-phase coexistence in a confined granular layer. *Physical Review E*, 2004, vol. 70, num. 5, page 050301. Cited on pages 19 and 20.

[23] M. SAINT JEAN, C. GUTHMANN and G. COUPIER, Relaxation and ordering processes in "macroscopic Wigner crystals". *The European Physical Journal B*, 2004, vol. 39, pages 61–68. Cited on pages 19, 21 and 85.

[24] G. COUPIER. *Élasticité et ancrage dans des cristaux de Wigner macroscopiques : un système modèle pour l'étude du piégeage faible*. Phd thesis, Université Paris Diderot, 2006. Cited on pages 19, 21 and 85.

[25] P. M. REIS, R. A. INGALE and M. D. SHATTUCK, Forcing independent velocity distributions in an experimental granular fluid. *Physical Review E*, 2007, vol. 75, num. 5, page 051311. Cited on pages 19, 20, 50, 84, 85 and 87.

[26] J. Schockmel, E. Mersch, N. Vandewalle and G. Lumay, Melting of a confined monolayer of magnetized beads. *Physical Review E*, 2013, vol. 87, num. 6, page 062201. Cited on pages 19, 21, 26, 79, 85, 87, 88, 165 and 166.

[27] I. S. Aranson, D. Blair, V. A. Kalatsky, G. W. Crabtree, W. K. Kwok, V. M. Vinokur and U. Welp, Electrostatically-Driven Granular Media: Phase Transitions and Coarsening. *Physical Review Letters*, 2000, vol. 84, num. 15, pages 3306–3309. Cited on page 20.

[28] I. S. Aranson and J. S. Olafsen, Velocity fluctuations in electrostatically driven granular media. *Physical Review E*, 2002, vol. 66, num. 6, page 061302. Cited on page 20.

[29] K. Kohlstedt, A. Snezhko, M. V. Sapozhnikov, I. S. Aranson, J. S. Olafsen and E. Ben-Naim, Velocity distributions of granular gases with drag and with long-range interactions. *Physical Review Letters*, 2005, vol. 95, num. 6, page 068001. Cited on pages 20 and 85.

[30] F. Lechenault and K. E. Daniels, Equilibration of granular subsystems. *Soft Matter*, 2010, vol. 6, num. 13, pages 3074–3081. Cited on page 20.

[31] K. Nichol and K. E. Daniels, Equipartition of rotational and translational energy in a dense granular gas. *Physical Review Letters*, 2012, vol. 108, num. 1, page 018001. Cited on page 20.

[32] I. Goldhirsch and G. Zanetti, Clustering Instability in Dissipative Gases. *Physical Review Letters*, 1993, vol. 70, num. 11, pages 1643–1647. Cited on pages 20 and 84.

[33] A. Puglisi, A. Gnoli, G. Gradenigo, A. Sarracino and D. Villamaina, Structure factors in granular experiments with homogeneous fluidization. *Journal of Chemical Physics*, 2012, vol. 136, num. 1. Cited on pages 20, 54, 84, 85, 87 and 88.

[34] A. Barrat and E. Trizac, Random inelasticity and velocity fluctuations in a driven granular gas. *European Physical Journal E*, 2003, vol. 11, num. 1, pages 99–104. Cited on pages 20 and 177.

[35] J. S. Van Zon and F. C. MacKintosh, Velocity distributions in dissipative granular gases. *Physical Review Letters*, 2004, vol. 93, num. 3, page 038001. Cited on page 20.

[36] S. J. Moon, J. B. Swift and H. L. Swinney, Steady-state velocity distributions of an oscillated granular gas. *Physical Review E*, 2004, vol. 69, num. 1, page 011301. Cited on page 20.

[37] S. E. Esipov and T. Poeschel, The Granular Phase Diagram. *Journal of Statistical Physics*, 1997, vol. 86, num. 5-6, page 1385. Cited on pages 20 and 175.

[38] T. P. C. van Noije and M. H. Ernst, Velocity Distributions in Homogeneously Cooling and Heated Granular Fluids. *Granular Matter*, 1998, vol. 1, pages 57–64. Cited on pages 20, 84, 172 and 176.

[39] A. Barrat, E. Trizac and M. H. Ernst, Granular gases: dynamics and collective effects. *Journal of Physics: Condensed Matter*, 2005, vol. 17, num. 24, page S2429. Cited on pages 20, 84, 87 and 177.

[40] W. LOSERT, D. G. COOPER and J. P. GOLLUB, Propagating front in an excited granular layer. *Physical review. E*, 1999, vol. 59, num. 5, pages 5855–5861. Cited on page 20.

[41] P. MELBY, F. V. REYES, A. PREVOST, R. ROBERTSON, P. KUMAR, D. A. EGOLF and J. S. URBACH, The dynamics of thin vibrated granular layers. *Journal of Physics: Condensed Matter*, 2005, vol. 17, pages S2689–S2704. Cited on page 20.

[42] G. CASTILLO, N. MUJICA and R. SOTO, Fluctuations and criticality of a granular solid-liquid-like phase transition. *Physical Review Letters*, 2012, vol. 91, page 012141. Cited on page 20.

[43] P. M. REIS, R. A. INGALE and M. D. SHATTUCK, Caging dynamics in a granular fluid. *Physical Review Letters*, 2007, vol. 98, num. 18, page 188301. Cited on pages 20 and 148.

[44] P. M. REIS, R. A. INGALE and M. D. SHATTUCK, Crystallization of a quasi-two-dimensional granular fluid. *Physical Review Letters*, 2006, vol. 96, num. 25, page 258001. Cited on pages 20 and 174.

[45] J. S. OLAFSEN and J. S. URBACH, Two-dimensional melting far from equilibrium in a granular monolayer. *Physical Review Letters*, 2005, vol. 95, num. 9, page 098002. Cited on page 20.

[46] E. BEN-NAIM, Z. A. DAYA, P. VOROBIEFF and R. E. ECKE, Knots and random walks in vibrated granular chains. *Physical Review Letters*, 2001, vol. 86, num. 8, pages 1414–1417. Cited on page 20.

[47] K. SAFFORD, Y. KANTOR, M. KARDAR and A. KUDROLLI, Structure and dynamics of vibrated granular chains: Comparison to equilibrium polymers. *Physical Review E*, 2009, vol. 79, num. 6, page 061304. Cited on page 20.

[48] L. OYARTE, P. GUTIÉRREZ, S. AUMAÎTRE and N. MUJICA, Phase transition in an out-of-equilibrium monolayer of dipolar vibrated grains. *Physical Review E*, 2013, vol. 87, num. 2, page 022204. Cited on pages 21 and 85.

[49] R. MESSINA, S. ALJAWHARI, L. BÉCU, J. SCHOCKMEL, G. LUMAY and N. VANDEWALLE, Quantitatively mimicking wet colloidal suspensions with dry granular media. *Scientific Reports*, 2015, vol. 5, page 10348. Cited on page 21.

[50] J. D. JACKSON. *Classical Electrodynamics*. New York, J. Wiley & Sons Inc., Third ed., 1999. Cited on pages 22 and 65.

[51] European Space Agency Space Grains Project. https://spacegrains.org/ (accessed: 2016-07-01). Cited on page 22.

[52] Marteau Lemarié, Billes de précision - billes acier et inox. http://www.marteau-lemarie.fr/billes-precision/billes-acier-inox/ (accessed 2016-04-18). Cited on page 26.

[53] B. M. SHAH, J. J. NUDELL, K. R. KAO, L. M. KEER, Q. JANE WANG and K. ZHOU, Semi-active particle-based damping systems controlled by magnetic fields. *Journal of Sound and Vibration*, 2011, vol. 330, num. 2, pages 182–193. Cited on page 26.

[54] K. ARA, Magnetic Characteristics of Ferromagnetic Stainless Steels. *IEEE Transactions on Magnetics*, 1989, vol. 25, num. 3, pages 2617–2623. Cited on page 40.

[55] G. Bertotti and I. D. Mayergoyz. *The Science of Hysteresis*. Elsevier, 2005. Cited on page 40.

[56] D. Blair and E. Dufresne. The matlab particle tracking code repository, http://site.physics.georgetown.edu/matlab/ (accessed: 2013-04-18). Cited on pages 47 and 56.

[57] S. H. Ahn. Convolution in 2D. http://www.songho.ca/dsp/convolution/convolution.html (accessed: 2016-06-01). Cited on page 48.

[58] J. A. Richards and X. Jia. *Remote Sensing Digital Image Analysis*. Springer, 2006, 439 pages. Cited on page 49.

[59] M. Shattuck. Particle tracking. http://gibbs.engr.ccny.cuny.edu/technical/Tracking/ChiTrack.php (accessed: 2013-04-18). Cited on pages 50, 52, 53 and 54.

[60] A. Patwardhan, Subpixel position measurement using 1D, 2D and 3D centroid algorithms with emphasis on applications in confocal microscopy. *Journal of Microscopy*, 1997, vol. 186, pages 246–257. Cited on page 54.

[61] J. Crocker and D. Grier, Methods of Digital Video Microscopy for Colloidal Studies. *Journal of Colloid and Interface Science*, 1996, vol. 179, num. 1, pages 298–310. Cited on page 56.

[62] P. J. Lu. *Gelation and Phase Separation of Attractive Colloids*. Phd thesis, Harvard University, 2008. Cited on page 58.

[63] D. J. Griffiths. *Introduction to Electrodynamics*. San Francisco, Pearson International Ed., Third ed., 2008. Cited on pages 65 and 66.

[64] W. F. Brown. Magnetic Materials. *In* E. U. Condon and H. Odishaw, editors. *Handbook of Chemistry and Physics*, chapiter 8. McGraw-Hill, 1958. Cited on page 70.

[65] J. Dobnikar, J. Fornleitner and G. Kahl, Ground states of model core-softened colloids. *Journal of Physics: Condensed Matter*, 2008, vol. 20, page 494220. Cited on pages 71, 102, 105, 123, 160 and 165.

[66] N. Osterman, I. Poberaj, J. Dobnikar, D. Frenkel, P. Ziherl and D. Babić, Field-Induced self-Assembly of suspended colloidal membranes. *Physical Review Letters*, 2009, vol. 103, num. 22, pages 2–5. Cited on page 79.

[67] K. Mueller, N. Osterman, D. Babic, C. N. Likos, J. Dobnikar and A. Nikoubashman, Pattern formation and coarse-graining in two-dimensional colloids driven by multiaxial magnetic fields. *Langmuir*, 2014, vol. 30, page 5088. Cited on page 79.

[68] B. G. Elmegreen, R. Koch, K. Yasuoka, H. Furusawa, T. Narumi, R. Susukita and T. Ebisuzaki, Numerical simulations of magnetic materials with MD-GRAPE: Curvature induced anisotropy. *Journal of Magnetism and Magnetic Materials*, 2002, vol. 250, pages 39–48. Cited on page 79.

[69] S. Gonzalez, A. R. Thornton and S. Luding, Free cooling phase-diagram of hard-spheres with short- and long-range interactions. *European Physical Journal: Special Topics*, 2014, vol. 223, pages 2205–2225. Cited on pages 79 and 174.

[70] D. FRENKEL and B. SMIT. *Understanding Molecular Simulation*. San Diego, USA, Academic Press, 2002, 638 pages. Cited on page 81.

[71] S. J. MOON, M. D. SHATTUCK and J. B. SWIFT, Velocity distributions and correlations in homogeneously heated granular media. *Physical Review E*, 2001, vol. 64, num. 3, page 031303. Cited on page 84.

[72] J. S. OLAFSEN and J. S. URBACH, Velocity distributions and density fluctuations in a granular gas. *Physical Review E*, 1999, vol. 60, num. 3, pages R2468–71. Cited on pages 84 and 87.

[73] J. STAMBAUGH, D. P. LATHROP, E. OTT and W. LOSERT, Pattern formation in a monolayer of magnetic spheres. *Physical Review E*, 2003, vol. 68, page 02026207. Cited on page 85.

[74] C. LAROCHE and F. PÉTRÉLIS, Observation of the condensation of a gas of interacting grains. *The European Physical Journal B*, 2010, vol. 77, num. 4, pages 489–492. Cited on page 85.

[75] D. LOPEZ and F. PÉTRÉLIS, Surface instability driven by dipole-dipole interactions in a granular layer. *Physical Review Letters*, 2010, vol. 104, num. 15, page 158001. Cited on page 85.

[76] A. GHAZALI and J.-C. S. LÉVY, Solid-liquid transition in 2D dipolar systems. *Europhysics Letters (EPL)*, 2006, vol. 74, num. 2, pages 355–361. Cited on page 85.

[77] P. DILLMANN, G. MARET and P. KEIM, Comparison of 2D melting criteria in a colloidal system. *Journal of Physics: Condensed Matter*, 2012, vol. 24, num. 46, page 464118. Cited on page 85.

[78] S. DEUTSCHLÄNDER, T. HORN, H. LÖWEN, G. MARET and P. KEIM, Two-dimensional melting under quenched disorder. *Physical Review Letters*, 2013, vol. 111, num. 9, page 098301. Cited on page 85.

[79] F. BOYER and E. FALCON, Two-dimensional melting of a crystal of ferrofluid spikes. *Physical Review Letters*, 2009, vol. 103, num. 14, page 144501. Cited on page 85.

[80] T. SCHEFFLER and D. E. WOLF, Collision rates in charged granular gases. *Granular Matter*, 2002, vol. 4, num. 3, pages 103–113. Cited on pages 85, 87 and 88.

[81] M. K. MÜLLER and S. LUDING, Homogeneous Cooling with Repulsive and Attractive Long-Range Potentials. *Mathematical Modelling of Natural Phenomena*, 2011, vol. 6, num. 4, pages 118–150. Cited on pages 85 and 88.

[82] T. van NOIJE, M. ERNST and R. BRITO, Ring kinetic theory for an idealized granular gas. *Physica A*, 1998, vol. 251, num. 1-2, page 266. Cited on page 87.

[83] G. GRADENIGO, A. SARRACINO, D. VILLAMAINA and A. PUGLISI, Non-equilibrium length in granular fluids: From experiment to fluctuating hydrodynamics. *EPL*, 2011, vol. 96, num. 1, page 14004. Cited on pages 88 and 174.

[84] P. N. PUSEY and W. van MEGEN, Phase behavior of concentrated suspensions of nearly hard colloidal spheres. *Nature*, 1986, vol. 320, pages 340–342. Cited on page 88.

[85] Y. Han, N. Y. Ha, A. M. Alsayed and A. G. Yodh, Melting of two-dimensional tunable-diameter colloidal crystals. *Physical Review E*, 2008, vol. 77, page 041406. Cited on pages 88, 89, 101 and 102.

[86] Y. Han, Y. Shokef, A. M. Alsayed, P. Yunker, T. C. Lubensky and A. G. Yodh, Geometric frustration in buckled colloidal monolayers. *Nature*, 2008, vol. 456, pages 898–903. Cited on pages 88, 89, 101 and 102.

[87] Z. Yao and M. Olvera De La Cruz, Topological defects in flat geometry: The role of density inhomogeneity. *Physical Review Letters*, 2013, vol. 111, num. 11, page 115503. Cited on page 88.

[88] R. Kubo, The fluctuation-dissipation theorem. *Reports on Progress in Physics*, 1966, vol. 29, pages 255–284. Cited on page 88.

[89] J. J. Brey, M. I. G. de Soria and P. Maynar, Breakdown of the fluctuation-dissipation relations in granular gases. *EPL*, 2008, vol. 84, num. 2, page 24002. Cited on page 88.

[90] N. Rivas, P. Cordero, D. Risso and R. Soto, Segregation in quasi-two-dimensional granular systems. *New Journal of Physics*, 2011, vol. 13, page 05018. Cited on page 89.

[91] M. C. Cross and P. C. Hohenberg, Pattern formation outside of equilibrium. *Reviews of Modern Physics*, 1993, vol. 65, num. 3, pages 851–1112. Cited on page 100.

[92] A. M. Turing, The Chemical Basis of Morphogenesis. *Philosophical Transactions of the Royal Society of London. Series B, Biological Sciences*, 1952, vol. 237, num. 641, pages 37–72. Cited on page 100.

[93] M. Seul and D. Andelman, Domain shapes and patterns: the phenomenology of modulated phases. *Science*, 1995, vol. 267, num. 5197, pages 476–483. Cited on page 101.

[94] K. De'Bell, A. MacIsaac and J. Whitehead, Dipolar effects in magnetic thin films and quasi-two-dimensional systems. *Reviews of Modern Physics*, 2000, vol. 72, num. 1, pages 225–257. Cited on page 101.

[95] A. Stoycheva and S. Singer, Stripe Melting in a Two-Dimensional System with Competing Interactions. *Physical Review Letters*, 2000, vol. 84, num. 20, pages 4657–4660. Cited on pages 101 and 102.

[96] M. Seul, L. R. Monar, L. O'Gorman and R. Wolfe, Morphology and Local Structure in Labyrinthine Stripe Domain Phase. *Science*, 1991, vol. 254, num. 5038, pages 1616–1618. Cited on pages 101 and 124.

[97] M. Seul, L. R. Monar and L. O'Gorman, Pattern analysis of magnetic stripe domains morphology and topological defects in the disordered state. *Philosophical Magazine Part B*, 1992, vol. 66, num. 4, pages 471–506. Cited on pages 101 and 105.

[98] M. Seul and M. J. Sammon, Competing interactions and domain-shape instabilities in a monomolecular film at an air-water interface. *Physical Review Letters*, 1990, vol. 64, pages 1903–1906. Cited on page 101.

[99] A. J. Dickstein, S. Erramilli, R. E. Goldstein, D. P. Jackson and S. A. Langer, Labyrinthine pattern formation in magnetic fluids. *Science*, 1993, vol. 261, pages 1012–1015. Cited on page 101.

[100] F. ELIAS, C. FLAMENT, J.-C. BACRI and S. NEVEU, Macro-Organized Patterns in Ferrofluid Layer: Experimental Studies. *Journal de Physique I France*, 1997, vol. 7, pages 711–728. Cited on page 101.

[101] B. SANDNES, H. A. KNUDSEN, K. J. MÅLØY and E. G. FLEKKØY, Labyrinth Patterns in Confined Granular-Fluid Systems. *Physical Review Letters*, 2007, vol. 99, num. 3, page 038001. Cited on page 101.

[102] B. SANDNES, E. G. FLEKKØY, H. A. KNUDSEN, K. J. MÅLØY and H. SEE, Patterns and flow in frictional fluid dynamics. *Nature communications*, 2011, vol. 2, pages 1–8. Cited on page 101.

[103] M. D. HAW, Growth kinetics of colloidal chains and labyrinths. *Physical Review E*, 2010, vol. 81, num. 3, page 031402. Cited on pages 102, 122, 123, 159, 160 and 165.

[104] G. MALESCIO and G. PELLICANE, Stripe phases from isotropic repulsive interactions. *Nature materials*, 2003, vol. 2, pages 97–100. Cited on pages 102, 104, 105 and 165.

[105] P. J. CAMP, Structure and phase behavior of a two-dimensional system with core-softened and long-range repulsive interactions. *Physical Review E*, 2003, vol. 68, num. 6, page 061506. Cited on pages 102 and 104.

[106] N. OSTERMAN, D. BABIČ, I. POBERAJ, J. DOBNIKAR and P. ZIHERL, Observation of condensed phases of quasiplanar core-softened colloids. *Physical Review Letters*, 2007, vol. 99, num. 24, page 248301. Cited on pages 102, 104, 123, 165, 166 and 167.

[107] J.-L. BARRAT and J.-P. HANSEN. *Basic Concepts for Simple and Complex Liquids*. Cambridge, England, Cambridge University Press, 2003. Cited on page 105.

[108] G. HUNTER and E. WEEKS, The physics of the colloidal glass transition. *Reports on Progress in Physics*, 2012, vol. 75, page 66501. Cited on pages 105, 123 and 127.

[109] F. H. STILLINGER and P. G. DEBENEDETTI, Glass Transition Thermodynamics and Kinetics. *Annual Review of Condensed Matter Physics*, 2013, vol. 4, num. 1, pages 263–285. Cited on page 105.

[110] B. REIMANN, R. RICHTER and I. REHBERG, Glasslike relaxation of labyrinthine domain patterns. *Physical Review E*, 2002, vol. 65, num. 3, page 031504. Cited on pages 105, 122, 123, 160 and 165.

[111] M. LE BERRE, E. RESSAYRE, A. TALLET, Y. POMEAU and L. DI MENZA, Example of a chaotic crystal: The labyrinth. *Physical Review E*, 2002, vol. 66, num. 2, page 026203. Cited on page 105.

[112] W. GOTZE and L. SJOGREN, Relaxation processes in supercooled liquids. *Reports on Progress in Physics*, 1992, vol. 55, pages 241–376. Cited on page 123.

[113] S. HAVLIN and D. BEN-AVRAHAM, Diffusion in disordered media. *Advances in Physics*, 1987, vol. 36, num. 6, pages 695–798. Cited on page 123.

[114] R. METZLER and J. KLAFTER, The random walk's guide to anomalous diffusion: a fractional dynamics approach. *Physics Reports*, 2000, vol. 339, pages 1–77. Cited on page 148.

[115] R. Pastore, A. Coniglio and M. Pica Ciamarra, From cage-jump motion to macroscopic diffusion in supercooled liquids. *Soft Matter*, 2014, vol. 10, num. 31, pages 5724–5728. Cited on page 148.

[116] R. Pastore, M. Pica Ciamarra, G. Pesce and A. Sasso, Connecting short and long time dynamics in hard-sphere-like colloidal glasses. *Soft Matter*, 2015, vol. 11, num. 3, pages 622–626. Cited on page 148.

[117] C. Scalliet, A. Gnoli, A. Puglisi and A. Vulpiani, Cages and Anomalous Diffusion in Vibrated Dense Granular Media. *Physical Review Letters*, 2015, vol. 114, num. 19, page 198001. Cited on page 148.

[118] H. Hinrichsen, Non-equilibrium critical phenomena and phase transitions into absorbing states. *Advances in Physics*, 2000, vol. 49, num. 7, pages 815–958. Cited on page 150.

[119] B. Néel, I. Rondini, A. Turzillo, N. Mujica and R. Soto, Dynamics of a first-order transition to an absorbing state. *Physical Review E*, 2014, vol. 89, num. 4, page 042206. Cited on page 150.

[120] L. Deike, B. Miquel, T. Jamin, B. Semin, M. Berhanu, E. Falcon and F. Bonnefoy, Role of the basin boundary conditions in gravity wave turbulence. *Journal of Fluid Mechanics*, 2014, vol. 781, pages 196–225. Cited on page 151.

[121] C. A. Angell, K. L. Ngai, G. B. Mckenna, P. F. Mcmillan and S. W. Martin, Relaxation in glassforming liquids and amorphous solids. *Journal of Applied Physics*, 2000, vol. 88, num. 6, pages 3113–3157. Cited on page 159.

[122] P. G. Debenedetti and F. H. Stillinger, Supercooled liquids and the glass transition. *Nature*, 2001, vol. 410, page 259. Cited on page 159.

[123] K. J. Strandburg, Two-dimensional melting. *Reviews of Modern Physics*, 1988, vol. 60, num. 1, pages 161–207. Cited on page 166.

[124] U. Gasser, C. Eisenmann, G. Maret and P. Keim, Melting of crystals in two dimensions. *ChemPhysChem*, 2010, vol. 11, pages 963–970. Cited on page 166.

[125] K. I. Golden, G. J. Kalman, P. Hartmann and Z. Donko, Dynamics of two-dimensional dipole systems. *Physical Review E*, 2010, vol. 82, num. 3, page 036402. Cited on page 166.

[126] R. Soto and M. Mareschal, Statistical mechanics of fluidized granular media: Short-range velocity correlations. *Physical Review E*, 2001, vol. 63, num. 4, page 9. Cited on page 174.

[127] S. Chapman and T. G. Cowling. *The Mathematical Theory of Non-uniform Gases*. New York, Cambridge University Press, 1970. Cited on page 174.

[128] P. Resibois and M. Leener. *Classical Kinetic Theory of Fluids*. New York, J. Wiley & Sons Inc., 1977. Cited on page 174.

[129] N. F. Carnahan and K. E. Starling, Equation of State for Nonattracting Rigid Spheres. *The Journal of Chemical Physics*, 1969, vol. 51, num. 2, page 635. Cited on page 174.

[130] A. GOLDSHTEIN and M. SHAPIRO, Mechanics of collisional motion of granular materials. Part 1. General hydrodynamic equations. *Journal of Fluid Mechanics*, 1995, vol. 282, pages 75–114. Cited on page 174.

[131] N. G. van KAMPEN. *Stochastic Processes in Physics and Chemistry*. Amsterdam, North-Holland, 1992. Cited on page 176.

[132] S. MCNAMARA and E. FALCON, Simulations of vibrated granular medium with impact-velocity-dependent restitution coefficient. *Physical Review E*, 2005, vol. 71, num. 3, page 031302. Cited on page 177.

Auto-organisation de particules magnétiques vibrées : Structure, dynamique et transitions

Résumé : Nous étudions l'auto-organisation dans un système modèle expérimental où l'agitation des particules et leurs interactions à distance sont en compétition. Ce système est composé de particules macroscopiques sphériques ferromagnétiques douces dans une cellule horizontale quasi-bidimensionnelle. Les particules sont agitées par vibration verticale de la cellule et acquièrent un moment magnétique induit en présence d'un champ magnétique externe vertical. En ajustant l'équilibre entre les forces dipolaires répulsives résultantes et l'agitation, nous provoquons des transitions entre des états de types fluides et solides. A faible densité de particules, nous examinons les phases et les transitions de phases rencontrées lorsque nous renforçons les interactions entre particules : d'abord un gaz granulaire dissipatif, puis un état dont les propriétés structurales et dynamiques s'approchent de celles d'un gaz idéal à l'équilibre thermodynamique, et enfin un état ordonné où les particules forment un réseau triangulaire. Nous nous intéressons aussi à l'auto-organisation du système à plus haute densité de particules, où nous observons un état labyrinthique désordonné principalement composé de chaînes de particules en contact. Ces chaînes, en zigzag entre la surface de la cellule et le couvercle, sont énergétiquement favorisées par l'anisotropie des interactions dipolaires. Nous caractérisons la transition de l'état de gaz granulaire vers cette phase labyrinthique. Enfin, nous explorons l'évolution temporelle de la phase labyrinthique au moyen d'une trempe magnétique. Nous observons une nucléation homogène aux temps courts et une augmentation de la taille typique des chaînes via une relaxation lente aux temps longs.

Mots clés : Milieux granulaires, systèmes hors équilibre, transitions de phase, états désordonnés, dynamique vitreuse.

Self-organization of vibrated and magnetized particles: Structure, dynamics and transitions

Abstract : We study self-organization in an experimental model system in which particle agitation competes with remote inter-particle interactions. This system is composed of macroscopic spherical soft-ferromagnetic particles in a horizontal quasi-two-dimensional cell. The particles are agitated by vibrating the cell vertically and are magnetized as induced dipoles by an external vertical magnetic field. By tuning the balance between the resulting repulsive dipole-dipole forces and agitation, we trigger transitions between fluid- and solid-like states. At low particle density, we examine the phases and phase transitions that occur as we strengthen the inter-particle interactions: from a dissipative granular gas, to a state whose structural and dynamical properties approach those of an ideal gas at thermodynamic equilibrium, to an ordered state in which the particles form a triangular lattice. We also investigate the self-organization of the system at a higher particle density, where we observe a disordered labyrinthine state mostly composed of chains of particles at contact. These chains, buckled between the top and bottom plates, are energetically favored due to the anisotropy of the dipole-dipole interactions. We characterize the transition from the granular gas state to this labyrinthine phase. Finally, we explore the temporal evolution of the labyrinthine phase by applying a magnetic quench. We observe homogeneous nucleation at short times and coarsening via slow relaxation at long times.

Keywords : Granular media, out-of-equilibrium statistical mechanics, phase transitions, disordered states, glassy dynamics.